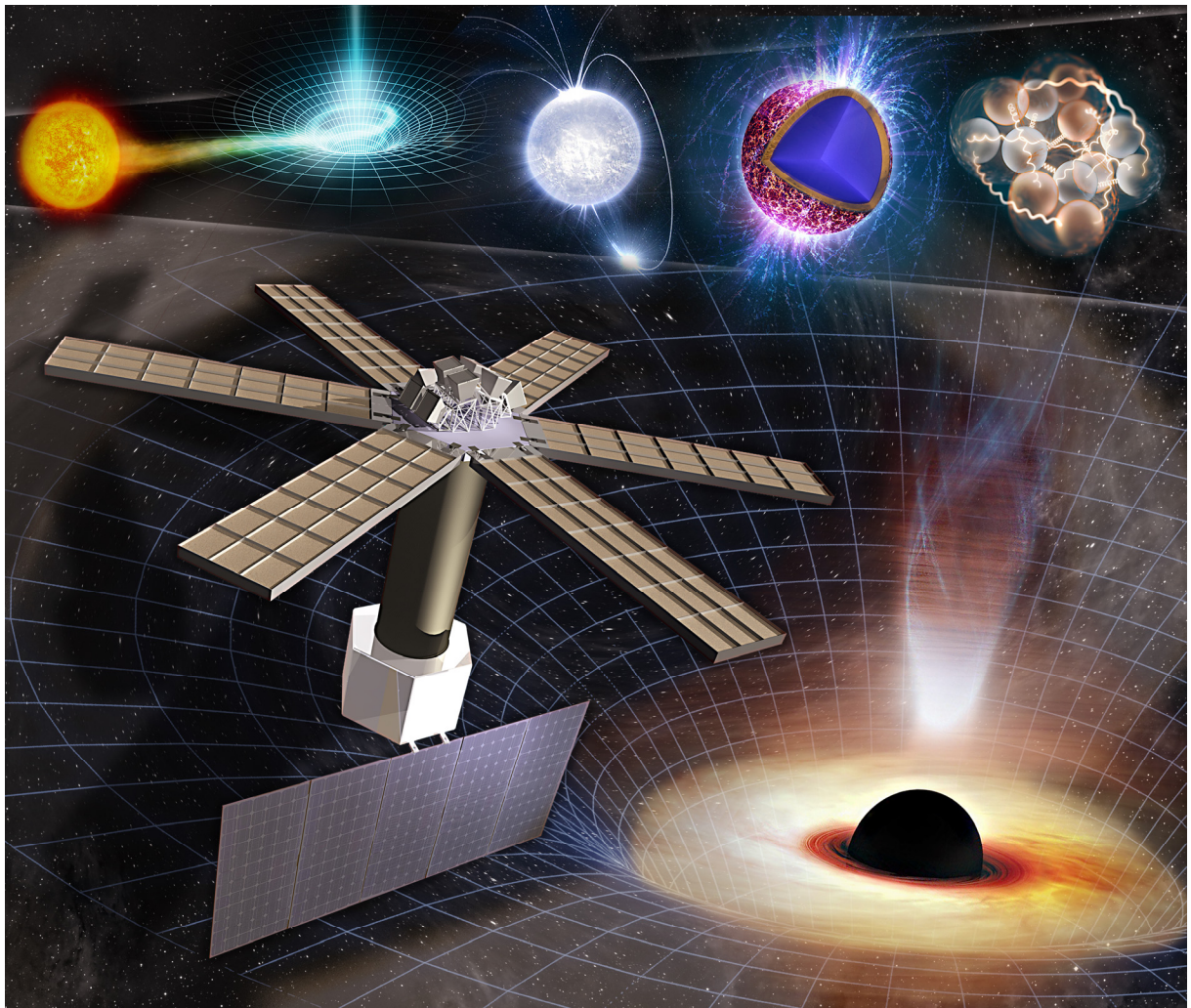


# LOFT

## The Large Observatory for X-ray Timing



Assessment Study Report

Artist view of LOFT with its prime science goals, from Supermassive Black Holes down to Nucleons in the ultra-dense Neutron Stars.

LOFT Assessment Study – Mission Summary				
<b>Key scientific goals</b>	<p><b>Equation of State:</b> Determine the pressure-density relation of cold ultra-dense matter: the Equation of State (EoS). The EoS depends on the composition of supra nuclear density matter (from purely nucleonic to strange quark matter) and on the nature of strong force and is observationally encoded in the neutron star mass-radius relation. Independent measurements of mass and radius with unprecedented accuracy will be performed for a number of neutron stars to accomplish this. Independent complementary techniques will be used to understand the systematic uncertainties.</p> <p><b>Strong Field Gravity:</b> Measure the effects of strong field gravity in the stationary spacetime metrics of black holes and neutron stars down to a few gravitational radii. Thanks to its large area combined with good spectral resolution, LOFT will for the first time study strong gravity on the timescales relevant to General Relativity close to black holes and neutron stars, such as rapid variations of relativistic iron lines and relativistic precession effects in quasi periodic oscillations.</p> <p><b>Observatory Science:</b> Use the unprecedented throughput of the LAD to perform spectral and timing observations of a wide variety of X-ray sources, producing for objects with fluxes down to ~1 mCrab the best energy resolved variability measurements ever obtained. With the WFM, monitor an exceptionally large fraction of the sky (<math>&gt; 1/3</math>) at any time with 5 arcmin resolution to catch transient sources and bright impulsive events and provide long-term variability records. These observations will revolutionize our understanding of sources such as gamma-ray bursts, magnetars, tidal disruption events and many other aspects of neutron stars, black holes and accretion physics.</p>			
	<b>Reference Core Payload</b>	<p><b>Large Area Detector</b></p> <p>Effective area: ~10 m<sup>2</sup> at 6 keV</p> <p>Throughput: 240.000 cts/s (1Crab)</p> <p>Maximum flux: 15 Crab</p> <p>Energy band: 2-30 keV (30-80 keV extended)</p> <p>Spectral resolution: 180-240 eV at 6 keV (CCD-class)</p> <p>Time resolution: 10 μs</p> <p>Timing capabilities: 15 × RXTE (variability S/N)</p> <p>Spectral timing capabilities: &gt; 200 × XMM-Newton (FeK<math>\alpha</math> variability S/N at &gt;0.2 Crab)</p> <p>Sensitivity: 0.1 mCrab in 100s (5<math>\sigma</math>)</p> <p>Field of view: 1 degree (collimated)</p> <p>Technology: 2016 Silicon Drift Detectors</p>	<p><b>Wide Field Monitor</b></p> <p>Source localization: 1 arcmin</p> <p>Angular resolution: 5 arcmin</p> <p>Energy band: 2-50 keV</p> <p>Spectral resolution: 300 eV FWHM (6 keV)</p> <p>Effective area: 170 cm<sup>2</sup> (peak)</p> <p>Sensitivity: 3 mCrab (5<math>\sigma</math>, 50 ks)</p> <p>Field of view: 4.1 steradian</p> <p>Onboard transient events localization</p> <p>Broadcast events coordinates &lt; 30 s</p> <p>Technology: 10 coded mask cameras, 40 Silicon Drift Detectors</p>	
<b>Overall Mission Profile</b>		<p>Lifetime: 3+2 years</p> <p>Consumables: 10 yr</p> <p>Launcher: Soyuz</p> <p>Launch date: 2022</p> <p>High gain antenna: steerable, X-band</p> <p>Data rate: 100 Gbit/day</p>		<p>Low-Earth Orbit: 550 km, &lt; 2.5° inclination</p> <p>Ground station: Kourou &amp; Malindi</p> <p>Pointing: 3 axis stabilized (15'' knowledge)</p> <p>Sky visibility: &gt;40% nominal &amp; &gt;65% extended</p> <p>Observing efficiency: &gt; 60%</p>
	<b>Description of the Spacecraft</b>	<b>Mass (Kg)</b>		<b>Power (W)</b>
LAD		967	LAD	1305
WFM		125	WFM	108
Service module		1254	Service module	389
Spacecraft dry mass		3472	Losses	200
Propellant		482	Battery charging	1450
Launch adapter		125	Total Power demands	3814
Total Mass (+ margins)		4070		

## Foreword

High-time-resolution X-ray spectral observations of compact objects provide direct access to strong-field gravity, to the equation of state of ultra-dense matter and to black hole masses and spins. A 10 m<sup>2</sup> class instrument with good spectral resolution is required to exploit the relevant diagnostics and answer two fundamental questions that are part of ESA's Cosmic Vision Theme "Matter under extreme conditions":

- What is the equation of state of ultra-dense matter in neutron stars?
- Does matter orbiting close to the event horizon follow the predictions of general relativity?

A proposal for such a large-area X-ray spectral timing observatory was submitted in response to the ESA call for M3 missions and subsequently selected for an assessment study.

The ESA M3 mission assessment activities for LOFT included an internal ESA study and two parallel industrial studies which were completed in early 2013. In addition payload studies were conducted for which two reviews were organized by ESA: the recommendations of the *Payload Review Committee* are addressed in a dedicated document<sup>1</sup> and many of them are also discussed in this yellow book (the justification of the science goals in §2; justification of the background estimates, sensitivity, effective area, spectral resolution and field of regard in §3). The number of AGNs in the core observational programme was updated to take the LOFT performance fully into account. Finally the ground segment responsibilities were agreed with ESA. The recommendations from the *Instrument Review panel* were addressed in detail in the instrument designs as described in the Preliminary Requirements Review data package that has been extensively reviewed by the ESA technical experts. Technology development activities are on-going in parallel to support relevant payload items. Whereas a descope of the mission is commonly required at this phase, in case of LOFT we have instead enhanced the mission performance in order to ensure the best scientific exploitation of the mission. This followed the selection of a launcher with greater capacity necessitated by the need to fit, with proper margins, the required 10 m<sup>2</sup> effective area, which remained essentially unchanged (see *Box 1*). Of course, this has affected the expected cost of the mission. Parallel to this work a large group of scientists worked together to study the science case and assess the expected quantitative results from the often qualitatively new types of information provided by the mission. This work, reported in this 'yellow book', in some cases led to new advances in the field, reported also in journal papers. The member states will procure the two instruments. ESA will provide the spacecraft, launch services and operations. To enhance the scientific productivity a set of small ground VHF receiving stations will be provided by member states. Member states also contribute to the science operations infrastructure.

The assessment study has successfully concluded that the concept of LOFT is rapidly maturing to the necessary Technology Readiness Level, earlier than required. Being judged as relatively low risk, then subject to a successful selection LOFT could be ready for a launch by the end of 2022.

### **Box 1: Mission enhancements since proposal submission**

Detailed analyses and simulations have confirmed that a 10 m<sup>2</sup> class instrument with good spectral resolution is required to attain the scientific objectives. Combining this area requirement with reasonable design margins led to the conclusion that a Soyuz launcher is necessary. Taking advantage of the extra launch capacity, the performance of the LOFT mission has been enhanced:

- Instantaneous field of view of the WFM has been increased from 3.4 sr to 4.1 sr in the anti-sun direction matching the accessible part of the sky while the sensitivity has been improved by adding 6 cameras to the original 4.
- A burst alert system has been added. The WFM allows for fast identification of GRBs and new transients and these will be dispatched to the scientific community within 30 s.
- The mission lifetime was increased from 2+1 to 3+2 years to ensure the observation of key transient events during the nominal mission lifetime. This also enables about 25 Ms for observatory science.
- Extend the instantaneous accessible fraction of the sky, by increasing the original 35% to 50% (requirement, but ESA studies show >65%), allowing for relaxed spectral resolution in the extended region.

<sup>1</sup> [http://www.isdc.unige.ch/loft/DOCS/publ/PRC\\_doc.pdf](http://www.isdc.unige.ch/loft/DOCS/publ/PRC_doc.pdf)

## Authorship, acknowledgements

This report has been prepared by the *LOFT* Team listed below.

<b>ESA Science Study Team (SST)</b>		
<i>Name</i>	<i>Affiliation</i>	<i>City, Country</i>
Barret, D.	IRAP	Toulouse, FR
Brandt, S. (WFM PI)	DTU Space	Copenhagen, DK
den Herder, J.-W.	SRON	Utrecht, NL
Feroci, M. (PI)	INAF-IAPS & INFN	Rome, IT
Hernanz, M.	IEEC-CSIC	Barcelona, ES
Pohl, M.	DPNC, University of Geneva	Geneva, CH
Santangelo, A.	Tübingen University	Tübingen, DE
Stella, L.	INAF-OA Roma	Rome, IT
van der Klis, M.	University of Amsterdam	Amsterdam, NL
Zane, S. (LAD PI)	UCL-MSSL	London, UK

The ESA Team supporting the activities is composed by:

<b>ESA study team</b>		
Ayre, M. (Study Manager)	ESA	ESTEC, Noordwijk, NL
Lumb, D. (Study Scientist)	ESA	ESTEC, Noordwijk, NL
Boenke, T. (Payload Manager)	ESA	ESTEC, Noordwijk, NL
Corral van Damme, C. (System Engineer)	ESA	ESTEC, Noordwijk, NL
Kuulkers, E. (Science Operations Study Manager)	ESA	ESAC, Villanueva de la Cañada, ES
<b>ESA Coordinator</b>		
Parmar, A.	ESA	ESTEC, Noordwijk, NL

LOFT Support Scientists have contributed significantly to the production of this Yellow Book, especially: A. Watts, University Amsterdam, NL (Dense Matter Working Group), J. Wilms, ECAP, Bamberg, DE (Observatory Science Working Group), E. Bozzo, ISDC, University of Geneva, CH (overall editing and coordination) and T. Courvoisier, ISDC, University of Geneva, CH (PI Science Data Centre).

# Table of contents

<b>1</b>	<b>EXECUTIVE SUMMARY .....</b>	<b>7</b>
<b>2</b>	<b>SCIENTIFIC OBJECTIVES .....</b>	<b>10</b>
2.1	Supranuclear Density Matter.....	10
2.1.1	Introduction.....	10
2.1.2	The nature of matter: major open questions .....	11
2.1.3	Methodology: how neutron star mass and radius specify the EOS.....	13
2.1.4	Techniques: how LOFT will measure M and R.....	13
2.1.4.1	Pulse profile modelling .....	14
2.1.4.2	Spin measurements .....	17
2.1.4.3	Asteroseismology.....	19
2.1.5	LOFT and Dense Matter in the 2020s .....	20
2.2	Strong Field Gravity.....	23
2.2.1	Introduction.....	23
2.2.1.1	LOFT in Strong Field Gravity .....	23
2.2.1.2	Main Diagnostics and Interpretation.....	24
2.2.1.3	Models and Simulations.....	27
2.2.1.4	LOFT’s Strong Field Gravity Objectives.....	28
2.2.2	Relativistic Line Profiles as a Probe of Strong Field Gravity.....	28
2.2.2.1	Precessing Inner Hot Flow [SFG2] .....	29
2.2.2.2	Reverberation [SFG4 & 5].....	30
2.2.2.3	Doppler Tomography of Orbiting Hot Spot Patterns [SFG4 & 5].....	31
2.2.2.4	Average Line Profiles [SFG4 & 5] .....	33
2.2.3	High Frequency QPOs as a Probe of Strong Field Gravity .....	34
2.2.3.1	Epicyclic Motion .....	34
2.2.3.2	Relativistic Waveforms .....	35
2.2.4	LOFT and strong field gravity in the 2020s .....	36
2.3	Observatory Science .....	37
2.3.1	Gamma-Ray Bursts.....	39
2.3.2	Accretion Physics .....	40
2.3.2.1	X-ray binaries.....	40
2.3.2.2	Supermassive Black Holes.....	41
2.3.2.3	Cataclysmic Variables.....	41
2.3.2.4	Tidal Disruption Events .....	41
2.3.3	Strongly Magnetized Objects.....	42
2.3.3.1	Accretion Columns .....	42
2.3.3.2	Isolated Neutron Stars: Radio Pulsars and Magnetars .....	43
2.3.4	Thermonuclear Explosions .....	44
2.3.4.1	X-ray Bursts .....	44
2.3.4.2	Novae .....	45
2.3.5	Stellar Coronae .....	45
<b>3</b>	<b>SCIENTIFIC REQUIREMENTS.....</b>	<b>46</b>
3.1	Science requirements .....	46
3.1.1	Effective Area and Energy Range .....	46
3.1.2	Spectral resolution .....	47
3.1.3	Background.....	49
3.1.4	Sensitivity .....	51
3.1.5	Sky visibility and field of regard .....	52
3.1.6	Transient monitoring (WFM) .....	52
3.1.7	Mission duration .....	53
3.2	Observation plan .....	53
3.3	Science requirements margins.....	54

3.3.1	Effective area .....	54
3.3.2	Spectral resolution .....	55
<b>4</b>	<b>PAYLOAD .....</b>	<b>57</b>
4.1	Large Area Detector .....	57
4.1.1	Instrument Description .....	58
4.1.2	Interfaces and resources .....	60
4.1.3	Operations .....	60
4.1.4	Manufacturing, Assembly, Integration and Test .....	61
4.1.5	Calibrations .....	62
4.2	Wide Field Monitor .....	63
4.2.1	Instrument Description .....	64
4.2.2	Interfaces and resources .....	65
4.2.3	Operations .....	66
4.2.4	Manufacturing, Assembly, Integration and Test .....	67
4.2.5	Calibration .....	67
4.3	Key technology .....	67
4.3.1	Silicon Drift Detectors .....	67
4.3.2	Low noise ASICs for readout .....	69
4.3.3	LAD collimator .....	70
<b>5</b>	<b>MISSION DESIGN .....</b>	<b>72</b>
5.1	Overview .....	72
5.2	Orbit and Launcher .....	73
5.2.1	Orbit .....	73
5.2.2	Launcher .....	73
5.3	Spacecraft Design .....	74
5.3.1	Payload Accommodation .....	75
5.3.1.1	Wide Field Monitor .....	75
5.3.1.2	Large Area Detector .....	76
5.3.2	Service Module .....	77
5.3.2.1	Attitude and Orbit Control System .....	77
5.3.2.2	Propulsion .....	78
5.3.2.3	Thermal .....	79
5.3.2.4	Telemetry and telecommanding .....	79
5.3.2.5	Power .....	79
5.3.2.6	Data Handling .....	79
5.3.3	Spacecraft Resource Budgets .....	80
<b>6</b>	<b>GROUND SEGMENT .....</b>	<b>82</b>
6.1	Overview .....	82
6.2	Mission operations .....	82
6.2.1	Mission Operations Centre .....	83
6.2.2	Ground stations .....	83
6.2.3	Mission phases .....	84
6.3	Science operations .....	84
6.3.1	Science Operations Centre .....	84
6.3.2	Science Data Centre .....	85
6.3.3	Observation planning and Targets of Opportunity .....	85
6.3.4	Instrument Operations Centre .....	86
6.3.5	LOFT Burst Alert System and LOFT Burst Alert Ground System .....	86
6.4	Data, software and data archiving .....	87
6.4.1	Data products .....	87
6.4.2	Processing software .....	88
6.4.3	Quick Look Analysis .....	88
6.4.4	Data archiving .....	89

---

<b>7</b>	<b>MANAGEMENT .....</b>	<b>91</b>
7.1	Project management .....	91
7.2	Procurement and member state contributions .....	91
7.3	Mitigation actions for top risks .....	92
7.4	Schedule .....	93
7.5	Science management .....	94
<b>8</b>	<b>COMMUNICATIONS AND OUTREACH.....</b>	<b>96</b>
<b>9</b>	<b>BIBLIOGRAPHY .....</b>	<b>97</b>
<b>11</b>	<b>LIST OF ACRONYMS.....</b>	<b>103</b>
<b>12</b>	<b>ACKNOWLEDGEMENTS.....</b>	<b>105</b>

# 1 Executive summary

**Transformational Science:** LOFT addresses the Cosmic Visions theme “Matter under extreme conditions” by probing dense matter and strong gravity, areas of fundamental physical as well as astrophysical interest which LOFT will revolutionize by observations of neutron stars (NSs) and stellar-mass and supermassive black holes. The nature of matter at the extreme densities of neutron star interiors is one of the great open unknowns in physics, making neutron stars unique laboratories for nuclear physics and quantum chromodynamics. The theory of General Relativity, verified to exquisite accuracies in the weak-field regime, e.g., in our Solar system, predicts large effects on the motion of matter under the influence of strong-field gravity, such as Lense-Thirring precession of the accretion discs or the very existence of the ISCO (innermost stable circular orbit).

The fundamental diagnostic of dense matter interactions is the pressure-density-temperature relation of bulk matter, the equation of state (EoS), observationally encoded as the neutron star mass-radius relation. The EOS provides key aspects of the microphysics, such as the presence of free quarks at high densities. The very large effective area (more than 15 times that of any X-ray mission ever flown) will allow detecting pulsations and vibrations of NSs at enormous signal to noise. LOFT will thus perform the first precise measurements of (M,R) values for several NSs, by using different complementary methods (pulse profile modelling of 3 types of pulsations, the mass-shedding limit from the spin distribution, vibrational modes in magnetars) enabling to overcome model systematics. This will result in the reconstruction of the equation of state of zero-temperature supranuclear density matter. Figure 1-1 (*left*) shows how LOFT measurements will track the mass-radius relation and determine the EOS.

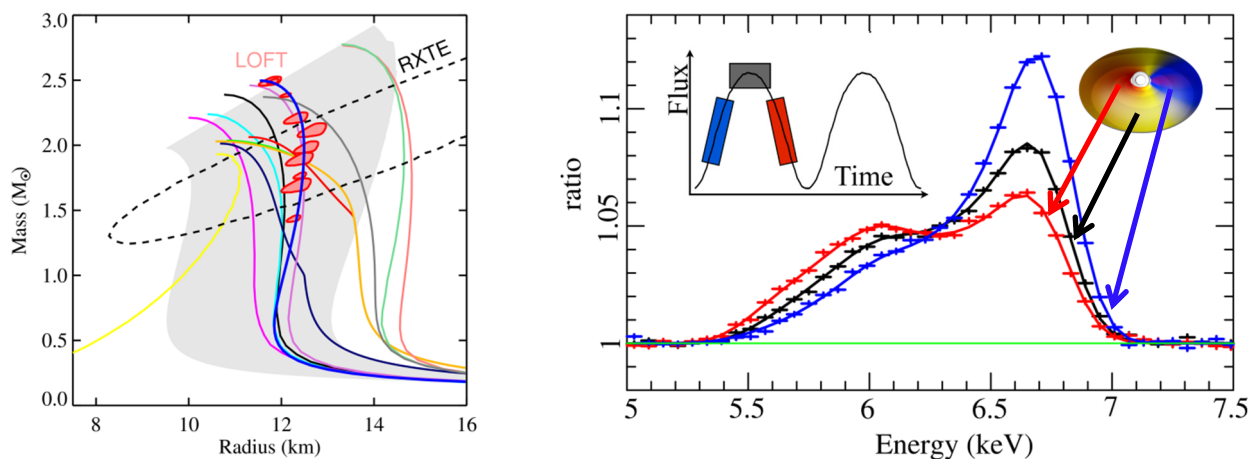


Figure 1-1 Left: Measurements of NS masses and radii (red error regions), will give very tight constraints on the dense matter EoS. The models shown illustrate the range of possibilities for the EoS, which depends on both the composition of supranuclear density matter (from purely nucleonic to strange quark matter) and on the nature of the strong force. All of the EoS shown are compatible with the recent discovery of two pulsars with masses  $\approx 2 M_{\odot}$ . Right: Changes in the Fe K line profile resulting from an inner hot BH accretion flow undergoing precession due to the relativistic frame dragging produced by the Kerr black hole in the center. The hot flow radiation sweeps over the less hot accretion disk around it and illuminates different parts of it at different times. The three Fe line spectra shown each correspond to 1000 s of data at given phase in a Low-Frequency QPO, and clearly show the line distortions predicted from relativistic precession.

CCD quality spectra, coupled with the enormous throughput of a pile-up free detector two orders of magnitude larger than previous (and planned) similar-resolution instruments, will allow to characterize, by complementary measurements, the motions of accreting matter down to distances a few Schwarzschild radii from BHs and NSs in X-ray binaries and bright AGNs. These include key timing features, such as high-frequency quasi periodic oscillations (QPOs), as well as spectra of the broadened Fe line in stellar-mass and supermassive BHs. Using relativistic spectral lines and their variations on relativistic time scales, LOFT will for the first time resolve the relativistic Fe lines simultaneously in time as well as energy at the enormous photon throughput required to directly witness the motions of matter near black hole event horizons. Figure 1-1 (*right*) shows how LOFT will measure the effect of relativistic frame dragging induced precession on the

disk Fe K line profile in phase resolved spectroscopy of a low frequency QPO. Figure 1-2 illustrates the enormous improvement in time variability studies LOFT will afford compared to the most sensitive predecessor, RXTE.

So, the design of LOFT is driven by ambitious, but precise, objectives in the areas of dense matter and strong gravity. The program to attain these objectives is based on proven phenomenology, so it leads to concrete, quantitative mission requirements. This approach was chosen in the full understanding that an instrument meeting these requirements would enable revolutionary results in a much wider range of investigations: those focusing on other sources, such as for example gamma ray bursts and tidal disruption events, and on other aspects of neutron star, black hole and accretion physics, and notably also on other aspects of dense matter and strong gravity which can be less easily quantified in advance. It is also clear that the combination of instrument characteristics embodied in LOFT, 10 m<sup>2</sup> effective area at 240 eV energy resolution and sensitive wide field monitoring covering 1/3 of the sky with 5 arcmin resolution, opens up an enormous discovery space that no doubt contains new avenues for compact object science and high energy astrophysics that cannot now be foreseen. These aspects of the LOFT programme are called Observatory Science and comprise approximately 50% of the programme.

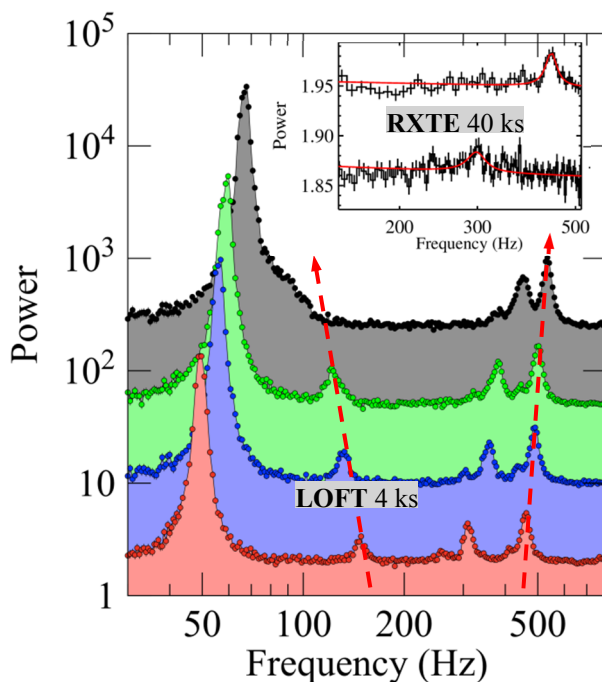


Figure 1-2 Improvement of the timing capabilities illustrated for the stellar mass black hole GRO J1655-40. Compared to a ~40 ksec observation where RXTE just detected the QPO frequencies (Motta et al. 2013), in much shorter exposure times (in these examples 4 ks) LOFT is able to: (i) detect more frequencies (including the 120-150 Hz radial epicyclic frequency, whose frequency decreases as the innermost stable orbit is approached); (ii) measure the correlated variation in frequencies as the inner radius of the accretion disk varies, thus permitting to probe GR-predicted orbital and epicyclic strong-field relativistic motions.

astronomy” facilities that will be operational in the 2020’s, such as, e.g., the LSST and SKA.

**Payload:** Silicon Drift Detectors (SDD) in combination with a collimator using micro-channel plate (MCP) technology allows a two order of magnitude jump in collecting area with CCD-class spectral resolution compared to telescope-based missions. The payload includes a large area detector (LAD, ~10 m<sup>2</sup> effective

LOFT provides a quantum leap in instrumental capabilities compared to earlier collimated X-ray timing missions such as EXOSAT and RXTE, and adds solid-state class spectral resolution so far only available in much smaller-area telescope X-ray missions. By focussing on two clear science topics, the instrument design has been optimized around the Fe-K line. This offers more than a factor 200 increase in throughput with respect to XMM (at 200 mCrab, accounting for pile-up and telemetry limitations, for brighter sources the improvement is even larger), with similar spectral resolution, resulting in a huge step forward in fast spectral time-variability studies. In addition, its anticipated launch date (2022) will bridge the gap between the end of the current generation of high-energy missions and the new large scale mission to study the Hot and Energetic Universe (Athena+). By its completely different optimization, LOFT will provide new insights which are outside the scope of Athena+ observations, by virtue of its 40 times larger effective area at 6 keV, where the cleanest signal from matter accreting in strong gravitational fields is found. We will demonstrate the uniqueness of LOFT in this landscape. Clearly, the optimization of the LOFT mission implies full complementarity to the other exciting science addressed by Athena+. LOFT’s wide field instrument (WFM), with its largest ever field of view, and good sensitivity and spectral resolution, will allow innovative spectral monitoring studies of the physics of galactic and extragalactic X-ray sources. The WFM will also monitor the sky down to weak limits and discover numerous new transients, complementing other powerful “time domain

area) with a good spectral resolution (240 eV) and a collimated field of view ( $1^\circ$ ) over a wide energy range (2-30 keV). A significant part of the sources are highly variable. The WFM monitors these objects and will identify also new transient sources. Following an interesting transient LOFT will be able to point and observe the source sufficiently fast to obtain high-quality time-resolved spectra. By a combination of the field of view of the WFM ( $>4$  sr), the area of the sky accessible to the LAD ( $>50\%$ ) and the mission duration (3+2 years), LOFT will be able to detect sufficient numbers of Black Holes with High Frequency QPOs and Accreting Millisecond X-ray Pulsar transients for its core science.

The *Large Area Detector* combines SDDs, inherited from the LHC experiment ALICE, with a collimator technology based on the MCPs as used, for example, in the ESA mission BepiColombo. Achieving the good

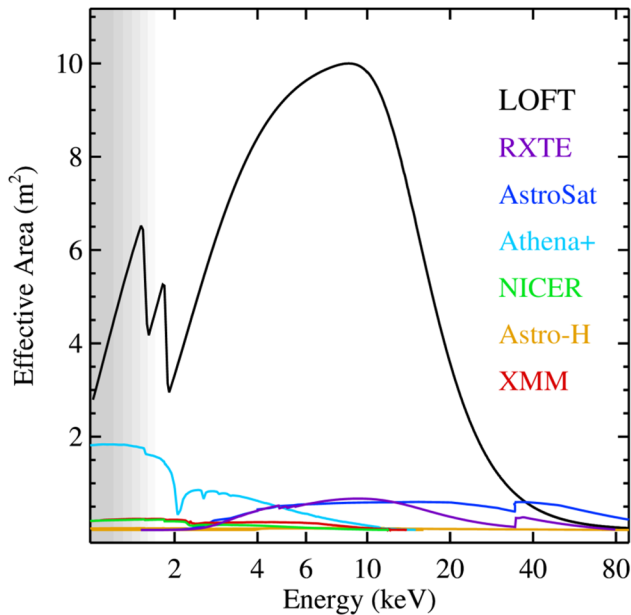


Figure 1-3 Effective area of the LOFT mission compared with operational and planned missions.

spectral resolution requires moderate passive cooling of the detectors to  $-10^\circ\text{C}$ . The very large number of read out channels implies the use of mixed signal ASICs with low power consumption and good performance, whose feasibility has been already demonstrated. The LAD consists of about 126 modules, each of which has 16 SDDs. The effective area of LOFT is shown in Figure 1-3 to outperform all current or planned missions by at least a factor of 15. The *Wide Field Monitor* is a coded mask instrument using almost identical detectors as the LAD. As these are near-1-dimensional cameras, two are required to determine the position of a source. Five camera pairs provide the required field of view and sensitivity. The combination of spectral resolution (300 eV FWHM), energy range (2-50 keV) and field of view (4.1sr) are unprecedented. **Science operations:** WFM data will be inspected daily to identify relevant changes in sources to allow for timely LAD observations. The Burst Alert System will identify bright new transients and GRBs ( $\sim 120/\text{year}$ ), broadcasting their coordinates to

VHF ground stations within 30 s. **Observation plan and data rights:** The *core science* program addresses Dense Matter and Strong-field Gravity and needs  $\sim 50\%$  of the observing time. The rest is dedicated to *observatory science*. Both are open to the community by selection through peer review, including a fraction of observing time reserved for instrument teams. The usual 1-year proprietary data right policy will be followed for the LAD data, whereas the WFM data will be made public promptly. **Implementation:** The detailed studies at ESA and industry showed that the  $10\text{ m}^2$  detectors can be accommodated on folded panels. Solar shielding and radiators maintain a detector temperature below the required  $-10^\circ\text{C}$ , with larger than required sky visibility. A large fraction of the sky (up to 75%) is visible with a slightly relaxed spectral resolution for further flexibility. The science goals are robust to some degradation in area or resolution as most science can be recovered by longer observations. The LOFT payload will be provided by a European consortium of institutes with long-standing tradition in space science in Denmark, Finland, France, Germany, Italy, Netherlands, Poland, Spain, Switzerland, and United Kingdom.

### Why we need LOFT to study SFG and EOS

The unique contribution LOFT will make to dense matter and strong gravity studies comes, of course, from the large jump in effective area first, coupled to its excellent spectral capabilities second. **Only LOFT** will be able to collect the numbers of photons required to simultaneously measure mass and radius of a dozen neutron stars and hence trace out the mass-radius relation and pin down the EOS. **Only LOFT** will be able to put relativistic line formation and relativistic variability together, go from 1-dimensional to a 2-dimensional diagnostic - combining dynamics and spacetime geometry - and measure the variation of Fe-line profiles on relativistic time scales, verifying the unique predictions GR makes for these variations.

## 2 Scientific objectives

In this section we present the science objectives of LOFT starting with dense matter, followed by strong field gravity and ending with the observatory science.

### 2.1 Supranuclear Density Matter

#### 2.1.1 Introduction

Neutron stars are the densest objects in the Universe, attaining physical conditions of matter that cannot be replicated on Earth. Inside neutron stars, the state of matter ranges from ions (nuclei) embedded in a sea of electrons at low densities in the outer crust, through increasingly neutron-rich ions in the inner crust and outer core, to the supranuclear densities reached in the centre, where particles are squeezed together more tightly than in atomic nuclei, and theory predicts a host of possible exotic states of matter (Figure 2-1). The nature of matter at such extreme densities is one of the great unsolved problems in modern science, and this makes neutron stars unparalleled laboratories for nuclear physics and QCD (quantum chromodynamics).

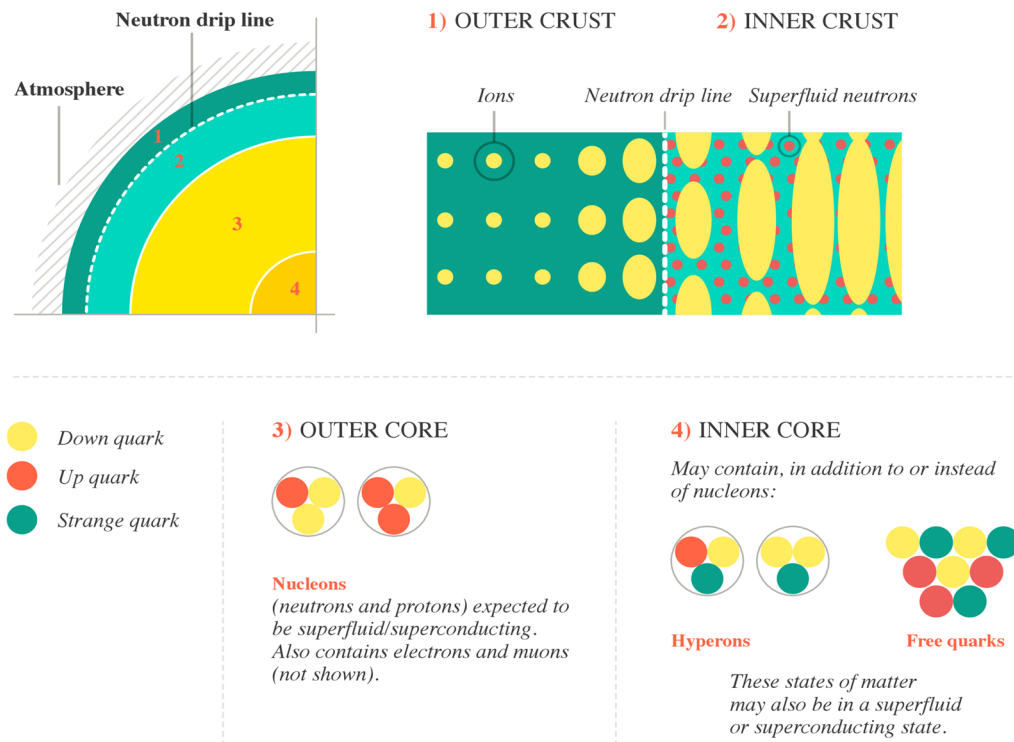


Figure 2-1 Schematic structure of a neutron star. The outer layer is a solid ionic crust supported by electron degeneracy pressure. Neutrons begin to leak out of ions (nuclei) at densities  $\sim 4 \times 10^{11} \text{ g/cm}^3$  (the neutron drip line), where neutron degeneracy also starts to play a role. At densities  $\sim 2 \times 10^{14} \text{ g/cm}^3$ , the nuclei dissolve completely. This marks the crust-core boundary. In the core, densities may reach up to ten times the nuclear saturation density of  $2.8 \times 10^{14} \text{ g/cm}^3$  (the density within normal atomic nuclei).

The most fundamental macroscopic diagnostic of dense matter interactions is the pressure-density-temperature relation of bulk matter, the equation of state (EOS). The EOS can be used to infer key aspects of the microphysics, such as the nature of the three-nucleon interaction or the presence of free quarks at high densities (§2.1.2). Measuring the EOS of supranuclear density matter is therefore of major importance to fundamental physics. It is also critical to astrophysics. The EOS is clearly central to understanding the powerful, violent, and enigmatic objects that are neutron stars. However, NS/NS and NS/BH mergers, prime sources of gravitational waves and the likely engines of short gamma-ray bursts (Nakar 2007), also depend sensitively on the EOS (Bauswein et al. 2012; Lackey et al. 2012). The EOS affects merger dynamics, black hole formation timescales, the precise gravitational wave and neutrino signals, any associated mass loss and r-process nucleosynthesis, and the attendant gamma-ray bursts and optical flashes (Rosswog 2010; Metzger et al. 2010; Hotokezaka et al. 2011). The cold EOS probed with neutron stars (§2.1.2), and the way it joins up with the hot EOS that determines explosion conditions (Janka et al. 2007), are also vital to understanding the late stages of core collapse supernovae, including their gravitational wave signal.

## 2.1.2 The nature of matter: major open questions

The properties of NSs, like those of atomic nuclei, depend crucially on the interactions between protons and neutrons (nucleons). NS moreover may be affected by more exotic physics occurring at high density. All of these are governed by the strong force. First principle calculations of the interactions for many-body QCD systems are however unfeasible, due to what is known as the fermion sign problem. Because fermion wave functions change sign upon exchange of particles, computing the expected energy of a system involves the addition of a large number of terms with alternating signs. This is particularly problematic at high density, and it is at present impossible to obtain direct predictions for strongly interacting quark matter. Instead one has to resort to phenomenological models.

### Box 2: Modelling neutron rich matter

In the absence of first principle QCD calculations, various approximate models have been developed for neutron-rich matter at high density. These are based on very different approaches, reflecting the difficulties of developing a theory that adequately addresses this regime (Steiner & Gandolfi 2012):

- **Nuclear potentials** (e.g. the Urbana/ Illinois or Argonne forces) that fit two-body scattering data and light nuclei properties (Wiringa et al. 1995; Pieper et al. 2001);
- **Microscopic nuclear Hamiltonians** that include two- and three-body forces from chiral effective field theories (Hebeler & Schwenk 2010);
- **Phenomenological forces** like the Skyrme interaction (Stone & Reinhard 2007).

At low energies, effective field theories based on QCD provide a systematic expansion of nuclear forces, which predict two- and many-nucleon interactions. While two-nucleon interactions are well constrained, three-body forces are a frontier in nuclear physics, especially for neutron-rich isotopes. Such exotic nuclei are the focus of present and upcoming laboratory experiments but they are very short-lived and difficult to detect. Neutron star observations, by contrast, challenge many-nucleon interactions at extremes of both density and neutron richness (Figure 2-2). Even in this relatively well-charted (nucleonic) regime, astrophysical input is desperately needed to make progress. Current models for neutron-rich matter all have major uncertainties at high density (Box 2). And while experimental information on matter near the nuclear saturation density ( $2.8 \times 10^{14} \text{ g/cm}^3$ , the density within normal nuclei) is plentiful, there are only a few experimental constraints at high densities and for neutron-rich matter (Box 3). Neutron stars provide a unique environment for testing models and providing guidance to nuclear theory.

At the very highest densities reached in neutron star cores, **transitions to non-nucleonic states of matter** are expected (Glendenning 2000). Some of the most exciting possibilities involve strange quarks: unlike heavy-ion collision experiments, which always produce very short-lived and hot dense states, the stable gravitationally confined environment of a neutron star permits slow-acting weak interactions that can form states of matter with a high net strangeness. Strange matter possibilities include the formation of hyperons (strange baryons), free quarks (forming a hybrid star), or color superconducting states (Alford et al. 2008). It is even possible that the entire star might convert into a lower energy self-bound state consisting of up, down and strange quarks, known as a strange quark star (Witten 1984). Other states that have been hypothesized include Bose-Einstein condensates of mesons (pions or kaons, the latter containing a strange quark) and Delta baryons (resonant states containing only up or down quarks). The densities at which such phases would appear, and the degree to which they might co-exist with other phases, are all highly uncertain. Figure 2-2 compares the parameter space that can be accessed within the laboratory to that which can be explored with neutron

### Box 3: Extremes of matter in the laboratory

Laboratory experiments to study the nature of matter (see Figure 2-2) use diverse techniques:

- Nuclear masses and their charge radii probe symmetric nuclear matter (Kortelainen et al. 2010).
- The neutron skin thickness of lead probes neutron-rich matter (Roca-Maza et al. 2011).
- Giant dipole resonances and dipole polarizabilities of nuclei (Trippa et al. 2008; Tamii et al. 2011; Piekarewicz et al. 2012) will also probe largely symmetric matter.

However all of the above techniques probe only matter at densities lower than  $3 \times 10^{14} \text{ g/cm}^3$ . Heavy-ion collisions performed at NSCL and GSI (and under development at FAIR, NICA and FRIB) probe hot and dense matter, but have uncontrolled extrapolations to zero-temperature (Tsang et al. 2009).

stars. The true ground state of ultradense matter is neutron-rich: it is gravitational confinement in neutron stars that permits this state to develop via weak interactions, and this ground state is out of reach of laboratory experiments. Indeed only neutron stars sample the required ‘zero temperature’ regime of the EOS. Moreover none of the exotic non-nucleonic states of matter described in the previous paragraph can be reached in the laboratory. **LOFT will provide a truly unique exploration space.**

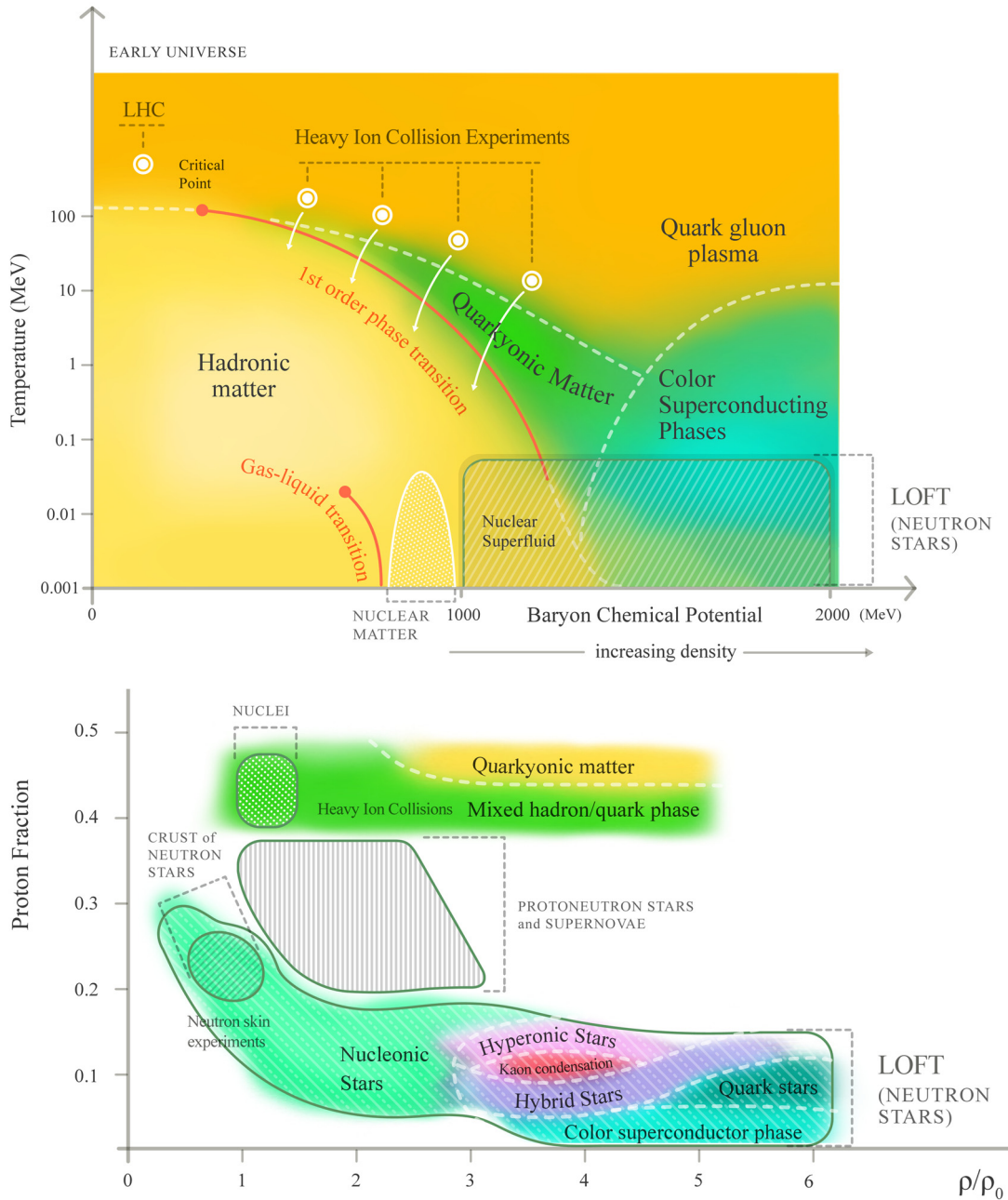


Figure 2-2 The parameter space and the states of matter accessed by LOFT’s neutron star programme, as compared to current and planned laboratory experiments on Earth. **Quarkyonic matter**: a hypothesised phase where cold dense quarks experience confining forces (McLerran & Pisarski 2007; Fukushima & Hatsuda 2011) The top panel shows temperature against baryon chemical potential (1000-2000 MeV corresponds to roughly 1-6 times the saturation density). The bottom panel shows proton fraction against density (in units of the nuclear saturation density  $\rho_0 = 2.8 \times 10^{14} \text{ g/cm}^3$ ). The stabilizing effect of gravitational confinement in neutron stars permits long-timescale weak interactions (such as electron captures) to operate, generating matter that is both neutron-rich and has potentially high net strangeness. Neutron stars offer unique access to the cold, high density regime with baryon chemical potential above  $\sim 1000 \text{ MeV}$ , and to matter with  $Z/A < 0.4$  above the saturation density. This opens up an entirely new regime of parameter space for studies of nucleonic interactions, including detailed study of nuclear superfluids. It also opens up the various exotic phases of strange matter, including the color superconducting state.

### 2.1.3 Methodology: how neutron star mass and radius specify the EOS

The macroscopic properties of neutron stars (see Box 4) are determined by the EOS at supranuclear density and ‘zero’ (below the Fermi) temperature, which is inaccessible in the laboratory. The maximum neutron star mass  $M$  is determined primarily by the behavior of this cold EOS at the very highest densities (a few times the nuclear saturation density). The presence of non-nucleonic phases (such as hyperons or condensates) tends to soften the EOS (reducing pressure support), leading to a smaller maximum mass (Lattimer & Prakash 2001). The radius  $R$ , on the other hand, depends more strongly on the behavior of the EOS near the nuclear saturation density. For nucleonic EOS it is highly sensitive to the three-nucleon interaction (Gandolfi et al. 2012). The presence of non-nucleonic phases that soften the EOS also tend to reduce radius.

#### Box 4: The Tolman-Oppenheimer-Volkoff equations

$$\frac{dm}{dr} = 4\pi r^2 \rho$$

Mass continuity

$$\frac{dP}{dr} = -\frac{(P + \rho)(m + 4\pi r^2 \rho)}{r(r - 2m)}$$

Force balance

$$\rho = \rho(P)$$

Equation of state (EOS)

The TOV equations are the relativistic equations of stellar structure for non-rotating stars (they can be modified to take into account rotation). They specify the total density  $\rho$  and pressure  $P$ :  $m$  is the mass within radius  $r$ . Note that the EOS should also include temperature: however for neutron stars, we are so far below the Fermi temperature that this can be neglected in computing bulk structure. The TOV equations relate the EOS of dense matter, which depends on the microphysics of composition and the strong force, to macroscopic observables including the mass  $M$  and radius  $R$  of the neutron star.

To measure the EOS, one requires a set of measurements of  $M$  and  $R$  spanning a range of masses. This mass-radius relation can then be inverted to obtain the functional form of the cold EOS. **In fact, it has been shown that there is a unique map between the EOS and the mass-radius relation (NS radius as a function of mass (Lindblom 1992)), a result LOFT will exploit. At least three separated measurements of  $M$  and  $R$  are necessary for this inversion to be successful (Özel & Psaltis 2009), and this drives LOFT’s observing plan.** Figure 2-3 illustrates the relationship between the EOS and the mass-radius relation.

To date, most efforts to measure the mass-radius relation have come from modeling the spectra of thermonuclear X-ray bursts and of low-mass X-ray binaries in quiescence (Suleimanov et al. 2011; Özel 2013; Guillot et al. 2013; Steiner et al. 2013). The constraints obtained are relatively weak: in Steiner et al. 2013, for example, for an *assumed mass*, the 1 sigma errors in  $R$  are  $\sim 11\%$ , resulting in uncertainties in the EOS in the range 60-150%. More seriously, there are many concerns about systematic errors in these methods, including absolute flux calibration (which introduces errors of at least  $\sim 10\%$ ), atmospheric composition, the role of residual accretion, non-uniform emission over the star, distance measurements, and identification of the Eddington flux. The techniques that will be the focus of the analysis of LOFT data, by contrast, are not affected by these systematic errors.

Complementary constraints on the EOS have also come from radio pulsar timing. The mass of neutron stars in compact binaries can be measured very precisely using relativistic effects. Since any given EOS has a maximum stable mass (Figure 2-3), high mass stars can rule out particular EOS. They cannot, however, measure the mass-radius relation and pick out a particular EOS among all the viable ones.

The recent discovery of two pulsars with masses  $\approx 2 M_{\odot}$  (Demorest et al. 2010; Antoniadis et al. 2013), the most massive to date, rules out EOS containing very large hyperon or condensate components, since these tend to soften the EOS at high densities. **However, as is apparent from Figure 2-3, a very broad range of EOS remains viable.** In fact even the measurement of a  $2.4 M_{\odot}$  neutron star (if one can exist) would only halve the size of the band of allowed parameter space in Figure 2-3 (Hebeler et al. 2013). LOFT will provide simultaneous high precision measurements of  $M$  and  $R$  over a range of masses allowing us to fit the functional form of the EOS (Figure 2-5).

### 2.1.4 Techniques: how LOFT will measure $M$ and $R$

One of LOFT’s main strengths as a dense matter mission is that it will employ **three different primary techniques to measure  $M$  and  $R$** : pulse profile modeling, spin measurements, and asteroseismology.

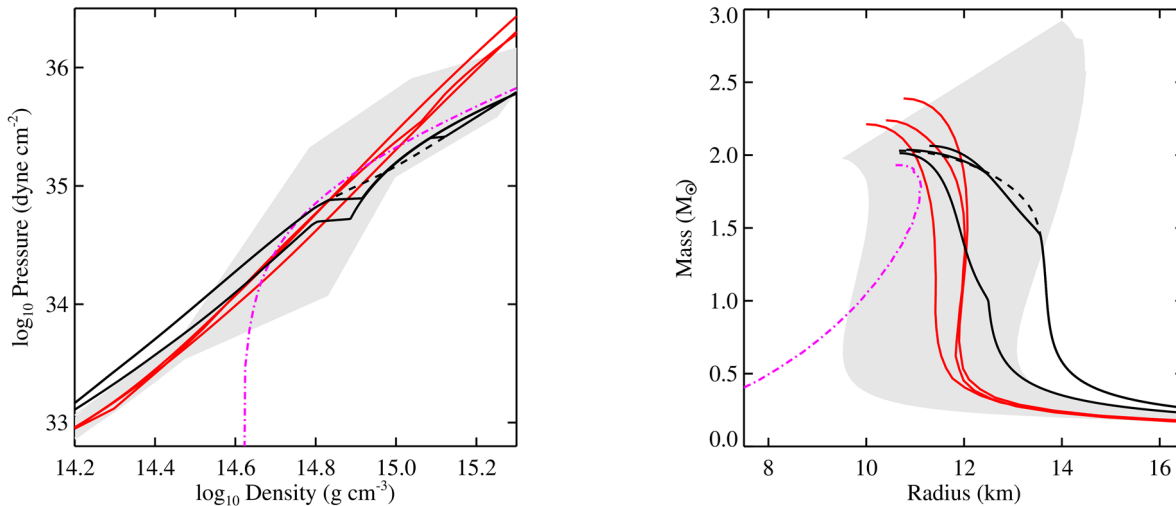


Figure 2-3 The link between uncertainty in fundamental nuclear physics, the EOS, and the neutron star mass-radius relation. The figure shows the pressure density relation (left) and the corresponding mass-radius relation (right) for different EOS models. Grey band: range of EOS based on chiral effective field theory (Hebeler et al. 2013). Black solid: Hybrid EOS from Zdunik & Haensel (2013). Black dashed: Nucleon + hyperon core EOS from Bednarek et al. (2012). These recent models are compatible with the discovery of a 2 solar mass neutron star. The other EOS are from Lattimer & Prakash (2001): Red (nucleonic); Magenta (quark stars).

These different techniques involve different classes of neutron star: accreting neutron stars with thermonuclear bursts, accretion-powered X-ray pulsars, and isolated highly magnetic neutron stars known as magnetars. The use of multiple techniques and different source types allows independent cross-checks on the EOS. In the following subsections we review the three primary techniques and demonstrate how LOFT's capabilities and the observational programme come together to deliver the scientific goals.

#### 2.1.4.1 Pulse profile modelling

[**Science Requirement EOS1**] Constrain the equation of state of supranuclear density matter by the measurement, using three complementary types of pulsations, of mass and radius of at least 4 neutron stars with an instrumental accuracy of 4% in mass and 3% in radius.

The flux we observe from a bright spot on the neutron star surface offset from the rotational pole will be modulated by the star's rotation. This periodic modulation at the spin frequency is called pulsation. As the photons propagate through the curved space-time of the star, information about  $M$  and  $R$  is encoded into the shape of the pulse profile. General relativistic light-bending, which depends on the compactness  $M/R$ , affects the amplitude of the pulsations. Special relativistic Doppler boosting and aberration, which depend on the projected velocity of the hotspot along the line of sight, introduce asymmetry and harmonic content. Since the angular velocity is known from the pulse frequency, this provides a constraint on  $R$ . The pulse profile thus yields  $M$  and  $R$  (Figure 2-4). There are of course other factors that affect the pulsations, and these must be taken into account when fitting for  $M$  and  $R$ . Relevant parameters include geometrical factors (hotspot size, shape and inclination  $\alpha$ , and observer inclination  $i$ ), and emission from the rest of the star and disk. Fortunately the resulting parameter dependencies can be resolved (see Box 5).

Extensive work by LOFT scientists on gravitational lensing in spinning neutron star spacetimes has quantified fully the various levels of approximation and their effects on the generation of pulse profiles (Miller & Lamb 1998; Poutanen & Beloborodov 2006; Cadeau et al. 2007; Morsink et al. 2007; Psaltis & Özel 2013; Bauböck et al. 2013). Four separate algorithms have been individually developed and cross-verified (from groups in Alberta, Oulu, Maryland/Urbana and Arizona), with agreement at the 0.1% level with the Oulu code for the same input parameters and emissivities. To determine the accuracy with which LOFT will measure  $M$  and  $R$  using pulse profile modelling, we have performed **the most comprehensive analysis of this technique to date**. Using synthetic pulse profile data generated using the verified codes described above, one can use a Bayesian approach and Markov Chain Monte Carlo sampling methods to fit the profiles, recover  $M$  and  $R$ , and determine the appropriate confidence regions in the  $M$ - $R$  plane. The full procedure is described in depth in Lo et al. (2013). In doing this analysis one can consider the complementary pulsations due to three types of

hotspot: accretion-powered pulsations (due to magnetic channeling of accreting material), and burst oscillations in the rise or tails of thermonuclear X-ray bursts (explosions that arise from unstable burning of hydrogen or helium).

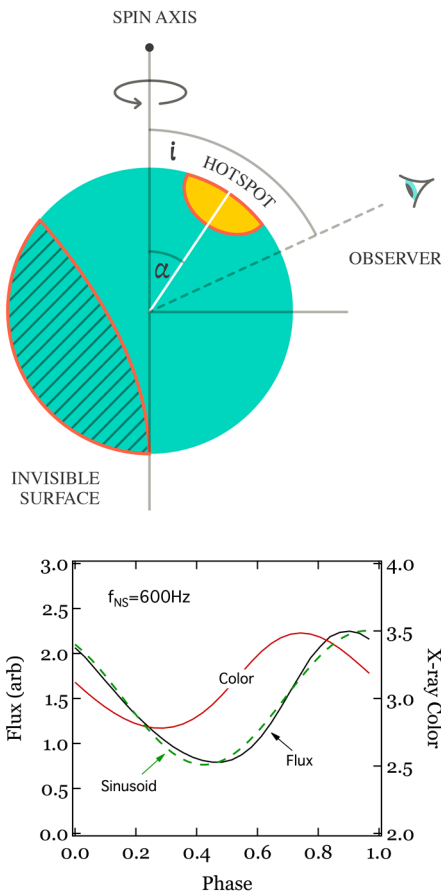


Figure 2-4 As a neutron star rotates, emission from the hotspot generates a pulse profile. General relativistic effects such as gravitational lightbending (which leads to partial visibility of the back side of the star) and special relativistic Doppler effects combine to encode information about mass and radius in the pulse profile. The panel shows the pulse profile and the phase dependence of spectral color for a neutron star spinning at 600 Hz, for a spot colatitude,  $\alpha$ , of  $40^\circ$  and observer inclination,  $i$ , of  $60^\circ$ . Spectral color is the ratio of the number of photons with energies above to those below the blackbody temperature. The color maximum occurs near the spot's line of sight approach velocity maximum, the flux maximum near the spot's projected area maximum. The former thus precedes the latter. The dashed line shows the sinusoid that most closely describes the flux oscillations. The energy-dependence of the pulse profile properties enables us to infer mass and radius (Psaltis et al. 2013).

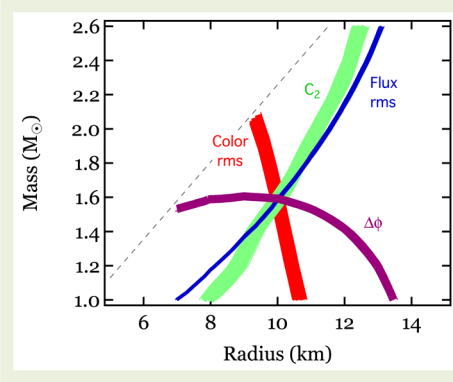
Ultimately we expect to be able to use all three types of pulsation to give complementary constraints, since many of the LOFT target sources show more than one type. However there is some uncertainty surrounding beaming effects in accretion-powered pulsations. By contrast, the spectrum of burst oscillation emission is well understood (Suleimanov et al. 2012), and studies show that atmosphere model uncertainties are  $\sim 1\%$ , i.e., lower than the fit statistics (Miller et al. 2013). Moreover, current data are consistent with a circular hotspot, as the model assumes (Artigue et al. 2013). We have therefore taken a fully conservative approach here and focused on burst oscillations in our demonstration of feasibility for this science case (but the other types of pulsations will be available as well to LOFT). The analysis performed by Lo et al. (2013) explores how the confidence regions in the M-R plane depend on

hot spot and observer inclinations, angular velocity, pulsed fraction, hot spot shape, emissivity pattern, and spectrum. Figure 2-6 shows the key results. The main conclusion is that **LOFT can measure M and R to accuracies of a few % with  $10^6$  pulsed photons, the latter being easily achievable** (see Table 2-1).

This conclusion is robust and takes into account that burst oscillation properties vary with time (frequencies often undergo slow drift), and several bursts are combined to obtain the requisite number of photons. Independent knowledge of any of the relevant parameters improves the uncertainties, with the biggest improvement coming from knowledge of the observer inclination. There are very good prospects for determining the angle of our line of sight to the axis of the binary orbit using Fe line modeling (Cackett et al. 2010; Egron et al. 2011; §2.3.2.1), Doppler shifting of burst oscillation frequencies (Strohmayer & Markwardt 2002; Casares et al. 2006), and burst echo mapping (Muñoz-Darias et al. 2008; requires simultaneous optical observations). Since the star's spin axis is expected to be aligned with that of the orbit in our target systems, this will yield observer inclination.

With this in mind it is worth emphasizing a key result from the Lo et al. (2013) study. Even when they explored significant systematic deviations from their assumptions, none of the systematics they examined (which included differences in the spot shape, beaming pattern, and energy spectrum from what was assumed in the model fits) simultaneously yielded (1) a statistically good fit, (2) apparently tight constraints on M and R, and (3) significantly biased masses and radii. *Thus if an analysis yields a good fit with tight constraints, the inferred mass and radius are reliable. This statement is currently unique among proposed methods to measure neutron star radii, and plays directly to the strengths of LOFT.*

Table 2-1 illustrates the prospects for the pulse profile modelling technique for several known burst oscillation sources, some persistent, some transient.



**Box 5: Parameter dependencies in pulse profile modelling**

Constraints on the neutron star mass and equatorial radius obtained from measuring four properties of a pulse profile: the fractional rms amplitude of the pulse profile, the rms amplitude  $C_2$  of the second harmonic, the fractional rms of the color oscillation, and the phase difference between the flux and color oscillations (Psaltis et al. 2013). The distinct dependence of the four observables on the system parameters breaks the degeneracy with the geometric factors (observer inclination and spot colatitude), allowing a unique recovery of neutron star mass and radius.

**Obtaining  $10^6$  pulsed counts is easily feasible within very reasonable observing times.** There are 24 known sources with either burst oscillations or accretion-powered pulsations and we expect more to be discovered in the LOFT era. Having such a large number of sources to choose from will help to select a sample with optimal observational characteristics (flux, pulse amplitude and harmonic content, etc).

As indicated above, somewhat depending on system geometry,  $10^6$  counts are sufficient to measure  $M$  and  $R$  to a few percent. For favorable geometry (reflected in higher harmonic content of the pulsations), obtaining constraints at the EOS1 target accuracy with  $10^6$  counts from the burst tails will be straightforward (Figure 2-5). Burst oscillations from accretion-powered pulsars have higher harmonic content, although for these sources a small uncertainty comes from the correction for accretion during the burst. Less favorable geometries take more observing time (errors on  $M$  and  $R$  scale roughly as total counts<sup>-1/2</sup>). While a mix of geometries among our sources is a reasonable expectation, our observing strategy is flexible enough to ensure that we meet our goals, no matter what system geometries we encounter. Our planning includes the option to observe fewer sources for longer, which would also allow us to obtain more counts from burst rise oscillations, which have high harmonic content (Bhattacharyya & Strohmayer 2005), but are less common and shorter-lived (~1s). We will use this flexibility also to be responsive to our preliminary findings by scheduling longer observations of the sources that are most constraining in the  $M$ - $R$  plane, in order to further reduce the size of their error ellipses. By thus tailoring our observations we can confirm key findings at a much higher confidence (see further discussion in §2.1.5). Figure 2-5 illustrates the type of constraints we expect to be able to obtain on the  $M$ - $R$  relation with this strategy.

LOFT also enables vital independent cross-checks of our findings. Several of the LOFT targets show both accretion-powered pulsations and burst oscillations, allowing checks using two independent pulse profile models. In addition, for many of the sources, we can obtain constraints by fitting detailed models to spectra of the continuum emission and any lines observed in the bursts. For example, fitting high-quality observations of the continuum spectra of many bursts from the same star using spectra from detailed, high-precision model atmosphere calculations produces a relation between  $M$  and  $R$  that comes mainly from the small deviation of the spectrum from a Bose–Einstein shape at low photon energies caused by the free-free opacity. This deviation allows one to determine  $(1+z)/g^{2/9}$ , where  $z$  is the surface redshift and  $g$  is the surface gravity of the star (Lo et al. 2013). Such a constraint is illustrated in Figure 2-5. Note that this technique does not depend on absolute

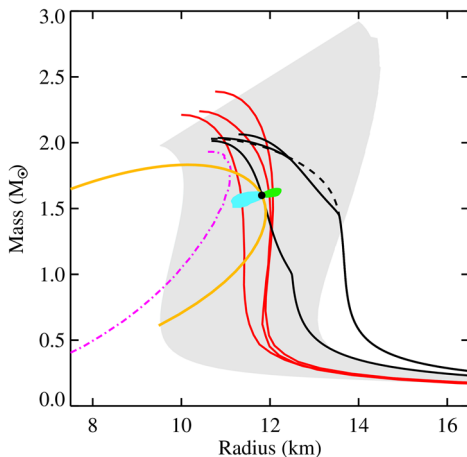


Figure 2-5  $M$  and  $R$  measurements from  $10^6$ -photon pulse profiles (Lo et al. 2013) produced by an equatorial spot at average pulsed fraction (as seen with RXTE). Black spot shows the input values;  $1\sigma$  confidence regions for observer inclinations of  $90^\circ$  (green) and  $60^\circ$  (cyan) were placed  $1\sigma$  away from the true value for display purposes. Corresponding errors on  $M$  are 3% and 6%, on  $R$ : 4% and 6%. All parameters including  $M$  and  $R$  were free in the fits: independent knowledge of parameters reduces the uncertainties further. The instrumental accuracy, achieved knowing all parameters except  $M$  and  $R$ , is 1-2%. The orange line shows points of constant  $g^{(2/9)}/(1+z)$ , illustrating the constraint from burst spectra (see text). For the other curves, see Figure 2-3

flux calibration. Observation of an identifiable atomic line in the hot-spot emission will also tightly constrain M/R (Bhattacharyya et al. 2005). If in addition the surface gravity can be determined from the equivalent width of the line, then  $M/R^2$  can also be determined (Chang et al. 2005). Combining these spectral line measurements will yield separate measurements of M and R. The constraints on M and R produced by these two additional methods are complementary to and independent of the constraints that will be obtained by fitting burst oscillation waveforms.

Table 2-1 Observing time required for potential target burst oscillation sources, based on RXTE observations of burst oscillations from each source. Some transient sources may not be active in the LOFT era, but similar sources will be active instead (§3.2). The observing time required to obtain  $10^6$  pulsed counts is calculated using burst oscillation properties and burst recurrence times from RXTE, including the percentage of those bursts that showed oscillations (Galloway et al. 2008). This estimate is conservative: it is possible to schedule observations during accretion states where burst oscillations are more common. \* Also accretion powered pulsar.

Source	Pulsed counts observed by LOFT in a single burst tail	Observing time needed to obtain $10^6$ counts (ks)	Notes
4U 1608-52	$8.8 \times 10^5$	250	Transient, regular outbursts
4U 1636-536	$3.4 \times 10^5$	139	Persistent
4U 1702-429	$4.4 \times 10^5$	84	Persistent
4U 1728-34	$3.3 \times 10^5$	150	Persistent
Aql X-1	$5.8 \times 10^5$	478	Transient, outbursts ~once per year
KS 1731-260	$2.3 \times 10^5$	509	Transient, one prior ~decade long outburst, currently in quiescence
SAX J1808.4-3658*	$11.6 \times 10^5$	195	Transient, outbursts every 2.5 years
XTE J1814-338*	$1.4 \times 10^5$	111	Transient, recurrence time unknown

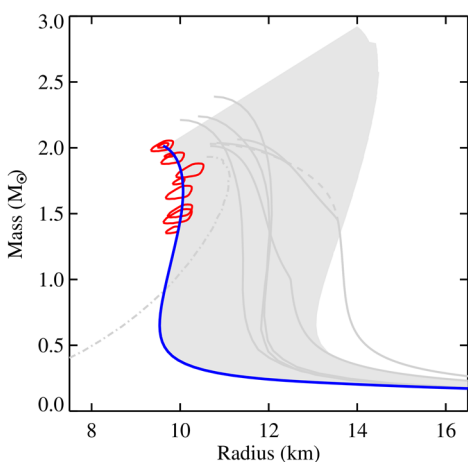


Figure 2-6 A preliminary assessment of LMXBs with pulsations is made as part of the core programme. At random orientation, 50% of systems are in the favorable range  $i=60-90^\circ$  (Lorimer 2008), so we expect to find  $>10$  sources in this range.  $1\sigma$  confidence regions (for equatorial hotspots, assuming no independent knowledge of parameters) would lie in the range shown in Figure 2-5. ESOI observing time will be dedicated to obtaining  $10^6$  pulsed counts on these  $\sim 10$  sources, and deep follow-ups of the 3-4 sources that best constrain the EOS in view of location on the M-R plane, potential for improving errors and obtaining complementary constraints from other pulsation types or spectral fitting. Scenario shown has  $10^6$  pulsed counts from 6 sources, and 4  $10^6$  pulsed counts for the four most constraining ones (resulting in factor 2 smaller errors). The best fit nucleonic EOS is shown in blue; rejected models in grey.

### 2.1.4.2 Spin measurements

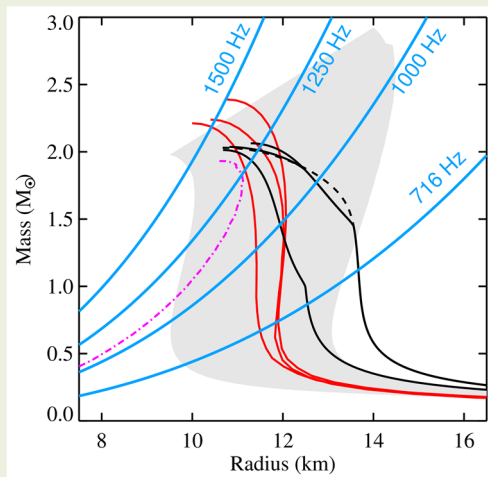
[Science Requirement EOS2] Provide an independent constraint on the equation of state by filling out the accreting neutron star spin distribution through discovering coherent pulsations down to an amplitude of about 0.4% (2%) rms for a 100 mCrab (10 mCrab) source in a time interval of 100s, and oscillations during Type 1 bursts down to typical amplitudes of 1% (2.5%) rms in the burst tail (rise) among 35 neutron stars covering a range of luminosities and inclinations.

The spin distribution of neutron stars offers another way of constraining the EOS, and LOFT, with its exquisite sensitivity to pulsations, offers a unique opportunity to fully characterise this function. At the very simplest level, one can obtain constraints from the most rapidly rotating neutron stars. The limiting spin rate, at which the equatorial surface velocity is comparable to the local orbital velocity and mass-shedding occurs, is a function of M and R and hence fast spins constrain the EOS (see Box 6). However the distribution itself also provides a guide to the torque mechanisms in operation and the moment of inertia, both of which can depend sensitively on the EOS. The spin distribution of neutron stars is poorly understood. The evolution of a neutron star born in a binary system (assuming that it survives the initial supernova) can follow various routes (Podsiadlowski et al. 2002; Tauris & van den Heuvel 2006; Lorimer 2008). This may include a period of accretion onto one of the neutron stars, from a main sequence or white dwarf companion, during which time

the system may be visible in X-rays. Spin-up due to such accretion is the basis for the recycling scenario that is thought to explain the formation of the Millisecond Radio Pulsars (Alpar et al. 1982; Radhakrishnan & Srinivasan 1982; Bhattacharya & van den Heuvel 1991; hereafter MSPs).

Several studies have attempted to link the properties of the MSPs to those of the neutron stars in Low Mass X-ray Binaries (LMXBs), the accreting systems that are supposed to be the progenitors of MSPs in the recycling scenario. The discovery of the first accreting millisecond X-ray pulsar by Wijnands & van der Klis (1998), and the recent detection of transitional objects that switch from radio to X-ray sources (Archibald et al. 2009; Papitto et al. 2013) seems to confirm this picture. However detailed comparisons of the properties (such as spin and orbital periods) of neutron star LMXBs and the radio MSPs reveal discrepancies between the predictions of current evolutionary models and observations (Hessels 2008; Kiziltan & Thorsett 2009; Tauris et al. 2012). This suggests shortcomings in our understanding of mass transfer, magnetic field decay, and accretion torques. It may even be necessary to consider alternative formation routes for the MSPs (Knigge et al. 2011). It is not clear that the spin distribution of the MSPs provides a good guide to the spin distribution of the accreting sources: and based on lifetimes and accretion torque estimates it is quite feasible that accreting NS may achieve higher spins than those measured for the MSPs (Cook et al. 1994).

**Box 6: The mass-shedding limit**



The mass-shedding frequency is given to good approximation (Haensel et al. 2009) by the empirical formula  $f_{\max} \approx C \left[ \frac{M}{M_n} \right]^{\frac{1}{2}} \left[ \frac{R}{10 \text{ km}} \right]^{-\frac{3}{2}}$  kHz, where M is the gravitational mass of the rotating star, and R is the radius of the non-rotating star of mass M. Softer EOS have smaller R for given M and hence have higher limiting spin rates. More rapidly spinning neutron stars place increasingly stringent constraints on the EOS. The deviation of C from its Newtonian value of 1.838 is determined by the precise external space-time, which in turn depends on the NS interior mass distribution. For a hadronic EOS (one that consists of baryons or mesons), C = 1.08, whilst for a strange star with a crust, C ≈ 1.15.

This can be recast as a limit on R:  $R < 10 C^{\frac{2}{3}} \left[ \frac{M}{M_n} \right]^{\frac{1}{3}} \left[ \frac{f}{1 \text{ kHz}} \right]^{-\frac{2}{3}}$  km.

Figure above: spin limits on the EOS. Neutron stars of a given spin rate must lie to the left of the relevant limiting line in the mass radius plane (shown in blue for various spins). EOS models as in Figure 2-3. The current record holder, which spins at 716 Hz (Hessels et al. 2006) is not constraining. However given a high enough spin individual EOS can be ruled out. Between 1 kHz and 1.25 kHz, for example, individual EOS in the grey band of nucleonic EOS would be excluded.

LOFT’s capabilities are well suited to discover many more neutron star spins. It is now known that accretion-powered pulsations from these sources can show up intermittently (Galloway et al. 2007; Casella et al. 2008; Altamirano et al. 2008), a phenomenon that observationally appears to be associated with the faster spin rates. Theory predicts intermittent episodes of channeled accretion onto weakly magnetized neutron stars in high accretion rate systems (Romanova et al. 2008), and intermittency is also likely in systems where the system is close to alignment (Lamb et al. 2009). So, sensitivity to brief pulsation trains is key. LOFT will detect brief pulse trains down to an amplitude of 0.4% (2%) rms for a 100 mCrab (10 mCrab) source (5σ, 128 s). This time interval matches the short duration of intermittent pulsations such as observed with RXTE (Casella et al. 2008). RXTE needed 15 times as long to reach the same sensitivity, so that brief pulse trains were severely diluted; longer pulse trains suffered from Doppler smearing. Weak pulsations are also expected in systems where magnetic field evolution as accretion progresses has driven the system towards alignment (Ruderman 1991). Searches with LOFT for weak (rather than intermittent) accretion-powered pulsations will use sophisticated search techniques such as those used to find the Fermi pulsars (Atwood et al. 2006; Abdo et al. 2009; Messenger 2011), to compensate for orbital Doppler smearing. Even at current computational capabilities, the LOFT core programme observations would yield 5σ pulsation sensitivities down to ~0.01% (rms) in bright NS (300 mCrab, and even better for the very brightest sources) and ~0.2% in faint NS (10 mCrab), somewhat depending on the level of prior knowledge about the orbit.

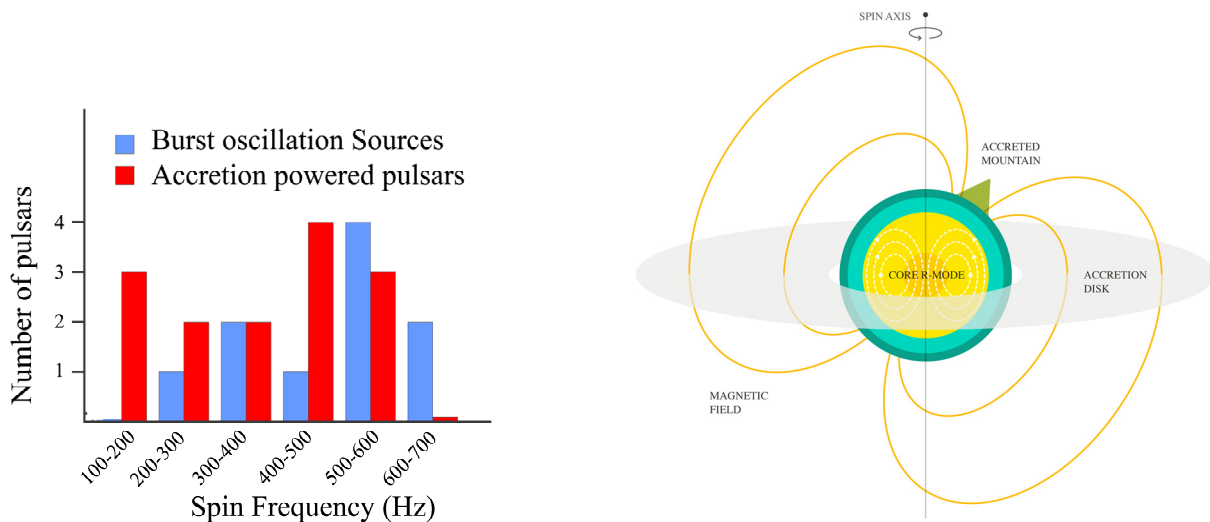


Figure 2-7 Left: The spin distribution for the fastest known accreting neutron stars. Right: The various torque mechanisms operating on an accreting neutron star. In addition to the accretion torque, which might involve magnetic channelling, there are gravitational wave torques such as caused by crustal mountains or core r-modes that depend sensitively on the dense matter EOS.

LOFT will be able to detect oscillations in individual Type I X-ray bursts to amplitudes of 1% (2.5%) rms in the burst tail (rise); by stacking bursts sensitivity improves. In rapidly spinning NS, **burst oscillations are predicted to be short-lived**, as rotation suppresses flame spread (Cavecchi et al. 2013). A single rapid spin provides a simple and very clean constraint on the EOS. It is possible, however, that with more spin detections we instead establish the existence of a pile-up in the distribution at a rotation rate well below the mass shedding limit (Bildsten 1998). **Discovery of an effect that prevents accretion-induced spin-up to reach this limit would be an important result and would suggest gravitational wave or magnetic braking mechanisms dominate neutron star spin histories.** The spin evolution of accreting neutron stars (Figure 2-7) is intimately connected to details of the internal physics, such as core r-mode oscillations (Ho et al. 2011) or crustal deformations such as ‘mountains’ (Johnson-McDaniel & Owen 2013) that generate gravitational waves, the response of the superfluid, and the moment of inertia. Disentangling the effects of magnetic accretion torques (see §3.2), will be important in this effort (Ghosh & Lamb 1978; Andersson et al. 2005). Excitingly, this will also enable us probe the physics of the weak interaction at high densities, since weak interactions control the viscous processes that are an integral part of the gravitational wave torque mechanisms (Alford et al. 2012)

#### 2.1.4.3 Asteroseismology

**[Science Requirement EOS3]** Probe the interior structure of isolated neutron stars by observing seismic oscillations in Soft Gamma-ray Repeater (**magnetar**) intermediate flares when they occur with flux  $\sim 1000$  Crab through high energy photons ( $> 20$  keV).

In this era of Corot and Kepler, asteroseismology has become firmly established as a precision technique for the study of stellar interiors. The detection of seismic vibrations in neutron stars thus is one of RXTE’s most exciting discoveries, as it allows a unique, direct view of the densest bulk matter in the Universe. Vibrations, detectable as QPOs in hard X-ray emission, were found in the tails of two so-called ‘giant flares’ from two magnetars (Israel et al. 2005; Strohmayer & Watts 2005). This opened up asteroseismology as a tool to study neutron star interiors. It was realized immediately that seismic vibrations from magnetars could tightly constrain the interior magnetic field strength (which is hard to measure directly) and the EOS (Samuelsson & Andersson 2007; Watts & Reddy 2007). Uniquely they can also go beyond the EOS, constraining the non-isotropic components of the stress tensor of supranuclear density material. Seismic oscillation models were quickly developed that include the effects of the strong magnetic field coupling solid crust to fluid core (Levin 2007; Gabler et al. 2013; Colaiuda & Kokkotas 2011), superfluidity, superconductivity and crust composition (Andersson et al. 2009; Steiner & Watts 2009; Passamonti & Lander 2013). This continues to be an extremely active field of research.

Giant flares are rare, occurring only every  $\sim 10$  years. This can be remedied using the less bright (still  $\sim 10^3$  Crab) intermediate flares, which occur yearly. They have similar peak fluxes as the tails of the giant flares, but are too brief ( $\sim 1$  s) to permit detection of similar QPOs with current instrumentation. As shown in Figure 2-8, LOFT will be sensitive to QPOs in intermediate flares with similar fractional amplitudes as those observed in the tails of giant flares, even for off-axis detection via higher-energy ( $\sim 40$ -60 keV) photons leaking through the collimator. The latter is important since intermediate flares are unpredictable, although we can increase the odds of capturing them by scheduling pointed observations during periods of high burst activity (Israel et al. 2008).

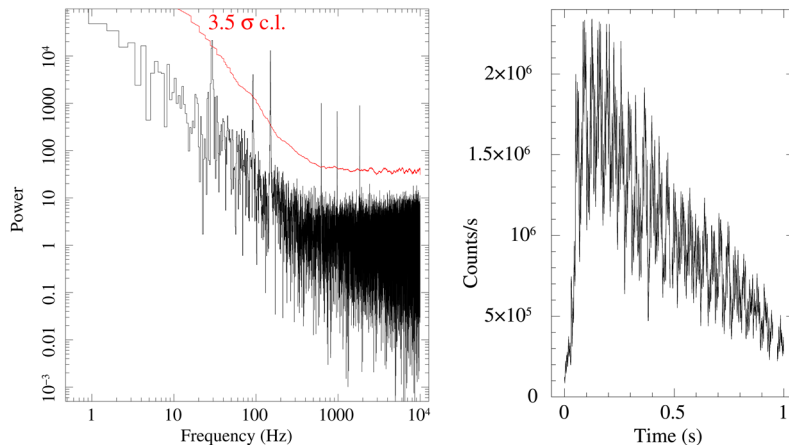


Figure 2-8 Time and frequency domain QPO detections for an intermediate flare detected  $10^\circ$  off-axis, assuming frequencies and amplitudes as in the SGR 1806-20 giant flare Power spectrum (left) with detection threshold (red) and light curve (right) of a magnetar Intermediate Flare (IF) with 1000 Crab peak flux (as observed in 2006 from SGR1900+14). All simulated QPOs are easily detected. Further simulations show significant QPO detections for fluxes  $> 100$  Crab, off-axis angles  $< 70^\circ$  and QPO amplitudes down to half that used here.

Theoretically the expectation of similar fractional amplitudes is justified: mode excitation at substantial amplitude by events releasing energies typical of intermediate flares is feasible (Duncan 1998). Empirically, QPOs in giant flares tend to appear rather late in the tails, when luminosities are similar to those in intermediate flares, and given that they appear and disappear multiple time in these tails, may be triggered by magnetic starquakes at these ‘low’ fluxes (Strohmayer & Watts 2006). As a result the development of similar fractional amplitude QPOs in intermediate flares is expected. Figure 2-8 illustrates the detection prospects for intermediate flares. The constraints that might be obtained from seismic models are shown in Box 7. The model presented here is simple: it does not incorporate

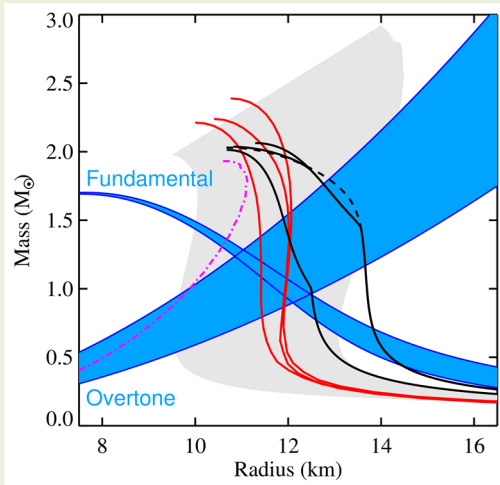
the effects of the magnetic coupling between crust and core, but shows the nature and precision of the resulting M and R measurements. More sophisticated seismic models are still under development, however the physics is known and much of the effort is focused on numerical implementation. The simple model discussed in the box provides a reasonable estimate of the magnitude and type of constraints that we will obtain with the fully implemented seismic models (this model would actually apply if core superfluidity shifts the low frequency magnetic oscillations towards higher frequencies (Passamonti & Lander 2013)).

### 2.1.5 LOFT and Dense Matter in the 2020s

A number of facilities aim to investigate the nature of dense matter using neutron stars from the present day to the mid-2020s. **LOFT is however unique in reconstructing the EOS.** Here we summarize the results expected from other telescopes, and explain what distinguishes LOFT.

*Radio telescopes (SKA, LOFAR, ASKAP and MeerKAT):* the next decade will see a major expansion in our ability to detect galactic radio pulsars. SKA and its pathfinders should find many relativistic binary radio pulsars for which precision mass measurements are possible via Post-Keplerian orbital parameters (Smits et al. 2009; O’Shaughnessy et al. 2008; Cordes et al. 2009). New EOS constraints would result if the maximum mass record is broken (§2.1.3), alternatively, current measurements may have already reached the maximum mass. In either case, **radio observations will not deliver the precision radius measurements needed to measure the EOS**, which is necessary to pick out the correct EOS among the allowed ones. At present there is only one known radio source, the Double Pulsar, whose moment of inertia (via spin-orbit coupling) will be determined to within 10% within the next 20 years (Lattimer & Schutz 2005; Kramer & Wex 2009). This would result in a constraint on  $R \sim 5\%$ .

Box 7: Measuring M and R via seismology



The QPOs detected in the aftermath of giant flares were initially modeled as torsional shear oscillations of the neutron star crust. Using the relativistic oscillation model of Samuelsson & Andersson (2007), one finds the following expressions for the frequency of the fundamental oscillation and the first radial overtone, respectively:

$$f_{\text{fundamental}} = 26.3 \left( \frac{10\text{km}}{R} \right) \sqrt{\frac{(H - 1 + 2\beta)(1 - 2\beta)}{(\beta H)}} \text{ Hz}$$

$$f_{\text{overtone}} = 117 \left( \frac{10\text{km}}{R} \right) \frac{(H - 1 + 2\beta)}{H - 1} \text{ Hz}$$

where  $\beta = GM/Rc^2$  and  $H \approx 1$  is a constant related to the baryon chemical potential that is relatively well constrained to lie in the range 1.04-1.07 (Lattimer & Prakash 2007). The Figure shows the constraints that arise from applying this model to data from the SGR 1806-20 giant flare.

Figure above: mass–radius diagram showing the constraints from neutron star seismology from the soft gamma-ray repeater SGR 1806-20, fundamental frequency 29 Hz and 1<sup>st</sup> radial overtone frequency 626 Hz. H values in the range 1.04 (lower boundaries of permitted regions) to 1.07 (upper boundaries) were assumed. The neutron star lies in the box where the constraints from the two frequency bands overlap. Once QPOs are detected, frequency measurement errors are negligible for this purpose. EOS models as in Figure 2-3.

*Gravitational wave telescopes (Advanced LIGO and VIRGO):* they will enter service in 2014-15 or later and operate well into the next decade. Gravitational waves from the late inspirals of binary neutron stars are sensitive to the EOS, with departures from the point particle waveform constraining M and R. Global seismic oscillations excited by coalescence also depend on the EOS (Bauswein et al. 2012). However, estimates are that **Advanced LIGO and VIRGO can achieve uncertainties of ~10% (1σ) in R**, for the closest detected binaries (Read et al. 2013), and even this precision requires future reliable and precise numerical simulations that correctly account for tidal effects of matter in dynamical spacetimes. Event rates are also highly uncertain, with estimates as low as 0.4 per year even for the full-sensitivity network expected in 2020.

*X-ray telescopes (NICER-SEXTANT and Athena+):* NICER-SEXTANT is a NASA Explorer Mission of Opportunity experiment on the ISS from late 2016. With a softer energy band and far smaller effective area than LOFT it targets radio pulsars whose masses must be measured separately using radio timing (Bogdanov et al. 2008) and for which radius is then inferred using soft X-ray pulse profile modeling. NICER-SEXTANT has one primary (and currently single) target: the bright pulsar PSR J0437-4715 (two fainter pulsars will be studied if time permits: both would yield lower precision constraints and for neither source is the mass known). Calculations that assume a well-understood pulsar emission mechanism and an independently known mass with zero uncertainty show that *under these assumptions* NICER-SEXTANT could achieve  $dR \sim 2\%$  (Bogdanov 2013; Gendreau et al. 2012). In reality the  $1\sigma$  mass uncertainty for this pulsar is  $\sim 10\%$  (Verbiest et al. 2008) and this is difficult to improve since the source suffers from timing instabilities (this, rather than signal to noise, is the main impediment to increased accuracy). This will increase the error in radius, since the radius determination depends on the mass uncertainty. In addition the pulsar emissivity model is highly uncertain, with several major sources of systematic error, including a significant surface temperature anisotropy (Bogdanov 2013), the fact that atmospheric composition could be quite different to the nonmagnetic hydrogen models that are assumed (Chang & Bildsten 2003; Chang et al. 2010) and uncertainty in the temperature profile. The latter is thought to arise from return currents in the magnetosphere and is very difficult to calculate since it depends on models for the stopping of the currents (Broderick et al. 2012). It is the temperature profile that determines the beaming of the radiation emerging from the surface, and hence the amplitude of the pulsations. The spectrum and beaming function of the burst oscillation emission targeted by LOFT’s pulse profile modelling, by contrast, is understood at the 1% level (§2.1.4.1). Table 2-2 summarizes the main differences between LOFT and NICER-SEXTANT: **although a NICER-SEXTANT data point would constrain the EOS, LOFT data will measure its full functional form**. The dense matter capabilities of Athena+, (the soft X-ray Observatory proposed to carry out the ESA L2 science theme), also bear comment.

Table 2-2 LOFT’s dense matter performance as compared to NICER-SEXTANT.

		NICER-SEXTANT	LOFT
<b>Energy band</b>		0.2-12 keV	2-30 (+30-80) keV
<b>Effective area</b>		2 000 cm <sup>2</sup> @ 2 keV 600 cm <sup>2</sup> @ 6 keV	40 000 cm <sup>2</sup> @ 2 keV 100 000 cm <sup>2</sup> @ 6 keV
<b>Available techniques</b>		1	3
<b>Anticipated results</b>		<b>Few % accuracy in R for 1 source, where the mass is known to ~10% from radio timing. Weaker constraints on other sources where mass is not known independently.</b>	<b>3-5% simultaneously in both M and R for ~ 10 sources</b>
<b>Known potential candidate sources (by technique)</b>	Pulse profile modelling	PSRJ0437-4715 for which M is known from radio. May be possible for 2 additional bright isolated X-ray pulsars, however for these M is not known	24 stars with burst oscillations and/or accretion-powered pulsations.
	Weak/intermittent pulsations	N/A	~100 NS LMXBs.
	Seismology	N/A	20 bursting magnetars.
<b>Model dependence for pulse profile modeling technique</b>		Depends on poorly understood pulsar emission mechanism (see text)	Spectrum of burst oscillation sources understood to within 1% (§2.2.4.1).
<b>Opportunity for cross-checks using independent methods</b>		N/A	3 independent methods. Burst spectroscopy gives complementary constraint on the burst oscillation pulse profile modeling sources. Analysis using at least two different pulsation types for 70% of potential pulse profile modelling targets.
<b>Impact</b>		<b>CONSTRAINS EOS</b>	<b>RECONSTRUCTS EOS</b>

Dense matter is not a primary science goal for Athena+, but it has been discussed in an associated white paper (Motch et al. 2013). Its capabilities in this science area are however not comparable to LOFT (Table 2-2). Burst oscillation or accretion-powered pulsation pulse profile modeling is not in range for Athena+ since its area is simply not large enough to collect the requisite pulsed counts in any reasonable observing time. Athena+ can do pulse profile modeling for the same isolated X-ray pulsars as NICER-SEXTANT: however the same problems apply. Although Athena+ has a larger collecting area than NICER-SEXTANT, this does not solve the issues of the large mass uncertainty (derived from radio measurements and difficult to improve), and the strong systematics and model dependence associated with the poorly constrained pulsar emission mechanism. Athena+ also aims to constrain the EOS by spectral modeling of neutron stars in quiescence or the cooling tails of X-ray bursts. The many problems associated with this technique (such as the need for high precision absolute flux calibration and distance determinations, and substantial uncertainties in atmospheric modeling due to residual accretion) have already been discussed in §2.1.3. **LOFT, with its multiple techniques and cross-checks, and its large-collecting area, goes far beyond what is feasible with Athena+ and NICER-SEXTANT for dense matter science.** LOFT will be the first mission to make precision measurements of M and R for a sufficiently large sample of neutron stars to enable reconstruction of the full functional form of the EOS.

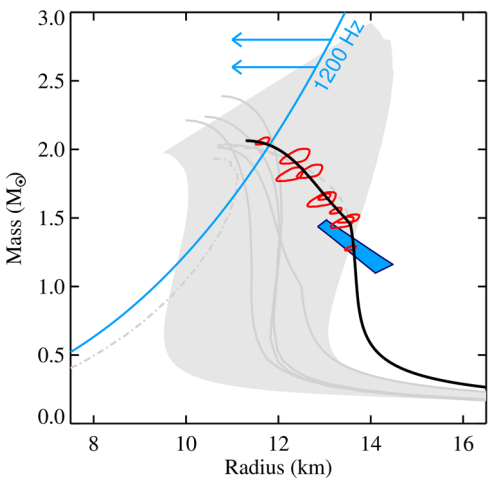


Figure 2-9 One potential outcome of the LOFT DM programme. Constraints are shown from pulse profile modelling (red contours, Figure 2-6), from a 1200 Hz intermittent pulsar (EOS must extend to the left of the blue line, as shown), and from seismic vibrations in a magnetar intermediate flare (blue box). In the scenario shown, preliminary results from pulse profile modelling have suggested that the EOS might be consistent with a hybrid star model (with flattening at high mass, kink at intermediate mass). Deep follow-up observations of the most constraining sources confirmed these features. The spin and seismic data are consistent with this EOS. The best fit hybrid EOS is shown in black, other models in grey. **The EOS uncovered by LOFT is consistent with models where neutron star cores contain stable strange matter, a breakthrough discovery.**

## 2.2 Strong Field Gravity

### 2.2.1 Introduction

#### 2.2.1.1 LOFT in Strong Field Gravity

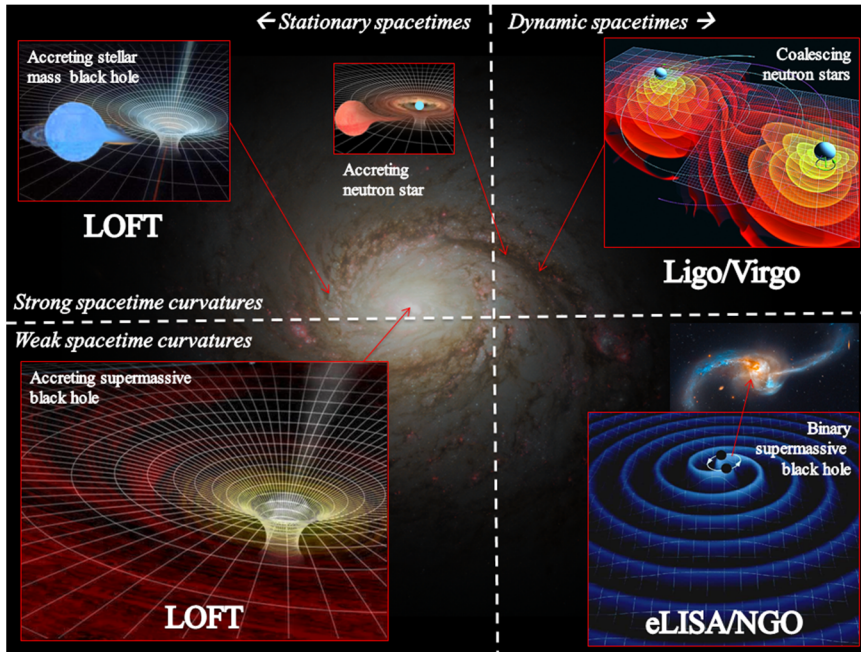


Figure 2-10 The roles of LOFT and gravitational wave observatories in strong gravity research. Uniquely, LOFT probes stationary strong gravity metrics by uniform methods near both stellar-mass and supermassive compact objects, spanning 16 orders in space-time curvature.

LOFT’s strong field gravity objectives are part of the broad effort to better understand gravity ranging from the very weak effects that dominate on cosmological scales (acceleration and the cosmological constant) via the dark-matter vs. modified-gravity debate, laboratory experiments and Solar system tests, to precision measurements

of binary millisecond radio pulsars. These pulsars orbit in gravitational fields of strengths also accessible in the Solar system, but nevertheless provide our current best constraints on strong field gravity theory (Taylor et al. 1992). However, there is no substitute for measuring the direct effects of a strong field gravity on the motions of matter (Psaltis 2008). For that reason, probing of strong field gravity (SFG) *in situ*, by direct observation of regions within a few Schwarzschild radii of black holes (BH) has the keen interest of both the physics and astrophysics communities.

Several different paths, all challenging, are currently being taken towards this goal. Instead of relying on very precise measurements of small effects as with pulsars, *in-situ* measurements address gross deviations from Newtonian physics, including qualitatively new effects that General Relativity (GR) predicts to occur near BH.

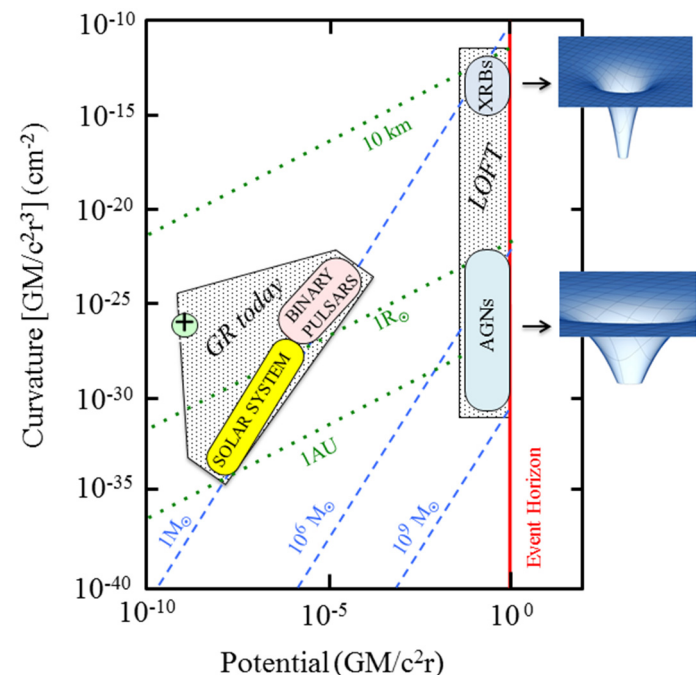


Figure 2-11 LOFT will measure gravity effects near NS and BH in XRB and near supermassive BH in AGN, exploring the regions of highest gravitational potential in the Universe, where current GR tests are constrained to potentials  $10^4$  times less. Supermassive and stellar mass black holes have the same topology but spacetime near their horizons has very different curvature, allowing LOFT to probe 16 orders of magnitude in curvature in a uniform astrophysical setting.

None of these have yet been verified, but initial indications have been reported (McClintock et al. 2011). LOFT provides a number of complementary methods, several of which unique, to probe BH surroundings and interpret the results in terms of gravitational effects. **LOFT/LAD for the first time merges the direct timing and spectral diagnostics we already know exist of the regions of strong field gravity: it resolves the relativistically**

**broadened Fe line profiles temporally as well as spectrally, and does so at up to several hundred times the photon throughput afforded by other designs. Hence, LOFT is able to see those line profiles vary on the fundamental strong-field relativistic timescales.**

Gravitational wave detectors (Sathyaprakash & Schutz 2009) will detect compact-object inspiral and merger events, where spacetime is being shaken by closely orbiting masses and hence *dynamic*. In contrast, LOFT addresses the *stationary* spacetime metrics of compact objects, probed by the X-ray emitting plasma of the accretion disk, essentially a luminous test fluid orbiting the BH with completely negligible self-gravity. The Event Horizon Telescope (Falcke et al. 2000; Doeleman et al. 2009) will provide sub-mm-band images of weakly accreting supermassive black holes in our own and a few nearby galaxies, diagnosing the relativistic paths of photons in stationary strong gravity. Extreme mass-ratio inspirals, and millisecond radio pulsars in close orbits around SgrA\* (if they exist), using instruments such as eLISA and SKA can eventually also probe matter motions in (virtually) stationary spacetimes, but only near supermassive black holes. LOFT uniquely covers not only supermassive but also stellar-mass black holes, and does so in completely analogous settings, performing comparative studies of BH spanning a factor  $10^8$  in mass via well-established diagnostics, using observables already clearly identified in current observations. Spacetime curvatures are small near supermassive BH event horizons (similar to that at the Sun's surface for a  $10^8 M_{\odot}$  BH) but scale as  $1/M_{\text{BH}}^2$ , and hence are a factor  $\sim 10^{16}$  higher near stellar-mass BH (and neutron stars, which LOFT will study for comparison, §2.2.1.2). X-ray observations uniquely provide access to these very-high curvature stationary metrics. GR predicts orbital dynamics are not affected by curvature (Psaltis 2008), and accretion flows across the black-hole mass scale probe this prediction over 16 orders of magnitude. If dynamics are affected, this would violate the no-hair theorem. **LOFT/LAD is the only instrument diagnosing the accretion flows in strongly curved spacetimes on the relevant spectral/timing resolutions at the signal to noise, fifty to hundreds of times higher than current and planned missions (§2.2.4), required to resolve motions down to the event horizon. It opens up the large collecting area regime where (forever after) stellar mass BHs provide  $\sim 10$  times higher signal to noise for dynamical time scale phenomena than AGN (even at zero background).**

In addition to the importance of strong-field gravity for fundamental physics, there is the wider astrophysical significance of understanding BH accretion. The growth of supermassive BH over cosmological time and the relation between the evolution of galaxies and their central BH, including the feedback effects of their relativistic jets and winds on the surrounding medium (Volonteri & Bellovary 2012), as well as the central engines of supernovae and gamma ray bursts (Piran 2004), all require a deep understanding of BH accretion, which is LOFT core business. BH spin, the only other intrinsic property beyond mass astrophysical BH are expected to have, is of great astrophysical significance. Because binary accretion roughly preserves spin and hence the birth record (King & Kolb 1999), stellar-mass BH spins carry information on BH formation in stellar collapse. Conversely, the spins of supermassive BH directly reflect their growth history through capture of gas and stars, and through mergers. BH spin can only be constrained by its relativistic signature of frame dragging. LOFT will allow measurement of the spin in a number of ways, timing and spectroscopy providing complementary probes (§2.2.2, 2.2.3).

### 2.2.1.2 Main Diagnostics and Interpretation

The two most important direct diagnostics of strong-field gravity near stellar-mass BH in X-ray binaries (XRB) and supermassive BH in Active Galactic Nuclei (AGN) that LOFT will use are relativistically broadened Fe lines (Fabian 1989; Tanaka et al. 1995) and relativistic time-scale variability, in particular, quasi-periodic oscillations, QPOs (van der Klis et al. 1985; Miyamoto et al. 1991; Strohmayer et al. 1996; van der Klis et al. 1996; Remillard et al. 1999; Gierliński et al. 2008). Our knowledge of these phenomena has exploded recently (van der Klis 2006; McClintock & Remillard 2006; Done et al. 2007; Miller 2007) thanks to (i) the growth in effective area and (ii) the attainment of sufficient spectral resolution in successive X-ray missions. **These two separate trends come together in LOFT. For the first time the spectral resolution required for the relativistic lines is combined with the photon throughput required to study their variability on time scales down to well below the dynamical time scale of the strong field region.**

The very broad Fe-K $\alpha$  profiles (Figure 2-12) reliably observed in both AGN and XRB are successfully modeled by X-ray reprocessing of a hard irradiating continuum by the accretion disk plasma in tight relativistic orbits around the BH. They provide a sensitive probe of the circumstances in the strong field region (*Box 8*), and estimates of BH spin. Some current stellar- as well as super-massive BH spin estimates based on measuring

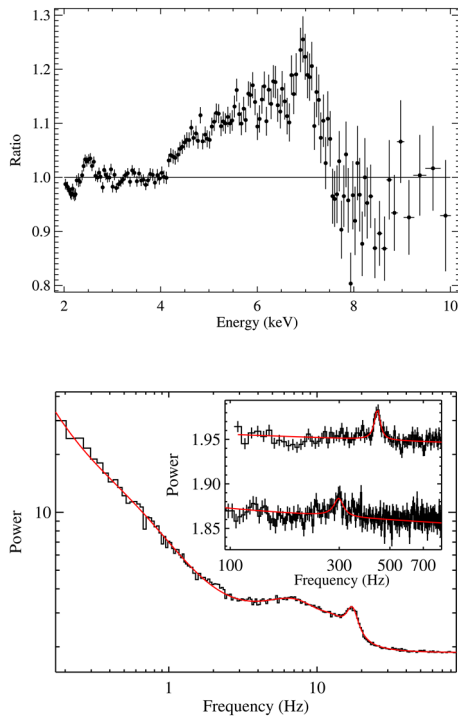


Figure 2-12 Top: Fe line profile (Miller 2007) and bottom: Fourier power spectra of relativistic precession frequency QPOs superimposed on broad band noise (Motta et al. 2013), all observed in the BH transient GRO J1655-40.

time-averaged line profiles suggest near-maximal spins (Reynolds 2013), but there are complications related to spectral complexity and (in XRB) pile-up, and significant discrepancies occur with other techniques, e.g. continuum fitting (McClintock et al. 2006).

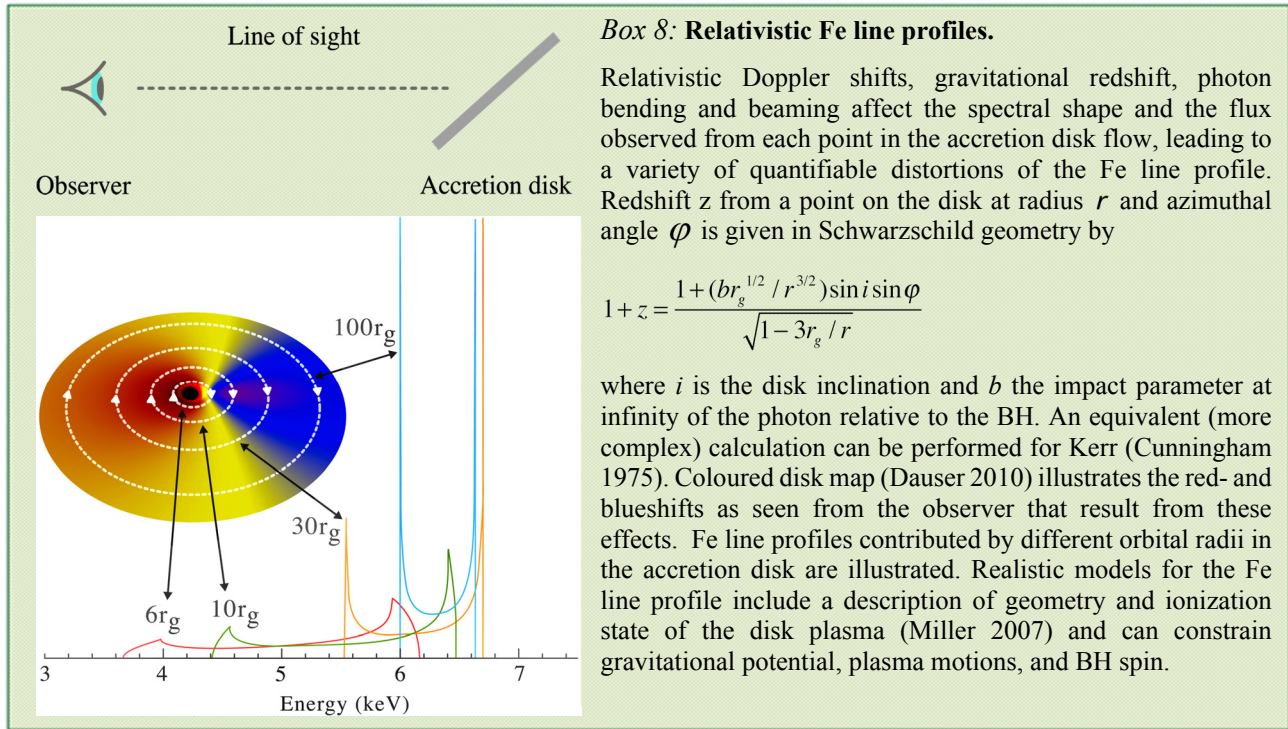
With the enormous S/N, good spectral resolution, virtually pile-up free LAD data it will be possible to address these issues (§2.2.2.4). However, **the most important advance afforded by LOFT lies in the capability to study rapid variability in the line profiles.** Rapid Fe line variability is well known to occur (Revnivtsev et al. 1999; Gilfanov et al. 2000; Wilkinson & Uttley 2009; Zoghbi et al. 2012; Kara et al. 2013), but energy resolution and signal to noise have been well below the level required to draw conclusions.

Rapid variability in broad band X-ray flux is a well-established feature of accreting compact objects. X-ray quasi-periodic oscillations (QPOs) and broad-band noise (Figure 2-12) are caused by plasma motions in the inner flow exhibiting local relativistic, turbulent and viscous time scales. The resulting inhomogeneities inevitably lead to variations in patterns of emissivity and illumination of the disk as seen from the observer, and **therefore produce distinctive line profile variations which encode flow characteristics.** Variations in emissivity patterns can occur due to orbiting inhomogeneities in the disk and can be analyzed using Doppler tomography techniques, where red- and blueshifts are used to reconstruct the loci of the inhomogeneities (§2.2.2.3). These techniques amount to QPO-phase dependent spectroscopy and will also make it possible to measure the QPO waveforms (§2.2.3.2). Variations in illumination can be produced by variable beaming of radiation incident on the disk (§2.2.2.1). They can also be caused by

light travel time effects causing the variability reflected from different parts of the disk to reach the observer with different time delays, and then be analyzed using reverberation mapping techniques where the delays map out the geometry (§2.2.2.2). **All** rapid variability, QPO, noise and even pulsations, can be used for these studies, and Doppler and reverberation mapping does not rely on any specific model for the fluctuations.

Because the ‘spectral timing’ techniques used to analyze these rapid line profile variations essentially combine three orthogonal diagnostics of the flow and its geometry, namely, (i) spectroscopy yielding velocities and redshift, (ii) timing of orbiting patterns revealing orbital periods in the disk and (iii) reverberation providing absolute length scales, they yield unprecedented insight in the processes in the inner flow. Spectral timing has already started to bear fruit in AGN, albeit with large errors: Fe line reverberation (Kara et al. 2013), as well as hints of orbiting hot spots (Yaqoob et al. 2003; Iwasawa et al. 2004; de Marco et al. 2009) have been seen. Indications for disk continuum reverberation have been observed in XRB in both BH (Uttley et al. 2011) and NS (Barret 2013). However, it requires the very high throughput coupled to good spectral resolution of LOFT to use these diagnostics to probe the plasma flows in the strong field regions at the necessary signal to noise. Spectral timing so far has been mostly limited to continuum spectroscopy and longer time scales; LOFT will measure rapid variability in narrow bands within the Fe line. QPOs in the X-ray flux are routinely observed (van der Klis 2006) in both stellar mass BH and neutron stars (NS) at frequencies within 10-20% of the relativistic orbital, epicyclic and precession frequencies in the inner disk, i.e., the fundamental frequencies of orbital motion in strong field GR (*Box 9*). The fastest QPOs occur on the time scale of orbital motion near the event horizon. They are much stronger in NS than in BH, presumably because fluctuations in mass accretion rate produce X-ray flux variations more efficiently at the NS-inner disk boundary layer (where about half of the accretion energy is released) than integrated (in BH) over the entire disk surface.

While in NS the frequencies vary strongly (up to 1250 Hz), BH high-frequency QPOs appear stable, at a frequency (40–450 Hz) that, as predicted for relativistic frequencies, scales inversely with black-hole mass. The BH QPOs are particularly intriguing, but weak and transient, so it has been impossible to determine if their frequencies are really fixed, or only appear to be so because we are only (just) detecting them when they are strongest.

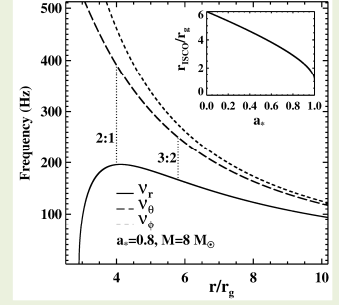
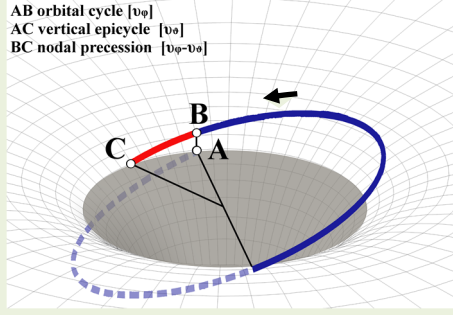
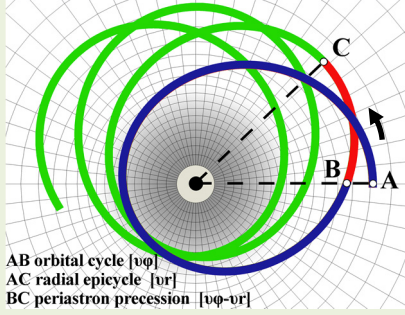


Their amplitude distribution is severely cut-off by current instrumental limitations (Belloni et al. 2012), but this will be remedied by LOFT (§2.2.3.1). In both BH and NS, QPOs have also been observed in the range predicted for Lense-Thirring precession in the strong field region (0.1-60 Hz), and with the predicted quadratic dependence on orbital frequency (Stella et al. 1999).

Several models have been proposed for these QPOs in terms of strong-field orbital and epicyclic motion in the disk flow, and interpretations along these lines have received support from large-scale simulations and from observational results; alternatives have been considered as well (§2.2.1.3). The frequencies observed in NS are close to, but not exactly, the relativistic ones, and some observations remain unexplained (van Straaten et al. 2003; Altamirano et al. 2012). This has been attributed to more prominent non-gravitational stresses in NS (due to magnetic field and surface radiation), than in BH, which are predicted to be fundamentally simpler (no-hair theorem). In support of this, the BH GRO J1655-40, at the edge of detectability with RXTE, has shown one set of 3 simultaneous QPO frequencies consistent with those predicted by GR at  $5.7r_g$  (Motta et al. 2013). For this reason the LOFT SFG objectives focus on BH, with, however, comparative observations of NS providing an important benchmark. NS spin rates can be measured directly, and there are various ways to reliably estimate mass and radius (see §2.1) and hence angular momentum, allowing *calibration* of the frame dragging effects of spin on the accretion flow in NS, that in BH are used to *measure* spin. These studies of NS disks also in principle constrain the NS mass-radius relation, providing a cross-check on the techniques of §2.1. In AGN, correlated QPOs analogous to those in XRB have not yet been found, with upper limits on their amplitudes of a few percent (Vaughan et al. 2011), but LOFT might find them, as it will be more sensitive to them than any previous mission (§2.2.3.1). AGN spectral timing is not affected by this, as broad lines and strong aperiodic variability abound (§2.2.2.2, 2.2.2.3). LOFT will also study QPOs in bright ultraluminous X-ray sources (ULX) such as M82 X-1 (Strohmayer & Mushotzky 2003) at high signal to noise (§2.2.3.1).

The transformative nature of LOFT's strong field gravity studies described in §2.3.2 and 2.3.3 comes from the LAD's breakthrough capabilities, which enable the collection of qualitatively new types of information: (i) precise measurement of Fe line variations on relativistic orbital, epicyclic and precession, and light-crossing time scales (SFG2,4,5), and (ii) QPO-phase spectroscopy and waveform detection of dynamical time scale QPOs (SFG3,4,5). These powerful new techniques to probe accretion flows close to the event horizon are currently photon-starved, but with LOFT they will flourish. LOFT will also obtain exceedingly precise *time averaged* Fe line profiles and power spectra, to precisely measure black hole spins (SFG4,5) and reveal the epicyclic and combination frequencies (SFG1).

**Box 9: Relativistic orbital motion**



In GR, each orbit is characterized by three different frequencies of motion: azimuthal (orbital), and radial and vertical epicyclic. This causes eccentric and/or tilted orbits to exhibit periastron and/or nodal precession at frequencies  $\nu_{peri} = \nu_\phi - \nu_r$  and  $\nu_{node} = \nu_\phi - \nu_\theta$  (left and middle figures), where  $\phi$  and  $\theta$  are azimuthal and vertical angles. For small tilt and eccentricity, orbits around a BH with mass  $M$  and angular momentum  $J$  are given by

$$r_g \equiv GM / c^2 \quad a_* \equiv Jc / GM^2$$

In Schwarzschild geometry ( $a_* = 0$ ):

$$\nu_\phi = \sqrt{GM / r^3} / 2\pi (1 + a_*(r_g / r)^{3/2})$$

$$\nu_\phi = \sqrt{GM / r^3} / 2\pi \approx 1200 \text{ Hz } (r / 15 \text{ km})^{-3/2} m_{1.4}^{1/2}$$

$$\nu_r^2 = \nu_\phi^2 (1 - 6(r_g / r) + 8a_*(r_g / r)^{3/2} - 3a_*^2 (r_g / r)^2)$$

$$r_{ISCO} = 6r_g = 6GM / c^2 \approx 12.5 \text{ km } m_{1.4} \text{ km}$$

$$\nu_\theta^2 = \nu_\phi^2 (1 - 4a_*(r_g / r)^{3/2} + 3a_*^2 (r_g / r)^2)$$

$$\nu_{ISCO} = (6^{3/2} / 2\pi)(c^3 / GM) \approx (1580 / m_{1.4}) \text{ Hz,}$$

so frequencies associated with given  $r/r_g$  (e.g., the ISCO at  $6r_g$  in Schwarzschild) scale as  $1/M$ . Right figure: Frequencies depend on orbital radius in different ways parametrized by mass and spin of the central object. In contrast to the other frequencies, the radial epicyclic frequency decreases with radius close to the compact object. Stable orbital motion is possible only for radii in excess of the innermost stable circular orbit (ISCO) radius. This radius decreases from  $6r_g$  at zero spin to  $1r_g$  for maximal spin (inset). At the ISCO the radial epicyclic frequency goes to zero. This, and the lack of stable orbits, both are genuine strong field GR effects.

**2.2.1.3 Models and Simulations**

Relativistic broadening inner disk reflection models for the Fe line of increasing sophistication now include full Kerr-metric GR calculations (Box 8) of flow dynamics as well as photon trajectories and Doppler and gravitational redshifts, and an advanced treatment of the radiation processes. Models reproduce the broad Fe K line, the fluorescent emission species at lower energies and the Compton hump at higher energies and include ionization and Fe abundance of the disk plasma, photon index and radial intensity distribution of the irradiating power law as well as inclination and BH spin (Brenneman & Reynolds 2006; Dauser 2010; Dauser et al. 2013; Risaliti et al. 2013).

Detailed fundamental frequency models for the QPOs describe how the relativistic orbital, epicyclic and/or precessional frequencies (Box 9 for quantitative expressions) are expressed in the bulk motions of the orbiting disk plasma. These models are based on global disk-oscillation and precession modes (Ingram & van der Klis 2013), or involve disk density fluctuations in approximate geodesic orbits (Stella et al. 1999; Wagoner et al. 2001; Abramowicz & Kluzniak 2001; Rezzolla et al. 2003; Török et al. 2005; Török et al. 2010; Török et al. 2012; Stuchlík et al. 2012) For example, in two competing epicyclic motion interpretations of BH high frequency QPOs, the relativistic precession model, RPM (Stella et al. 1999), and the epicyclic resonance model, ERM (Abramowicz & Kluzniak 2001), the QPO frequencies are related to GR azimuthal, radial and vertical frequencies for orbits near the event horizon. Indeed, the observed maximum QPO frequencies (§2.2.1.2) are close to those predicted at the ISCO and scale with  $1/M$  as predicted. In NS specific predictions by the RPM about QPO frequencies in terms of azimuthal and radial epicyclic motions were confirmed by observations of Cir X-1 (Boutloukos et al. 2006). In the Ingram & Done (2012) model for low-frequency QPOs based on large scale hydrodynamical simulations of Fragile et al. (2007), the Lense-Thirring precession frequencies at different radii in the inner hot accretion flow combine into a surface density weighted average nodal precession frequency of the flow as a whole. This model successfully predicts observed BH and NS power spectra up to  $\sim 100$  Hz. It also predicts Fe line profile variations at the nodal precession frequency easily

detectable with LOFT (§2.2.3.1). Calculations of emitting patterns in geodetic motion in the accretion flow (Bao et al. 1994; Bao & Ostgaard 1995; Dovčiak et al. 2004) predict intricate relations between QPOs and Fe line profiles (§2.2.2), and specific “fingerprint” patterns of power spectral components (§2.2.3), that LOFT can detect, and will use to probe strong field gravity accretion flows. The high energy processes producing the X-ray spectra and the inhomogeneities responsible for the time variability of the radiation are co-located in the hot, unstable plasma flows in the strong field region, and hence merging these diagnostics will probe those regions to an unprecedented degree. The models discussed above form the basis of the simulations (§2.2.2, 2.2.3) explicitly quantifying LOFT performance relative to science objectives SFG1-5. While models not including relativistic disk reflection cannot explain the data (Risaliti et al. 2013), partially ionized absorption also plays a role in the line formation (Miller 2007) and this is taken into account in our simulations (§2.2.2). Alternative explanations for QPOs have also been discussed (Tagger & Varnière 2006; Lai & Tsang 2009; McKinney et al. 2012), however, these do not succeed in predicting the observed correlated variable QPO frequencies similarly to fundamental frequency models.

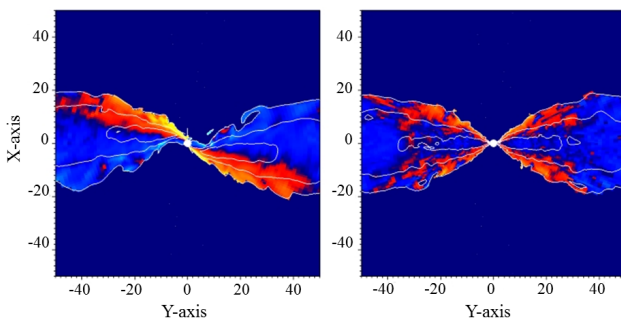


Figure 2-13 Sophisticated large-scale black hole hydro-flow simulations. Nodal and possibly also periastron precession have been observed in these simulations (Fragile & Blaes 2008).

There has been considerable progress with large scale first-principle MHD computations of accretion flows onto compact objects (Blaes 2013; Fragile 2013; Fragile & Blaes 2008; Henisey et al. 2009; McKinney et al. 2012; Dolence et al. 2012; O’Neill et al. 2012; Romanova et al. 2013). Taking into account projected

improvements in computation, full-GR global 3D MHD simulations may be possible by in the early 2020’s, and be tested with LOFT data that begins to flow at that time. Although QPOs are still elusive in current computations, some of the results (Fragile & Blaes 2008) already illustrate the role of epicyclic and precessional motion in disks that are tilted from the equatorial plane of the compact object (Figure 2-13). However, radiative transfer and stresses are still hard to include in the computations, so theory, computation and observation can be expected to continue to go hand in hand also in the LOFT era.

#### 2.2.1.4 LOFT’s Strong Field Gravity Objectives

LOFT will probe strong field gravity at several levels. It will determine (i) time scales, velocities and orbital frequencies in the inner disk, thus directly measuring the motions in strong gravity. It will measure (ii) frame dragging through Lense-Thirring precession as well as (iii) nodal precession to the higher orders predicted by GR for the strong field region near Kerr black holes. Another genuinely strong field effect LOFT will measure is (iv) the progressive decrease of the radial epicyclic frequency as the BH ISCO is approached. This will confirm the existence of the ISCO in the GR sense, and go beyond just detecting the inner edge of the accretion disk, whose location may be affected by many effects other than gravity (Krolik & Hawley 2002).

## 2.2.2 Relativistic Line Profiles as a Probe of Strong Field Gravity

In this section we present detailed simulations of LOFT/LAD observations of the Fe line profile and its rapid variability associated with QPO and noise phenomena. This ties in to science objectives SFG2, 4 and 5.

**[Science Requirement SFG2]** Detect disk precession due to relativistic frame dragging with the Fe line variations in low frequency QPOs for 10 neutron stars and 5 black holes.

**[Science Requirement SFG4]** Constrain fundamental properties of stellar mass black holes and of accretion flows in strong field gravity by (a) measuring the Fe-line profile and (b) carrying out reverberation mapping and (c) tomography of 5 black holes in binaries providing spins to an accuracy of 5% of the maximum spin ( $a/M=1$ ) and do comparative studies in 10 neutron stars.

**[Science Requirement SFG5]** Constrain fundamental properties of supermassive black holes and of accretion flows in strong field gravity by (a) measuring the Fe-line profiles of 20 AGNs and for 6 AGNs (b) carry out reverberation mapping and (c) tomography, providing BH spins to an accuracy of 20% of the maximum spin (10% for fast spins) and measuring their masses with 30% accuracy.

2.2.2.1 Precessing Inner Hot Flow [SFG2]

In the Ingram & Done (2012) model for BH low-frequency (LF) QPOs, an optically thin ( $\tau \sim 1$ ) and geometrically thick hot inner flow precesses as a solid body due to relativistic frame dragging. The precession is quasi-periodic due to a varying mass load in the inner flow. This leads to the commonly observed 0.03-30 Hz BH LF QPOs, producing a quasi-periodically rotating illumination pattern of the geometrically thin thermal disk outside the inner flow (*Box 10*). Different parts of this relativistic flow are quasi-periodically ‘lit up’.

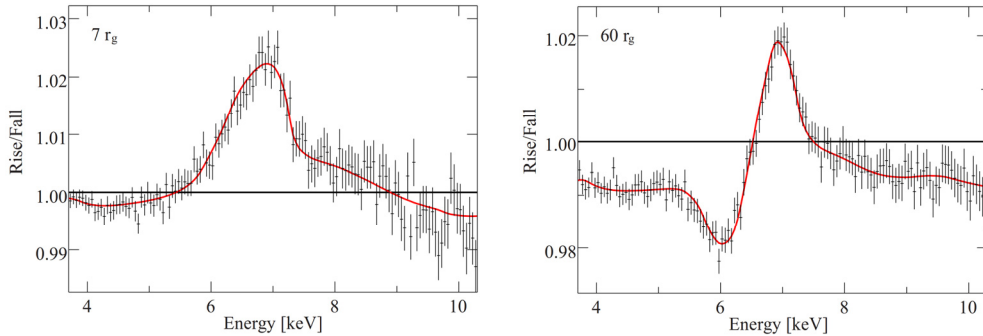


Figure 2-14 Line profile ratios between QPO cycle rise/fall for two different values of inner disk radius as indicated. The blue wing is enhanced and the red wing suppressed in the QPO rise when the approaching sector of the disk is illuminated. In the

$7r_g$  simulation the suppression of the red wing is compensated by the strong gravitational redshift dominating over the Doppler shift and light bending close to the BH. Both 5 ks simulations use a full reflection and continuum model (REFLIONX+DISKBB+NTHCOMP) and a realistic illumination pattern by an oblate spheroid central flow. Disk inclination  $60^\circ$  0.36 and 0.66 Crab flux, 0.1 and 10 Hz QPO frequency.

**Box 10: Precessing hot flow.** Disk irradiation patterns and associated line profiles in the Ingram & Done (2012) model. As the toroidal hot flow precesses, the illumination pattern sweeps over the approaching (blue sector in maps) and receding parts of the disk, respectively, and the blue and red wings of the line are successively amplified. These profiles are not folded with the instrument spectral resolution

Simulations show strong line profile differences between the rise and fall of the QPO cycle, with the boosted blue wing of the Fe line profile being alternately emphasized and suppressed (Figure 2-14). Analyzing the simulated data in a realistic fashion, collecting data for QPO rise and fall from the simulated light curve, and then fitting the ratio spectra with an emission model, we measure the inner radius of the thermal disk to a precision of 3–6% (the smaller error for  $7r_g$ ) and the inclination  $\sin i$  of the disk to 0.3%. The observation provides definitive confirmation of the precession model (SFG2). It takes only a few ks to obtain accurate data over the wide range of QPO frequencies commonly observed, allowing the measurement of the relation between QPO frequency and inner disk radius, for which the relativistic frame dragging scenario makes specific predictions. Similar LF QPOs, in the 15–60 Hz range, are seen in NS, and comparative observations will be performed of those. These QPOs are common, and will be studied in 5 BH and 10 NS to cover a range of inclination angles and masses.

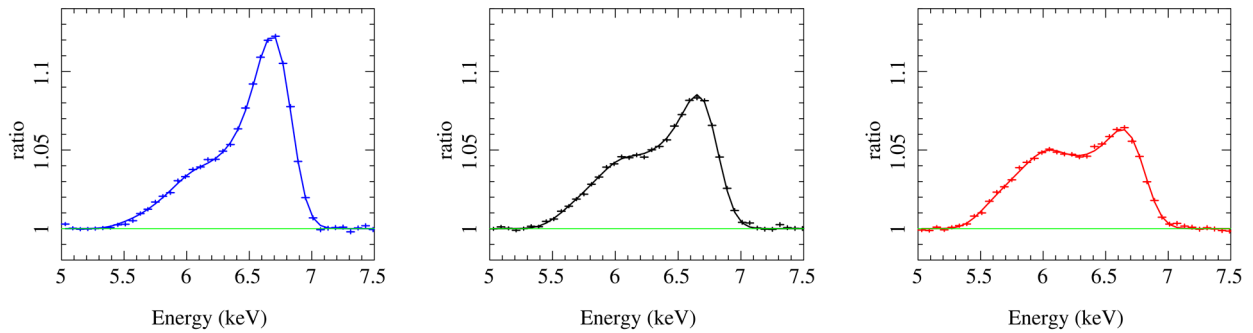
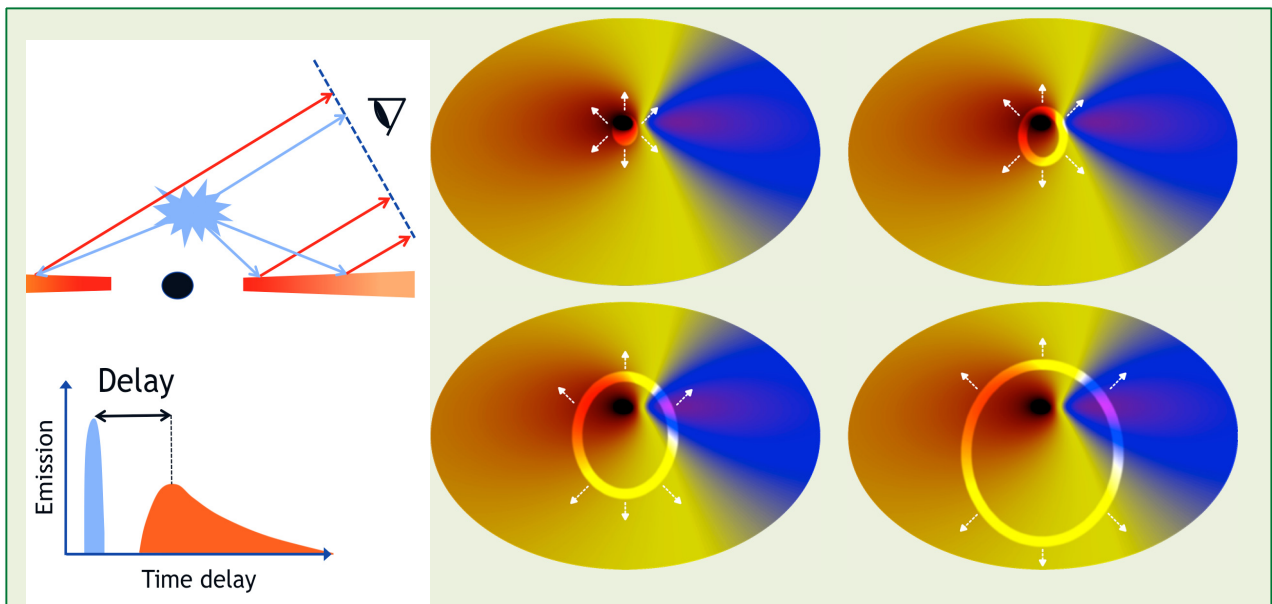


Figure 2-15 Simulation of a 50ks LOFT observation for which the QPO has been resolved into 50 phase bins, each with a total exposure of 1ks. The three phases shown represent snapshots when the flux is rising (blue), at a peak (black) and falling (red). The simulated data and model are presented as a ratio to the power law continuum ( $\Gamma=1.7$ ). The changes in the line profile resulting from the inner flow illuminating different azimuths of the Keplerian disk at different phases of the precession cycle are clearly recovered to a high accuracy by LOFT.

### 2.2.2.2 Reverberation [SFG4 & 5]

Reverberation (radiation ‘echoing’) of the variability of an incident hard continuum off the disk leads to light travel time lags between energy bands (§2.2.1.2). These constrain the geometry on an absolute length scale (km), and in particular, diagnose the absolute size of the inner radius of the reflecting disk (Box 11). Simulations show that LOFT will be able to perform such measurements to high precision for bright BH binaries and nearby AGN, verify orbital motion patterns in the strong field region and measure black hole spins and masses.

Figure 2-16 shows simulated LAD time lag spectra in a 100 ks observation of a 0.7 Crab, 10  $M_{\odot}$  BH in a typical hard or intermediate state using realistic X-ray spectra and variability characteristics (i.e., no arbitrary ‘flare’ is assumed to calculate a theoretical response function, but instead a realistic 60–200 Hz variability power spectrum – as actually measured in these BH – is used). The hard continuum is produced at the center and reflects off a thermal disk.



**Box 11: Reverberation.** *Left:* Light travel time effects cause variations in the irradiating continuum (blue) to reach different parts of the disk, and the reprocessed radiation (red) to reach the observer, at different times. The resulting signal contains light echos called ‘reverberation’ and can be used to map the accretion flow. *Right:* Expanding illuminated and reflecting ring caused by a flare in the irradiating flux. This method uniquely provides absolute length scales (in km, as  $c$  is known) to complement the geometrical information provided by the Fe line profile, giving lengths scaled to  $r_g=GM/c^2$ , and by the QPOs, giving absolute periods (in seconds) related to the orbital time scale  $\tau_{orb}=(GM/r^3)^{1/2}$

Time lags relative to a broad (2-20 keV) reference band can be measured to a precision of  $1.3 \mu\text{s}$  in 200 eV bins near 6 keV, and allow measuring the inner disk radius to a precision of 1.8 km ( $0.12r_g$ ) which for known black hole mass constrains the BH spin to a precision of 2% of maximum spin (SFG4b). Black hole mass could be obtained from the binary orbital motion (modulo  $\sin i$ ). As these reverberation measurements encode the various relativistic effects distorting the line profiles, including redshift and strong-field Shapiro delays, as a function of absolute radius (Wilkins & Fabian 2013), black hole mass and spin can be directly derived from these curves, and the GR predictions of the radius dependencies verified at high precision. Similarly, in a 100 ks LAD exposure of a 2 mCrab,  $4 \times 10^6 M_\odot$  AGN, again using realistic variability amplitudes and nominal background levels and systematics, a very clear time lag spectrum with strong Fe feature is observed that allows measuring the inner disk radius to a precision of  $6 \times 10^6$  km ( $1.0r_g$ ), which for known mass constrains BH spin to a precision of 13% of maximum (SFG5b). LOFT shall be able to perform such Fe line reverberation measurements (and Doppler tomography, §2.2.2.3) for at least 6 sources  $>6 \times 10^{-11} \text{ erg cm}^{-2}\text{s}^{-1}$  (2-10 keV; see details in the LOFT Science Requirements Documents, SciRD<sup>2</sup>). The geometry of reverberation in NS is expected to be different from that in BH (the boundary layer rather than the ‘corona’ providing the source of irradiation of the disk), and high frequency variability is much stronger in NS, so comparative studies in NS will provide strong additional constraints (SFG4). It is interesting to note that the difference in signal-to-noise (S/N) between XRB and AGN apparent in Figure 2-16 is *not* due to background effects, but instead is a consequence of the much higher flux we receive from XRBs (§2.2.4).

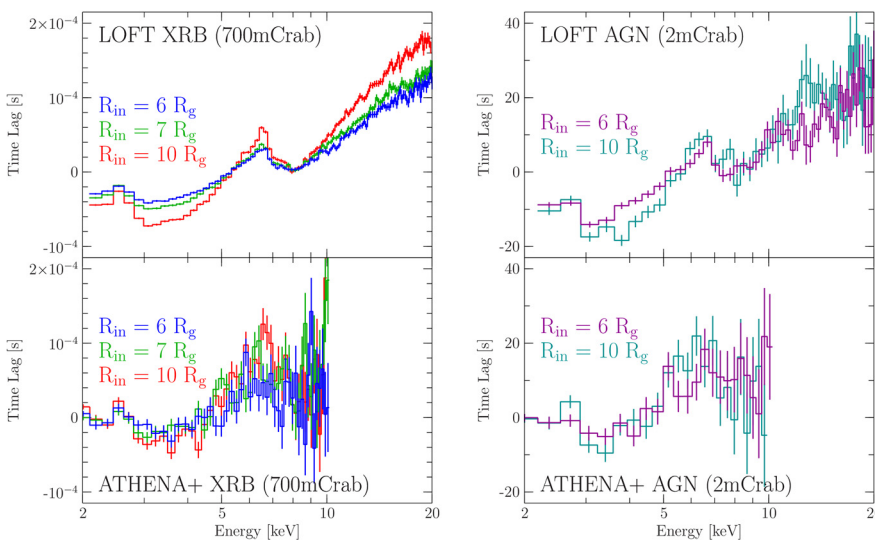
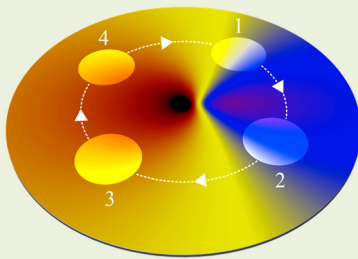


Figure 2-16 Time lag spectra due to reverberation light travel time delays using the 60-200 Hz broadband variability in a  $10 M_\odot$  XRB BH (left) and the 0.3-3mHz variability in a  $4 \times 10^6 M_\odot$  AGN (right). Three different inner disk radii  $r_{in}$  are illustrated for the XRB. Disk inclination  $30^\circ$ . The Fe line lags the continuum due to light travel time delays from hard continuum source to disk, the reflection bump shows larger lags as it is less diluted by direct continuum radiation. Spectral model:  $\Gamma=2$  power law + reflionx. For comparison the results that would have been obtained with Athena+ are shown. XMM would have achieved slightly worse results.

### 2.2.2.3 Doppler Tomography of Orbiting Hot Spot Patterns [SFG4 & 5]

Orbiting hot spot patterns in the accretion disk undergo alternating Doppler redshifts and blueshifts, which lead to quasi-periodic distortions of the spectrum, including the broad Fe line profile (Box 12). In XRB, thanks to the enormous S/N of the LAD data, it will be possible to measure the spectral signal of random patterns of



**Box 12: Orbiting blob Doppler tomography.**

An orbiting luminous blob in the accretion disk will cause a feature to move back and forth through the line profile as the blob transits the red- and blue-shifted regions. This signal can be used to reconstruct the geometry by the technique of Doppler tomography. Four different locations of the blob in its orbit are illustrated.

<sup>2</sup> [http://www.isdc.unige.ch/loft/DOCS/publ/LOFT\\_SciRD\\_20130911.pdf](http://www.isdc.unige.ch/loft/DOCS/publ/LOFT_SciRD_20130911.pdf).

orbiting hot spots even if they are not detected in the time series directly; in some cases they will be, see §2.2.3.2, in which case the quality of the data will improve further.

Figure 2-17 illustrates what LOFT shall be able to do using a realistic  $\sim 216$  Hz 2% rms amplitude QPO produced by patterns of hotspots in the disk occurring randomly in time and azimuth, and orbiting at frequencies near the QPO frequency. The periodic curve in the dynamic energy spectrum (*left*) is the Fe line shifting up and down in energy due to the quasi-periodic Doppler shifts caused by the orbiting patterns, reconstructed using Fourier methods. This radial velocity curve for orbital motion in strong field gravity is non-sinusoidal (Dovčiak et al. 2004): the rise to maximum line energy and the maximum itself last shorter than the fall to minimum and the minimum itself. LOFT measurements can be seen to clearly exhibit these GR-predicted effects in strong-field orbital motion. Approaching and receding phase produce blue- and red-shifted line profiles (*right*), that can be reconstructed, and whose energies can be estimated to accuracies of 0.5% and 2%, respectively, already from a 25 ks integration (in Figure 2-17 an integration time of 100 ks was used for clarity).

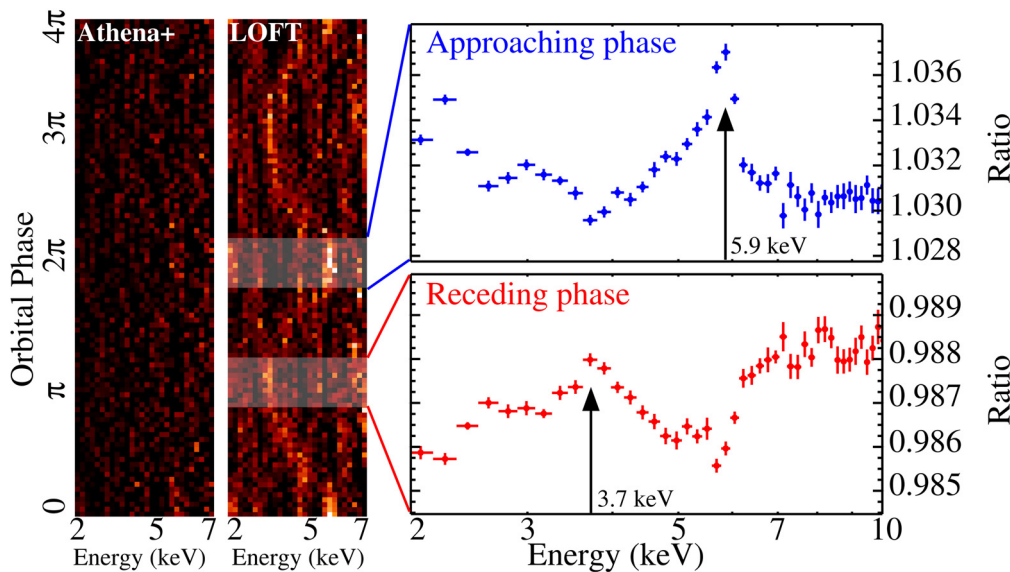


Figure 2-17 Dynamic energy spectrum (*left*) and phase selected spectra (ratios to average spectrum, *right*) as obtained in a 100 ks exposure of a 1 Crab BH transient in the intermediate state as observed. A fluctuating pattern of weak, randomly occurring,  $\sim 1r_g$  wide hot spots orbits in the disk at  $6 r_g$  and produces a 2% rms amplitude  $Q=5$  high-

frequency QPO, consistent with observations (Belloni et al. 2012). Two statistically independent cycles are shown. Image was processed for display purposes to remove steep gradients due to Doppler boosting.

Given spin (which can be estimated from the average line profiles, §2.2.2.4), the average line energy shift combined with hot spot orbital period (well-known as it is the inverse QPO frequency) can be used to measure the gravitational redshift  $z$  and hence  $r/r_g$  of the hotspots (in this example, to 1% precision), and solve for orbital radius  $r$  and black hole mass  $M$  to  $\sim 1\%$  and 1.5% accuracy, respectively (SFG4c). Amplitude provides hot spot line of sight orbital velocity in km/s (to 2%) and hence disk inclination  $i$ .

Note that any pattern of variable local enhancements in emission of the accretion disk can be used for analyses of this type, including patterns orbiting at a wide range of radii. A disk irradiated by the rotating beam of a central pulsar will produce strong, coherent, signals of this type as well and in comparative neutron star studies this will provide a cross-check on the black-hole results.

In AGN, LOFT will be able to follow the distortion of the Fe line profile due to the orbiting hotspot in the time domain. Spectra covering  $60^\circ$  in orbital phase clearly show the excess Fe line emission alternate between deboosted redshift and boosted blueshift (Figure 2-18). As these measurements rely on variability in the residuals, any narrow lines in the profile (arising by necessity at larger radii and hence varying much slower than the 10 ks inner disk orbital period) drop out automatically. Hot spot orbital radius  $r/r_g$  can be measured to a precision of 1-2% and combined with the spin measurement from the average line profile allows measuring the mass to  $\lesssim 30\%$  (SFG5c). LOFT will perform such measurements in at least 6 AGN.

Another type of Fe line tomography that LOFT will be able to perform is eclipse mapping, using X-ray eclipses of AGN by broad-line region clouds with durations of hrs-days (Elvis et al. 2004; Puccetti et al. 2007; Maiolino et al. 2010; Risaliti et al. 2011; Risaliti et al. 2011; Brenneman et al. 2012) where the approaching and receding parts of the disk are subsequently eclipsed, allowing observation of red and blueshifted line profiles separately.

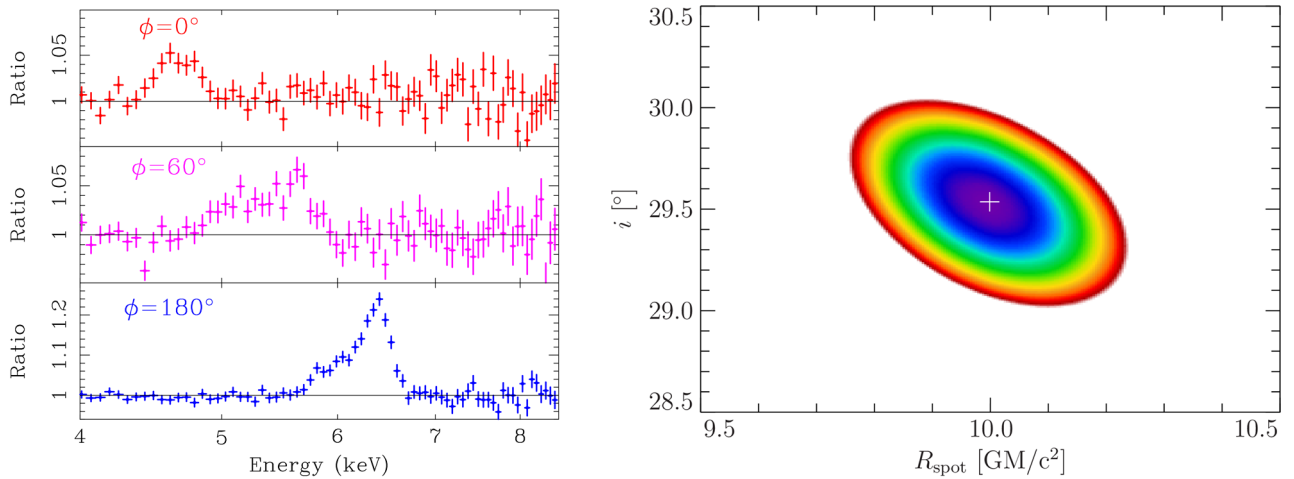


Figure 2-18 Fe line profile ratios to line average resulting from two 10-ks orbits of a coronal hot spot around a  $10^7 M$ , spin  $a^*=0.5$  black hole at  $10 r_g$  and contributing 10% of the Fe line flux in a 2.5 mCrab AGN observed under an inclination of  $30^\circ$  for a total of 20 ks ( $\sim 3000$  s per profile plotted). Only the fluorescent spectral component is plotted (Dovciak 2004). Error contours (1, 2, and  $3\sigma$  in blue, green and red, respectively) of disk inclination vs. hotspot orbital radius resulting from a fit to the line profiles in the three different phases.

2.2.2.4 Average Line Profiles [SFG4 & 5]

Average Fe line profiles will be measured to very good precision with LOFT in both XRB and nearby AGN. This will allow using state of the art reflection models to measure black hole spins. Our simulations show that in AGNs the LAD, at the required response and background, distenangles the spectral complexities in the Fe K region and successfully extracts the relativistically broadened line, recovering the BH spin at  $\sim 20\%$  accuracy [SFG5c], despite the presence of narrow neutral and ionized lines (Figure 2-18).

So, narrow line complexes are correctly dealt with in the LAD fits – also, they arise in the outer emission regions and hence are expected to be constant for years. In the bright AGN LOFT targets they were already measured with Chandra, and they will be again with other missions. Based on the XMM, BAT and Suzaku AGN catalogues, at the nominal (requirement) 0.25% (0.01 mCrab), background systematic error, LOFT will carry out such detailed broad Fe line modeling on a sample of at least 20 AGNs (see details in §3.1.3). For stellar mass BHs LAD data allow measuring the BH spin in a 1 Crab object with maximum spin (such as microquasar GRO J1655-40) with 1-2% accuracy [SFG4a] in just 100 s using state of the art models including complex absorption (see Figure 2-20).

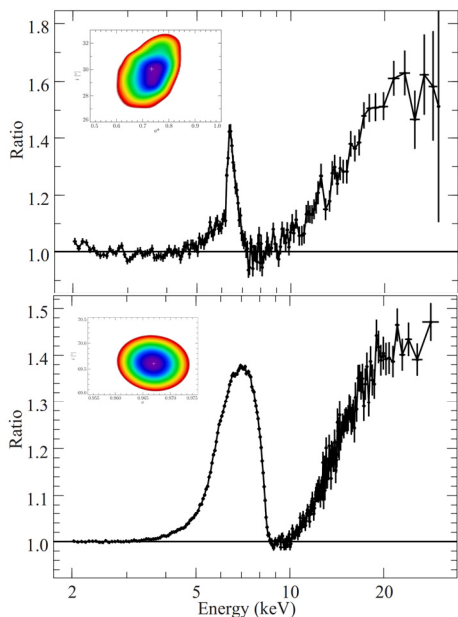


Figure 2-19: Fe line and reflection hump observed in a 2.5mCrab spin  $a^*=0.7$  AGN in 10 ks. S/N is about 400 (2-10 keV). Ratio to power law spectrum is shown. The self-consistent spectral model includes neutral reflection for narrow Fe  $K\alpha, K\beta$ , Ni  $K\alpha$  lines + reflection continuum (pexmon), relativistic ionized reflection (kerrconv\*reflionx), photoionized hot gas ionized lines with  $\log(x_i)\sim 3.5 \text{ erg cm}^{-1}$  (xstar), with parameters typical for of MCG6-30-15 (Miniutti et al. 2007) and LAD requirement B/G level and systematics. Inset: confidence levels for the disc inclination vs. BH spin (1, 2, and  $3\sigma$  in blue, green and red, respectively). The spin and inclination angle are measured to within  $\sim 10\%$  accuracy ( $1\sigma$ ).

Figure 2-20: Left: Fe line and reflection hump in a 0.1 ks integration of a 1 Crab, spin  $a^*=0.97$  XRB BH. Ratio to power law spectrum is shown. Simulated high soft state spectrum includes highly photoionized absorption ( $\log(x_i)=3.6 \text{ erg cm}^{-1}$ ) due to an outflow producing narrow lines/edges in the Fe K region as observed in GRO1655-40 (Diaz Trigo et al. 2007). Right: confidence levels for the disc inclination vs. BH spin (1, 2, and  $3\sigma$  in blue, green and red, respectively). The spin and inclination angle are measured to within 1% ( $1\sigma$ ).

## 2.2.3 High Frequency QPOs as a Probe of Strong Field Gravity

### 2.2.3.1 Epicyclic Motion

**[Science Requirement SFG1]** Detect strong-field GR effects by measuring epicyclic motions in high frequency QPOs from at least 3 black hole X-ray binaries and perform comparative studies in neutron stars.

LOFT will measure BH high frequency QPOs (which are currently barely detected; §2.2.1.2) at very high S/N, in some cases coherently, and hence will be able to distinguish between proposed fundamental frequency explanations (§2.2.1.3) and measure the orbital, epicyclic and precessional motions of the plasma in the strong field region.

Figure 2-21 shows a comparison of the QPO peaks in the power spectrum, at frequencies corresponding to orbital and epicyclic motions, as well as their harmonics and combination frequencies for the relativistic precession model (RPM) and the epicyclic resonance model (ERM; §2.2.1.3). In the RPM frequencies vary with the variable inner disk radius, in the ERM they are constant, at resonant radii in the disk. The RPM calculation (*left*) simulates the emission of elongated (as expected from shear) luminous regions orbiting in the accretion disk; various predicted frequencies are clearly detected, including the tell-tale 100-200 Hz radial epicyclic frequency whose frequency dependence on radius is inverted. The ERM calculation (*right*) simulates the global modes of a luminous toroidal part of the accretion flow. The strong peaks at 300 and 450 Hz correspond to the radial and vertical epicyclic modes, respectively, of a  $10.8 R_g$  torus around a  $2 M_\odot$  BH in a 2:3 resonance. Both sets of calculations were performed in full GR (Kerr metric) for both the dynamics of matter motions and the photon propagation towards the observer (Bakala et al. 2013). Clearly, while in both cases the average power spectra (*top*) are consistent with previous observations, LOFT distinguishes between these models at very high confidence, and in either case obtains detailed information on the epicyclic motions in the strong-field region. The precise relation between the three frequencies in the RPM as measured in this simulation verifies GR to high precision and constrains the BH spin parameter to a precision of  $6 \cdot 10^{-4}$ .

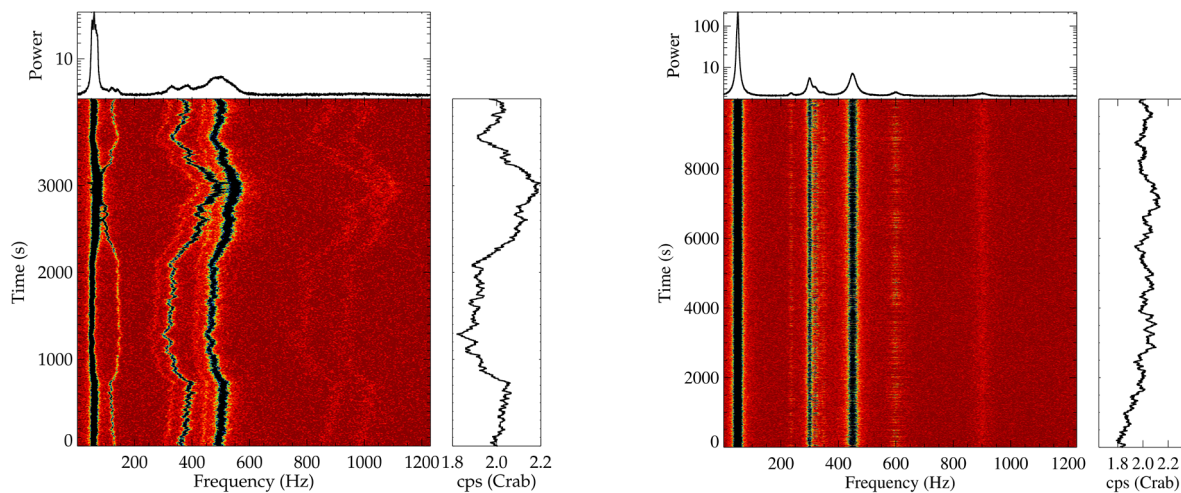


Figure 2-21: Dynamical (time-frequency) power spectra of QPOs in a 1 Crab BH of  $7.1 M_\odot$  and spin  $a^* = 0.60$  at disk inclination of  $63^\circ$  observed with LOFT for two different epicyclic-frequency models. The tracks in the images show the QPO frequency variation (or its lack) in either model. Left: Relativistic precession model. Frequencies observed due to the emission of an elongated ( $315^\circ$ ) luminous region with radial extent of  $0.5r_g$ , in geodesic motion at radii that vary with flux (right panels) between  $4.0$  and  $4.5 r_g$ . Frequencies most clearly visible (low to high frequency) are due to: Lense-Thirring precession, radial epicyclic motion (note the inverse dependence on radius compared to all other frequencies), periastron precession, orbital motion; several other combination frequencies are present as well. Right: Epicyclic resonance model. Radial and vertical epicyclic frequencies and their harmonics are observed due to vibrations of a toroidal mass flow in 2:3 resonance at 300 and 450 Hz. The low frequency QPO is not predicted in this model and arises through another mechanism.

The possibly related NS high frequency QPOs are known to have strongly tunable frequencies (§2.2.1.3). In most models, one of these QPOs occurs at the orbital frequency of the inner disk radius. However, the QPOs drop below the detection level before they reach the high frequency and the small inner disk radius, predicted for the ISCO (Méndez et al. 2001). LOFT will observe these NS QPOs for comparison to BH, and follow their

evolution to higher frequency. This will provide a cross-check on their interpretation by simultaneous spectral estimates of inner disk radius, and confirm the ISCO by the GR-predicted maximum in the orbital frequency, and drop to zero of the radial epicyclic frequency there (Box 9). LOFT will also search for the expected similar QPOs in AGN, attaining a  $15\sigma$  sensitivity of 0.5% (rms) for a HF QPO equivalent signal in a 1 mCrab source. ULX QPOs such as those seen in (0.8 mCrab) M82 X-1 (Mucciarelli et al. 2006) are detected at  $16\sigma$  in a 20 ks observation, and are detectable (in 20 ks at  $4\sigma$ ) in sources down to  $\sim 0.3$  mCrab.

### 2.2.3.2 Relativistic Waveforms

**[Science Requirement SFG3]** Detect kHz QPOs at their coherence time, measure the waveforms and quantify the distortions due to strong field GR for 10 neutron stars covering different inclinations and luminosities.

Another qualitatively new capability that LOFT will provide is the measurement of waveforms of dynamical-timescale QPOs. LOFT's large effective area will allow us to measure these waveforms either directly, for QPOs that will for the first time be detected coherently, or by Fourier reconstruction. Coherent detection requires the collection of a sufficient number of photons for detection within the signal's coherence time, and hence can be confidently predicted for signals that are only incoherently detected in current data. The required count rate is  $I_x \gtrsim n_\sigma^2 / \tau_{coh} r^2$ , where  $n_\sigma$  is the required signal to noise and  $\tau_{coh}$  the coherence time. A power spectral feature of width  $\Delta\nu$  in the frequency domain has  $\tau_{coh} = 1 / \pi \Delta\nu$  in the time domain. So far, coherent detection has been constrained to only the lowest frequency, highest coherence QPOs, and even in those cases S/N, spectral resolution, or both were insufficient to study the phase dependence of the Fe line profile. With LOFT, coherent detection will be common for low-frequency QPOs (§2.2.2.1). Neutron star high frequency QPOs are well detected in previous missions, and with LOFT we shall be able to detect many of them for the first time coherently. For BH high frequency QPOs this will occasionally also be possible.

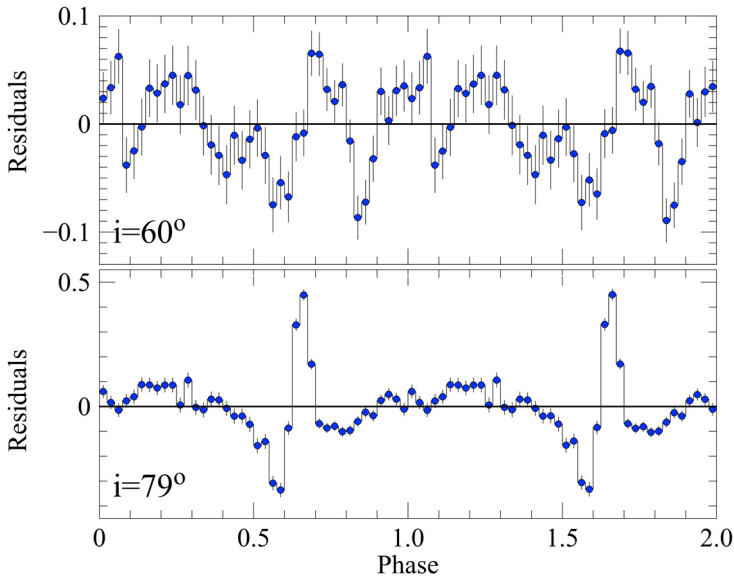


Figure 2-22. Strong-field GR waveform distortions for different disk inclinations as indicated. Curve plotted is the residual to the corresponding waveform using Newtonian gravity and special relativity only, normalized to the Newtonian waveform semi-amplitude. Relativistic light bending produces a spikier light curve at higher inclination. Simulation is for the average of 100 wave trains of a 950 Hz, 6% rms amplitude QPO with duty cycle 50% and  $Q=150$  in a 250 mCrab neutron star.

When a QPO signal is detected within its coherence time, the time series can be folded on instantaneous QPO period and the resulting waveform and its relativistic distortions directly studied. Direct QPO-phase spectroscopy becomes possible, including measurement of phase dependent Fe line profile variations to complement the

methods discussed in §2.2.2.3. The measured waveforms can be compared to theoretical predictions for the physical processes leading to their formation (e.g., periodic Doppler boosting of orbiting inhomogeneities; global oscillation modes of luminous tori). In high inclination systems, these waveforms encode information on strong relativistic light deflection (by tens of degrees) and strong field Shapiro delays, to be compared with the predictions of the photon geodesics equation in the strong field regime. Figure 2-22 illustrates waveform distortions (relative to the waveform predicted from special relativity and Newtonian gravity only) that LOFT would be able to measure coherently in a 250 mCrab NS from an orbiting bright spot of infinitesimal extent. LOFT easily detects the waveform, and its distortions can be quantified to high precision. The light curve of a finite luminous region can be estimated from these curves by convolution (Greens function approach).

For QPOs not detected coherently, it will still be possible to reconstruct waveforms by applying Fourier methods to measure the amplitudes and relative phases of the QPO frequency harmonic structure, much like

the reconstructed Fe line profile variations illustrated in §2.2.2.3. Of course, these waveforms will be an average over a longer integration time.

### 2.2.4 LOFT and strong field gravity in the 2020s

As discussed in §2.2.1.1, LOFT strong gravity science, with its precise probing of both strongly and weakly curved stationary spacetimes near the event horizon of stellar-mass and supermassive BH, is complementary to gravitational wave studies of interacting compact objects, which probe dynamic spacetimes. The 2030's timeframe L3 theme focused on gravitational waves is, therefore, an excellent follow-on to LOFT strong field gravity work. The L2 'Hot and energetic Universe' theme focuses on the distant universe, and in the area of compact objects will excel at the study of the growth of black holes over cosmological time and their feedback to the universe. LOFT instead excels at studying the closest and hence brightest black holes and neutron stars which LOFT will study with signal to noise levels  $\sim 100$  (for the black holes and neutron stars in our galaxy) times the signal to noise that current and planned capabilities attain. As demonstrated in detail by the simulations presented in the sections above, such signal to noise levels are necessary to understand the precise way matter moves in the extreme gravity close to the event horizon, the goal set out in Cosmic Vision. Figure 2-23 illustrates this by displaying the suitability of instruments of various effective area to Fe line spectral timing at relativistically relevant time scales. Compared to current capabilities (XMM), LOFT improves signal to noise by a factor of 6 in bright AGN (and for such objects LOFT is as good as a  $4\text{m}^2$  (4mCrab) to  $0.8\text{m}^2$  (0.4mCrab) zero-background instrument, where Athena+ attains  $0.3\text{ m}^2$  at 6 keV). In XRB, S/N improves by a factor 300 over XMM and 100 over Athena+. Vertical bars show current and future true capabilities taking account of pile-up and sampling limitations, for LOFT assuming requirement background. Estimates include realistic photon energy and variability power spectra. Even at zero background, for effective detector areas in the several  $\text{m}^2$  class and beyond, X-ray binaries always provide an approximately factor 10 better S/N than AGN. While AGN of course provide more photons per dynamical time scale, at effective areas such as provided by LOFT and beyond, this is more than compensated for by XRB providing both much higher count rates and many more dynamical time scales per observation.

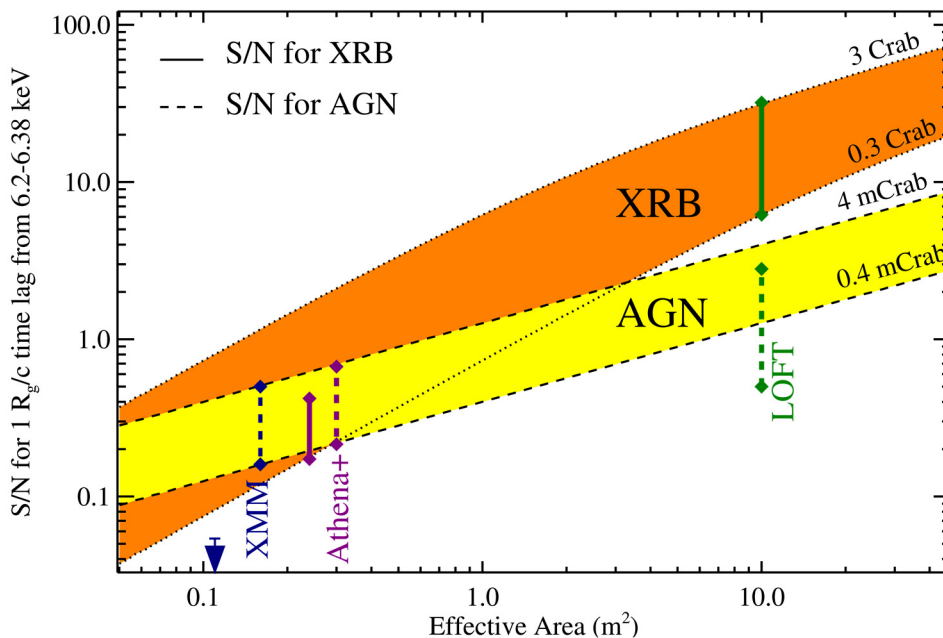


Figure 2-23 Spectral timing signal-to-noise. Diagram illustrating the transformative nature of the detection regimes opened up with LOFT. Orange and yellow bands show the S/N of a time lag of  $r_g/c$  (light travel time across one gravitational radius) in 100 ks in a narrow band within the Fe line, for XRB and AGN in flux ranges indicated at zero background and pile-up. Horizontal scale is detector effective area. Up to  $\sim 10\text{ m}^2$ , XRB S/N improves rapidly, as detections are in the incoherent regime (§2.2.3.2), beyond that it increases at the same pace as in AGN, which are always in the coherent regime. Vertical bars illustrate the capabilities of the missions indicated. LOFT S/N for AGN is less than the theoretical maximum due to background, whereas XMM and Athena+ S/N for XRB is limited by bright source pile-up and sampling limitations. XMM and Athena+ effective area for XRBs is less than for AGN due to limitation to pn instead of pn+MOS for XMM and bright-source windowed read-out for Athena+.

## 2.3 Observatory Science

With its combination of instruments providing high throughput, good spectral resolution and a wide field of view, LOFT is very well suited to a range of studies complementing those focused on dense matter and strong gravity described in the previous sections. These studies are discussed here under the heading of “Observatory Science”. The Large Area Detector (LAD) will enable deep spectroscopic and time variability studies across objects exhibiting a wide range of highly energetic physical phenomena powered by accretion, thermonuclear and magnetic processes as well as various types of gravitational collapse. For objects  $\geq 1-2$  mCrab it will provide the best variability information and mid-resolution spectroscopy observations ever across the 2-30 keV band. The Wide Field Monitor (WFM) will make LOFT a discovery machine for the variable and transient sky, revealing many new sources for follow-up with LOFT-LAD and other facilities. Experience with, e.g., RXTE-ASM, BeppoSAX/WFC, Swift-BAT and INTEGRAL/ISGRI shows that new, unforeseen types of source will turn up and provide new, unexpected insights into fundamental questions (Remillard et al. 1999; in 't Zand et al. 1998; Wijnands & van der Klis 1998; Burrows et al. 2011; Eckert et al. 2013; Papitto et al. 2013). In addition, the WFM will be monitoring hundreds of known sources simultaneously, to catch unexpected events as well as provide long-term records of their variability and spectroscopic evolution (Figure 2-25). These capabilities make LOFT a uniquely powerful X-ray partner of other large-scale facilities across the spectrum that will be available in the 2020s, such as SKA and pathfinders in the radio, LSST and E-ELT in the optical, and CTA at TeV energies, as well as gravitational wave and neutrino telescopes (Figure 2-24). The observatory science program is designed to be flexible and open to new developments, but extrapolating from current knowledge, it is likely that many of the observations will fit into the following overarching themes: accretion, strong magnetic fields, cosmic explosions. Table 2-3 lists the strongly time-variable and transient objects that LOFT will observe to study these themes. Some classes of object (e.g., LMXBs, magnetars) will also be observed for LOFT’s dense matter and strong gravity objectives and some observatory science goals can actually be pursued from these same observations; these have been de-emphasized in the descriptions that follow below.

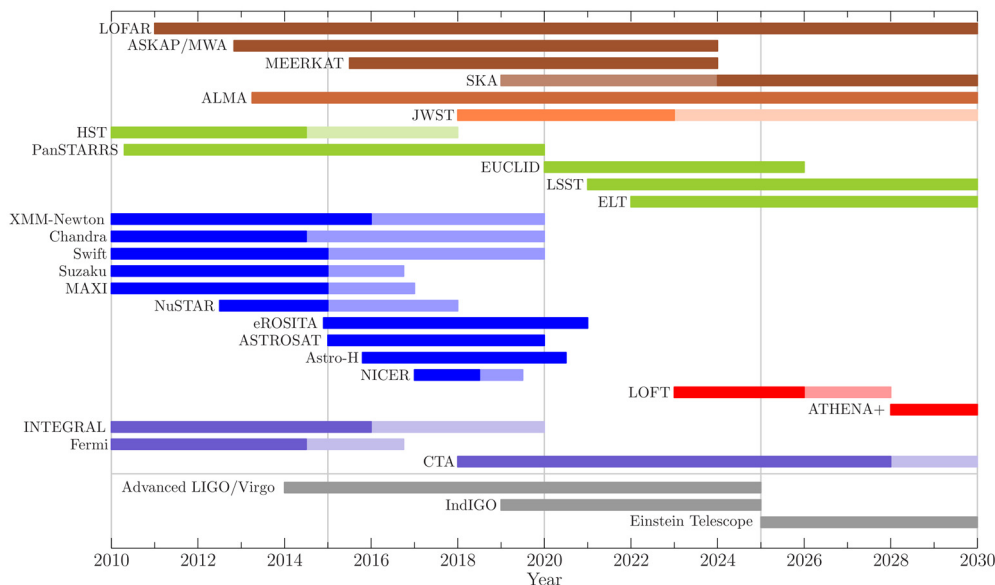


Figure 2-24: Multi-wavelength facilities of relevance to LOFT science. Colours indicate similar wavebands from the radio (top) via IR and optical to X-rays and gamma rays. Grey bands: gravitational wave detectors. Dark colours: current end of funding, light colours: expected lifetime, where known, independent of funding decisions. Missions might last longer.

Some objects (e.g., accreting white dwarfs, blazars), while not part of the core objectives, in addition to their relevance to the observatory science themes can provide useful comparative insights for the core science objectives as well. In view of the available space, the following sections summarize only a selection of such observations, illustrating the scope of LOFT’s observatory science. There are other exciting areas of research to which LOFT will contribute significantly but that cannot be discussed here because of space limitations. In this context we single out here Terrestrial Gamma-ray Flashes (TGFs), bright hundred microsecond long bursts of X and gamma photons up to several tens of MeV launched into space by source regions at the cloud tops of active thunderstorms. The LAD will detect 1-2 TGFs per day shining through the collimator above 30 keV providing TGF observations at the largest effective area and the densest coverage at equatorial latitudes. As another example, the WFM by virtue of its very large field view and good sensitivity will be among the key instruments to carry out searches for the electromagnetic counterparts of gravitational wave candidate events

detected by Advanced LIGO/Virgo. Conversely the position and times of GRBs detected by the WFM, especially those from short GRB (which LOFT will detect at a rate of  $\sim 10$  per year), will be used as triggers for gravitational wave searches in the Advance LIGO/Virgo era.

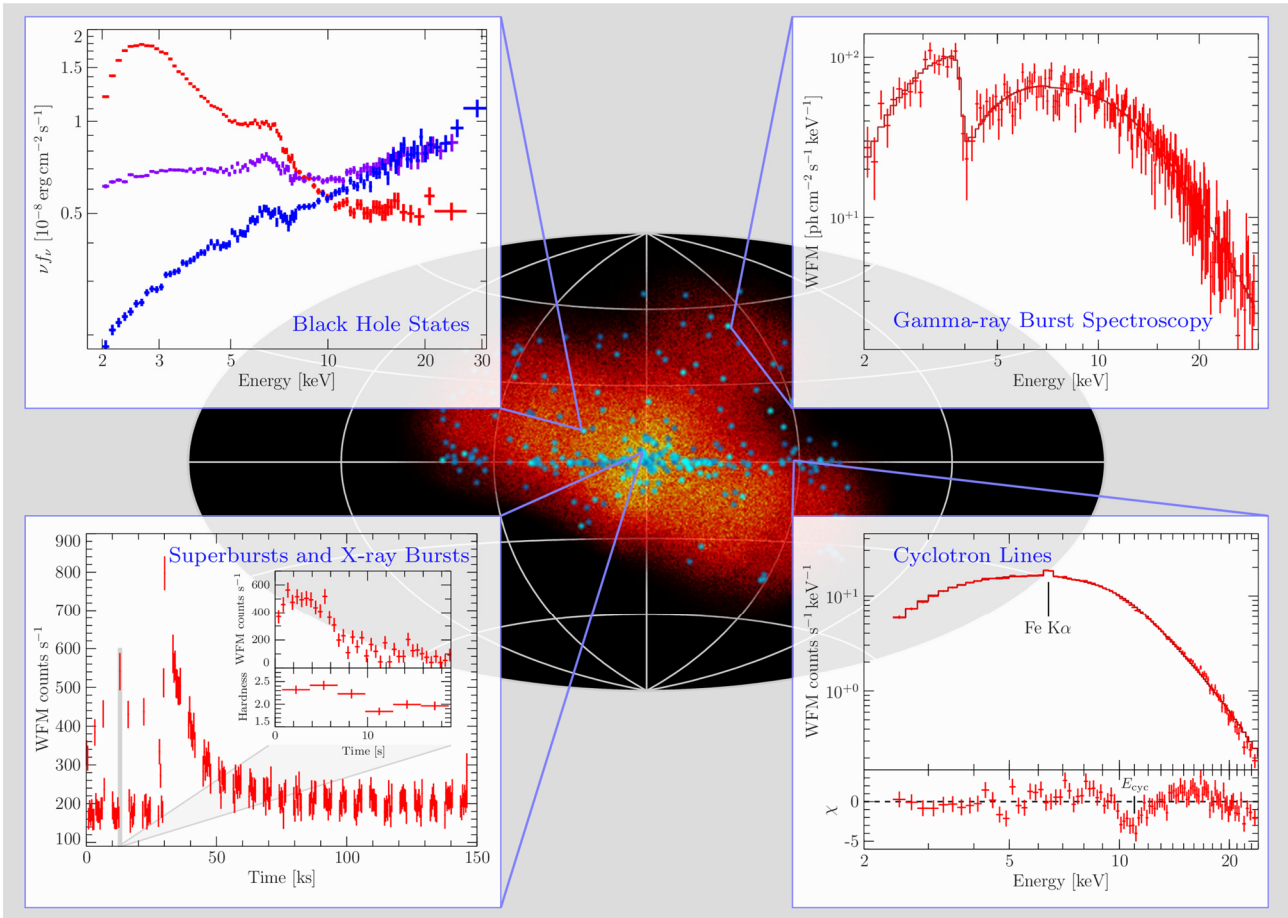


Figure 2-25: The figure shows the potential of the instrument by highlighting astrophysical events that can be detected during selected pointings performed in the direction of the Galactic Center. As an example, it is shown how the WFM would be able to: (i) track state changes during a transient BH outburst and detect the relativistic Fe K $\alpha$  line (top left panel, 15 ks exposure, source flux 300 mCrab); (ii) measure the energy and follow the evolution of cyclotron features during the outbursts of neutron star in X-ray pulsar binaries, unveiling the strength and geometry of their magnetic fields close to the polar caps (bottom right panel, 20 ks exposure, assumed line energy of  $\sim 11$  keV and  $\sim 22$  keV; Müller et al. (2013)); (iii) detect Gamma-ray bursts and reveal transient absorption features in their prompt X-ray emission (top right panel, here a feature similar to that detected in GRB990705 was simulated; Amati et al. (2000)); (iv) catch bursting activity and rare events such as superbursts from known and newly discovered sources (bottom left).

Table 2-3: Observatory science themes and associated astrophysical objects: L: LAD. W: WFM.

	Accreting White Dwarfs	Low Mass X-ray Binaries	LMXB (X-ray Bursters)	High Mass X-ray Binaries	Isolated Neutron Stars	Magnetars	Stars	Nearby Galaxies	Tidal Disruption Events	Bright AGN (Seyferts, Blazars)	Gamma-ray Bursts
Accretion physics	L,W	L,W	L,W	L,W	L			L,W	L,W	L,W	L,W
Strong B-field	L	L,W		L,W	L	L,W	L,W	L,W			
Cosmic explosions	L,W		L,W			L,W		L			W

### 2.3.1 Gamma-Ray Bursts

Gamma-ray bursts (GRBs) are among the most intriguing and challenging mysteries in astrophysics. Because of their complex phenomenology and extreme energetics, connections with core-collapse supernovae and compact-object mergers, and high redshifts, GRBs are key to a variety of astrophysical fields, from ultra-relativistic plasma physics via black hole formation to cosmology. Likely, GRBs longer than a few seconds are a final stage in the evolution of some fast spinning massive stars, while less energetic, short GRBs signal the merger of two compact objects, (NS-NS, NS-BH or BH-BH). However, many aspects of GRBs, such as the physics of the prompt emission and the origin of GRB sub-classes (long, short, X-ray flash, sub-energetic) remain to be discovered. In addition GRBs provide a probe of star formation up to  $z \sim 10$ , and of cosmological parameters (Mészáros 2006; Gehrels et al. 2009).

LOFT will provide a unique contribution to these studies. It has a softer response and higher throughput than any current and foreseen GRB mission (Amati et al. 2013) such as Fermi-GBM, Swift-BAT or SVOM (Figure 2-27). The WFM will measure the spectral shape and follow the hard to soft evolution of the prompt emission of hundreds of GRBs in the 2-50 keV band (Figure 2-26), where GRB models, such as, e.g., synchrotron shock, Comptonization and photospheric emission in kinetic-energy dominated fireball or magnetic re-connection emission in Poynting-flux dominated fireball, make different predictions (Zhang & Mészáros 2002; Ghirlanda et al. 2007). Discriminating among these models provides crucial information on composition and magnetization of the emitting plasma (most likely collimated into a jet), site and geometry of the emission, structure of the jet and surrounding material, clarifying the nature and physics of the still obscure central engine, and progenitors. The WFM energy range and resolution provide unprecedented sensitivity to absorption features (Figure 2-25) in tens of medium bright GRBs each year, probing the surroundings of GRB progenitors (Amati et al. 2000; Gehrels et al. 2009). The WFM is uniquely sensitive (detection rate  $\sim 40$ -50 / year) to X-ray flashes, an enigmatic sub-class of soft/ultrasoft events which may constitute the bulk of the GRB population (Pelangeon et al. 2008). For a 3-year (5-year extended) mission the WFM, thanks to its soft response, might well detect, out of a total of  $\sim 120$ /year,  $\sim 6$  ( $\sim 10$ ) GRBs at  $z > 6$  and a few at very high  $z > 8$  (Figure 2-26), further contributing, after Swift, to our knowledge of the star formation rate evolution, the ISM, and, possibly, population III stars (Salvaterra et al. 2012). GRBs will be promptly localized on-board to within 1 arcmin and followed up in multi-wavelength campaigns triggered by the LOFT Burst Alert System, which within about 20-30 seconds broadcasts position and trigger time of the brightest events to a ground system of VHF receivers covering the Earth's equatorial region and providing full coverage of LOFT's orbit. This will trigger robotic telescopes, allowing observations of the optical/NIR afterglows, host galaxies, and  $z$  measurements with the largest telescopes of the 2020s.

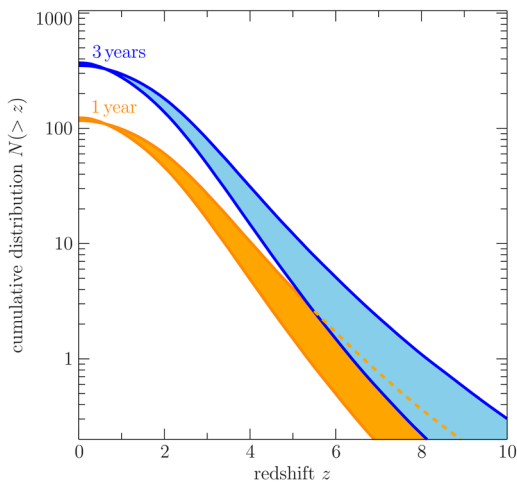


Figure 2-26: Cumulative redshift distribution of long GRBs predicted for LOFT/WFM. A broken power-law GRB luminosity function and pure density evolution (Salvaterra et al. 2012) were assumed. We predict  $\sim 6$  GRBs at  $z > 6$  in a 3-year mission.

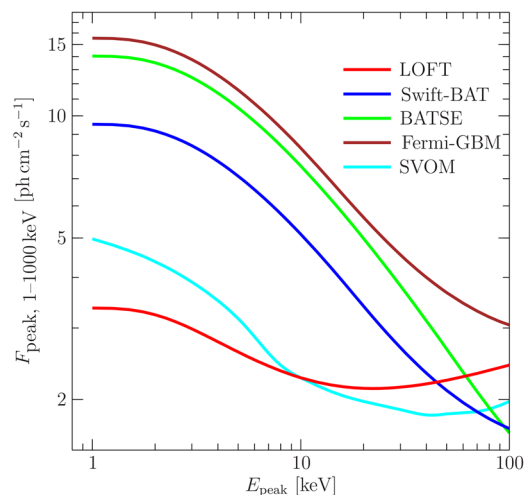


Figure 2-27: Minimum detectable 1-1000 keV peak flux for the LOFT-WFM, Swift-BAT, CGRO-BATSE, and Fermi-GBM as a function of the peak energy of the burst (Band 2003).

## 2.3.2 Accretion Physics

Accretion physics is crucial to subjects as diverse as star and planet formation, Type Ia supernova progenitors, and AGN feedback. Accretion and ejection processes are highly variable, on timescales ranging from milliseconds to many decades, and radiate over a broad range of wavelengths. In compact object accretion, X-rays hold a special role, as they diagnose the deepest regions of the gravitational potential well, where most of the energy is released. LOFT's unique characteristics – throughput, resolution, broad energy range, sky coverage – will provide unprecedented diagnostic power on subjects such as:

- the link between the accretion disk inflows and the wind and relativistic jet outflows;
- the ubiquitous accretion disk instabilities;
- the Blazar emission mechanism.

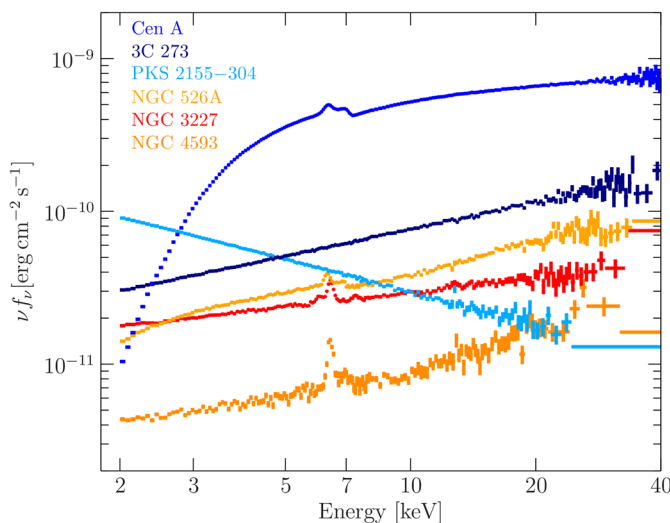


Figure 2-28:  $\nu f_\nu$  LAD spectra of prominent bright radio loud (blue colours) and radio quiet (red colours) AGN. The short 10 ks exposure time assumed here already results in spectra with a very high signal-to-noise ratio as required, e.g., for monitoring campaigns done jointly with other facilities. Uncertainties include the systematics of the LAD background modelling.

### 2.3.2.1 X-ray binaries

Jets are associated with accretion on all astrophysical scales. Powerful and fast – often relativistic – outflows occur in a wide range of settings, from proto-stellar objects via white dwarfs and neutron stars to stellar-mass and supermassive black holes. Despite recent progress, many fundamental questions remain open, including how jets are launched and

powered. State transitions are key to the physics of the compact object accretion/ejection process and are best studied in stellar-mass compact objects, where they happen on timescales of hours or days. In stellar mass black holes, within hours, emission can change from thermal Comptonization of soft photons in a hot ( $kT_e \sim 50$ – $100$  keV) plasma to  $kT \sim 1$  keV disk blackbody radiation. At the same time the outflow properties, inferred in the radio and optical/IR bands, change dramatically. During such transitions, and analogous ones in neutron stars and white dwarfs, a reconfiguration of the flow takes place, from a regime where a large fraction of the accretion energy (and/or the rotational energy of the compact object) is transferred to plasma around the accretion disk, or in the base of a jet, to a regime where most of the energy is radiated away by the disk and a disk wind sets in (Markoff et al. 2005; Maitra et al. 2009; Sobolewska et al. 2011; Zdziarski et al. 2012; Ponti et al. 2012). In some cases evidence was found that BH relativistic jets are baryon loaded, suggesting that their energy is tapped from accretion, rather than spin (Margon et al. 1979; Díaz Trigo et al. 2013).

As the energy is released in structures encompassing a wide range of scales, multi-wavelength observations are required, with radio to optical/IR diagnosing the jet, and the 2–50 keV X-ray emission probing the accretion flow (bolometric luminosity, temperature of the disk, temperature and optical depth of the Comptonizing plasma, and, through reflection features, accretion geometry; e.g., Nowak et al. (2011)). Much of what we know comes from just a few campaigns (Wilms et al. 2006; Russell et al. 2012). However we still lack the extensive coverage of a number of source and transitions that is required to address key questions such as the mechanisms responsible for triggering the transition, redistributing the energy among the different components and launching the jet. Because of the limited resolution and throughput of X-ray wide-field instruments, effective X-ray monitoring so far required expensive pointed observing campaigns. The WFM will revolutionize this, providing densely sampled broad-band 2–50 keV observations, with the spectral resolution and sensitivity required to follow in detail state transitions in X-ray binaries. For the brighter sources (e.g. Cyg X-1), the WFM data alone will provide us with accurate measurements of the evolving physical parameters of the Comptonizing plasma across transition, on an orbit by orbit basis, without the need for pointed observations. In this context, LAD pointed observations, besides addressing in greater detail the properties of individual sources states, will be used to study weaker systems and fainter states of transient X-ray binaries.

Dense radio monitoring, crucial but equally difficult to achieve, will become easier with the advent of radio facilities such as the Square Kilometer Array and LOFAR. Moreover several next-generation observatories (both wide-field fast-survey, and large-area telescopes) that will be operational at the same time as LOFT, will greatly extend the range of the monitoring in the sub-millimeter (ALMA), optical/IR (E-ELT, JWST, LSST), and gamma (CTA) bands.

### 2.3.2.2 *Supermassive Black Holes*

The evolution of galaxies and supermassive BHs is intrinsically linked; therefore it is of fundamental importance to understand how the BH interacts with the galaxy environment: what are the geometry, dynamics and energetics of the BH accretion and ejection flows? As recent XMM-NuStar observations show (Risaliti et al. 2013) answering such questions requires broad band X-ray observations.

For the requirement on background systematics (i.e. 0.25% of the total background in 2-10 keV), the LAD can easily detect changes in the spectral shape up to energies of 20-30 keV, for a sample of about 100 AGNs in the local universe (fluxes  $\gtrsim 1$  mCrab). This sample will encompass, for instance, radio-loud AGNs. It will allow us to push the inflow-outflow connection discussed in §2.3.2.1 to supermassive BHs and Blazar jets, which are excellent laboratories to study acceleration processes and the production of cosmic rays. LOFT will greatly extend the sample of power spectra from the X-ray light curves of Seyfert galaxies, and provide further constraints on the similarity of Seyferts' variability with that of Galactic sources (McHardy et al., 2006). The X-ray flux variability will be studied both with discrete sampling of LAD observations (which will provide very high sensitivity down to timescale of few tens of seconds) as well as the 'continuous' sampling afforded by the WFM (which will monitor timescale variations up to years). This monitoring, together with the observation of the reflection components (i.e. narrow Fe line around 6 keV and reflection hump above 10 keV) originating in a distant medium (Broad Line Regions or torus), will provide the distance of the emitting gas by measuring the time lags between the emission line's fluxes and the continuum. This reverberation will provide a map of the regions up to kpc distances from the central BH.

The emission of Blazars originates in a relativistic jet pointed at the observer; their typical two-peaked broad band spectrum is interpreted as synchrotron (S) and inverse-Compton (IC). Jet structure, location of the flaring emission, acceleration mechanisms, and contribution of different seed photon fields to the inverse Compton process are among the key issues to be addressed. In High Energy Peaked BL Lac objects (HBL), whose synchrotron component peaks at UV/X-ray energies, the LAD will probe the synchrotron emission above, or close to, its peak, where the variability is strongest, providing an ideal match with CTA (TeV) observations of the inverse Compton bump. The detection of flaring activity on very short timescales in the X-rays and TeV would prove the existence of very compact synchrotron self-Compton (SSC) emission regions ( $\sim 10^{14}$  cm). The LAD can measure variability and lags down to tens of seconds (an order of magnitude faster than current instruments e.g., Aharonian et al. (2009)) in Blazars with flux  $> 5$  mCrab, similar to the timescales afforded by the CTA. This will provide a unique diagnostic tool to constrain SSC multi-zone scenarios and the origin of TeV photons. By virtue of LOFT's large field of regard, the WFM will be effective at triggering simultaneous LAD - CTA observations as most of the targets are sufficiently bright X-ray sources.

### 2.3.2.3 *Cataclysmic Variables*

In dwarf nova outbursts (white dwarfs accreting at high rate from their low mass companion) a variety of oscillations have been detected: 3–40 s oscillations in the optical/EUV and soft X-rays (Warner 2004), 80–100 s oscillations at  $< 2$  keV (Mauche 2002), and 100-1000 s oscillations in soft or hard X-rays (Wheatley et al. 1996; Ramsay et al. 2001). These outbursts have fluxes in the 1-10 mCrab range, so LAD observations will provide enormously improved signal to noise on these signals, needed to test proposed numerical magneto-hydrodynamic accretion flow models. Some high magnetic field cataclysmic variables show 1–10 s optical oscillations (Middleditch 1982), thought to be due to thermal instabilities in shocks (Wu 2000; see also §2.3.1). Current instruments cannot detect the X-ray oscillations predicted from these models (Beardmore & Osborne 1997; Ramsay & Cropper 2007). With the LAD a direct test of the thermal instability model can be made.

### 2.3.2.4 *Tidal Disruption Events*

Stellar dynamics predicts that once every  $10^3$ – $10^5$  years a star passes within the tidal radius of a galaxy's central BH and produces a tidal disruption event (TDE). It is torn apart by tidal forces, and debris falls back onto the

BH, producing a luminous flare in the optical/UV/soft X-rays followed by a power-law decay,  $\dot{M} \propto t^{-5/3}$  (Rees 1988). While state transitions in supermassive BHs are expected (scaling from stellar mass BH) to occur on timescales of centuries, TDEs evolve over weeks and thus provide a unique window on the onset of accretion in a supermassive BH experiencing a very wide range of accretion rates. Only a handful of TDEs has been detected so far (Komossa 2002; Gezari et al. 2009; Gezari et al. 2012). These events are generally associated with thermal emission from the disc and/or the wind. In the 2020s TDEs will be detected in large numbers ( $\sim 10^3/\text{yr}$ ) with, e.g., LSST. Most TDEs are too soft for LOFT.

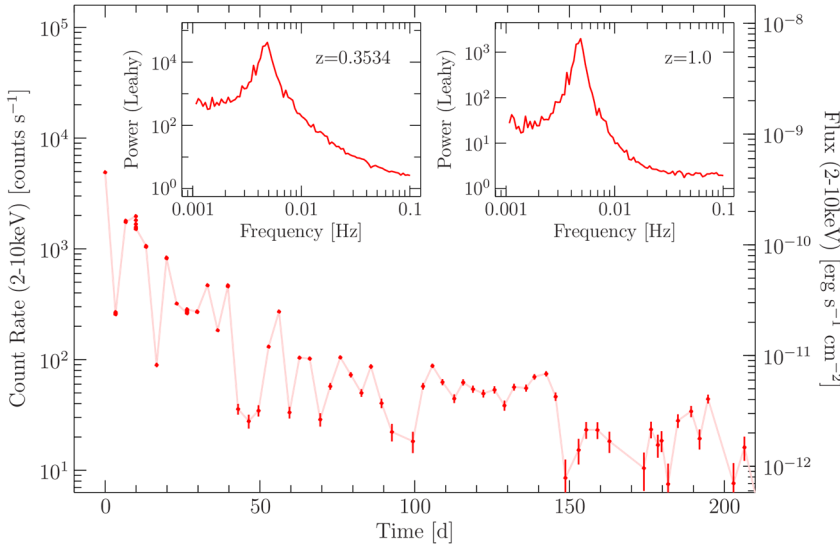


Figure 2-29: Simulated LAD lightcurve of a Tidal Disruption Event, based on Swift J164449.3+573451 (from a series of 10 ks exposures). Insets: power spectra from 100 ks LAD pointings. QPOs such as the one found by Reis et al. (2012) are easily detected even in the late phase of the event.

However, recent Swift-BAT observations (Burrows et al. 2011; Cenko et al. 2012) revealed TDEs with harder emission, likely beamed non-thermal emission from a relativistic jet pointing toward us. Swift J164449.3+573451, at  $z = 0.35$  had an extreme X-ray luminosity of  $3 \times 10^{48} \text{ erg s}^{-1}$  for

several days, a power law spectrum (photon index  $\sim 1.8$ ), and increasing radio activity a few days after outburst (Levan et al. 2011). Together with radio telescopes such as SKA, LOFT will characterize the formation and evolution of jets during TDE outbursts, and it may detect the disk through X-ray QPOs such as the 200s ones reported in Swift J1644 (Reis et al. 2012). Simulations show that the LAD will be able to detect such QPOs out to  $z \sim 1$  (Figure 2-29). The WFM will also provide an independent identification and light curve monitoring of a sub sample (a few per year) of TDEs discovered in radio. Accounting for uncertainties in the BH mass functions and jet beaming factors, it is expected that SKA will detect between a few hundred (for bulk Lorentz factors of  $\Gamma=5$ ) and a few thousand (for  $\Gamma=2$ ) jetted TDEs per year (Berger et al. 2012). The LOFT/LAD will be able to follow up between tens and hundreds of these jetted TDEs out to redshift  $\sim 2$  each year. Combining X-ray and radio data is the most promising strategy to confirm and study jets from TDEs. Moreover, a comparison with optical data (e.g. LSST), which select mostly disc dominated TDEs, will be an important test for models of jet formation and evolution (see §2.3.2.2).

### 2.3.3 Strongly Magnetized Objects

X-ray observations allow probing magnetic fields from  $\sim 10^8 \text{ G}$  in magnetic white dwarfs (WD), via  $\sim 10^{12} \text{ G}$  in neutron stars (NS), to beyond the QED critical field of in magnetars ( $\sim 10^{15} \text{ G}$ ) and to study the physics of matter in B-fields much stronger than those attainable in the lab. Questions addressed by LOFT in this area include:

- How are accretion columns formed in magnetized White Dwarfs and Neutron Stars?
- What is the structure of the magnetic field around a pulsar?
- How do the strongest magnetic fields lead to production of persistent and impulsive high-energy radiation?

LOFT will probe regimes difficult to study in other wavebands, at a time when powerful numerical tools for advanced modelling of the behaviour of matter in these environments will be available.

#### 2.3.3.1 Accretion Columns

The accretion flows onto magnetized WD and NS are disrupted at the magnetospheric (aka Alfvén) radius, where magnetic forces exceed gravity. The accreting plasma follows the magnetic field lines and eventually falls onto the magnetic poles of the compact object, where it is abruptly stopped in a plasma shock or a radiative

shock, and where its kinetic energy is converted into heat and radiation. If the compact object rotates, X-ray pulsations are observed. In high magnetic field accreting WDs of the Polar and Intermediate Polar classes (in the latter the accretion disk extends down to the magnetospheric radius, while in the former the strength of the B-field prevents the formation of a disk), pulse phase spectroscopy diagnoses the accretion column physics: temperature and density structure of post-shock regions, shock height, and pre-shock absorbers (Ezuka & Ishida 1999; Bernardini et al. 2012). Reflection of X-rays from cold material in the pre-shock region or on the surface, manifesting in a prominent Fe K $\alpha$  line is also expected to contribute in the 15–30 keV continuum (Hayashi & Ishida 2013). The few phase resolved studies of bright systems (Ramsay & Cropper 2004; Anzolin et al. 2009) are mostly limited to <10 keV, and cannot constrain the reflected hard radiation. This leads to a large systematic uncertainty in the continuum parameters, including the inferred high shock temperatures. Hence, LOFT observations sensitive >10 keV are crucial to determine the shock height and WD mass.

The most extreme accretion columns occur in strongly magnetic ( $B \gtrsim 10^{12}$  G), highly luminous NSs, where the accreting plasma is stopped by radiation forces (Becker & Wolff 2007). Most of these systems are Be transients, which go into outburst when the NS accretes from the Be-star companion outflow. The WFM will discover, and then follow over several weeks to months, transient outbursts, tracking changes in the shocked region of the accretion column as a function of mass accretion rate by measuring the energy of the cyclotron line. This scales with B-field in the emitting region ( $E_{\text{cyc}} = 12 (B/10^{12} \text{ G}) \text{ keV}$ ), and hence relates to the altitude of the region above the NS where it is produced. Currently, this requires pointed observations with narrow field instruments (Caballero & Wilms 2012), but the WFM will measure  $E_{\text{cyc}}$  whenever a Be transient outburst is in its field of view (Figure 2-25). The LAD will measure the parameters (absorption, photon index) of 150 mCrab spectra from Be transients to 5 $\sigma$  in <10 s, thus constraining for the first time the pulsar magnetic field topology by measuring the pulse phase dependence of  $E_{\text{cyc}}$  on a pulse-to-pulse basis (Klochkov et al. 2011; Becker et al. 2012). Instabilities in accretion columns due to Rayleigh-Taylor instabilities in the area where the matter couples to the B-field (Orlandini & Morfill 1992; Shakura et al. 2012) or due to buoyant photon bubbles in the opaque accretion column (Arons 1992; Klein et al. 1996) are predicted to produce characteristic  $\mu\text{s}$  variability ("shots" caused by the clumps). These can be detected by searching for deviations of the arrival time difference distribution of photons at the microsecond levels from an exponential distribution. Simulations show that for typical, moderately bright (10-100 mCrab) even a granularity of 10% is detectable with the LAD. The detection of photon bubbles would be of great astrophysical importance, as it would provide a direct measurement of a magnetohydrodynamic instability also dominant in disrupting giant molecular clouds in starforming galaxies (Murray et al. 2010) and possibly explaining ultraluminous X-ray source spectra (Finke & Böttcher 2007).

### 2.3.3.2 Isolated Neutron Stars: Radio Pulsars and Magnetars

The strongest magnetic fields (up to at least  $\sim 10^{15}$  G) in the Universe are observed in some rotation powered pulsars and in magnetars (magnetically powered neutron stars) and pulsations provide a powerful probe of the physics in these extreme circumstances. However, both the macrophysics (magnetospheric B-field geometry, gap topology, currents) and the microphysics (particle acceleration, emission mechanisms, radiative transfer) of the pulsar emission mechanism are enigmatic. Pulsar emission tends to be extremely broad band, from radio to HE  $\gamma$ -rays. The  $\gamma$ -ray pulse profiles obtained by Fermi for many pulsars proved to be an extremely powerful diagnostic, provided the first meaningful constraints on emission geometry (Venter et al. 2012) and pulse phase spectroscopy yielded the first tests of radiation models (Abdo et al. 2010), challenging traditional standard geometrical models. LAD can contribute crucially to the characterization of these pulsar's 2-50 keV emission. Based on observed properties of radio pulsar at soft X-ray energies, we estimate that the LAD will provide energy resolved pulse profiles in the 2-50 keV range with unprecedented detail for more than 70 pulsars, and will perform phase-resolved spectroscopy of the  $\sim 30$  brightest of these, fill the gap between radio and  $\gamma$ -rays and probe completely different magnetospheric particle populations. Coupled with studies in the optical (E-ELT), and TeV (CTA) bands, realistic models for the magnetosphere (e.g. dissipative ones including pair cascades, including geometry) will constrain *the actual pulsar electrodynamics* (and not just geometry), which could settle one of the longest debated issues in astrophysics. Radio pulsar emission varies on timescales of nanoseconds to years (Keane 2013), giant pulses being the most intense short-term phenomenon. Correlations between stochastic variability in coherent radio and incoherent high-energy emission may reveal time dependent/stochastic particle acceleration processes, adding a key ingredient to pulsar emission models. LAD will *detect individual pulses* from Crab (never done in any pulsar outside the radio band) and X-ray pulse-to-pulse variability down to the 0.3%, and study any X-ray signature of giant radio pulses. The surprising

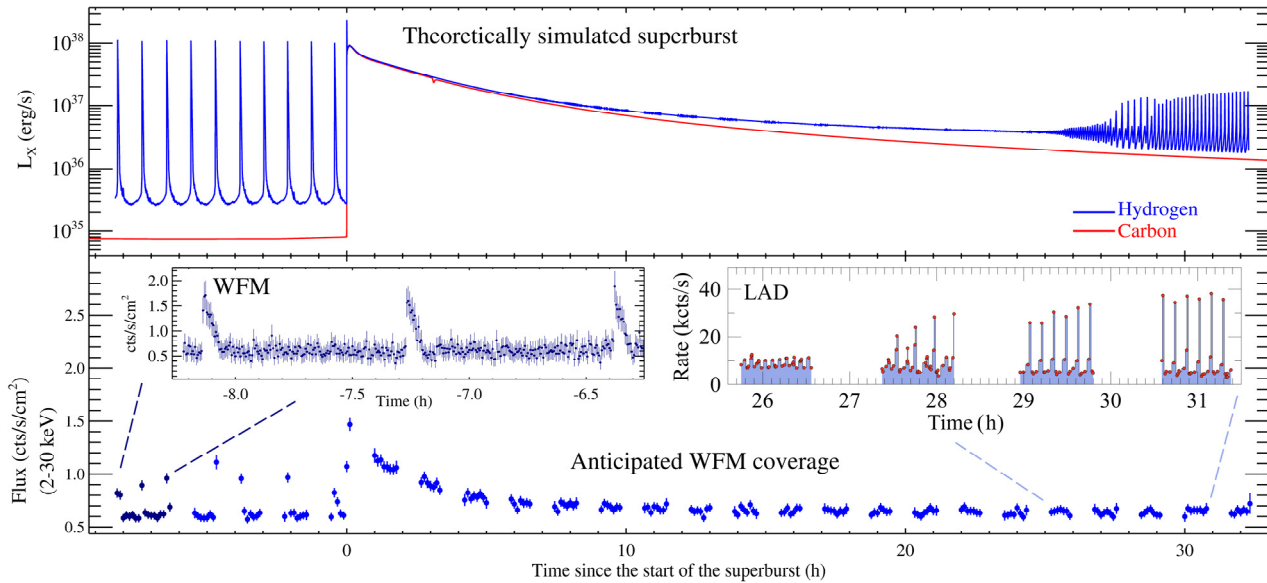


Figure 2-30: Bursting behaviour around a superburst in a H-rich system (Keek et al. 2012). The superburst quenches ordinary bursts for one day followed by marginal burning characterized by mHz QPOs. These events can be easily discovered by the WFM and repointed with the LAD (bottom panel).

discoveries of a relation between radio pulse modes and spin-down (Kramer et al. 2006; Lyne et al. 2010), of simultaneous mode changes in radio and X-rays (Hermsen et al. 2013), and of mode changes in  $\gamma$ -rays (Allafort et al. 2013) indicate rapid, global magnetospheric changes. The LAD can detect mode changes in a number of pulsars, and help to sort out this challenge to pulsar emission theories.

Magnetars are characterized by persistent X-ray emission of up to  $10^{35}$  erg/s, and X/soft gamma-ray burst/flare events on covering a vast range timescales (tens of milliseconds to minutes) and luminosities ( $10^{38}$ - $10^{46}$  erg/s; Mereghetti (2008)). These events are believed to be triggered by either crustal fractures or by magnetospheric instabilities and in the case of the most energetic "giant" flares, they are related to global magnetic field rearrangements (Thompson & Duncan 1995). In the past few years, new discoveries showed the potential of using magnetars to tackle problems such as the interplay between dense matter, radiation and strong magnetic fields. Key recent discoveries (besides the QPOs discussed in §2.1.4.3) were: i) a number of transient magnetars encompassing more the four orders of magnitude in persistent luminosity (Rea & Esposito 2011); ii) the discovery of a broad-phase-dependent spectral feature, likely due a proton cyclotron resonant scattering, during the outburst of a transient magnetar (Tiengo et al. 2013). Major steps forward in this field will be made possible by the LAD's very large effective area to monitor with good spectral capabilities the crustal cooling and the field rearrangements during the outbursts, and the WFM's large field of view to catch more transient events for magnetar population and burst studies. Both instruments will also allow us to perform detailed pulse-phase spectroscopy during the outbursts to search for cyclotron resonant features, and map the surface temperature anisotropies. Both are crucial to model the magnetic field geometry close to the magnetar surface.

## 2.3.4 Thermonuclear Explosions

### 2.3.4.1 X-ray Bursts

LOFT X-ray burst work done for measuring the EOS (§2.1), will greatly help understand NS crust and ocean physics. X-ray bursts (Lewin et al. 1993; Strohmayer & Watts 2006) are due to thermonuclear flashes of H and He in the upper few metres of accreted matter on NS. Burning starts at one point and spreads over the star in typically  $\sim 1$  s. Temperature rises to  $\sim 2.5$  keV, followed by cooling lasting  $10$ - $10^5$  s for ignition column depths from  $10^{8-12}$  g/cm<sup>2</sup>. The early flux may exceed  $L_{\text{Edd}}$ , resulting in temporary matter uplifting. CNO and  $3\alpha$  burning can explain most bursts, but to confirm this the composition of nuclear ashes must be measured. In the strongest bursts, convection can dredge up the ashes and display their X-ray absorption edges, hints for which were seen with RXTE (in't Zand & Weinberg 2010). The larger area and higher spectral resolution of LAD are required for conclusive detection. The LAD will be able to detect K-edges in typical bursts (i.e., with peak flux 1 Crab unit) for nickel and iron (at 7.1 and 8.3 keV rest energy) down to limiting sensitivity in abundance of  $X_{\text{Ni or Fe}}=0.01$ .

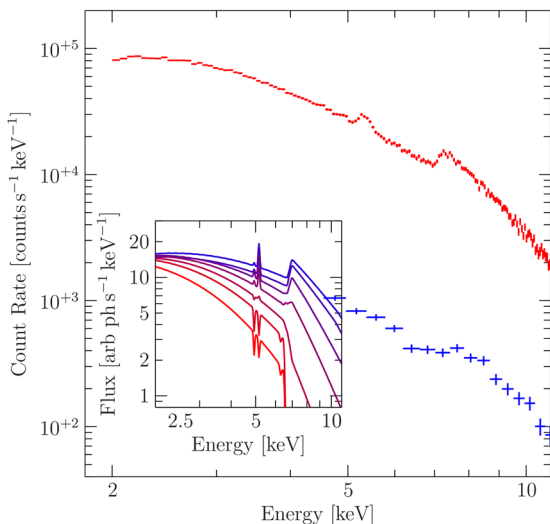


Figure 2-31: Simulation of LOFT-LAD (red) and RXTE-PCA (blue, 3 active PCUs) spectra of a burst with  $kT = 1.9$  keV (1 s exposure). The spectrum is based on a NS atmosphere model with a Fe abundance of several times solar, calculated with TLUSTY (F. Paerels, priv. comm.). The inset shows how the theoretical photospheric spectrum varies as a function of temperature (the range shown is from 0.9 to 2.1 keV in steps of 0.2 keV). LAD will easily be able to distinguish between these spectra. Due to gravitational redshift the Fe K $\alpha$  line emerges at  $\sim 5$  keV.

Once detected, their **gravitational redshifts** will constrain the compactness  $M/R$  of the NS to complement the methods of §2.1 (Figure 2-30). 0.1% of X-ray bursts are carbon-fuelled “superbursts” (Cumming & Bildsten 2001; Strohmayer & Brown 2002; Cornelisse et al. 2000) igniting at  $10^{3-4}$  times the column depth of ordinary bursts, much closer to the crust and probing its thermal properties. Superbursts ignite sooner than expected (Keek et al. 2008),

which suggests crust thermal balance (set by crust nuclear reactions and core neutrino cooling) differs from model predictions. We estimate that the WFM will detect tens of superbursts (only 22 have been observed to date), showing the recurrence time and accretion history between bursts (Figure 2-30). The ensuing “quench” phase will be followed up with LAD observations, when for days to weeks increased temperatures at ordinary burst ignition depths ( $\sim 10^8$  g cm $^{-2}$ ) stabilize He-burning, quenching burst activity and possibly giving rise to unusual phenomena such as aborted X-ray bursts (Keek et al. 2012). The LAD can detect the short precursors that are expected in the early phases of the most super-Eddington bursts, such as the tens-of-ms ones due to explosive shell expansion (in’t Zand & Weinberg 2010) and  $\mu$ s shock-breakout precursors (Weinberg & Bildsten 2007; Keek & Heger 2011). The shock breakout light curve is a probe of the composition and pressure profile above the ignition depth (the shock may be able to ignite separate reservoirs of fuel at different depths depending on the amount of local overpressure of the shock). The flame spreading in bursts with deep ignition depths is highly relevant to understanding other thermonuclear events as classical novae or Type Ia SNe.

### 2.3.4.2 Novae

Nova systems contain a WD which undergoes thermonuclear runaways on its surface. Some nova types are considered viable SN1a progenitors: this adds significantly to the value of understanding them as fully as possible. Novae (symbiotic recurrent and classical novae) were recently, surprisingly found to produce X-ray emission up to  $\sim 50$  keV (Bode et al. 2006; Nelson et al. 2008; Sokoloski et al. 2006; Schwarz et al. 2011), and, even more unexpectedly, with Fermi/LAT, VHE  $\gamma$ -rays (Cheung et al. 2012; Hays et al. 2013; Abdo et al. 2010). The hard X-rays could be due to shock acceleration in symbiotic novae possibly due to collisions of ejecta with the red giant wind – in classical novae, such shocks are not strong enough so particle acceleration in ejecta internal shocks is likely the cause (Tatischeff & Hernanz 2007; Dubus 2013). Given these new findings, the WFM will catch the brightest novae. Their outburst can then be followed by LAD, for the first time measuring the temperature and density evolution over a range of fluxes. Comparison of X-ray measured temperatures with ejecta velocities from optical emission lines, yields information on the cosmic ray production efficiency of the shock, which can exceed the radiative efficiency (Hernanz & Tatischeff 2012).

### 2.3.5 Stellar Coronae

Stellar coronal activity probed in X-rays is a key to understanding convection in stars (Nordlund et al. 2009) and an important probe of the rotation, and hence age, of low mass stars (Barnes 2003). Bright X-ray flares detectable with LOFT are shown by late type stars such as RS CVn and Algol-type stars (binaries with tidally locked subgiants; Schmitt (1999)), UV Ceti flare stars (late K and M dwarfs, (Osten et al. (2010))), and young solar-type stars like AB Dor (Maggio et al. 2000). Typical X-ray flare distributions (Pye & McHardy 1983) predict detection of many tens of stellar flares per year with the WFM, most from stars not yet classified as active. Together with optical flare data from LSST this will provide important insights into the coronal heating process and, with data from new wide field radio monitors, into electron acceleration in extreme coronal flares. The WFM will also provide spectroscopy allowing the study of X-ray lines from such flares.

### 3 Scientific requirements

#### 3.1 Science requirements

In this section we summarise the rationale of the key science performance requirements which have been derived from the scientific objectives described in §2. A detailed Science Requirements Document (SciRD) covering all aspects including the flow down from top level science goals is also available. Most of the requirements have been systematically verified and traded-off through detailed simulations using a variety of response matrices and spectral fitting tools (XSPEC etc. see for example Lo et al. 2013), as well as specific simulation packages (e.g., GEANT). The LOFT key science requirements are recalled in Table 3-1. These requirements call for a set of instrumental and mission parameters which are correlated (e.g. mission duration and area can at a certain level be interchanged). The prime science parameter is the spectral-timing sensitivity. This can be optimized by the simultaneous optimization of all parameters, with the science impact varying very slowly and smoothly with each of them. The main parameters are: effective area, spectral resolution, sky visibility, mission duration. Each of these has potential margins which can be used to compensate a loss on another: ~10-20% on effective area, ~15% on sky visibility (FoR and eFoR), ~400% on radiation damage, ~7 °C on operating temperature for the spectral resolution and ~15% on mission lifetime. In this section we justify the science requirements and illustrate the interplay of these parameters and relative compensations.

Table 3-1 The LOFT Core Science Objectives

<b>EOS1</b>	Constrain the equation of state of supranuclear-density matter by the measurement, using three complementary types of pulsations, of mass and radius of at least 4 neutron stars with an instrumental accuracy of 4% in mass and 3% in radius.	<b>SFG1</b>	Detect strong-field GR effects by measuring epicyclic motions in high frequency QPOs from at least 3 black hole X-ray binaries and perform comparative studies in neutron stars.
<b>EOS2</b>	Provide an independent constraint on the equation of state by filling out the accreting neutron star spin distribution through discovering coherent pulsations down to an amplitude of about 0.4% (2%) rms for a 100 mCrab (10 mCrab) source in a time interval of 100 s, and oscillations during type I bursts down to typical amplitudes of 1% (2.5%) rms in the burst tail (rise) among 35 neutron stars covering a range of luminosities and inclinations.	<b>SFG2</b>	Detect disk precession due to relativistic frame dragging with the Fe line variations in low frequency QPOs for 10 neutron stars and 5 black holes.
<b>EOS3</b>	Probe the interior structure of isolated neutron stars by observing seismic oscillations in Soft Gamma-ray Repeater intermediate flares when they occur with flux ~1000 Crab through high energy photons (> 20 keV).	<b>SFG3</b>	Detect kHz QPOs at their coherence time, measure the waveforms and quantify the distortions due to strong-field GR for 10 neutron stars covering different inclinations and luminosities.
		<b>SFG4</b>	Constrain fundamental properties of stellar mass black holes and of accretion flows in strong field gravity by (a) measuring the Fe-line profile and (b) carrying out reverberation mapping and (c) tomography of 5 black holes in binaries providing spins to an accuracy of 5% of the maximum spin ( $a/M=1$ ) and do comparative studies in 10 neutron stars
		<b>SFG5</b>	Constrain fundamental properties of supermassive black holes and of accretion flows in strong field gravity by (a) measuring the Fe-line profiles of 20 AGNs and for 6 AGNs (b) carry out reverberation mapping and (c) tomography, providing BH spins to an accuracy of 20% of the maximum spin (10% for fast spins) and measuring their masses with 30% accuracy.

##### 3.1.1 Effective Area and Energy Range

The key innovation of LOFT is the access to CCD-class spectroscopy studies of phenomena occurring on short and still unexplored timescales. The ~10 m<sup>2</sup> effective area requirement for the core science derives from two main observational needs: reduce Poisson noise for relatively bright sources to access weak timing features (e.g., EOS1-3, SFG1-3) or gather high-quality spectra for phenomena occurring on intrinsically short time scales in weak (SFG5) or bright sources (SFG2,4). Examples of the first category are the measurement of epicyclic frequency QPOs (SFG1) or intermittent X-ray pulsars (EOS2) within the time that these signals

persist unchanged (minutes). Examples of the second category are the direct observation of millisecond orbital motion close to stellar mass black holes (SFG4), and Fe-line tomography in AGNs to derive ~10%-20% constraints to the spin of the supermassive black hole (SFG5).

This area is defined for the peak energy (~8 keV) but we further require that the LAD effective area does not change by more than ~20% over the energy interval (5-8 keV) in which the broad Fe-K lines are detected and studied (SFG4-5). The energy range limits can further be specified because the soft spectrum must be used to model photo-absorption or strong red wings in very broad Fe lines. For the hard response the measurement of the continuum emission of binaries and bright AGNs up to 30 keV is needed to anchor reflection effects which, as demonstrated by Nustar/XMM (Risaliti et al. 2013), provide additional independent constraints to the broad Fe line. Further extension to 80 keV, in counting mode, ensures that QPOs can be detected during intermediate flares of SGR/AXP (EOS3). These different aspects define effective areas of ~4 m<sup>2</sup> and ~1 m<sup>2</sup> at ~2 and ~30 keV respectively. Figure 3-1 shows the anticipated LAD effective area, as compared to the past/ongoing/planned largest X-ray missions. The low energy bound requirement is 2 keV. Reaching lower

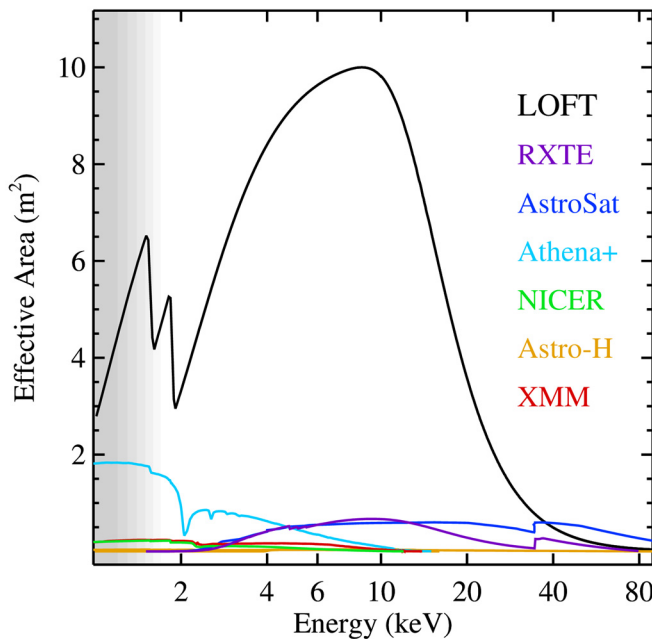


Figure 3-1 The effective area of LOFT/LAD as compared to the largest past, on-going and approved missions. The shaded area below 2 keV indicates the fact that the LAD will outperform its science requirement of 2 keV low energy threshold, by extending its sensitivity down to ~1-1.5 keV.

energies would be beneficial in characterizing the ultrasoft spectra of BH thermal disks, and when observing sources with complex absorption structures (e.g., AGNs in SFG5). The expected performance is to be able to operate down to 1-1.5 keV, providing 2-3 m<sup>2</sup> effective area (Figure 3-1). As a large part of the science information is derived from the time variability of the detected counts, any systematic effects on the detected rate are required to be at a negligible level as compared to the intrinsic variability of astrophysical origin. This is captured by the requirement on the **response stability**, a combination of the pointing

stability requirement with the “insensitivity” of the instrumental response to small offsets (related to the alignment requirement). The requirement on the response stability is set in each frequency band by taking into account the expected astrophysical signal per frequency range, from 2% per frequency decade below 10 mHz to 0.02% per octave at ~1 kHz.

### 3.1.2 Spectral resolution

A good spectral resolution is required for a number of LOFT core science objectives (but not all of them), namely strong-field gravity through studies of gravitationally broadened Fe K $\alpha$  line. The requirement on the end-of-mission spectral resolution integrated over the full detector (240 eV FWHM @ 6 keV) was set as the resolution allowing to measure the Fe-line parameters enabling SFG2, 4, 5, e.g., the BH spin with a minimum accuracy on a/M of 10-20% in 20 AGN and 5% in 5 stellar mass black holes. Figure 3-2 shows this quantitatively in a simulated example: starting with spin a\*=0.7, we are able to recover the SMBH spin at the required level of accuracy, in a complex spectrum also including a ionized absorber with narrow Fe K $\alpha$ , Fe K $\beta$ , Ni K $\alpha$  and ionized lines due to a "hot gas" emitter with ionization parameter log( $\xi$ )~3.5. Clearly the required energy resolution is not a firm threshold significant constraint to the BH spin (order of ~40%, which can be in many cases acceptable) can still be achieved even in the event of a 10% worsening of the spectral resolution with respect to the requirement. Indeed, the anticipated performance for spectral resolution is significantly better than requirement. As shown in Figure 3-3, within the Sun Aspect Angle (SAA) constraints defining the Field of Regard (FoR, the instantaneously accessible sky fraction enabling fulfilment of all requirements), the anticipated energy resolution ranges from 180 eV to 220 eV, depending on the spacecraft concept, as compared to the required 240 eV.

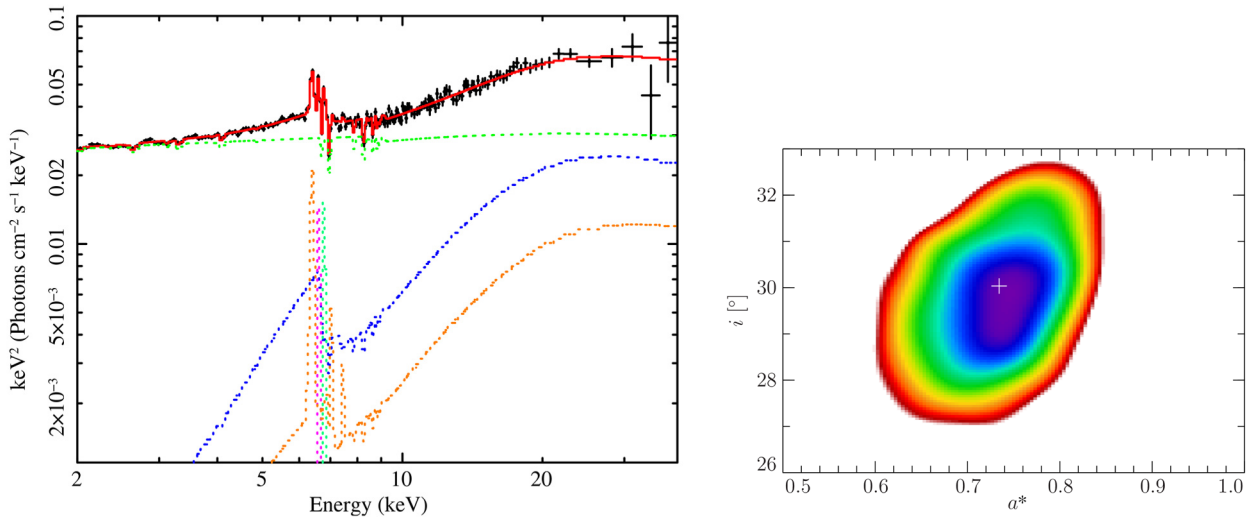
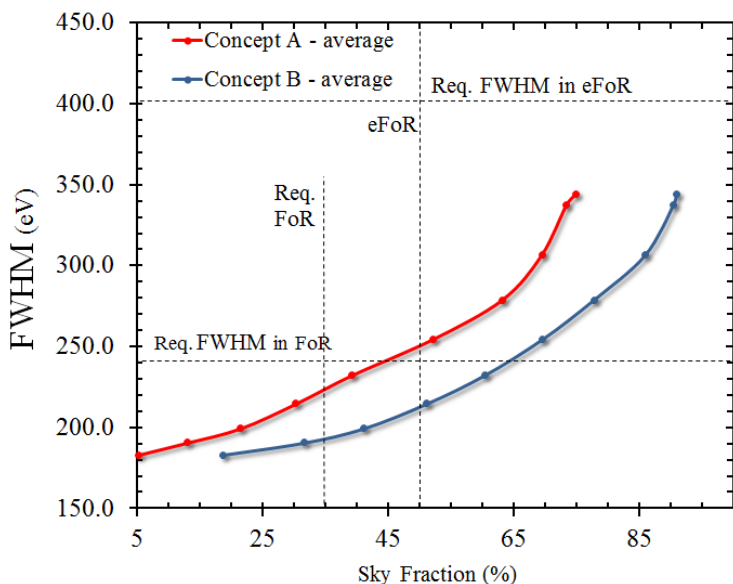


Figure 3-2 Left: LAD simulation of a realistic AGN spectrum with  $S/N=400$  (black) including the ionized absorber and the continuum (green), the cold reflection and narrow Fe line  $K\alpha$ , Fe- $K\beta$  and Ni- $K\alpha$  (orange), the ionized lines FeXXV (40 eV EW; magenta) and Fe XXVI (40 eV EW; cyan) and the relativistically broadened Fe-line and ionized reflection components from the inner disk regions (blue). The total spectral model is represented in red. Right: confidence contours (68% in blue, 90% in green and 99% in red) for the spin reconstruction with a LOFT observation with the requirement spectral resolution.

The same result may be seen from the perspective of the FoR width: the anticipated FoR is 45% or 65%, depending on the spacecraft concept, as compared to the 35% requirement (set to comfortably allocate with good margins all the observations requiring nominal energy resolution, thanks to the unconstrained long observations of AGN targets). The energy resolution and the FoR requirement are therefore both satisfied with ample margin. Always, 40% of the photons (the single anode detections), i.e., an event rate equivalent to 4 m<sup>2</sup> of effective area, are detected at 26% better resolving power.

Not all core science goals require optimal spectral resolution. The latter is partly determined by the detector dark current which depends on detector temperature. For the benefit of observation types which are insensitive to a lower spectral resolution, we defined an extended Field of Regard (eFoR) as a range of SAAs beyond the FoR where a relaxed energy resolution can be accepted (<400 eV FWHM, all events). This offers access to an even larger sky fraction and/or a larger pointing and scheduling flexibility. The requirement for the eFoR was set at >50% (goal at 75%). As seen in Figure 3-3, also this requirement is largely satisfied by both spacecraft designs, actually reaching close to the goal of 75%.

Detailed analysis of the mock observation plan, which includes the targets for the core science, has demonstrated that the required energy resolution for the various categories of targets is met with large margins



(indeed, most of the targets will be observed with better spectral resolution than required). In addition to that, the operating temperature profiles guaranteed by both spacecraft studies will allow nominal energy resolution (or better) for many targets of the observatory science as well.

Figure 3-3 LAD Full Width at Half Maximum Energy resolution (total events) at End of Life as a function of the sky fraction, for the realistic operating temperature provided by the two industrial studies (including a 10° design margin). The plot shows that the energy resolution is significantly better than the requirement (FoR requirement 35%; eFoR requirement 50%) for large fractions of the sky. This implies that most of the LAD observations will be done with better spectral resolution than requirement.

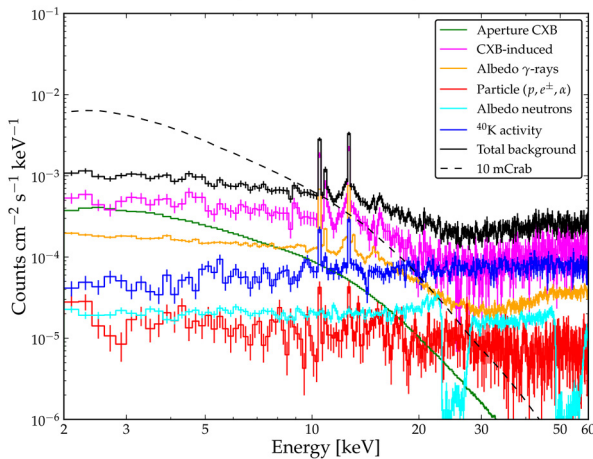


Figure 3-4 The simulated LAD background spectrum, showing all individual components. Black solid line is the total background, while the dashed line is the 10 mCrab energy spectrum. The total background rate is compliant with the requirement in the 2-30 keV energy range, while it is 2 times better in the most important energy range 2-10 keV.

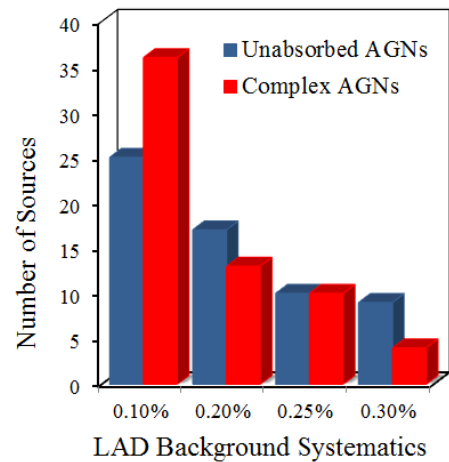


Figure 3-5 Number of available AGN targets for broad Fe-line studies, as a function of the background systematic uncertainty. A requirement of 20 AGNs translates into a requirement of 0.25% systematics.

### 3.1.3 Background

Most of the studies driving the LOFT core science are performed on relatively bright sources (100 mCrab or more), for which the background rate is not critical, while the key objective is the reduction of the Poisson noise by collecting large number of counts. Background is instead critical for the SFG studies with AGNs, where the signal is dim. In a distributed instrument as the LAD, the resources for an active anticoincidence would conflict with those for the instrument itself and such an implementation would eventually result in a smaller collecting area. The required 10 mCrab background level is a trade-off between these two objectives. The design of the passive shields of the instrument (collimator, backside Pb shield) is the result of a trade-off analysis based on accurate Monte Carlo simulations including a detailed instrument description in the GEANT package. The baseline design provides a background level (Figure 3-4) which satisfies the requirement in the 2-30 keV and it is about 2 times better (<5 mCrab) in the most critical energy range for science 2-10 keV (Campana et al. 2013).

For the studies of the relativistically broadened Fe-line in AGNs the key parameter is not the background level, but rather the systematic uncertainties left in the source spectrum after its subtraction, moving the science requirement to the knowledge of the background (control and modelling). Extensive simulations were carried out to assess the impact of background systematics on the AGN Fe-line studies (see the note LOFT-IAPS-LAD-TN-0006 in the IPRR data package and the SciRD). Higher systematics increase the limiting flux of the sample of AGN targets where sensible broad Fe-line studies can be carried out. Requiring that this sample is large enough to allow for a solid assessment of the variable broad Fe-line properties basically determines the required maximum systematics. To achieve a sample of at least 20 AGNs, conservatively based on the current source catalogues (namely, CAXIA, Suzaku and BAT), the residual uncertainty after background subtraction should not exceed ~0.01 mCrab in 2-10 keV, which corresponds to 0.25% of the currently estimated background level. This is shown in Figure 3-5, where the number statistics of the available AGN targets is shown as a function of the background systematic uncertainty.

A value of 0.25% systematics can be achieved. As a comparison, the RXTE PCA experiment reached 0.5% (Shaposhnikov et al. 2012), despite a sub-optimal orbit, causing a ~250% background modulation, and the use of gas-filled proportional counter detectors with massive collimators. LOFT/LAD will operate in a much better configuration: the low-altitude (550 km) and low inclination (<2.5°) orbit for LOFT guarantee the lowest and least modulated particle environment, primarily because of the limited range of geomagnetic coordinates the spacecraft will span, nearly skipping the South Atlantic Anomaly (Figure 3-6).

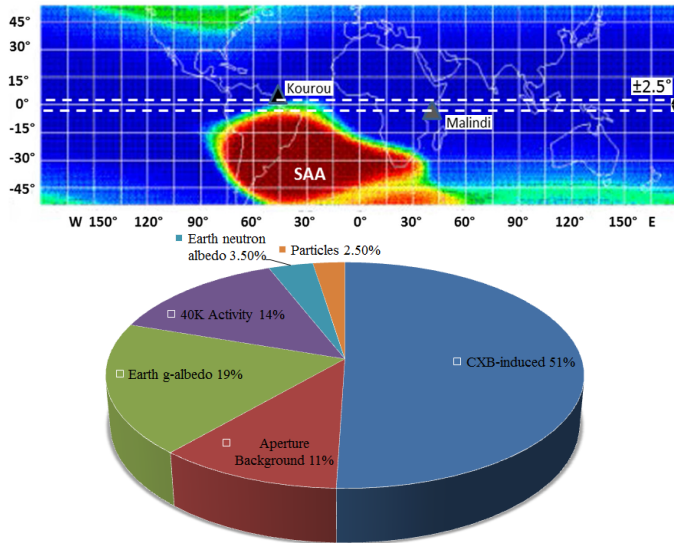


Figure 3-6 Top: LOFT orbit guarantees the lowest and least modulated particle environment, primarily because of the limited range of geomagnetic coordinates the spacecraft will span, nearly skipping the South Atlantic Anomaly. Bottom: the relative weight of the LAD background components, showing that the particle-induced background is less than 5% of the total, the rest being photon background.

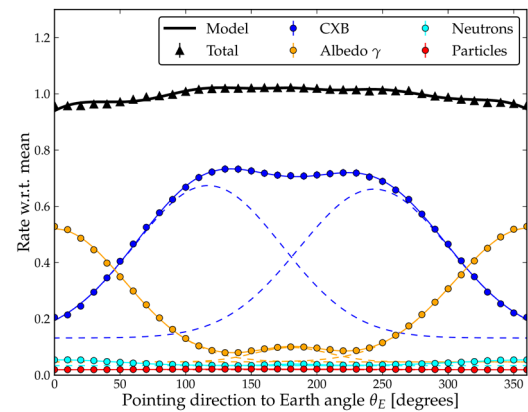


Figure 3-7 Time-dependent Monte Carlo (GEANT) simulations of the LAD background, over the duration of 1 orbit and integrated between 2-30 keV. The geometrical modulation of the CXB- and Albedo-induced background produces an overall background orbital modulation of ~10%, accurately predictable as due to pure geometry. Dashed curves show the individual components of the model (e.g., the blue curves are front- and back-side illumination of the module from CXB)

In addition, the combination of silicon solid-state detectors and a very light collimator in a compact design allow for a very low internal (particle-induced) background about a factor ~4 to 5 lower than PCA. Indeed, our Monte Carlo simulations show (Figure 3-6) that the internal (particle) background in the LAD is a minority component: the largest component comes from high energy photons of the Cosmic X-ray Background (CXB) or from the Earth Albedo which is transmitted through the collimator structure. In fact, while efficiently shielding below ~30 keV, for higher energies the capillary plate collimator becomes inefficient. This represents indeed at the same time an asset to detect and measure timing properties of intense and hard bursting events from outside the field of view (e.g., magnetar flares, EOS3).

As 97% of the background is due to steady diffuse sources such as the internal K40 radioactivity of the collimator, CXB and the Earth albedo, any variability in the background rate is due to a gradually varying geometry of viewing angles and not to intrinsic variability of the background sources, as in the case of the particle background. A detailed analysis of the background variability shows that the expected orbital modulation of the total background rate is lower than ~10%. In essence, due to the varying relative Earth-spacecraft geometry along the orbit, the instrument rotates in a photon field which has CXB on 70% of the solid angle and Earth albedo on the remaining 30%. The spectrum and intensity difference of these two components determines the rate variability.

Figure 3-7 shows the estimated orbital variability of all background components, as obtained from time-dependent GEANT simulations, together with their total rate (black points). In terms of individual components, the largest modulation comes from the CXB and Earth-albedo induced background. As expected, being only due to geometrical effects and centred 180° off-set one another, their variability is in anti-phase, resulting in a very shallow modulation of the total rate.

The purely geometrical nature of the background variability and the intrinsic orbital periodicity allows building an accurate model for the modulation, combining the geometrical effects and GEANT simulations (dashed lines in Figure 3-7). Current estimates based on detailed simulations (see the note LOFT-IAPS-LAD-TN-0003 in the IPRR data package) show that, when benchmarked with in-flight blank-field data, this model will be able to reproduce the background variations to <0.15% (versus a 0.25% requirement). This is indeed not surprising, when compared to the 0.5% actually achieved by RXTE/PCA against a ~250% variable background and largely due to particles.

As discussed above, the LAD background modulation is expected to be very smooth and slow. This implies that a real-time monitoring would not need to constrain instantaneous variations rather a repeating and steady functional form. This can be achieved with a detector area much smaller than the main instrument. GEANT simulations show that a detecting area corresponding to a single LAD module (16 detectors, ~0.8% of the whole LAD area) equipped with a “blocked collimator” (same material and mass, but no holes) would be able by itself to reconstruct the background modulation to an accuracy of ~0.25%, completely independently of the overall geometrical model benchmarked with blank fields discussed above. This “blocked module” will then be used in support to the background modelling, with the additional benefit of providing real-time monitoring of any impulsive event (e.g., solar flares), for which anyway the monitoring of the WFM will be continuously available as well.

### 3.1.4 Sensitivity

The enormous effective area of the LAD implies an unprecedented counting statistics. The “standard candle” of X-ray astronomy, the Crab Nebula, is expected to provide a count rate as high as 240,000 cts/s. This means that the statistical LAD  $3\sigma$  sensitivity for persistent sources is tremendously high (see Figure 3-8). For longer integrations ( $\geq 10^4$  s) the statistical uncertainties become so small that systematics in the background subtraction dominate. In Figure 3-8 the LAD sensitivity curves are provided as a function of the exposure time, for different levels of required signal-to-noise ratio, under the assumption of the required 0.25% background systematics as well as the expected value of 0.15%. The sensitivity curves show that a  $5\sigma$  detection of a 0.1 mCrab sources takes ~100 s. A signal to noise of ~100 such as required for sensitive spectral line studies is reached after  $10^4$  s for a 0.5-1 mCrab source. These curves apply to the observation of persistent sources. When observing rapidly variable (as compared to the orbital background variation) signals, the sensitivity is not affected by any incoherent residual background systematics and continues to improve at long integration times. This includes not only timing analysis but spectral variability as well, as long as it is rapid enough.

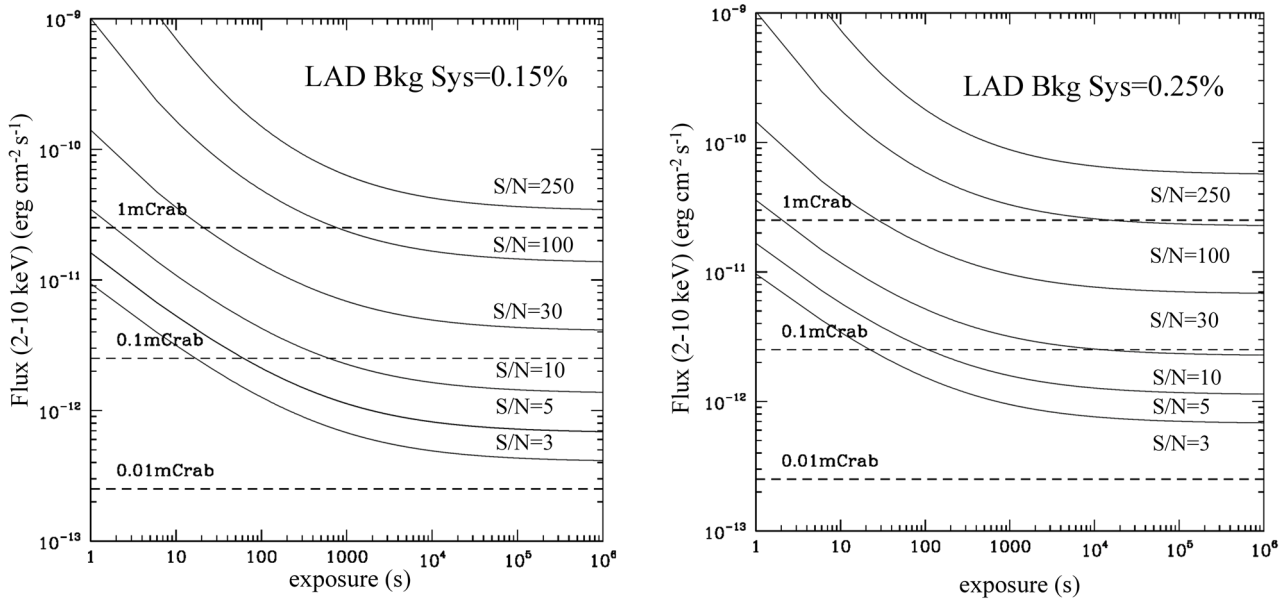


Figure 3-8: LAD sensitivity versus exposure time for different signal-to-noise levels. Both the cases of the requirement (0.25%) and expected (0.15%) background systematics are provided.

### 3.1.5 Sky visibility and field of regard

The sky visibility is defined through the range of Sun Aspect Angles (the strip in the sky determined by the SAAs, see Figure 3-9) allowed during nominal observation. Unlike many other missions, the (LAD) sky visibility for LOFT is not primarily limited by the power constraints, which are indeed satisfied for a wider range of SAAs by either steerable or oversized solar arrays in both industrial studies, rather from the thermal constraints deriving from the operating temperature requirements. For this reason, the LAD sky visibility is essentially expressed in terms of Field of Regard (FoR) and Extended Field of Regard (eFoR), as defined in §3.1.2 and illustrated in Figure 3-9.

The science requirement of 35% FoR and 50% eFoR derive from the availability of the source types which enable to fulfil (with proper margins) the core science objectives. These were analytically determined on the basis of a mock-up observing plan, described in §3.2, in which all science objectives were implemented through hypothetical observations of specific targets and identifying those requiring full energy resolution (FoR) and those for which a 400 eV spectral resolution is sufficient (eFoR).

As indicated in §3.1, the eFoR is aimed at extending the sky visibility for those science goals/targets which do not require the best energy resolution. From the scientific point of view, the eFoR is preferably achieved extending in the anti-Sun direction, a region more easily accessible from the ground and for this same reason a WFM unit has been added to monitor this sky region. The goal eFoR is 75%, which would correspond to  $+30^\circ/-90^\circ$  SAA.

Both industries completed their spacecraft studies with full compliance with the FoR and eFoR requirements, actually providing sky visibility close to the goal of 50% FoR and 75% eFoR.

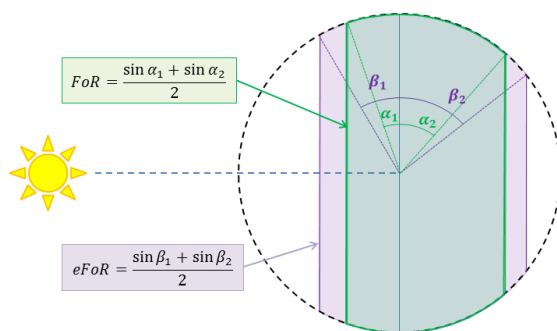


Figure 3-9 The geometry of sky visibility. The region of the sky accessible to the LAD at any time is a strip defined by the maximum angles allowed by the requirements on the operating temperature:  $\alpha_1$  and  $\alpha_2$  define the FoR, whereas  $\beta_1$  and  $\beta_2$  define the eFoR

### 3.1.6 Transient monitoring (WFM)

Many of the sources which are key to the success of the mission are variable sources and LOFT should observe these in the relevant bright state. Therefore the LOFT mission includes a Wide Field Monitor. This instrument will be used to monitor the state of the relevant sources but will also alert the wider scientific community about transient events in known sources as well as identify new and unexpected sources. These requirements are best achieved by optimizing the field of view. The baseline WFM design envisages a simultaneous sky coverage as large as 1/3 of the whole sky with  $>20\%$  of its peak effective area. This responds to its main requirement of monitoring at least 50% of the sky fraction accessible to the LAD at any time (for transient monitoring). The co-alignment of the WFM and LAD field of view will also allow use of the arcmin-resolution imaging capability of the WFM to monitor the field of view observed by the LAD at the same time.

The shape of the field of view of the WFM, shown in Figure 3-10, reflects the asymmetry of the eFoR of the LAD (see §3.1.5) which extends into the anti-Sun direction. This solution also offers the major advantage of monitoring a region of the sky with the best accessibility from ground observing facility (e.g., optical telescopes), providing a major asset to the follow-up of Gamma Ray Bursts. In fact, considering the wide sky simultaneous coverage, the arcmin-location capability, the 130 mCrab peak sensitivity in 10 s and the  $\sim 300$  eV spectral resolution (vs 500 eV requirement), the WFM qualifies as a major facility for GRB detection and localization (current estimate is localization of  $\sim 120$  GRBs/year). For this reason, the instrument is equipped with autonomous onboard GRB triggering and localization capability and with a VHF-based communication system, required to communicate the GRB coordinates to the ground observers no later than 30 s after the event detection onboard.

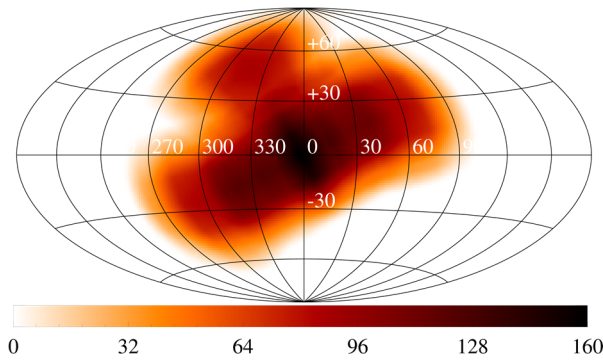


Figure 3-10 Map in Galactic coordinates of the active detector area for a sample observation performed in the direction of the Galactic centre.

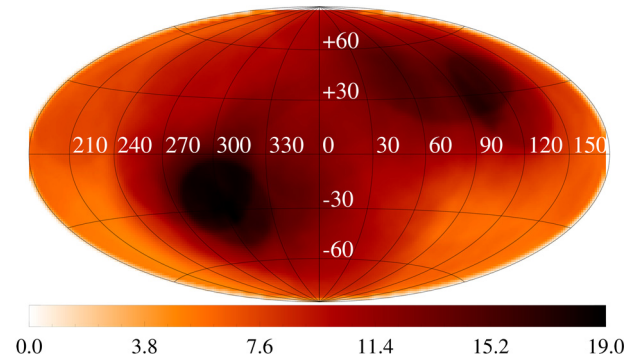


Figure 3-11 1 year exposure map in Galactic coordinates for positions covered by at least  $10 \text{ cm}^2$  per observation. Map scale is given in Ms.

### 3.1.7 Mission duration

The requirement of mission duration was analysed during the assessment study. The key elements are i) the overall observing time, ii) accessibility of required sources, iii) the probability to catch rare outbursts of transient Black Hole candidates (BHCT) and Accreting Millisecond X-ray Pulsars (AMXPs). The analysis of the required exposure time shows that a total exposure time of  $\sim 25$  Ms is required to execute the core program. Even with the minimum requirement of 40% mission availability (industrial studies show an observing efficiency  $>60\%$ ) 25 Ms are available in less than 2 years.

The third and effectively driving requirement comes from a  $>95\%$  probability to detect at least 3 outbursts from BHCT (in their intermediate states, where high-frequency QPOs required by SFG1 are detectable) and 3 AMXP outbursts. This was calculated on the basis of the available statistics from about 15 years of RXTE observations, under different assumptions on the sky visibility. For the core-science observation of AMXP outbursts and for strong-gravity objective SFG1 the full energy resolution is not required and therefore the relevant sky visibility here is the eFoR. A detailed table is provided in the Science Requirements Document. The conclusion is that with a sky visibility of  $+30/-70$  degree, as is guaranteed by the two industrial studies, the mission duration is 3 years. A reduced sky visibility of  $+30/-50$  degree could be compensated by a longer (4 year) required mission duration.

## 3.2 Observation plan

Based on the scientific objectives discussed in §2, the observing time per core science goal has been split over the different target types and the number of required sources per category. For each source category we have determined the optimal number of pointings, the observation time per pointing and the campaign durations. From these requirements a mock observation plan was produced, and used by industries to assess the impact on the system designs. In finer detail, it was specified per target whether the spectral resolution is important for the science goal (e.g. Fe-line characterization), which provides Solar aspect angle (SAA) constraints per target. Pre-identified transients mentioned in this plan will likely not be on, but serve as placeholders for similar transients that will be discovered by LOFT WFM or other means (the full detailed mock observing plan is provided in the LOFT SciRD).

Observing times and schedules in a significant part of observations are set by intrinsic source state variations. Sources have different spectral/timing states and we need to sample each state over a range of luminosities in order to understand the processes we are detecting with LOFT, or in order to catch a source in the right state to see the process in the first place. Conversely for NS burst oscillations, the time to accumulate  $\sim 10^6$  pulsed photons during bursts is a driver.

The total observing time required for the core science goals is 24.7 Ms (see Table 3-2). The Observatory Science target list was adopted from comparable targets of such source classes observed by RXTE, or otherwise assumed to be randomly distributed about the sky with similar distribution as the core science targets. An allocation of 25 Ms was allowed to scope this Observatory Science plan. The resulting observing plan was then elaborated to calculate visibility constraints, slew times etc, and each industry study produced an estimate

for availability in view of thermal and AOCS relaxation times, Earth occultation, calibration exposures etc. In both cases, an observing availability of 60% was estimated which would allow for a mission lifetime of < 3 years to complete the science program.

With the estimated FoR and eFoR this is sufficient to ensure a good probability to observe the rare transient events (3 BHCT in the intermediate state where HF QPOs occur, and 3 AMXPs) needed for some of the science goals. The total observation time for these sources, ~3.4 Ms (included in the core science above), is not predictable in time, and may occur when the Galactic Bulge is poorly visible. The probability of these transients occurring was accounted for. This probability was folded with the different fields of regard of the mission (to establish if LOFT can observe the source meeting the viewing constraints). Again for these sources the campaign lengths were assessed (BHCT ~ 100–300 days, only a few weeks of which exhibit the HF QPOs required for SFG1, and the AMXPs ~ 20 days with total required ~300 ks per AMXP). For a SAA +30°/-70°, the expected probability to observe 3 BHCTs and 3 AMXPs is ~95% each for a mission duration of 3 years and ~99.5% with an extended mission of 5 years. 2 BHCTs and 2 AMXPs are observed with probability >99% in all cases. For SAA +30-50 approximately the same probabilities are attained in one year more.

Table 3-2 Summary of Observing Plan durations

All observations	Time [Ms]	Observations with viewing constraints	Time[Ms]
<b>Total core science on Galactic Bulge</b>	12.4	Core science on Galactic Bulge with nominal spectral resolution	8.1
<b>Total core science</b>	24.7	Total core science with nominal spectral resolution	18.8
<b>Total General Observatory science</b>	25	General Observatory science on Galactic Bulge	9.8
<b>Total Observing Time</b>	<b>49.7</b>		

The total available observing time for LOFT with a 60% observing availability in 3 years (following from the industrial studies) is around 56.8 Ms which shows a significant margin with the required 49.7 Ms. In summary the observing plan is very robust to observing constraints, allowing for large expansion in core science durations/target numbers if deemed useful/necessary, or allowing for significantly expanded guest observer programs.

### 3.3 Science requirements margins

The scientific requirements for the instrument are feasible, based on the instrument and spacecraft designs. Nevertheless the effect of a reduced effective area or spectral resolution has been studied in detail. As we discussed in the SciRD and report below, a reduction in effective area, spectral resolution, field of regard can be compensated by longer observations. This implies, of course, that the balance between the core science and the observatory science may change, but the goals of the mission will still be accomplished. Furthermore the two prime goals of the mission the Equation of State of supra-nuclear dense matter and the Strong Field Gravity effects are each studied by different type of observations. Also in this respect there is a certain level of intrinsic redundancy in the mission.

#### 3.3.1 Effective area

For the full satisfaction of the core scientific goals, the 9.5 m<sup>2</sup> requirement is inter-related with several other requirements, including the spectral resolution, the field of regard and the mission duration. In the Science Requirement Document a detailed analysis of the critical dependency of the core science objectives on the LAD effective area is reported. The result is that even with effective area reduction of ~10-20% most of the science goals are fully recovered by nearly proportionally longer exposure/mission duration. This is shown in Table 3-3. For a few cases, namely SFG3 (waveform analysis on QPO coherence timescale) and SFG5 (Fe-line tomography in AGNs), longer observations cannot compensate a smaller effective area and the latter translates into a higher limiting flux, leading to a comparably smaller sample of observable targets, yet not compromising the science goal.

The requirement value of 9.5 m<sup>2</sup> is reached by accommodating a minimum number (121) of Modules on the spacecraft, each one carrying a minimum effective area (800 cm<sup>2</sup>). At spacecraft level, the industrial studies demonstrate that both mission designs can accommodate the required number of modules, with 3-4 module margins. At Module level, the key design parameters to guarantee the required module effective area are the

70% open area ratio of the collimator and the 1-arcmin pore to pore alignment. The latter is already demonstrated in the heritage of the BepiColombo capillary optics. The 70% open area ratio is expected to be demonstrated by the on-going development activity. The currently available technology at the collimator manufacturer is 66.5%, which implies a worst case effective area reduction of 5%. This is smaller than the 10% considered in Table 3-3 which can be compensated by longer observation times.

Table 3-3 The impact of any reduction in the effective area on the observing time / number of targets / limit flux for the core science objectives, showing that they are basically entirely recoverable by longer observations, which are fully compatible with the large margins in observing times/mission duration (see §3.2), while the number of targets for SFG3 and SFG5 decreases marginally (table gives total number and targets for tomography).

Relative Area	EOS1	EOS2	EOS3	SFG1	SFG2	SFG3	SFG4	SFG5
100%	1.00	1.00	Flux>1000 mCrab	1.00	1.00	Targets >10 NS	1.00	1.00 Targets >20(6) AGN
90%	1.11	1.11	1110 mCrab	1.23	1.13	9 NS	1.23	1.11 20(6) AGN
80%	1.25	1.25	1250 mCrab	1.56	1.25	8 NS	1.25	1.25 19 (5) AGN

### 3.3.2 Spectral resolution

Spectral resolution requirement is achieved through design as well as operational solutions. The technical driver is the read-out noise of the detector channel, which depends on the read-out electronics and detector properties. Once the read-out chain is optimized at design level, the end-of-life spectral performance depends primarily on the “leakage (or dark) current” in the detector. This can be minimized by using different approaches: i) manufacturing technology processes to reduce the intrinsic (i.e., starting) value, ii) minimizing the radiation damage in orbit and by iii) reducing the operating temperature (leakage current halves every 7°C). Table 3-4 lists the critical dependency of the main components of the spectral resolution, showing that all of them are indeed already achieved in the current design with significant margins. The noticeable exception is the noise performance of the baseline read-out ASIC, SIRIUS. This is actually not due a technology limit, rather a delay in development due to a late start of this activity. In fact, the other ASIC (VEGA, developed in Italy) already shows basically in-spec performance, demonstrating technology feasibility (as well as a back-up technical solution).

Table 3-4 The main components of the spectral resolution (at 6 keV, end of life): requirements and current status

	Critical Dependency	Units	Requirement	Current Status/ Expected
Fano noise	Silicon-intrinsic	eV (FWHM)	118	118
Intrinsic leakage current (@20°C)	Manufacturing technology	nA/cm <sup>2</sup>	≤0.14	0.09
Read-out Noise	ASIC design	e <sup>-</sup> rms	≤17	26 <sup>(*)</sup>
Radiation-induced leakage current (@20°C)	Orbit	nA/cm <sup>2</sup>	0.04	Designed to tolerate up to 0.08
Residual read-out spread	ASIC design	%	≤0.25	<0.14

<sup>(\*)</sup> Noise figure of SIRIUS V1 prototype. Improvements are planned/expected in the next versions. The available VEGA prototype realized in Italy already demonstrated ~18 e<sup>-</sup> with no specific optimization.

The minimization of radiation damage in orbit is achieved by selecting a low-Earth equatorial orbit, with low altitude (550 km, fully benefiting of the shield to particles offered by the Earth magnetosphere and below the Van Allen belt) and low inclination (<2.5°, avoiding almost entirely the South-Atlantic Anomaly; see Figure 3-6). An in-depth study by both Consortium and ESA EEC-TEC was carried out using radiation belt models and data from past missions in a similar orbit to confirm the radiation environment in the LOFT orbit, while the radiation effects on the detectors were assessed through extensive particle irradiation tests (see §4.3.1). A further factor 2x design margin was added to this when setting the requirement on the leakage current, following ESA standard. On top of this, the Consortium has set the requirement on the detector operating temperature assuming a further 2x margin on the current (see Table 3-4). It is also worth noticing that even in the unlikely event of a radiation environment exceeding even such large margins, the worsening of the spectral resolution is very slow, reaching a 10% only with a further 3x factor (Figure 3-12), whereas, as shown in

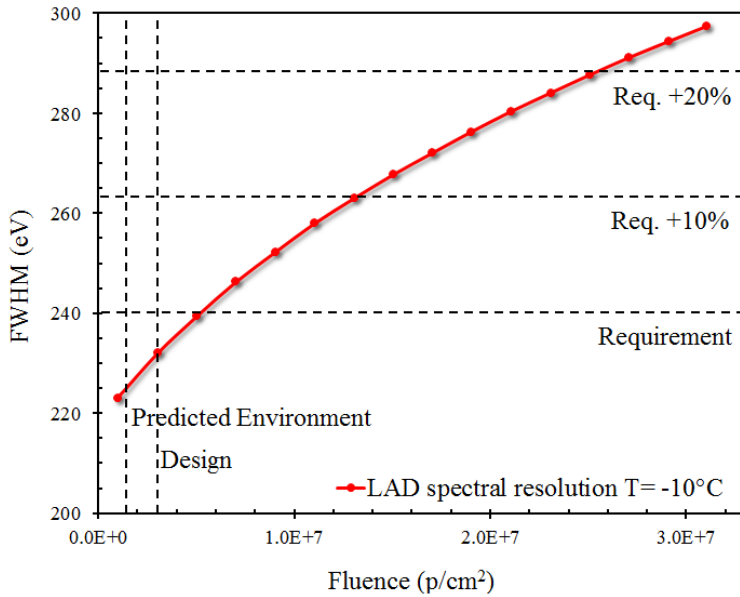


Figure 3-12 Sensitivity of the end-of-life spectral resolution on radiation environment. The vertical dashed line indicates the estimated (required) radiation environment, whereas the dashed vertical line is the adopted design margin (2x). The energy resolution requirement is satisfied with significant margins at the predicted radiation environment. A ~4x worse than design margin particle flux causes only a 10% spectral resolution worsening.

Figure 3-3, the spectral resolution is indeed expected to be typically better than the requirement. Finally, we also performed a sensitivity analysis of the risks associated with a potential non-compliance of the LAD energy resolution parameter with the requirement. Even in the event of an

energy resolution not meeting the requirement, consequences for the science objectives can be mitigated by longer observations, with the exception of the Fe-line profile fitting shown in §3.1.2 where a 10% spectral resolution degradation is still acceptable but a 20% degradation will not meet the requirements. This is summarized in Table 3-5. Of course, this conclusion depends on the assumption that we have a correct understanding and description of the spectra of these sources (and with a better energy resolution this will be verified more easily).

Table 3-5 Sensitivity analysis of the impact of 10% and 20% non-compliance for the spectral resolution requirement

Science goal	~270 eV resolution	~300 eV resolution
Relativistic frame dragging in LF QPOs	Observing time x 1.1	x 1.2
Reverberation mapping	x 1.2	x 1.4
Tomography <sup>1</sup>	x 1.2	x 1.4
Fe-line profile fitting	Increased uncertainty but close to requirement	Increased uncertainty by about a factor 2 above the requirement

<sup>1</sup>Compensation is feasible assuming the hot spots last sufficiently long.

## 4 Payload

The payload consists of the Large Area Detector (LAD) which is the prime instrument and the Wide Field Monitor (WFM) which will continuously monitor the sky and recognize changes in source states, allowing the mission to respond to this. The two instruments are described below. As the instruments use the same detectors, we will provide detailed information about the critical technology in §4.3. A full and detailed description of the payload is available as part of the data package to the Instrument Payload Requirements Review, thoroughly and successfully reviewed.

### 4.1 Large Area Detector

The Large Area Detector (LAD) is a 10 m<sup>2</sup>-class instrument with ~15 times the collecting area of the largest timing missions so far (RXTE) for the first time combined with CCD-class spectral resolution. This provides the capability to revolutionize the studies of variability from X-ray sources on millisecond time scales. The LAD will operate in the energy range 2-30 keV (up to 80 keV in expanded mode) with good spectral resolution (<240 eV @ 6 keV, FWHM) and a time resolution of 10 μs. The required 10 m<sup>2</sup> area can only be realistically achieved by a collimated instrument where the detectors are mounted on panels and the field of view is limited by a passive collimator. The key instrument requirements including the expected performance are summarized in Table 4-1 (see also SciRD). The basic concept of the instrument is to employ silicon detectors to record the X-rays and limit the field of view by the collimator to about 1 degree (to reduce background from sources outside the field of view). Such large detector became feasible thanks to recent developments in detector technology. Silicon Drift Detectors were developed for the ALICE experiment at CERN and later optimized for the detection of photons to be used on LOFT. With a typical size of 11 x 7 cm<sup>2</sup> we need in total about 2000 detectors. Each detector is segmented in two halves with 112 channels each which ensures that the effect of the recording of two events too close in time and position (pile-up) is negligible. To maintain a good energy resolution the detectors need to be moderately cooled (-10 °C). Considering the large size of the detector this can only be achieved passively. For the read-out of the detector we need to have dedicated mixed-signal ASICs with very good performance and low power per channel. In total we need about 28000 ASICs. Finally, collimation is supplied by Micro Pore Collimators (MPC).

Table 4-1 LAD scientific requirements

Item	Requirement	Anticipated performance
<b>Effective area</b>	3.8 m <sup>2</sup> @ 2 keV 7.6 m <sup>2</sup> @ 5 keV 9.5 m <sup>2</sup> @ 8 keV 0.95 m <sup>2</sup> @ 30 keV	4.4 m <sup>2</sup> (averaged between 1.5-2.5 keV) 9.0 m <sup>2</sup> 9.8 m <sup>2</sup> 1.3 m <sup>2</sup>
<b>Energy range</b>	2 – 30 keV nominal 30-80 keV extended (for monitoring events outside LAD FoV)	1.5 (7.5 σ) lower threshold, 100 keV for maximum energy
<b>Energy resolution in Field of Regard (FWHM, end of life)</b>	240 eV @ 6 keV	180 eV @ 6 keV at the center up to 190-220 eV at the edge of the FoR (35% sky fraction), depending on the spacecraft design.
<b>Energy Resolution in extended Field of Regard</b>	400 eV @ 6 keV	190-220 eV @ 6 keV at the center up to 220-250 eV at the edge of the eFoR (50% sky fraction), depending on the spacecraft design.
<b>Absolute time accuracy</b>	2 μs	1 μs
<b>Dead time</b>	< 1% @ 1 Crab,	< 0.7% @ 1 Crab,
<b>Background</b>	< 10 mCrab	9 mCrab (5 mCrab in 2-10 keV)
<b>Background knowledge</b>	0.25% at 5-10 keV	0.15% at 5-10 keV
<b>Max flux (sustained)</b>	> 500 mCrab	650 mCrab
<b>Max flux (continuous 300 min)</b>	15 Crab	15 Crab

### 4.1.1 Instrument Description

The large area will be achieved by a modular design (called LAD modules). Each LAD module will have a set of 4 x 4 detectors and 4 x 4 collimators including the electronics needed for biasing and read-out. It will interface the instrument control units through a digital and power interface only. The LAD modules will be mounted on deployable panels of the satellite. Depending on the satellite design (§5.3) there will be either 2 or 5 panels and the number of LAD modules also differs slightly (124 and 125 modules). To meet the effective area requirement 120 modules and 1 blocked are needed. Each LAD module will encompass 16 Silicon Drift Detectors (SDD). Each photon is detected in a SDD layer 450 microns thick, and the cloud of electrons liberated then drifts towards the anodes. The anodes are separated by 970  $\mu\text{m}$ . Each anode is read-out by its own amplifier which is integrated in an analogue/digital ASIC with low power consumption. The dynamic range of the read-out allows operation in the energy range 2-80 keV. Dead time of the instrument is accurately controlled as this is very important for a timing instrument. The field of view of the LAD will be limited to <1 degree by X-ray collimators. These are micro-channel plates, in our case based on manufacturing developments for BepiColombo and consist of a 5 mm thick sheet of Lead glass with a large number of square pores,  $\sim 83 \mu\text{m}$  pore width and  $\sim 16 \mu\text{m}$  wall thickness, giving an open area ratio of 70%. The stopping power of Pb in the glass over the large number of walls that off-axis photons need to cross is effective in collimating X-rays below 30 keV. At the back side of each module there will be a radiator (for the passive cooling of the detector) and a shield will be applied to reduce the background. An exploded view of the module is shown in Figure 4-1.

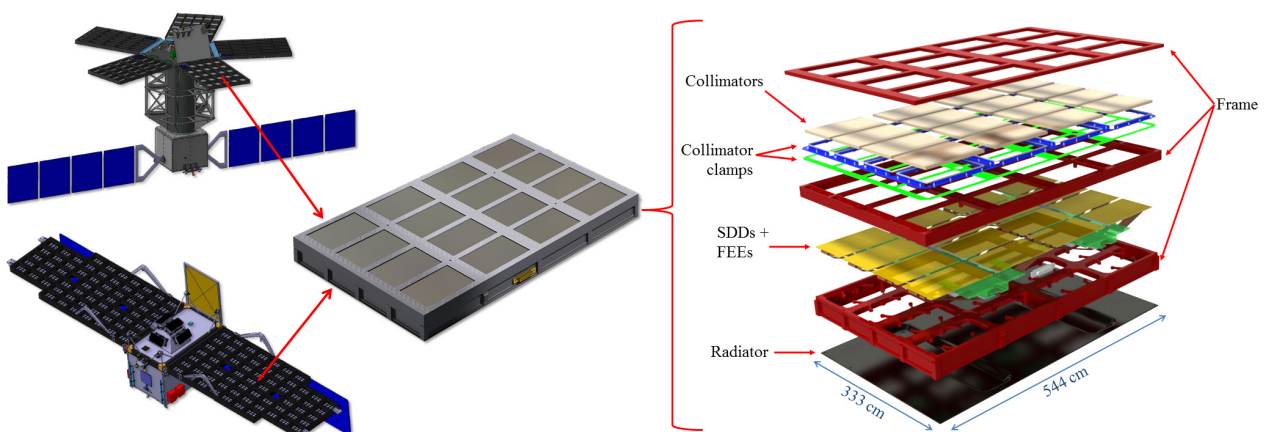


Figure 4-1 LAD design: each panel (left) supports a number of modules (shown in the middle). Each module (right) is a composite of a detector tray holding 4 x 4 detector together with the front end electronics and Module Back End Electronics, Power Supply Unit and the relevant supporting structure and shielding. The top part is the collimator tray which holds 16 co-aligned collimators.

As is shown each module contains:

- A collimator tray containing 16 co-aligned MPC tiles (one per SDD). Each MPC tile has an aluminium film ( $\sim 80 \text{ nm}$ ) deposited on the top surface to reflect sunlight, needed to keep the module temperature below  $-10^\circ\text{C}$  irrespective of the pointing.
- Between the collimator tray and the detector tray is a thin ( $\sim 1 \mu\text{m}$ ) Kapton film, coated with  $\sim 40 \text{ nm}$  Al (similar and same manufacturer as the filter flying on Chandra). This filters out UV light, while having good transmission for X-rays of  $> \sim 1\text{-}2 \text{ keV}$ .
- A detector tray containing 16 SDDs and Front End Electronics. Each SDD has 224 anodes. Each FEE has 14 ASICs, to read out the signals from the anodes. The ASICs amplify and digitise the anode charge pulses resulting from X-ray events ( $650 \mu\text{W}$  per channel,  $17e^-$  rms per read-out channel). A schematic drawing derived from the detailed CAD design is shown in Figure 4-2.
- A Power Supply Unit (PSU) converting the supply power (28V) to a Low (3.3V), Medium (100V) and High (1.3 kV) voltages. The latter two are needed to bias the SDD and ensure a proper electrical field in the direction of the charge collecting anodes.

- The Module Back End Electronics (MBEE) which controls the detectors, the ASICs and PSU, and reads out the digitised events. It formats and time-stamps each event and transmits it to the Panel Back End Electronic (PBEE).
- A Pb back-shield, to reduce the background events in the SDDs.
- A radiator to dissipate heat from the module (lower SDD temperature improves the energy resolution).

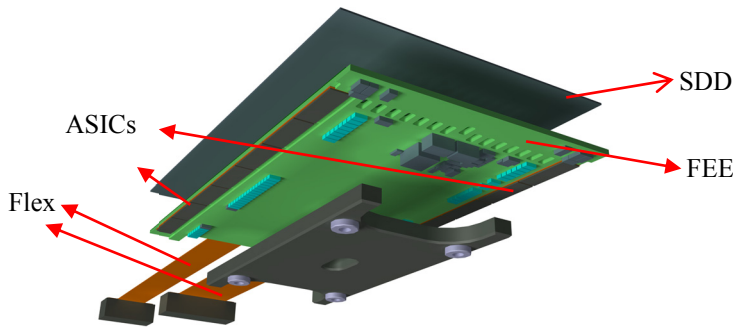


Figure 4-2 Simplified schematic drawing derived from the detailed CAD design of the detector and its front end electronics. The SDD is shown at the top and is glued to a FEE-PCB. This PCB holds the 14 ASICs which are bonded directly to the SDD anodes. Also seen are two flexible leads (power and signals) to the MBEE.

Twenty-five (one satellite design) or 31 modules (other satellite design) are controlled by a single Panel Back End Electronics (PBEE) which is located near the modules (so there will be 5 or 4 PBEEs depending on the S/C design). The PBEE sends commands to the MBEEs, and distributes the clocks and power to the modules. It receives data (science and HK) from the MBEEs, and sends it on to the ICU, which is mounted on the optical bench. The ICU houses the Data Handling Unit (DHU), mass memory and Power Distribution Units (PDU). The DHU receives the data from the PBEEs, and formats and compresses this data for telemetry. The ICU manages the PBEEs, handles telecommands (TCs), manages instrument mode, and monitors instrument health and performance. The organisation and structure of the LAD is shown in Figure 4-3. Whereas the ICU will be cold redundant, thanks to its modular design no redundancy is needed for the PBEEs and Modules. Of course, the design will be such that there will be no error propagation from detector to MBEE, from MBEE to PBEE and from PBEE to ICU.

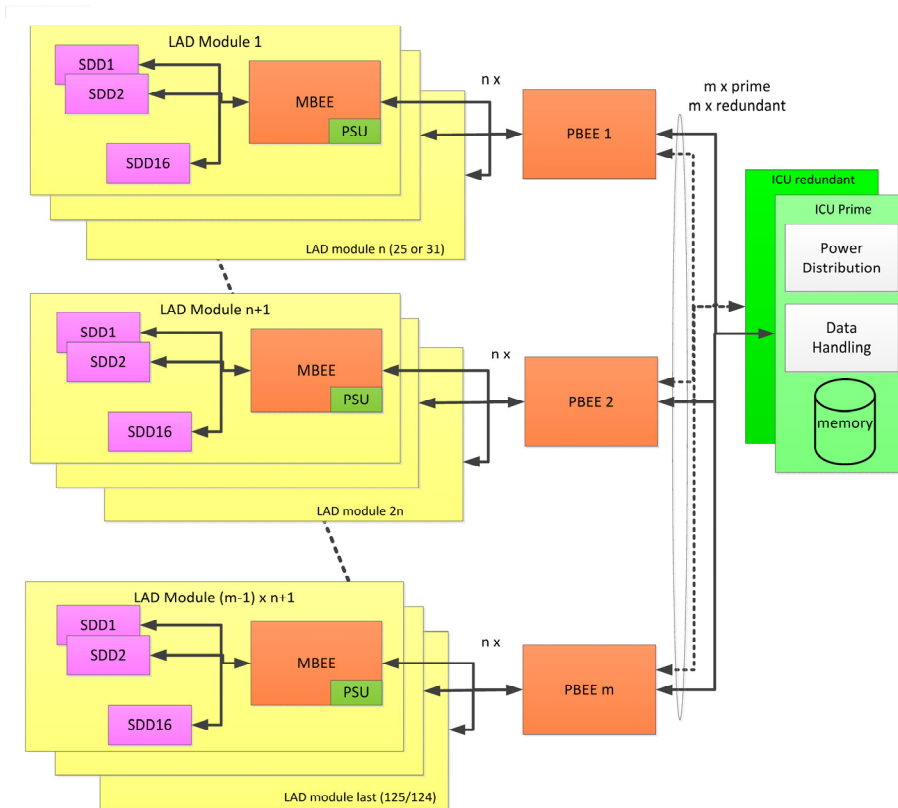


Figure 4-3 Functional breakdown of the LAD. The number of Panel Back End Electronic units depends on the satellite design (4 or 5). Number "m" of lines connecting ICU and PBEEs depend on the spacecraft design.

In addition to the development of the key technology, various prototyping activities have been performed including acoustic tests of a representative filter (see §4.3), mechanical vibration of a collimator tray and the breadboarding of the MBEE (see Figure 4-4) and the PBEE.

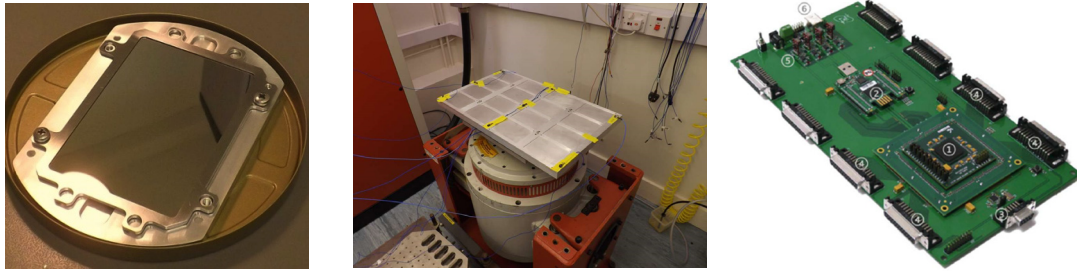


Figure 4-4 Some relevant hardware for the LAD (from left: thermal filter, collimator tray holding 16 collimators on the shaker, the MBEE breadboard)

### 4.1.2 Interfaces and resources

The mass, volume, and power budgets of the current design of the LAD are summarized in Table 4-2. Special attention has been given to the alignment budget as this is split between spacecraft and payload limiting the associated loss of effective area to an acceptable level while not over constraining payload and spacecraft MAIT needs. As the LAD is designed to extract weak timing signals special care has been paid to the effect of vibrations induced by the satellite on the science data as a small jitter in a certain frequency band in pointing of the modules (with a correlated change in effective area) could be incorrectly interpreted as a signal from the source. Detailed analysis has shown that the transfer function between the disturbing elements (e.g. reaction wheels) and the LAD modules is small and also largely out the frequency band for which we are sensitive.

The LAD telemetry budget is almost solely driven by the LAD event-by-event data (24 bits per event). At a source strength equivalent to 500 mCrab this corresponds to 1730 kbps for this data. Adding the scientific rate meters and housekeeping increases this to 1870 kbps. Taking into account a compression factor of 1.77 (verified by software tests; see the IPRR data package) this gives a total rate of 1020 kbps. For stronger sources options for additional rebinning and onboard storage of event data up to 15 Crab for 300 minutes is foreseen. This data can then be transmitted during the following orbits.

Table 4-2: mass, power, size and volume budget for LAD instrument (20% design margins have been assumed for mass and power) and a total of 126 LAD modules and 6 PBEEs is assumed for the totals (from the original M3 proposal). As the industrial designs assume 2 or 5 panels with 4 or 5 PBEE units this number is an upper limit. Harness between units is taken into account in the spacecraft budget.

Item	Mass (incl. margn) [kg]	Power (incl. margin) [W]	Size per unit [mm x mm x mm]	Number of Units	Comment
ICU	18	26.4	300 x 300 x 200	2 (1 cold red)	Unit includes DHU and PDU
PBEE	2.64	5.28	220 x 220 x 100	4(AST) or 5 (TAS)	Properties given for PBEE for 21 Modules Number depending on spacecraft design
Module	7.26	9.90	544 x 333 x 65.5	124 (AST) or 125 (TAS)	Number depending on spacecraft design
<b>TOTAL</b>	<b>967</b>	<b>1305</b>			Upper limit, assumes 126 LAD modules and 6 PBEEs (old consortium reference design)

### 4.1.3 Operations

The Instrument Control Unit (ICU) controls the LAD instrument and interfaces with the satellite. It includes three distinct functional blocks: the data handling unit, the mass memory and the power distribution unit. It will be implemented cold redundant. It will include all necessary functions to operate the instrument:

- Setting the configuration of the instrument (telecommanding, instrument parameters as setting ASICs, voltages etc.).
- Collecting housekeeping data from the instrument (e.g., temperatures, voltages, ..).

- Managing the data streams from all PBEEs and applying the appropriate selections and packetisation of the data according to user specified criteria. The photon data includes the energy, the timing information and some relevant housekeeping data (module id etc.). The energy information is rebinned above 30 keV (as the extended energy range does not require the full spectral accuracy). Whereas in general photon-by-photon data will be transmitted (up to 500 mCrab sustained) additional data reduction can be applied for sources brighter than 500 mCrab.
- Storage of photon data for very bright transients in the mass memory for later transmission to the ground (to handle the 300 minutes of a bright (15 Crab source) this memory will be 210 Gbyte.
- Time information will be received from the satellite (GPS system) and distributed via the PBEEs.
- Performing health checking of the ICU and automated transitions to a safe state if needed.

At the heart of the DHU is the Leon processor, on which the software runs.

#### 4.1.4 Manufacturing, Assembly, Integration and Test

Manufacture, Assembly, Integration and Test (MAIT) has been recognized since the very beginning as challenging for the LAD and all design steps have taken it into account during their optimization. Detailed analysis of the MAIT sequence and the calibrations have been performed in view of the scale of LAD in terms of: i) physical size, ii) number of units, iii) number of participating institutions, and iv) number of geographical locations and transport. At the same time the mission schedule (with a launch in late 2022) requires that the typical production speed for the completion of all 120 - 130 LAD modules is 2 years (hence more than 1 per week). The production, integration, assembly and test sequence has been studied in great detail (see IPRR data pack) and optimized and some precautions have been implemented to reduce any related risks, including flexibility, margins and growth potential at all steps of the MAIT:

- early development of critical technology (accomplishment of TRL 6 is expected already at mission adoption);
- significant early ‘test’ of mass production for the engineering model (a few modules require quite a lot detectors) already a long time before the launch;
- planning with significant margin on capacity (no 24 hours/7 days per week manufacturing thus potential availability of week-end work and/or night shifts to recover from any unexpected problems);
- inclusion of facility down time for holidays and maintenance in the schedule;
- early start of critical element mass production (SDDs and MPCs) thanks to the very advanced and stable module definition;
- first modules will be ready for integration a long time before integration into the S/C, so in case of problems this is kind of a buffer as it allows us to set up additional production lines if needed;
- the following parallel activities will be implemented: FEE manufacture + verification and FEE-ASIC-SDD integration (DPNC); SDDs manufacture and verification, detector tray energy calibration (INFN/INAF); ASICs manufacture and verification (IRAP); Collimator Plate manufacture (ESA), verification and integration with collimator trays (Leicester University); detector tray integration, module construction, module integration, area calibration of the module, PSU manufacture and verification, flight software (all at MSSSL). Implementation of parallel activities for various activities is foreseen and can be enhanced, if needed.
- A large part of the production will be done in industry and their direct involvement already in the Assessment phase in the planning and analysis of capability show that this is feasible based on past experience.
- Implementation of additional scheduling tools including stock management (to ensure that the production flow can continue)
- Comparison with existing instruments (where team members participated) demonstrate that LOFT will not be the first mission handling large volumes and it has been done in shorter time than allocated for LOFT (INFN: Fermi/GLAST, 84 m<sup>2</sup>; DPNC: AMS2, 6.4 m<sup>2</sup>; INAF: AGILE, 3.5 m<sup>2</sup>).

An important aspect is the split of responsibilities between the spacecraft (ESA) and the instrument team. As the panels are also a structural element of the spacecraft this, together with the deployment mechanism, should be part of the spacecraft design. All modules, the MBEE, PBEE and ICUs will be provided fully tested to the spacecraft. Harness, especially those which need to be routed over the panel hinges, will be provided by the

industry as the most critical part of this is the flexibility during deployment of the panels. Mounting of the modules and the alignment from module to module is responsibility of the spacecraft as this is closely related to both the structural and thermal design of the satellite. This resulted in a production-line approach where various activities are pipelined at various partners (industry or institutes). Figure 4-5 shows the flow of the AIT and calibration processes. At the top are the initial components (e.g. collimator tiles, SDDs, MBEEs). Progressing down the diagram, the initial components are assembled into higher levels of integration with relevant test and calibration, culminating in the delivery of the units at the bottom of the diagram. The principal AIT steps (somewhat simplified for brevity) are as follows, with the numbers required for flight.

- A. Integration of tested 1 SDD, 14 ASICs and 1 FEE to produce a detector assembly, tested and delivered for detector tray integration. This is repeated for 2016 detectors.
- B. Integration of 16 detectors, tested 1 MBEEs and 1 PSU into a detector tray, tested and delivered for energy calibration. Repeated for ~126 detector trays.
- C. Energy and deadtime calibration of the detector tray, then delivery for module integration. Repeated for all detector trays.
- D. Integration of 16 verified collimator tiles into a collimator tray, followed by alignment measurements, then delivery for module integration.
- E. Integration of a collimator tray and a detector tray to form a module, followed by full acceptance tests.
- F. Module effective area calibration, then delivery for panel integration.

After this, the units will be delivered and the modules integration on the panels (including the alignment verification) is foreseen at industry level. The instrument team will support this and provide technical support (for the electrical and mechanical integration).

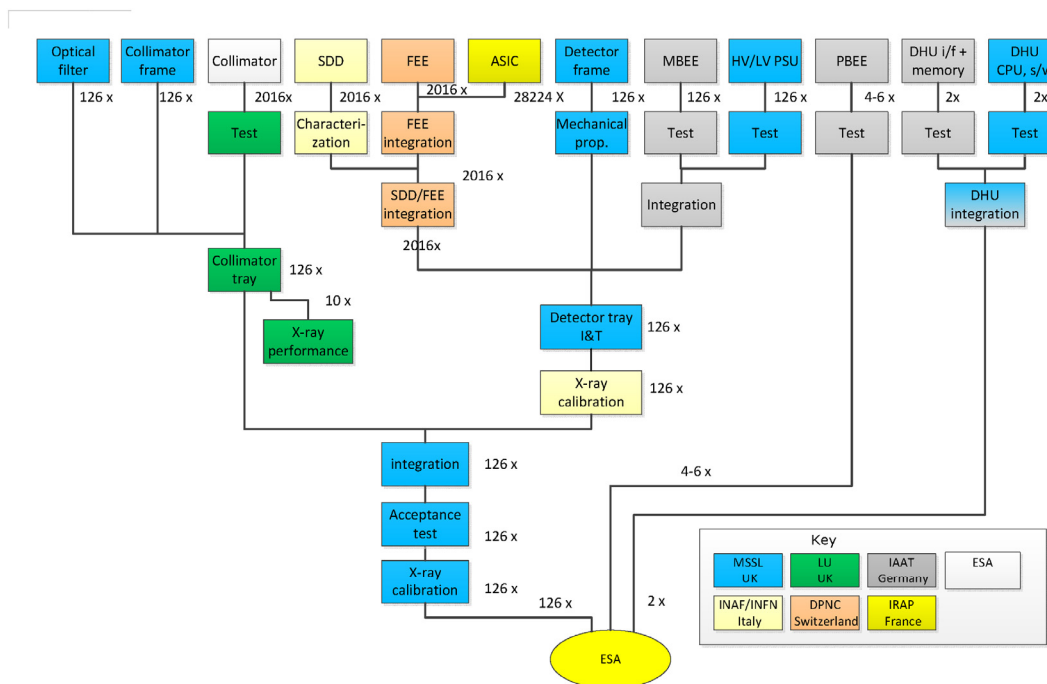


Figure 4-5 Representative integration flow up to the module level including responsible institute and an identification of the typical numbers.

### 4.1.5 Calibrations

The calibration of the instrument is achieved by a combination of ground measurements and inflight calibrations. The ground calibrations include the following steps:

- detector characterization (setting of operational parameters, energy band, linearity and resolution as function of temperature for all individual channels);
- collimator calibration (collimator response as function of energy and incident angle) and the collimator to collimator alignment within a module (using optical metrology);
- effective area calibration (on and off-axis effective area as function of energy);

- dead time using sources and using electronic stimuli.

The ground calibrations will be done in a sequential approach: characterization of the detector once 16 detectors are integrated in a detector tray, the collimator calibration and the collimator to collimator alignment in a collimator tray once these are assembled and the effective area will be done after integration of a full module at module level.

The in-orbit calibration will be used to verify the performance of the LAD on a number of known sources (Crab, Tycho, Cas A). A scan across the source over the field of view will give the relative LAD angular response and thus also the bore-sight with respect to the star tracker, repeated measurements of stable sources (supernova remnants) will provide information about detectors performance changes. For this in-flight calibration about 2% of the net observing time will be required. On top of that, the background as function of orbit and pointing will be calibrated to achieve the 0.25% accuracy in this knowledge. Earlier instruments with a much higher background and background modulation have shown this a not too demanding requirement and the expected accuracy is 0.15%. In addition to specific in-flight calibration activities, simulations show that fluorescence of Pb-L lines (10 keV and 12 keV) from the collimator glass and rear shield will produce detectable lines which can be compared with spectra to verify energy scale on long timescale.

## 4.2 Wide Field Monitor

The Wide Field Monitor is a coded mask camera with solid state-class energy resolution. This is achieved through the use of Silicon Drift Detectors (SDDs) very similar to the LAD detectors. Since these detectors provide accurate positions in one direction, whereas they deliver only gross positional information in the other direction, pairs of two orthogonal cameras are used to obtain precise two dimensional source positions. This is illustrated in Figure 4-6 where the point spread functions of two orthogonal cameras are combined. The effective field of view of one camera pair is about  $70^\circ \times 70^\circ$ . The dimensions of each camera are chosen to match the required sensitivity and the location accuracy. To provide the full required sky coverage, 5 pairs of cameras are foreseen, as shown in Figure 4-6. The key instrument requirements are summarized in Table 4-3 along with the expected performance (see also SciRD).

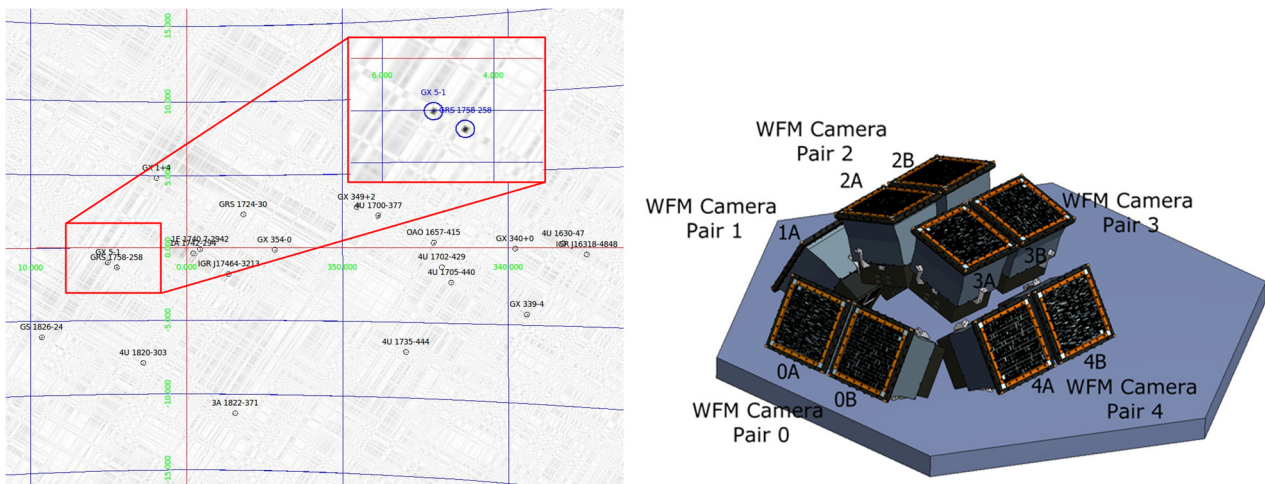


Figure 4-6 left: Simulated WFM pointing in the direction of the Galactic Center. For clarity only a small fraction of the FoV is shown. Right: combination of 5 camera pairs gives the required sky coverage of 4.1 steradian.

Table 4-3 A listing of some of the key WFM scientific requirements

Item	Requirement	Anticipated performance
Location accuracy (2D)	<1 arcmin	<1 arcmin
Angular resolution (2D)	<5 arcmin	<4.3 arcmin
Peak sensitivity in LAD direction (5 $\sigma$ )	1 Crab (1 s) 5 mCrab (50 ks)	0.6 Crab (1s) 2.1 mCrab (50 ks)
Field of view	3.2 steradian around the LAD pointing	5.5 steradian at zero response, 4.1 at 20% of peak camera response
Energy range	2 – 50 keV primary	2 – 50 keV primary
Energy resolution,	500 eV @ 6 keV	< 300 eV @ 6 keV
Energy bands for images	>=8	256
Absolute time calibration	2 $\mu$ sec	1 $\mu$ sec
Availability of triggered WFM data	3 hours	<3 hours
Broadcast of trigger time and position	< 30 sec after the event for 65% of the events	< 25 sec after the event for 65% of the events

### 4.2.1 Instrument Description

The principle of a coded mask camera is shown in Figure 4-7. This type of imager has flown on several past X-ray missions (e.g., BeppoSAX, INTEGRAL). The shadow pattern of the mask cast by a point source uniquely identifies the source position. Multiple sources in the field can be extracted through cross correlation techniques. The 10 identical cameras are composed of a number of components:

- The mask is made of Tungsten (0.15 mm thick) and has an open area of 25% which optimizes the sensitivity for weaker sources. It is supported by a pre-tensioning mechanism. For high imaging quality mask flatness and stability is essential. Past experience and extensive thermo-mechanical studies and tests on a small-scale prototype performed during the study demonstrate compliance with the requirements.
- The collimator which supports the coded mask is a 3 mm thick CFRP grid structure. To shield against background it will be covered by a Tungsten shield (0.15 mm thick). On the outside the collimator will be covered by MLI to improve the thermal stability of the camera.
- The detector tray holds 4 SDDs with ASIC based and the Front End Electronics. The design and functionality of this FEE is very similar to those of the LAD, however position resolution is important here. Therefore the separation (pitch) of the anodes is smaller (145  $\mu$ m compared to 970  $\mu$ m in the LAD), the number of channels per ASIC is higher (64 compared to 16) and the alignment and stability requirements are stringent. Stability is achieved by design and control of the temperature of the detector.
- The large field of view of the WFM make it necessary to protect against micrometeorite impacts. This is achieved by placing a 25  $\mu$ m thick Beryllium window above each SDD.
- The Back End Electronics (BEE) and Power Supply Unit (PSU) are similar to those used in the LAD, again with some exceptions, such as the need for additional computing capability to determine photon positions. The small anode pitch of the WFM SDDs allows a position resolution of <60  $\mu$ m along the direction of the anode row. In the drift direction a position resolution of <8 mm is achieved through analysis of the spread of the charge cloud across a group of anodes (Campana et al. 2011). Although quite moderate, this is important for limiting potential cross talk between multiple sources in the images.
- The electronics is passively cooled through radiation via the back side of the cameras.
- The Instrument Control Unit (cold redundant) will control the instrument, interface with the satellite and perform also the onboard data reduction to identify bright transient sources (see §4.2.3). The ICU controls each of the 10 cameras independently.

The functional breakdown of the WFM assembly is shown in Figure 4-8.

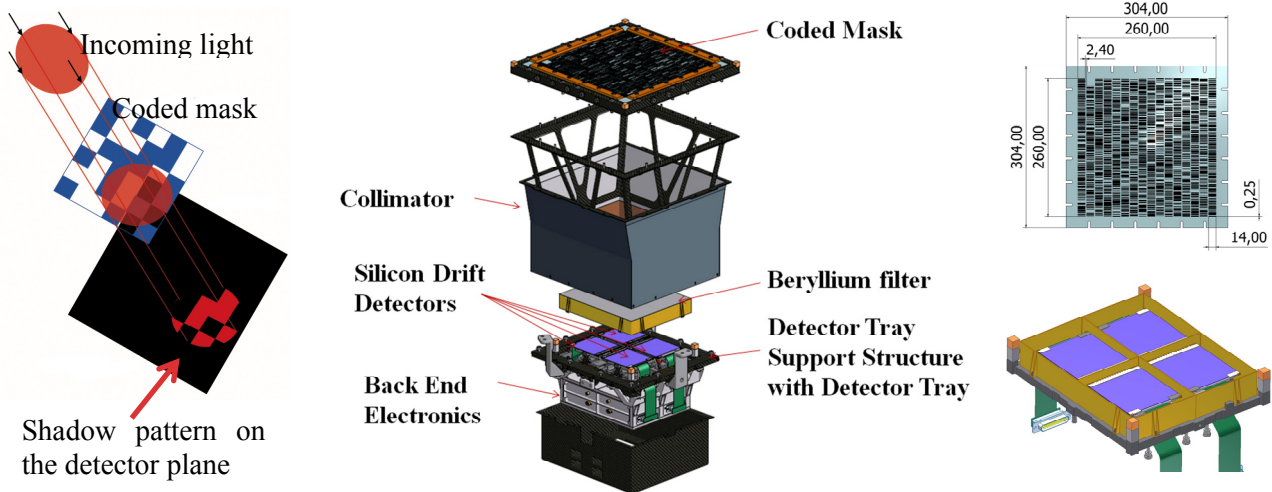


Figure 4-7 Left: the basic working principle of a coded mask camera. Centre: exploded view of a single camera and Right: the mask pattern (top, measures are indicated in mm) and the 4 detectors forming the detection plane.

### 4.2.2 Interfaces and resources

The mass, volume and power budgets of the WFM are summarized in Table 4-4. It is important that the field of view of each camera is not obstructed. The cameras are located in the centre of the optical bench (see Figure 4-6). Another important constraint is the thermal environment. The temperature is controlled by placing the WFMs behind a sunshield and using passive cooling. The temperature of the detectors is controlled, as it is important to maintain the internal alignment of the cameras.

The WFM telemetry budget is limited to an average of 90 kbits/s (~10% of the LAD allocation). The science data will be rebinned and compressed to stay within this limit. Normal WFM science data has 4 components:

- images (2048 x 32 pixels) in 256 energy bands integrated for a nominal 300 s period
- rate meter data with 16 ms resolution
- energy spectra integrated for 30 s
- Photon-by-photon data for 300 s for the relevant cameras, when a burst trigger occurs.

All the above integration times (except for the ratemeters) are tunable in flight by telecommand.

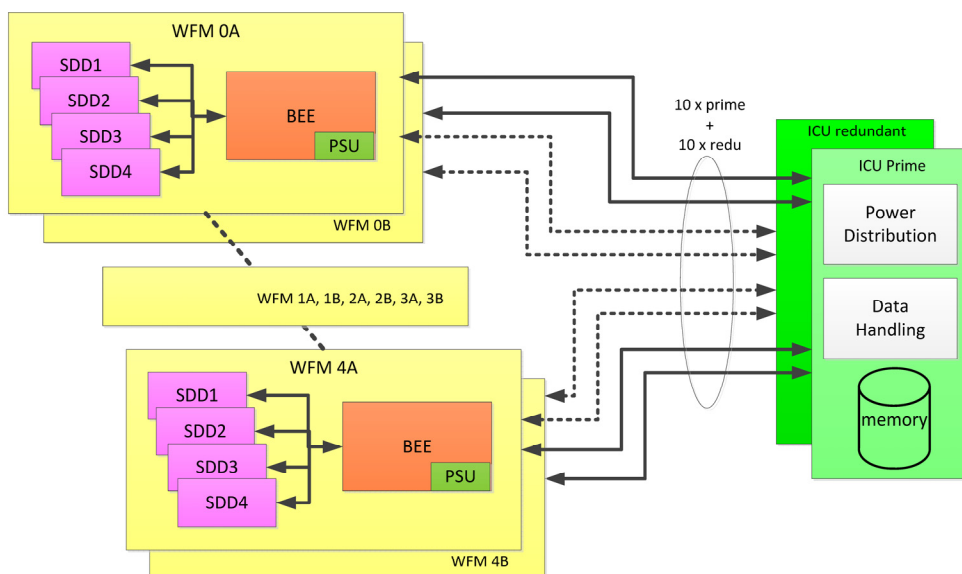


Figure 4-8 Functional breakdown of the WFM. Each camera has its own Back End Electronics and Power Supply unit. Power, control and data are combined in a single harness (one prime and one redundant per camera). For simplicity not all cameras are shown.

Table 4-4 Mass, volume and power budget for the WFM (numbers include 20% design margins).

Item	Mass (incl. margin) [kg]	Power (incl. margin) [W]	Size per unit [mm x mm x mm]	Number of Units	Comment
ICU	4.32 per unit	17.60	308 x 185 x 82	2	Cold redundant
Camera	11.15 per camera	9.07	357 x 345 x 343	10	
Harness ICU-camera	0.247 per camera/ICU	-	1 m nominal length	20	Harness between each camera and ICU
<b>TOTAL</b>	<b>125</b>	<b>108</b>			

The detector images are compressed by encoding the distance between filled pixels. The triggered data will be transmitted in 40 bits per photon. The telemetry rate will depend on the intensity of the X-ray sources in the field of view and the selected number of energy bands. The highest data rate is expected for cameras pointing in the direction of the Galactic Centre. Detailed simulations (see the IPRR data package) show that even in this case the average telemetry rate for images, spectra and rate meter data will normally be below 50 kbits on average with 8 energy bands and about 100 kbits/s for 256 energy bands. The LOFT telemetry is organized with the flexibility to allocate any temporarily available bandwidth to WFM data. This will be used to transmit the event-by-event data of the most interesting WFM unit(s) (based on their pointing direction) during, for example, long LAD observations of dim AGN sources.

The ICU will employ an onboard capability of locating transient events in real time, in particular gamma ray bursts, with ~1 arcmin accuracy. The time and location of the transient can be transmitted to ground using the spacecraft onboard VHF system in a message of ~1 kbits. The design of this subsystem benefits of the heritage of the SVOM mission concept, as well as past team experience on similar systems on BeppoSAX, HETE-2, AGILE.

### 4.2.3 Operations

The Instrument Control Unit controls the WFM instrument and the interfaces with the satellite. It includes three distinct functional blocks: the power distribution unit, the mass memory and the Data Handling Unit. The ICU will be cold redundant. The DHU performs the routine activities:

- Setting the configuration of the instrument (telecommanding, setting ASICs, voltages and controlling the onboard data processing steps).
- Managing the mass memory
- Collecting housekeeping data from the instrument
- Performing health checking of the ICU and automated transitions to a safe state, if needed.

In addition a number of instrument specific functions will be implemented:

- Controlling the temperature of the SDD detector plane
- Produce detector images in predefined energy bands, detector energy spectra, and rate meter data for predefined integration times and perform lossless compression of data for transmission to ground
- Store photon-by-photon data for transmission to the ground in case of a burst trigger (or if excess telemetry band width is available)
- Detect transient events in the WFM images. Relevant information (position and time) will be sent to the satellite onboard data handling unit for transmission to the ground using the VHF system. To avoid unwanted triggers the onboard software will have knowledge about the pointing, the position of the Earth and known sources. With this information known sources (e.g., coming out of the Earth shadow) can be filtered out.

The convolution of coded mask detector images into sky images by fast Fourier transform (FFT) is quite demanding. Therefore at the heart of the DHU is a powerful VIRTEX-5 processor.

## 4.2.4 Manufacturing, Assembly, Integration and Test

The manufacturing, assembly, integration and test of the WFM is less demanding in terms of schedules compared to the LAD, as the numbers of units, SDDs and ASICs are by far much smaller. By timely production of these components it is not expected that the schedule will be depending on their availability. The overall assembly, integration and test procedure will be:

- Integration of 1 SDD, 14 ASICs and 1 FEE to produce a detector assembly
- Integration of 4 detector assemblies with the BEE and PSU in a detector tray
- Calibration and characterization of a detector tray
- Integration of the detector tray with the collimator and coded mask. During this phase also the Be protective windows and the MLI will be mounted.
- Acceptance testing of the camera and checking of the proper interfacing with the ICU
- Calibration at the camera level

These activities have been distributed over the different partners in the WFM team, which implies that the team can work simultaneously on subsystems and cameras in various states of completion.

## 4.2.5 Calibration

The calibration of the instrument is performed at different levels:

- the detector characterization (setting of operational parameters such as thresholds and pedestals and determination of energy resolution, linearity, position resolution map as a function of temperature);
- verifying the performance of an integrated camera by illuminating the full camera by a near-parallel X-ray beam at different off-axis angles;
- a final check-out with X-ray sources will be performed after integration of the spacecraft (but the alignment of the individual cameras is not critical, as this will be done in space).

In orbit the calibration will be verified by the observation of known X-ray sources in different positions of the wide field of view. The field of view of the cameras partly overlap, allowing for a proper camera-to-camera cross calibration. The 4 centrally placed cameras will have the source being observed by the LAD in their fully illuminated fields of view ( $\sim 15^\circ$  off axis in each camera), which provides for excellent cross calibration. Normal WFM observation of known X-ray sources will provide calibrations of the source localization accuracy, as the positions of most of these sources are known within  $\sim 1$  arcsec. Secondary lines from the collimator (Cu, Mo and W) allow verifying the energy resolution and energy scale of the WFM cameras at all times.

## 4.3 Key technology

In this section we briefly overview the key technologies of the LOFT mission: Silicon Drift Detectors, read-out ASICs, capillary plate collimators. An extensive description of the devices, their status and technical documentation about their qualification and TRL are provided in the IPRR data package.

### 4.3.1 Silicon Drift Detectors

The detectors for the LAD and WFM are large-area Silicon Drift Detectors (Vacchi et al. 1991; Rashevsky et al. 2001): the charge generated by the absorption of an X-ray photon is collected in the middle plane of the detector (thickness is  $450 \mu\text{m}$ ) and then drifted towards the read-out anodes at the edge of the detector by an electric field sustained through a series of cathodes on both faces of the detector. While drifting to the anodes, the charge cloud widens due to diffusion. The size of the cloud (which is basically energy-independent) reaching the anodes depends on the absorption point. For LOFT typical parameters (drift field 1300 V) the charge cloud reaches a maximum size of about 1 mm, when the photon is absorbed at the bottom of the 35 mm long drift channel (corresponding to the central line of the Silicon tile). The drift time is about  $7 \mu\text{s}$ . Figure 4-9 illustrates the working principle of the large-area SDDs and a photograph of the LOFT/LAD detector.

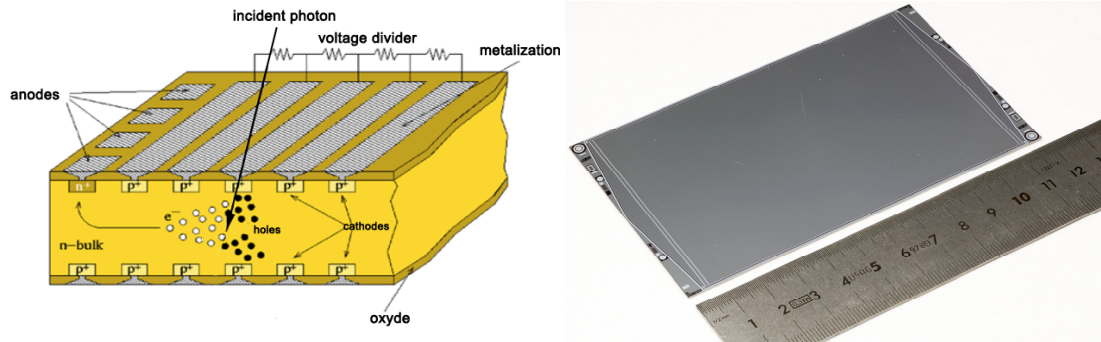


Figure 4-9: Left: working principle of the large-area SDD: charge generated by the absorption of an X-ray photon is collected in the middle plane and side-ways drifted to the read-out anodes Right: The LOFT/LAD detector (full size). The lateral triangular structures identify the built-in voltage divider sustaining the drift of the charge.

When the charge cloud is collected on more than one anode the signal-to-noise worsens, as the same charge has to confront the read-out noise of multiple anodes. On the other hand, it also encodes the distance to the absorption point, enabling a 2D position resolution (fine in the anode direction and gross in the drift direction, e.g., Campana et al. 2011). For a non-imaging application as the LAD a large anode pitch is more favourable: an optimization including all relevant and read-out power parameters, resulted in a 970  $\mu\text{m}$  anode pitch. With this choice,  $\sim 40\%$  of the events are completely read-out on 1 anode (singles, with 200 eV energy resolution) and  $\sim 60\%$  on 2 anodes (doubles, with 260 eV energy resolution) meeting the overall requirement of 240 eV. In the WFM detector a wider charge division enables a higher positional accuracy, at the expenses of a larger noise and read-out power. A 145  $\mu\text{m}$  anode pitch was selected. The size of the detector for the LAD optimizes the ratio between the active and geometric area (the integrated voltage divider has a fixed size, while the active area is a repetition of the anode pattern) for a 6-inch Si wafer, while keeping the drift length at 35 mm to preserve the heritage of the ALICE detectors. Table 4-5 summarizes and compares the main detector design parameters for the LAD and WFM. The WFM detector is smaller and nearly squared, to optimize imaging.

The LOFT SDDs are based on the detectors for the ALICE/ITS experiment at the LHC at CERN, where 1.4  $\text{m}^2$  of such detectors, designed by INFN, are in operation since 2008. Four versions of SDDs have been produced at FBK, gradually implementing and testing all the different optimizations for LOFT case with the last one reaching the required resolution and the right size (Figure 4-9). This is illustrated in Figure 4-10 where the representative detector is read-out by a dedicated ASIC, VEGA (Ahangarianabhari<sup>3</sup> et al. 2013), developed by Polytechnic of Milan and Univ. of Pavia on the heritage of the StarX32 project. The low-noise and the low power consumption of VEGA allowed us to essentially demonstrate already the required energy resolution for the LAD detector, in a configuration similar to its final implementation (Figure 4-10). Due to a known higher leakage current of these first FBK prototypes, demonstration of the 200 eV FWHM energy resolution by X-ray tests was achieved by lowering the operating temperature to simulate the nominal EoL requirement. The LAD full-scale detector prototypes show already a leakage current of  $\sim 0.09 \text{ nA/cm}^2$ . This value is  $\sim 40\%$  better than the required  $0.14 \text{ nA/cm}^2$ . All key detector design requirements for the LAD are then already demonstrated.

Table 4-5 Major differences between the LAD and WFM detector (thickness, drift length, and drift field are equal)

Parameter	LAD	WFM
Active Area	108.5 mm X 70.0 mm	65.1 mm X 70.0 mm
Anode Pitch	970 $\mu\text{m}$	145 $\mu\text{m}$
Number of anodes	2 x 112	2 x 448
Anode capacitance	350 fF	85 fF

<sup>3</sup> This paper has been submitted for publication. A copy of the submitted version can be retrieved at: [http://www.isdc.unige.ch/loft/DOCS/publ/VEGA\\_FINAL.pdf](http://www.isdc.unige.ch/loft/DOCS/publ/VEGA_FINAL.pdf)

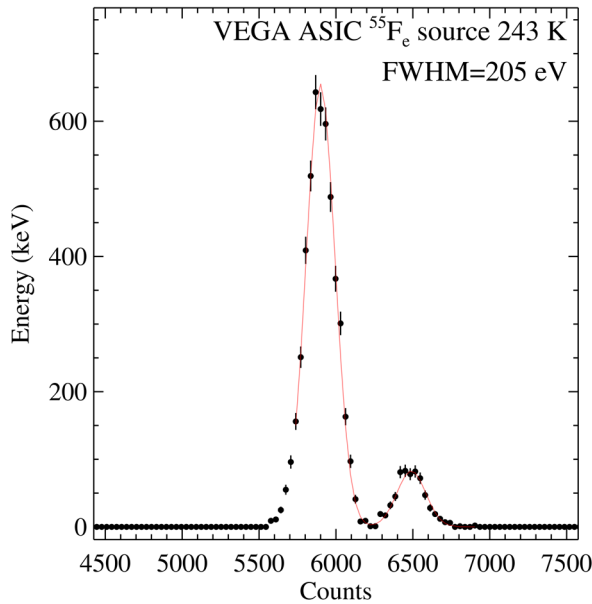


Figure 4-10 Energy spectrum (single events) of a  $Fe^{55}$  radioactive source (lines 5.9 and 6.4 keV) obtained with the FBK detector (3<sup>rd</sup> run) at -30 °C, read-out with the VEGA ASIC breadboard. Energy resolution (FWHM) is about 205 eV, with a detector leakage current of 5-6 pA/anode, close to the 7 pA/anode end-of-life requirement for LAD.

As discussed in §5.2.1 the LOFT orbit was selected to minimize the radiation damage to the detectors and allow for the highest operating temperature. Extensive radiation tests were carried out on the SDD detectors using soft (200 keV and 800 keV) and hard (10 MeV and 50 MeV) protons. The four proton irradiation test campaigns confirmed the radiation damage (Total Ionizing Dose, Non Ionizing Energy Losses, Charge Collection Efficiency) predicted by the models and fully qualified the detectors for their operation in a space radiation environment. Considering the large exposed area of the LAD it is expected that approximately ~10 debris/micro-meteorites will directly impact on the SDDs over 5 years of operation in orbit. Detailed tests show that the damage is actually an increase of leakage current limited to the specific anode which is a negligible loss of area at end-of-life. Due to larger field of view, the WFM would suffer a higher impact rate and anodes loss. For this reason a Beryllium shield was included in the design. This reduces the impact rate on the SDDs to virtually zero.

*The current Technology Readiness Level estimated for the LOFT SDDs is 4-5, planned to reach 5 before the end of 2014 and TRL 6 before mission adoption.*

### 4.3.2 Low noise ASICs for readout

The front-end read-out of the LAD and WFM detectors will be based on mixed-signal ASIC technology. As the LAD and WFM uses the same type of detector, the ASIC design is the same, with the only differences being related to the different anode pitch, and consequently stray capacitance and leakage current. Adapting the LAD ASIC pre-amplifier to the lower leakage current and capacitance of the smaller WFM anodes allows to directly meet the noise requirements. The key specifications of the LOFT ASICs are summarized in Table 4-6.

Table 4-6: main differences in the ASICs for LAD and WFM (all other parameters such as operating temperature, shaping time, thresholds, ADC resolution and deadtime being equal)

	LAD	WFM
Max power consumption	0.65 mW/channel	0.72 mW/channel
Detector pitch	970 μm	145 μm
Assumed SDD leakage current (EoL)	7 pA	3 pA
Assumed input capacitance	350 fF	80 fF
Noise (rms, EoL) at 7 pA	17 e <sup>-</sup>	13 e <sup>-</sup>
Number of channels	16	64

The complexity in the ASIC requirements comes mostly from the combination of low-noise and low-power, on a mixed-signal ASIC. The number of channels and pitch are also lower when compared to ASIC equipping past experiments.

The ASIC for LOFT has an outstanding heritage from the ESA StarX32 ASIC project offering a mixed-signal ASIC with about 18-19  $e^-$  rms noise (no detector) and 500  $\mu$ W/channel power consumption in a 1024-channel matrix. R&D activities in Italy starting from this ASIC were the basis for the development of the VEGA ASIC used in the tests reported in §4.3.1, showing a 17-18  $e^-$  rms noise (with detector), with 0.4 mW/channel. This demonstrates the feasibility of these ASIC requirements.

The ASIC for LOFT is a new development carried out by Dolphin Integration<sup>4</sup>. The *Sirius* ASIC development was kicked-off on May 2012. The first prototype, aimed at demonstrating the most critical parameters (low-noise and low-power on the analogue section), is an 8-channel device, with 4 channels with 145  $\mu$ m pitch and 4 channels with 970  $\mu$ m pitch. Each channel includes the key analogue functions: charge pre-amplifier, shaper amplifier, peak detection & hold, with their associated electronics and test input. The shaper has a RC-CR<sup>2</sup> type, with selectable shaping time between 1 and 4  $\mu$ s. The ASIC is implemented using TSMC MS/RF 0.18  $\mu$ m CMOS technology. The performance of the *Sirius* V1 prototype is already not far from the LOFT requirements. Figure 4-11 shows the noise performance as a function of temperature, with no detector load, and the power consumption is also as expected. The design of the second prototype *Sirius* V2 was completed in October 2013 and submitted to the foundry for production. The first samples are expected by January 2014. V2 has a full layout of 16 channels (it will enable a full performance test with X-rays) and implements all digital functions, including the built-in A/D converter.

The current schedule for V2 includes radiation tests (dose, latch-up, SEU), *reaching TRL 5 before the end of 2014 and allowing the LAD Module and WFM detection plane to reach TRL 6 before mission adoption (end-2015)*.

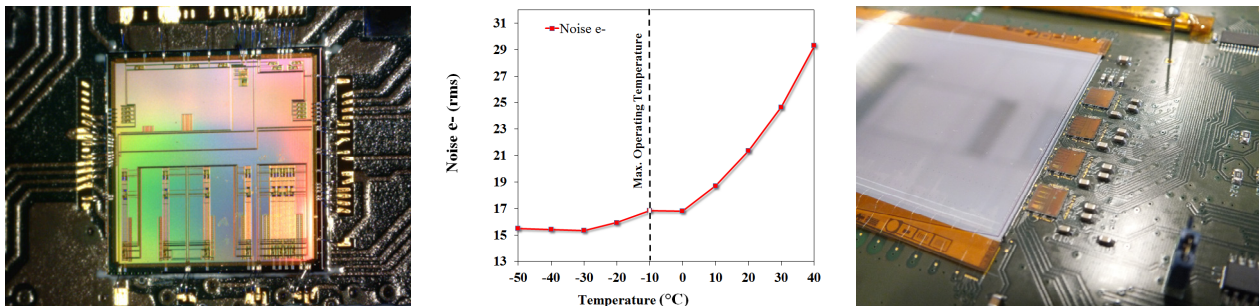


Figure 4-11 ASIC development for LOFT. Left the *Sirius* ASIC V1, middle the performance as function of temperature and right bonded to the SDD prototype.

### 4.3.3 LAD collimator

The collimator technology selected for LOFT is the Lead-glass capillary plate (CP), based on the mature and proven technology of micro-channel plates (MCPs). The Lead content offers sufficient stopping power for X-rays up to  $\sim$ 30 keV, while the 83  $\mu$ m pore size allows a compact and light design. The main requirements are: (a) the field of view of 1°, determined by the pore size and plate thickness (b) the shielding for X-rays up to 30 keV to reduce the background (c) the open area ratio of 70% to guarantee the effective area of the experiment (d) the 1-arcmin pore-to-pore alignment, also to guarantee the effective area and (e) the reduced volume (5 mm thick) and mass ( $\sim$ 6 kg/m<sup>2</sup>). The key parameters for the LAD collimator are reported in Table 4-7. The baseline manufacturer is Photonis<sup>5</sup> which has recently completed the MCP for the BepiColombo mission (MIXS instrument) using the same technology, under the responsibility of Leicester University, as for LOFT. CP collimators were successfully flown already on the ESA EXOSAT mission (1980's) and large-area

<sup>4</sup> Dolphin (Grenoble, France, <http://www.dolphin.fr>).

<sup>5</sup> Photonis (Brive, France, <http://www.photonis.com/en/ism/21-microchannel-plate.html>).

MCPs are flying on Chandra (size larger than required for LOFT and also produced by Photonis). A large-area LOFT CP prototype has been manufactured by Photonis and tested at the University of Leicester.

Table 4-7: the LOFT collimator specifications, as compared to BepiColombo/MIXS and the specific LOFT collimator prototype developed for the Consortium. All types use the same substrate (Lead glass, Philips 3502, and have the same pore-to-pore alignment (1 arcmin) and pore to surface alignment (1 arcmin). Manufacturer is Photonis in all three cases.

Item	LOFT Requirement	BepiColombo/MIXS	LOFT Prototype
Unit size	111.0 mm x 72.5 mm	40 mm x 40 mm	50 mm x 50 mm
Thickness	5 mm	0.8-2.5 mm	6 mm
Aspect ratio	60:1	55:1	60:1
Pore size	83 $\mu\text{m}$ , squared	20 $\mu\text{m}$ , squared	100 $\mu\text{m}$ , squared
Wall thickness	16 $\mu\text{m}$	6 $\mu\text{m}$	15 $\mu\text{m}$
Open Area Ratio	70%	60%	60%
Number Units	2016 (total, flight units)	40 (total, flight units)	2

The details of the LOFT CP prototype are displayed in Figure 4-12. The magnified picture nicely shows the accuracy of the pore geometry, while the picture at smaller magnification shows the boundary between multi-fibre stacks. As the LAD is a collimated instrument, as long as the stacking is not perfect but co-aligned, the structures seen at the junction corners of the multi-fibres only negligibly affect the Open Area Ratio (indeed, the alignment demonstrated for BepiColombo directly satisfies the LAD requirement as well).

Currently an ESA program is running at Photonis to produce a prototype collimator meeting all the requirements. *The Technology Readiness Level for the LOFT collimators is currently estimated 4-5, planned to reach 5 early-2015 and TRL 6 before mission adoption (end-2015).*

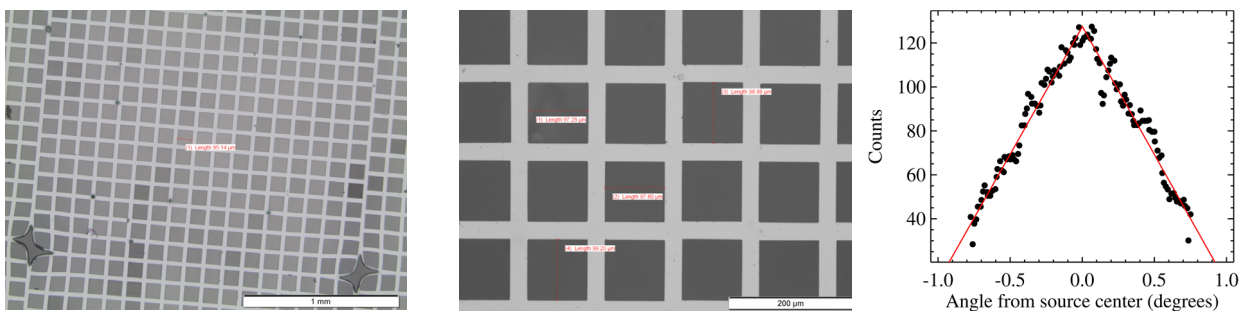


Figure 4-12 Left and middle: collimator produced at Photonis shown with different magnification. Right: Measured response to 22 keV photons of the LAD CP prototype (6 mm thick, 100 $\mu\text{m}$  pore).

## 5 Mission design

In this section we describe the mission design including the payload and service modules, the orbit and the resources. Details about the ground segment are given in §6.

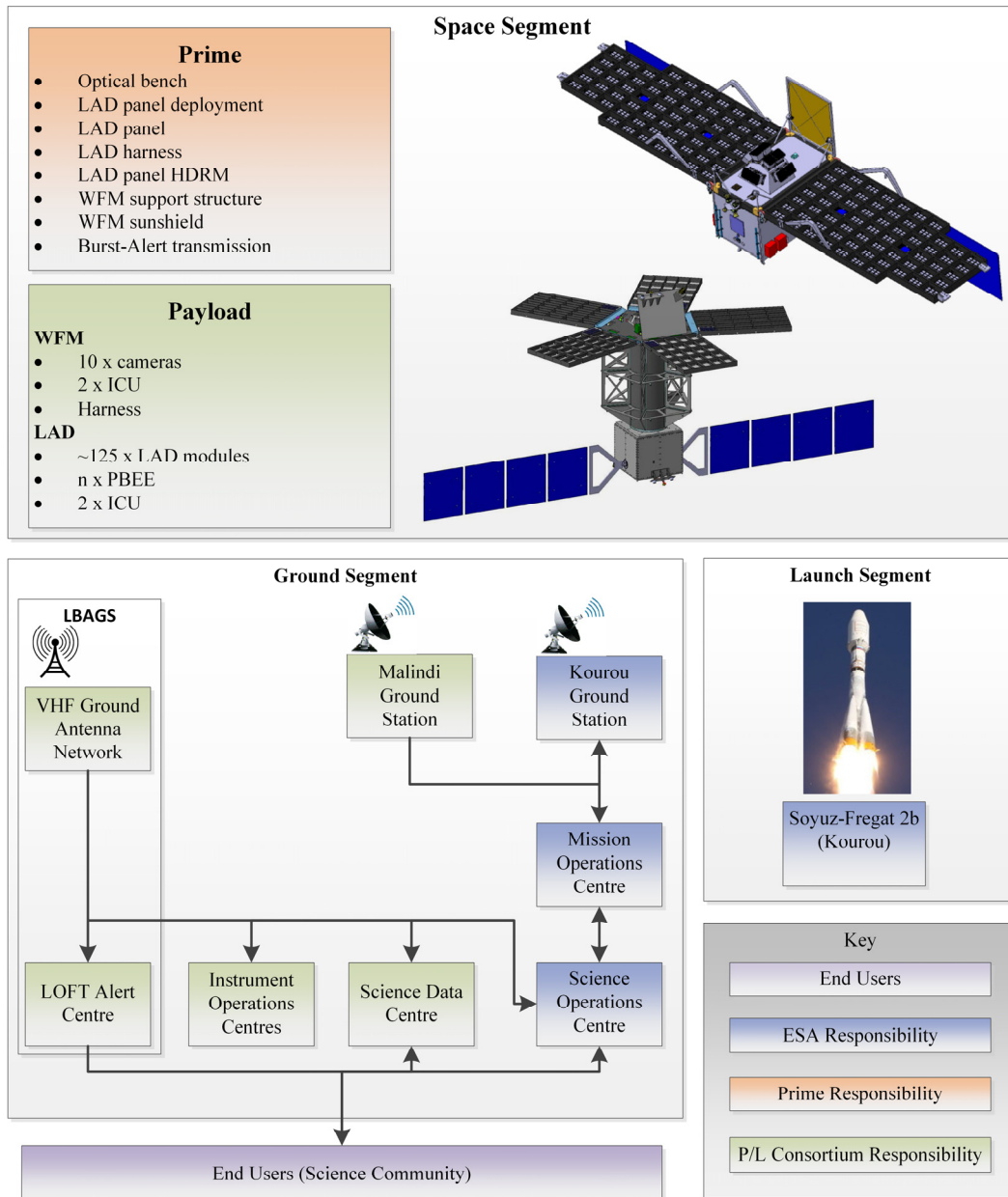


Figure 5-1 Overview of the mission architecture including responsibilities

### 5.1 Overview

An overview of the mission is shown in Figure 5-1 where we show the space segment, the ground segment and the launcher. Also indicated in this figure is the prime responsibility for each component. Already clear in this figure is that there are two different realizations for the satellite by the two industrial teams.

## 5.2 Orbit and Launcher

### 5.2.1 Orbit

#### *Orbit selection*

LOFT will be placed in to an equatorial Low Earth Orbit (LEO), with an inclination  $<2.5^\circ$  and altitude 550 km. This orbit has been selected to minimise the radiation dose (and subsequent NIEL damage), to the SDDs, allowing them to be operated at temperatures which are compatible with passive thermal control ( $-10^\circ\text{C}$  at the end of the nominal mission), while maintaining the required energy resolution performance of the instruments (the LAD energy resolution of 240 eV FWHM being the most driving requirement).

This orbit provides near-complete shielding of the Spacecraft (SC) by the geomagnetic field against solar particle events and cosmic rays – damage to the SDDs is then dominated by contributions from trapped proton populations due to (i) the van Allen belts and (ii) charge-exchange (Petrov) soft protons<sup>6</sup>. The low altitude and inclination serve to minimise the trapped charged particles in the van Allen belts as seen by the SC, avoiding especially the South Atlantic Anomaly (Figure 3-6). Petrov protons reside at equatorial latitudes, but their flux is highly directional (with maximum flux encountered at  $90^\circ$  to the local magnetic field vector), and they are soft ( $<\text{few MeV}$ .) Accordingly, when the FoV and pointing profile of the instruments is taken into account, the Petrov contribution to the total dose of the instrument SDDs is insignificant compared to the reduction in van Allen protons obtained by selecting a low altitude/inclination. Consequently, the effects of radiation damage to the SDDs are minimised.

A thorough study of the populations and effects of these two sources of trapped protons has been conducted during the assessment phase (by the Payload Consortium, industry and ESA) using AP8/AP9 and Petrov radiation models (including comparison with previous missions in LEO, e.g. BeppoSAX). In combination with analytical and experimental investigation to determine the leakage noise increase of the SDD due to radiation damage, this has demonstrated that the required energy resolution is achievable at the end of mission with temperatures of the SDDs using passive cooling only.

#### *Orbit maintenance*

At 550 km altitude there is a significant residual atmosphere, with significant variations in density driven mainly by UV solar radiation. This residual atmosphere will exert drag force on the SC over time, reducing the orbital altitude if left uncompensated. Accordingly periodic discrete orbit maintenance manoeuvres are required to maintain the SC altitude throughout the mission. The required  $\Delta V$  over the mission will strongly depend on the altitude control band selected (e.g. 20 km between 550-530 km), the SC cross-section presented to the velocity direction (a function of the SC geometry and observation plan), and the level of solar activity (represented in proxy by F10.7 or sunspot indices). Analysis using conservative assumptions, particularly on solar activity and hence atmospheric density, has demonstrated that up to 2-3 manoeuvres will be required per year of operations, for a total  $\Delta V$  over the mission duration of  $<100$  m/s.

#### *Controlled de-orbiting*

Given the mass and composition of the LOFT SC, and the launch date and orbit, analysis performed early in the assessment phase demonstrated that an uncontrolled re-entry would pose an unacceptably high risk (to be no higher than 1:10,000 probability of a casualty in order to comply with ESA regulations). Accordingly it is necessary for the SC to perform a controlled de-orbit at end-of-life. This requires an additional  $\Delta V$  of up to  $\sim 150$  m/s for the controlled de-orbit, which will be separated into several discrete manoeuvres in order to limit gravity losses and constrain the required thrust capability.

### 5.2.2 Launcher

The performance of the Soyuz-Fregat launch vehicle (from Kourou) to the chosen orbit is considerable (over 6000 kg, taking into account ESA margin policy of 5% reduction in predicted launcher capability). Against this, both industrial SC designs have very large mass margins (the synthesised mass budget in Table 5-1 displaying  $\sim 1$  tonne of spare launcher capability when all margins are taken into account). In one of the designs

---

<sup>6</sup> A trapped population of soft protons at equatorial latitudes and below the radiation belts.

the volume of the fairing will be the limiting factor although it should be recognized that even in this implementation (Concept B design) the number of LAD modules is 124 whereas 121 are needed to meet the science requirements.

### 5.3 Spacecraft Design

The key aspects of design of the LOFT SC are driven by the accommodation of the LAD (~15 m<sup>2</sup> of geometric area, at least 121 LAD Modules) its absolute temperature (-10°C at EoL to achieve the nominal energy resolution of 240 eV) and thermal stability (significantly relaxed due to a new ASIC design in the instrument), and pointing and availability requirements (1 arcmin class, effective area stability requirements expressed as percentages in the frequency domain).

ESA design activities commenced with a Concurrent Design Facility study in 2011, which refined the Payload Consortium Reference Design with 6 LAD panels, one PBEE per panel and 21 Modules per panel (126 Modules in total). During this time it was determined that due to mass and volumetric constraints, the originally envisaged Vega-launch is not possible.

During the Assessment Phase the reference launch vehicle became the Soyuz-Fregat, and two SC designs were derived under industrial contract, leading to different accommodation concepts of the LAD instrument w.r.t. the number of Panels, number of PBEEs and number of LAD Modules.

- A. Configuration with 5 Panels, 5 PBEEs and 25 Modules per Panel (125 Modules in total - Figure 5-2).
- B. Configuration with 2 Panels, 4 PBEEs (2 per Panel) and 62 Modules per Panel (124 Modules in total - Figure 5-3).

These two quite different industry approaches have been taken in order to prioritise performance features such as available field of regard<sup>7</sup>, thermal performance etc. Nevertheless both industrial designs provide both a realization consistent with requirements, and there is good confidence that a mission profile satisfying the overall science requirements will be achieved.

The SC is divided into a Payload and a Service Module (PLM and SVM). Clearly the SC is dominated by the LAD panels, which by necessity are deployable in order to achieve the accommodation of the required number of modules.

The Wide Field Monitor is housed on top of the PLM (such that the centre of its response is aligned with the LAD bore-sight) on a platform whose plane is parallel with the nominal sun direction, and located behind a dedicated sun shield. The SC section of the Payload Module comprises the structural supports for the LAD and WFM and Payload Data Handling Units, Star Trackers (to minimise AOCS reference frame distortion w.r.t to instruments), and in the case of one design a separate Payload Data Handling Unit (PDHU), which provides services such as mass memory, science data and burst data management, control of payload heaters and distribution of PPS time signals.

---

<sup>7</sup> The LOFT field of regard is the sky area which can be observed with the nominal energy resolution. On top of that there is an extended field of regard with a slightly reduced energy resolution. This allows for more flexible and longer observations of science cases where the energy resolution is not driving the science.



Figure 5-2 View of the LOFT SC concept [A] in the deployed (left) and stowed (right) configuration. This design assumes 5 panels with each 25 modules and one PBEE per panel.

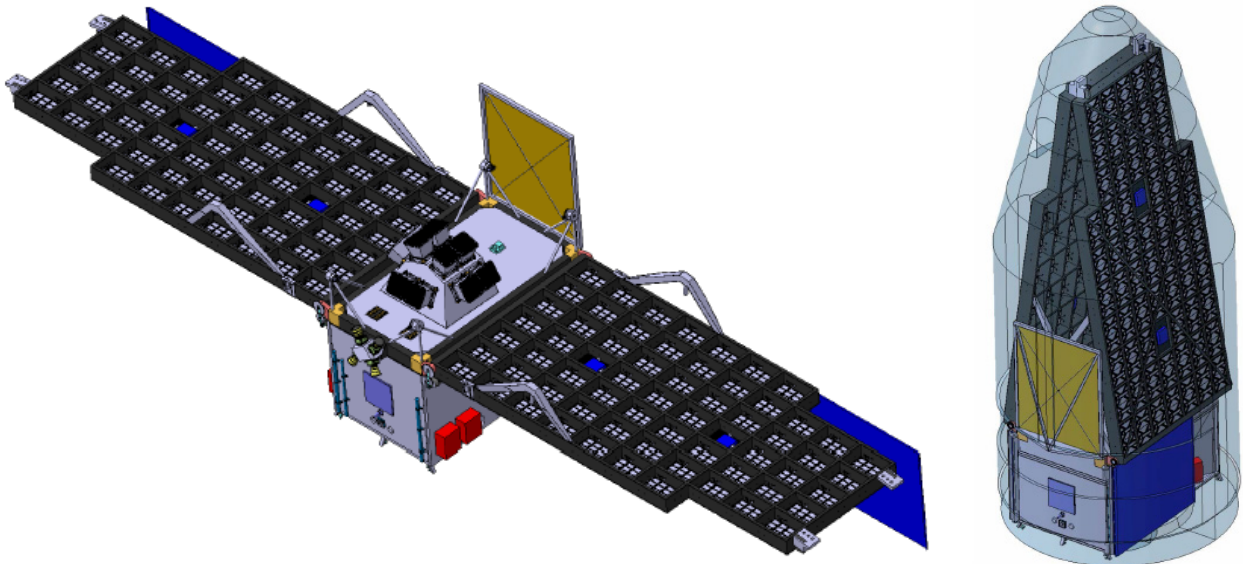


Figure 5-3 View of the LOFT SC concept [B] in the deployed (left) and stowed (right) configuration. This design assumes 2 panels with each 62 modules and two PBEEs per panel

### 5.3.1 Payload Accommodation

The payload modules of the two industrial studies are quite different, showing that the requirements can be achieved in different ways. In this section we will show how the payload is accommodated, focusing on thermo-mechanical aspects. Payload accommodation and SC operation are largely driven by the thermal requirements of the instruments: for both instruments, the SC thermal design and operational profile has to accommodate the variable Earth albedo load around the orbit, widely varying solar loads (as a function of the instantaneous attitude), and internal instrument dissipation. The main element in the strategy to meet these requirements is to restrict the solar flux seen by the instruments.

#### 5.3.1.1 Wide Field Monitor

For the WFM there are two main considerations for the accommodation:

- **Thermal accommodation:** Proper thermal stability of the camera to ensure a stable imaging quality (stability of the coded mask with respect to the detector plane). This has been achieved by locating the WFM behind a sunshield, applying MLI around the camera structure and implementing passive

cooling of the detector. The absolute temperature requirements of the WFM detectors (in support of the instrument energy resolution of 500 eV and 2 keV lower threshold) are quite relaxed and subsequently a secondary consideration.

- **Mechanical accommodation:** A large unobstructed field of view for the WFM which also matches the sky visibility of the LAD. This has been realized by locating the WFM on the top (and in the centre) of the optical bench. The configuration is chosen to match the part of the sky accessible to the LAD (Solar Aspect Angle  $+30^\circ$  to  $-70^\circ$ )

In both SC designs the WFM is housed on top of the PLM (such that the centre of its response is aligned with the LAD bore-sight). It is protected by a sunshield to provide the required thermo-mechanical stability and compliance to operating temperature limits. SC-provided heaters will ensure (non-)operating temperature limits are respected. The WFM cameras can use the rear plate of the Camera or the WFM support structure itself as a radiator, while all other camera external surfaces are covered with MLI. The detector node is provided with a thermal strap to additional radiator area.

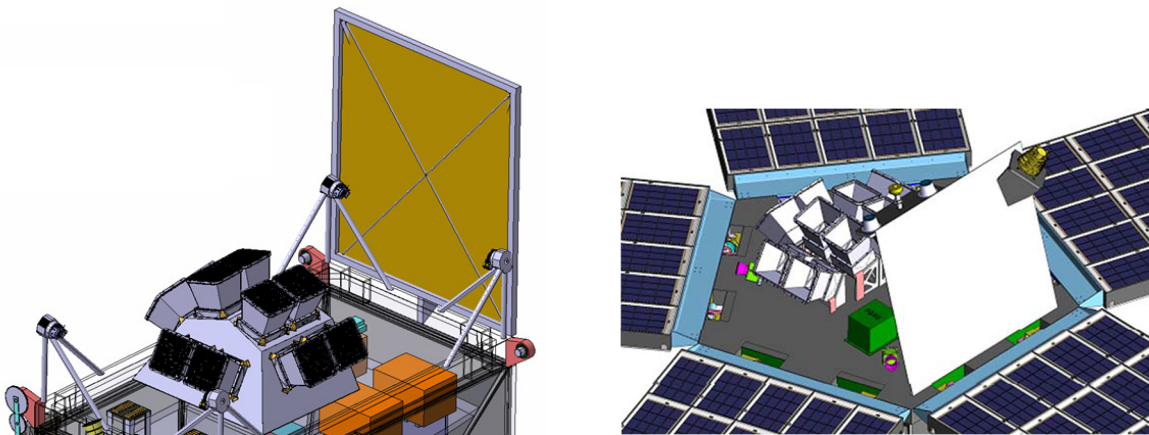


Figure 5-4 In both SC designs, the WFM is accommodated on a dedicated support structure, and behind a sunshield (both SC-provided)

### 5.3.1.2 Large Area Detector

For the LAD there are several considerations for the accommodation:

- **Thermal accommodation:** Control of the LAD drives the mission/SC design, and LAD cooling must be achieved passively (certainly no active cooling can seriously be considered over the large area). The EoL LAD detector temperature requirement of  $-10^\circ\text{C}$ , over the nominal FoR (in support of the 240 eV nominal energy resolution requirement), is the driving requirement that influences the thermal control and mission operations concept. It can be noted that, for some science cases, the energy resolution is not a driver, and an extended Field of Regard (FoR) can be allowed where the temperature may increase to  $+11^\circ\text{C}$ . LAD temperature stability requirements also exist, related to detector ASIC gain and offset stability, but these are quite relaxed and do not drive the design.
- **Mechanical accommodation:**  $>121$  LAD Modules need to be accommodated on the SC, and aligned to 3 arcmin accuracy to restrict losses in effective area due to collimator pore-misalignment. Deployment of the LAD panels is mandatory given the fairing volume constraints.
- **Electrical/Data accommodation:** While the I/F to the platform at the instrument ICU is fairly simple, the routing of the LAD harness over the panel hinge-line and across the panel has to be considered carefully, as does the additional harness required for SC-controlled survival heaters.

The Field of Regard of the LAD constrains the solar flux seen by the LAD modules (§3.1.5). In the Concept B SC design this is taken further by using the structure of the LAD panels (on the front side), and the solar arrays (on the back side), as sunshields which provide full protection from the sunlight during operations throughout the extended FoR. The Concept A industrial design favours local radiator extensions to the LAD Modules to lower their temperature without recourse to shading them from the sunlight.

Analysis has considered LAD solar aspect angles from 30° to -90°, hot cases at End- and Beginning of Life, cold case with 0° SAA on the LAD (for heater sizing), panel stowed configuration and survival mode, worst case transients (hot → cold , cold → hot) and transients due to slewing at eclipse transitions.

Figure 5-5 shows the achievable LAD temperature (predicted orbital average, taking into account modelling uncertainties etc.) as a function of sky fraction, and as a function of LAD detector plane SAA, for both the industrial designs. It can be noted that the Concept B design provides a superior performance (higher sky visibility for a particular LAD equivalent temperature), a consequence of the design concept which shadows the LAD Modules from direct sunlight. The Concept A design also meets the requirements, and both designs provide significantly better detector temperatures over the nominal and extended FoR than the requirements, which are met only at larger angles than required by the FoR; energy resolution performance will typically be significantly better than the requirements.

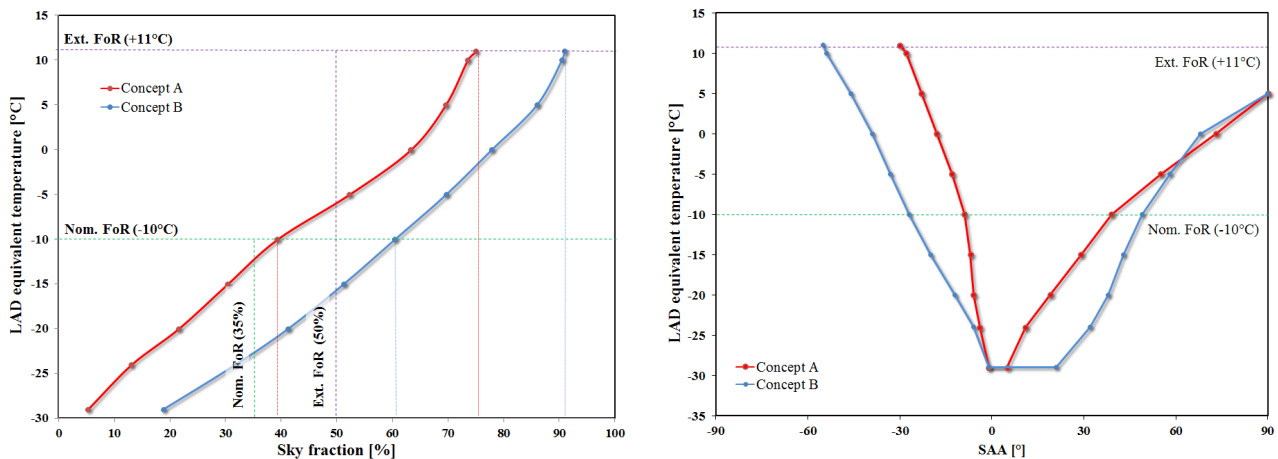


Figure 5-5 Left: achievable LAD equivalent temperature (predicted orbital average) as a function of sky fraction, taking the average of the two SC designs. Indicated are the Nominal and extended Field of Regard requirements and the required temperatures. Right: Achievable LAD equivalent temperature. The SAA=0° is the cold position where the sun illumination of a LAD module is minimal.

The transient analyses have demonstrated that out-of-FoR targets can be accessed for several hours (depending on initial conditions, i.e. the previous attitude) as a consequence of the significant thermal inertia of the LAD instrument – this provides a capability far beyond that originally envisaged (where short-term ~10min observations would occur during eclipse only). In practice this implies that for significant periods of time (~several hours) observations outside the Field of Regard are feasible whilst maintaining nominal energy resolution. This can be exploited to observe interesting transients regardless of their position in the sky (except close to the Sun), or to intelligently include regular out-of-FoR observations in the mission planning. This functionality is complemented by the anti-sun bias in the WFM FoV, provided by the 5<sup>th</sup> Camera pair pointing in the anti-sun direction.

For the deployment, the industry designs consider the use of actuated hinges comprising springs and self-lubricated bearings with deployment speed controlled via viscous damping, or reuse of the Sentinel-1 antenna motor. To ensure final pointing accuracy requirements are met, the panels will be latched, but with a flexible stop to reduce the deployment shock. Full kinematic and dynamic analysis of the deployment has been made, together with detailed reliability analysis. The chosen technologies have high TRL with flight heritage (e.g. METOP, SMOS).

### 5.3.2 Service Module

#### 5.3.2.1 Attitude and Orbit Control System

The Attitude and Orbit Control System (AOCS) sub-system is required to support: Payload pointing (1' class for both instruments) and LAD effective area stability (expressed as RPE in the frequency domain during the assessment) requirements; the required SC agility to comply with the pointing profile of the LAD instrument (as defined by the reference observing plan); provision of *a posteriori* pointing knowledge for subsequent use in analysing instrument data. Most fundamentally the system must accommodate a large satellite inertia, while providing a high observation availability to the LAD instrument.

For sensing, both industrial designs favour 4 STRs, oriented so as to ensure Earth occultation does not interrupt pointing control by affecting all of them simultaneously. The Concept A design also employs a medium-class gyro. Other sensors include 3-axis magnetometers for MTQ control, and RMUs and CSS for coarse control during sun acquisition and safe modes. Two GPS receivers (2 antennae per receiver) provide orbit determination and a high accuracy timing reference for distribution to the instruments.

For actuation, both SC designs will rely on RWs for nominal actuation (maximum momentum 70 Nms, maximum moment 300 mNm), off-loading them continuously using MTQs. Typical observation plans of several weeks have been simulated to size the actuators, accounting for the full range of SC attitudes seen during a typical observing sequence. This analysis demonstrates that RW-control with MTQ-off-load is possible for both designs, despite the poor authority of MTQs in near-equatorial orbits around the relatively constant  $\beta$ -field vector.

The possibility of course exists to dump remaining torques via thruster firings, but the RCS has rather been designed to support LEOP attitude control and Safe Mode events (redundant system, fast rate-damping and Sun acquisition). While no resulting thruster off-loading is expected, an allocation has been made of 5m/s  $\Delta V$ . Assuming a baseline of 4 RW of  $\sim 70$  Nms capacity, it has been demonstrated that very little momentum accumulation occurs, and in the worst case small optimisations of slew manoeuvre timing can be relied on to manage the momentum.

The LAD response stability requirement (expressed as a function of frequency) is critically important in order to avoid convolution of variations in the effective area of the LAD with variations in the source intensity which the instrument measures. These variations in effective area are, in principle, related to the relative pointing of the source in the FoV as the effective area decreases with off-axis angle. Both Concept B and Concept A have performed detailed analysis to assess their compliance to this requirement, employing AOCS models which capture all the salient features which affect this parameter (SC flexible modes, tank sloshing etc). Dynamic analysis of the solar and LAD panel and module resonances confirms that naturally damped resonant frequencies will not affect the pointing jitter on scale more than one order of magnitude below the requirements (e.g.  $\ll 1$  arc second/ $\sqrt{\text{Hz}}$  at 1 Hz).

Overall, both SC designs are compliant to the pointing and agility requirements with good margins.

### 5.3.2.2 Propulsion

The propulsion sub-system is required to support: LEOP and safe mode periods; regular orbital maintenance manoeuvres throughout the mission; safe de-orbiting at the end of life.

Thrust authority (main engine sizing) is not driven by orbital maintenance manoeuvres, which are individually of low magnitude ( $\sim$ few m/s), but rather by the manoeuvre magnitudes during the de-orbiting manoeuvre at end-of-life.  $\sim 100$  N thrust is required in order to limit the gravity-losses and number of manoeuvres to reasonable values, and is provided by multiple smaller units for redundancy. The de-orbit manoeuvre sequence is sized according to the SC dry mass and a strategy for several perigee-lowering burns culminating in eventual re-entry at a perigee-altitude of 40 km over the Pacific Ocean. The total  $\Delta V$  of  $>100$ m/s is the largest single component of the  $\Delta V$  budget and accordingly drives the tank-selection.

Despite the large SC mass, a monopropellant system is preferred for both industrial designs due to better heritage of classical accommodation with easy interfaces, limited sloshing impact on the attitude control (monopropellant tanks with diaphragms have been selected, which are not available in bipropellant systems), as well as reduced cost and complexity.

The industrial designs are therefore fundamentally quite similar, but differ in thruster and tank sizing, and pressurisation strategy. The Concept A design favours (4+4) x 22N to provide thrust and torque control, fed by two large tanks operating in blow-down mode throughout the entire mission. The Concept B SC design favours (6+6) x 1N thrusters for attitude control and (2+2) x 90N-thrusters for orbit control, operating in blow-down with a re-pressurisation towards the end of the mission to improve the thrust at end-of-life for the de-orbit manoeuvre sequence. The overall propellant budget has been sized to  $\sim 500$ kg in both cases.

### 5.3.2.3 *Thermal*

For the Service Module, classical approaches of MLI on external surfaces, heaters for cold case operation and second surface mirrors for radiative panels suffice. Each industry has taken a different thermal design, according to the specific requirements driven by different geometries.

### 5.3.2.4 *Telemetry and telecommanding*

The TT&C sub-system is required to support: Downlink of 6.7 Gbit science and housekeeping data per orbit to the Kourou and Malindi ground stations; uplink of telecommand rates of 64 kbps during contact (occasionally needed to load calibration data to the instruments); ranging during LEOP (nominal operations ranging will be provided by GNSS); VHF transmission for the burst-alert system (LBAS).

X-band frequencies of 7.2 and 8.5 GHz have been selected for up and down-link. The system has been designed for redundancy in both receive and transmit sections, while also accommodating requirements for low power configurations during ranging and low-rate telemetry operations. The SC pointing profile necessitates an omnidirectional transmission, and to provide coverage for two hemispheres, two antennae are required, though for easing launch adapter constraints, three LGA antennae can be proposed. There are high TRLs for all telemetry subsystems.

Link budgets have been calculated for transponder power  $>5$  W, for both ground stations between minimum elevation ( $5^\circ$ ) and  $90^\circ$  elevations over the ground segment horizon. Ground contact time is a minimum of 560s for Kourou, and slightly more for Malindi (combined contact duration per orbit is  $\sim 20$  minutes). There are significant margins demonstrated for a data rate of 8.6 Mbit/second. In case Kourou would not be available (e.g. due to weather conditions) then a whole orbit data downlink can be provided for in a single Malindi pass. The baseline is to make use of 14 passes/day for Malindi and 4 passes/day for Kourou (2 of which also for TC uplink).

Timeliness requirements on WFM data (no more than 2 orbits delay after generation) will be met by transmitting this data ( $\sim 10\%$  of the total bandwidth) during the centre of a pass. For the LBAS, a separate low-power VHF transmission system is proposed, comprising two antennae on the opposite sides of the SC, transmitting to the network of small ground stations distributed around the equator.

### 5.3.2.5 *Power*

The power sub-system is required to support: a power requirement of  $< 2.5$  kW, while accommodating the frequent and deep battery discharge cycles during the eclipse ( $\sim 35$  min every  $\sim 95$  min), requiring another  $\sim 1.5$  kW for battery charging; the LAD panel electronics require  $\sim 50$  V supplies, other payload standard voltages are  $\sim 30$  V while TBD voltages may be required for thermal and other SVM sub-systems. Various trade studies have been performed for: a moveable solar array versus providing a larger array to cover the range of illumination angles associated with the SC pointing profile; regulated or unregulated buses of different voltage; the form of controlling power regulation. There arise no strong arguments for particular solutions, and all are available with good heritage.

For the Concept A design a rotatable array of  $\sim 18\text{m}^2$  has been chosen (the ability to rotate the solar array provides a more optimised sizing to the requirements, and full freedom to point the LAD to out-of-field targets, particularly in the anti-sun direction.) The Concept B design uses a fixed array of  $\sim 20\text{m}^2$  (fixed in order to perform a shadowing function for the underside of the LAD Modules to optimise their temperature, a key feature of the Concept B SC design concept).

An interim preferred choice for the EPS architecture is for 50 V unregulated bus with a derived 30 V supply, and MPPT array regulation. Large margins have been taken for array degradation and cell efficiency, battery depth of discharges, capacity losses and temperatures. Critical areas for the power harnesses have been investigated, and feasible solutions identified for (e.g.) routing to the LAD panels.

### 5.3.2.6 *Data Handling*

The Data-Handling sub-system is required to support: interface to the Payload Data handling, to SVM equipment and the TT&C; transitions between and set-up for the various platform modes; autonomy of the SC through up-linked and stored timelines and FDIR.

The instrument data is stored within the respective payload Instrument Control Units (ICUs), and the SVM DH performs only the telemetry buffering. Similarly the WFM detects and transfers burst alert data to the SVM C&DH via SpaceWire interface, and the SVM C&DH appends any required additional data (TBC) before transferring the data to the VHF transmitter via a MIL standard bus.

Another key science requirement fulfilled by the C&DH is to distribute the time reference. The C&DH On Board Time (OBT) will be synchronised with GPS time and synchronisation pulses. The C&DH then transmits this OBT as well as PPS (Pulse Per Second) synchronisation signal to each instrument unit. Current analysis shows this can be achieved with better than 1µs accuracy, as required. In principle this could be improved with a more direct distribution of the GPS output with additional units or harness components.

### 5.3.3 Spacecraft Resource Budgets

Table 5-1 shows a synthesised overview of the two SC design mass and power budgets, demonstrating a ~4-5 tonne SC (depending on the concept) with all margins (compared to a ~6 tonne launcher capability to the target orbit) and a power demand (including battery-charging) of ~4kW. In view of these margins the differences between the two spacecraft designs are not relevant for the feasibility of the mission.

Table 5-1 Synthesised mass and power budget obtained by comparing technical solutions from both industry studies (the mass capability of Soyuz-Fregat to a 550 km 2.5° inclination orbit is >6000kg before error margins); note that the PLM mass includes payload-support items, and therefore is greater than the sum of the payload masses reported in Table 4-2 and Table 4-4.

	CBE	DMM (%)	DMM (kg)	CBE incl. margin	Watts
<b>Payload Module</b>	<b>1360</b>		<b>354</b>	<b>1632</b>	<b>1423</b>
LAD	806	20	161	967	1305
WFM	104	20	21	125	108
Payload Avionics	10	20	2	12	10
Payload Structure/Mechanisms	440	20	88	528	-
<b>Service Module</b>	<b>1082</b>		<b>172</b>	<b>1254</b>	<b>389</b>
AOCS	100	5	5	105	172
Xband TT&C	25	15	4	29	40
DHU	25	10	3	28	75
Power Subsystem	215	15	32	247	50
Structure	590	20	118	708	-
Thermal	27	20	5	32	50
Propulsion	100	5	5	105	2
<b>Nominal Dry Mass</b>		<b>2886</b>			<b>Nominal Power</b>
<b>System Margin</b>		20%			System Margin
<b>Total Dry Mass</b>		<b>3463</b>			<b>Total Power</b>
<b>Propellant</b>		482			Harness Loss
					PCDU Loss
<b>Total S/C Mass</b>		<b>3945</b>			<b>After Losses</b>
<b>Launch Adapter</b>		125			Battery Charging
<b>Launch Mass</b>		<b>4070 kg</b>			<b>Total Power</b>
					<b>3814</b>

Table 5-2 shows an example LAD availability budget, analysed to assess if the nominal science observing plan can be accommodated within limits of Field of Regard, slewing and other operational losses. Both industrial studies indicate an availability of >60%. Together with the large extended field of regard this enables the core and observatory net observing time requirements of the LAD in ~3 years with a margin of 16%.

Table 5-2 LAD availability budget summarising the items affecting observational efficiency – calculations performed with detailed simulations from observing plan and spacecraft designs.

Observation Loss Item	Duration	Outage	Comment
<b>Earth Occultation</b>		31%	Based on observation plans
<b>South Atlantic Anomaly</b>	< 4 mins / orbit	4%	Depends eventual inclination
<b>STR reference loss</b>		1%	Occultation simulation
<b>GNSS reference loss</b>		5%	Allocation from antenna pattern
<b>RSS observing attitude</b>		32%	Root sum square of all above
<b>Slew</b>		5%	Based on spacecraft agility and target distances in observing plan
<b>Safe Mode</b>	2* 4 days / year	2%	Specified in MRD
<b>Orbit maintenance</b>	1 hr / yr	<0.1%	
<b>Tranquilisation</b>		<0.1%	Dynamical analysis
<b>Non-availability</b>		<b>39%</b>	<b>Linear sum</b>
<b>Availability</b>		<b>61%</b>	

## 6 Ground Segment

In this section we provide an overview of the *LOFT* ground segment. This will be a combined effort of ESA and the member states that will contribute through the Instrument Operation Centres, the Science Data Centre, and the *LOFT* Burst Alert Ground Segment.

### 6.1 Overview

The Ground Segment (GS) provides the means and resources to manage and control the mission via telecommands, to receive and process the telemetry from the satellite, and to disseminate and archive the generated products. The *Operations* Ground Segment (OGS) consists of the Mission Operations Centre (MOC) and the ground stations which receive the telemetry. The *Science* Ground Segment (SGS) consists of the Science Operations Centre (SOC), the Science Data Centre (SDC), the Instrument Operations Centres (IOCs, the LAD and WFM teams which provide the instruments) and the *LOFT* Burst Alert Ground Segment (LBAGS). The latter includes the *LOFT* Alert Center (LAC) and a network of ground VHF receivers. The development and operations of the SDC, IOCs and LBAGS are funded nationally. An overview of the GS is given in Figure 6-1. The OGS and SGS are described in the following two subsections.

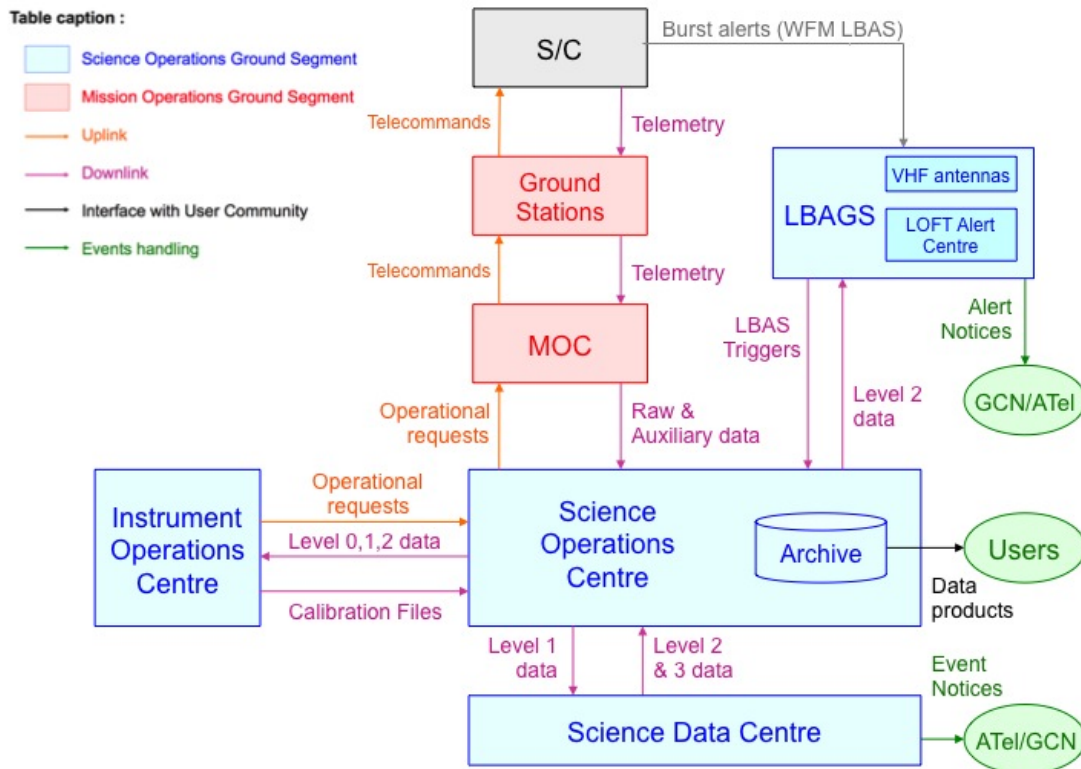


Figure 6-1 Overview of the *LOFT* Ground Segment, including the data flow between the various elements of the Ground Segment.

### 6.2 Mission operations

The Mission Operations Centre will be responsible for the spacecraft operations. This is described below together with the functioning of the ground stations and the LBAGS. A summary of the observation planning process and handling of Target of Opportunities (ToO) is also provided. The latter are particularly relevant for *LOFT* as many of the key science targets are transient sources and the corresponding observational programs are initiated through ToOs.

### 6.2.1 Mission Operations Centre

The Mission Operations Centre (MOC) is responsible for the commanding of the spacecraft and instruments, including overall mission planning, for ensuring the spacecraft safety and health, for provision of Flight Dynamics support including determination and control of the satellite’s orbit and attitude, and intervention in case of anomalies. The MOC performs all communications with the satellite through the ground stations for the upload of the platform and payload telecommands (based on the observation schedule provided by the SOC, see below), and reception of the downloaded telemetry data. They are also responsible for collecting the science data and its transmission to the SOC, along with the raw telemetry, housekeeping and auxiliary data. The MOC does not receive WFM burst-alert transmissions from the LOFT Burst Alert System (LBAS). LBAS alerts are communicated to a VHF ground network and then distributed via the LOFT Alert Centre (LAC) to interested parties. The VHF network and LAC together form the separate LBAGS. The ground station utilisation has been studied assuming one contact per orbit using Malindi, and supplemented with several contacts per day to Kourou (4x, including uplink).

Due to the non-continuous coverage, the spacecraft will be mainly controlled via off-line operations. Anomalies will typically be detected by the MOC only during the passes which are manned by Spacecraft Controllers. After the initial spacecraft commissioning, all telecommands required to carry out the mission will normally be loaded in advance on the Mission Timeline for later execution. The spacecraft will be able to continue nominal operations without ground contact for a period of up to 7 days. On-board Control Procedures will allow autonomous execution of complex procedures, including decision loops which the GS cannot support due to the limited ground coverage. The MOC will provide telecommand history and other auxiliary data (including attitude history, time calibrations and barycentric corrections) to the SOC.

Flight Dynamics staff and Flight Operations Engineers will be on-call for the preparation of the ToO operations, and a number of ground passes per day will be pre-planned by MOC for potential use for uplink of ToO operations.

### 6.2.2 Ground stations

The science data rate is dominated by the LAD event streams and a requirement for 6.7Gbit per orbit allows nominal data rates for all to be accommodated, together with the continuous WFM streams. This rate is managed with one pass per orbit to an X-band antenna at Malindi and several (4 per day) at Kourou.

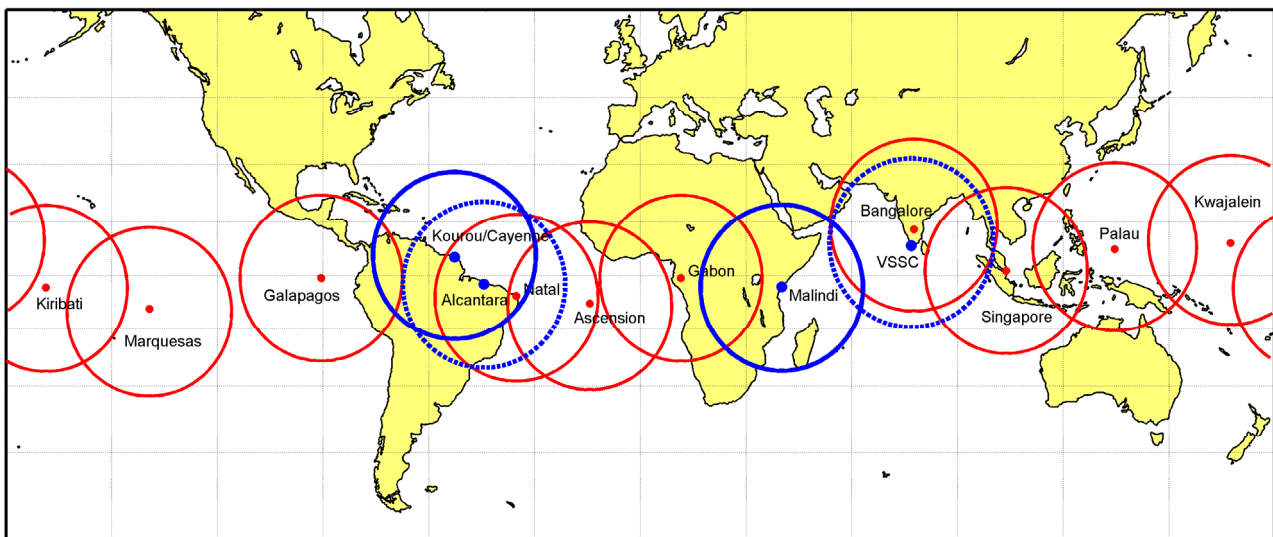


Figure 6-2 Baseline LOFT X-band ground stations in Kourou and Malindi are used for uplink and downlink. Two other potential X-band ground stations that might be offered by India and Brazil are also shown (these will in case enhance the science). On top of that there will be a set of ~10 VHF receivers for the burst alert system. These will be provided by the instrument consortium.

### 6.2.3 Mission phases

The mission timeline is summarised in Figure 6-3. Launch and Early Operations Phase (LEOP) will entail a direct launch and injection into the chosen orbit. The deployment of solar arrays and LAD panels will occur during ground contact periods. During Commissioning Phase the instruments will gradually be configured to operating status, with electronic stimulations allowing end-to-end test of functionality of systems without relying on the cosmic X-ray signals. The planning cycles, up- and down-link functionality will be commissioned and the basic instrument modes exercised. Scientific commissioning and basic calibration verification will be completed with selected targets, including pointing and sensitivity stability demonstrations on compact non-varying targets. During Performance Verification Phase selected targets will be observed to confirm timing resolution and frequency response performance, energy and effective area calibrations, count rate capabilities and selected key science target demonstrations, together with ToO, burst alert and ground segment capability confirmation. It is anticipated that normal science operations of the first Announcement of Opportunity (AO) and the Guaranteed Time Observations (GTO) targets will start after ~3 months when satisfactory performance has been demonstrated.

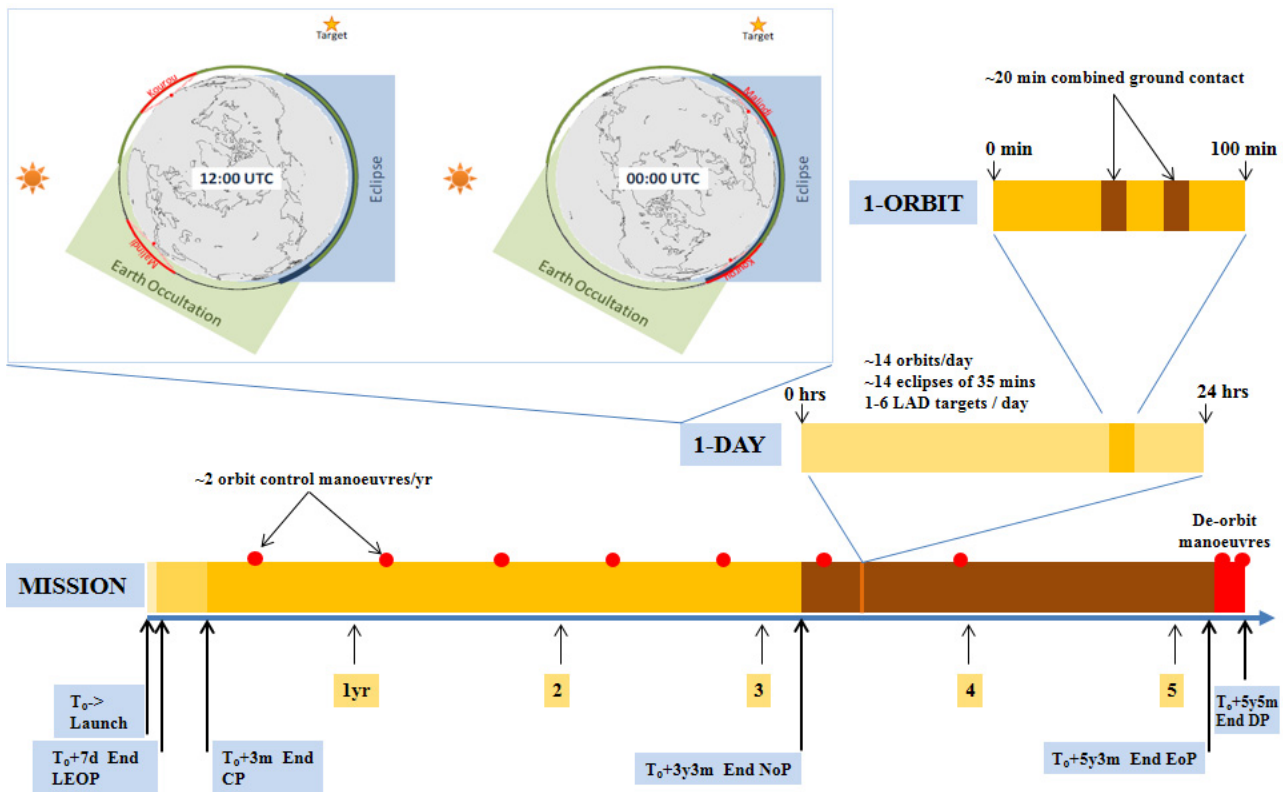


Figure 6-3 Mission timeline- in each orbit there can be up to ~20 minutes ground contact to 2 stations. For the 14 orbits per day, observations may be interrupted by eclipses and/or occultations, depending on target location. This is sized for a Nominal Operations duration of 3 year plus an extension of 2 years.

## 6.3 Science operations

### 6.3.1 Science Operations Centre

The SOC will be based at the European Space Astronomy Centre (Spain). The SOC will be the unique point of contact to the MOC for providing detailed operational requests, and it will plan the payload operation activities. The SOC is also the first point of contact of the scientific user community (through a centralized helpdesk). It provides support to the community in the exploitation of the mission throughout all mission phases.

The overall SOC activities include the following:

- Science observations planning and proposal handling
- Raw to Level 0 production and Level 0 to Level 1 data processing (see §6.4.1)
- Automatic quick-look analysis (QLA) of core science targets (monitoring)
- LOFT Science Data Archive
- Observation and performance simulator
- User Support; the SOC is responsible for communications with respect to AOs and observations, while the SDC (see below) is responsible for issues related to analysis software, data processing, data quality and data characteristics.

The software for the data processing and QLA will be developed by the SDC (in collaboration with the SOC and IOCs). The development and validation of the observation and performance simulator is a responsibility of the IOCs. The integration of the software is the responsibility of the SOC.

### 6.3.2 Science Data Centre

The Science Data Centre (SDC) will be established through national funding. The SDC is responsible for providing interactive and pipeline data-analysis software, and a Quick-Look Analysis (QLA) software system for checking the scientific progress of observations. The SDC will perform part of the pipeline processing of science data (Level 1 to 2 and Level 2 to 3) and deliver the products to the SOC for archiving. The science data processing and re-processing will include all necessary calibrations. These data products will enable systematic trend analysis, production of valued-added products, catalogues and surveys. It is supported by the SOC and the IOCs in the quality control of the science data.

The SDC will perform sky monitoring primarily using the WFM data and provide the publicly available results to the community. The SDC will support the IOCs in the instrument calibration activities, and provides support to the LOFT user community related to analysis software, data processing, data quality and data characteristics. Together with the SOC it may organize workshops for training in data analysis and software usage, in addition to science communications conferences. Also, in collaboration with the IOCs and the SOC, the SDC contributes to the testing and validation of new releases of the archive products and the overall SGS operational system.

### 6.3.3 Observation planning and Targets of Opportunity

Nominal routine mission observation planning is carried out by SOC personnel in a single shift per day, 5 days a week. Starting with the list of successful proposals to the AO, their targets are assessed for sky visibility and estimated available science time. A long-term planning schedule is created using the science planning utilities based on existing tools.

For the short-term planning, the SOC identifies detailed planning constraints (e.g., sky visibility, and mission resources such as power and telemetry). It generates plans, schedules, timelines and commands for (scientific) payload activities. The observational plan also takes into account which observations require the nominal Field of Regard and which can be executed with the extended Field of Regard (for which the energy resolution is not important). This short-term planning cycle will be an iterative process

Payload operations exclusion windows and on-board resources envelopes for payload operations will be defined by the MOC. The MOC enhances the planning files with suitable platform operational commands (e.g., pointing, telemetry maintenance, momentum management, etc.), and will undertake final detailed checks against mission, environmental and resource constraints. This includes events like eclipses, occultations, Earth-limb approach, etc. The final short-term time schedule is uplinked by the MOC through the GS network to the spacecraft. All commands are uplinked in advance and stored on-board the satellite for later execution. The commanding plan covers typically one day (Observation Day, or OD) and the planning cycle will take place typically every week covering one week of OD planning files. This basic Mission Planning approach for all the routine science operations phases will be built on the experience of previous missions, such as *XMM-Newton*, *Herschel*, and *INTEGRAL*.

The *LOFT* flight software will have a set of standard operating modes (including normal pointing, manoeuvre, sun hold, and safe-mode), and a limited number of standard, well-defined, and calibrated science observing modes (or instrument/engineering operations modes).

The science observation plan will be modified for Target of Opportunities (ToOs), using nominal observing procedures. ToOs will primarily come from the WFM data as this instrument provides a ‘continuous’ monitoring of relevant sources for the core science. On top of that some may come either from the LBAS or are provided by other observations at any wavelength on the ground or in space. Whereas the total time for these sources will be up to about one third of the total observing time, the number of re-planning cycles is much smaller as a state change in a source may result in a regular monitoring campaign of this source. The mission is designed to react within hours from the notification to the SOC of a ToO to the start of the associated science observations. However, the response time of *LOFT* is not critical, as the intensity for the relevant sources will only slowly decay (weeks to longer time scale, e.g., transient black-hole candidates in outbursts).

A significant part of the traditional ToOs will be pre-proposed, where the target and nominal observation details are already submitted as part of the calls for observing proposals (i.e., Announcement of Opportunities, AOs). The proposal will include triggers for QLA monitoring of the target, such as flux/hardness trigger levels, start/stop criteria, plus planning information like coordinates, exposure times, detector modes, etc. The SOC will automatically use QLA products to monitor core science targets for the trigger conditions. Another aspect which may alter a pre-planned observation schedule is the termination of on-going observation campaigns. Such campaigns can be terminated if the science goals have been reached or when the source transits to a state where further observations do not help the science anymore (e.g., when an X-ray transient turns off). The trigger for such termination is to be derived primarily by the QLA of the WFM and/or LAD data. The typical reaction time for such a re-plan is about a week.

Also, ToO proposals can be made to the SOC for an observation of a target outside the AO process. Of course, *LOFT* will provide additional triggers through the LBAS system or the WFM data at varying time scales: duration of up to seconds, such as Gamma-Ray Bursts, and duration up to hours, such as Type I X-ray bursts, superbursts, or Soft-Gamma-Ray Repeater activity, stellar flares. *LOFT* is not designed to respond automatically to each of these triggers (these *LOFT* data can be used though as the basis for a ToO proposal to the project scientist who will decide on the basis of the scientific merit). Only a limited number of such proposals is foreseen.

### **6.3.4 Instrument Operations Centre**

The two Instrument Operations Centres (IOCs) are part of the LAD and WFM instrument teams set up under the national funds. They provide support to ESA for maintenance of the instruments after launch, operations, processing algorithms and calibration. They will be responsible for characterising and calibrating the instrument responses, and for monitoring the science performance of the instruments and long-term trend analysis of the instruments. They provide inputs for the instrument modelling at the SOC, and instrument specific data-analysis software for pipeline and interactive analysis, as well as the QLA, to the SDC. The IOCs will transfer their instrument knowledge to the SOC for the long-term maintenance of the expertise and knowledge of the instrument operations, performance and calibration. This is partially realized by the provision of so-called Instrument Operations Scientists to the SOC.

### **6.3.5 LOFT Burst Alert System and LOFT Burst Alert Ground System**

The *LOFT* Burst Alert System (LBAS) receives event-alert signals from the WFM instrument, and disseminates the position and times of new sources or bursts, through the GRB or other community facilities (such as VOEvent) for the widest possible broadcast in near-real time. The time and position of these triggered events will be broadcast within a few seconds of detection by the WFM instrument. These burst-alert packages are not part of the regular telemetry flow to the MOC, but are distributed from the WFM through the onboard VHF antenna to a network of VHF ground receivers distributed around the equator (see Figure 6-2). The receivers will cover as large as possible a part of the *LOFT* orbit and relay the information through the net to the *LOFT* Alert Centre (LAC) and other registered users. It is estimated that, after initial verification, the time between the onboard detection of transient event to the end user is less than 30 s. The corresponding WFM data (event-by-event and images) will be telemetered to the MOC and processed at the SOC (raw to Level 0 to Level 1) and SDC (Level 1 to Level 2); during normal conditions the full instrument data will be publicly

available no later than 3 hours after the event. The LAC uses these WFM science data to perform the quality checks on the alerts, and will receive from the WFM IOC all information regarding the health of the WFM and on hardware changes that might affect the reliability of the triggers. Relevant information are disseminated from the LAC to the science community. The VHF ground receivers and the LAC constitute the *LOFT* Burst Alert Ground Segment (LBAGS), and are operated under national funds.

## 6.4 Data, software and data archiving

### 6.4.1 Data products

The data from the spacecraft is received at the MOC and sent in real time to the SOC where they are automatically processed into Level 0 and Level 1 data (see below). These products are called Near Real Time (NRT) as they will be available almost in real time (within 2 orbits for the WFM and up to 1 day for the LAD). Further processing of the data and the generation of level 2 and level 3 data is performed by the SDC. The same data products will also be produced for the consolidated (CONS) telemetry data (about a week later) to allow for any correction of the NRT data. Typical Level 0, 1, 2 and 3 data will be stored in FITS format and are defined according to the scheme below:

- Level 0:** Raw spacecraft telemetry is de-commutated and split into functionally independent parallel streams. The data will be organized per observation and readable with standard tools. The LAD data will contain event files. The WFM data will include images sliced in time and energy, rate meters, spectra, and (for events that triggered the LBAS) photon-by-photon data. On-board calibrations will be applied to both the LAD and WFM data.
- Level 1:** All corrections (such as aspect correction, time calibration, barycentric corrections) and instrument-specific calibrations (such as detector gain and good-timing information) are applied to level 0 data to produce cleaned level 1 data for both the LAD and WFM.
- Level 2:** Data from multiple observation intervals that constitute an observation are combined to create uniform sets of data for the LAD and the WFM. Pre-defined science products will populate the archive. LAD data will include: light curves, energy and power spectrum, photon lists for the observed target. WFM data includes: sliced images in time and energy (predefined number of energy bands and minimum integration time), light curves and spectrum for each source. It will also include triggers as processed from the LBAS system.
- Level 3:** Data containing enhanced, higher level, scientific products such as catalogues and mosaics, and long-term light-curves of individual sources. Further science enhancement for legacy products and cross-correlation with multi-wavelength catalogues.

An overview of the data products is given in Box 13.

The WFM data are made public immediately to the science community in order to exploit at best the mission capabilities. Proper interfaces will be made available to conveniently access and display WFM NRT science products. A “sky monitoring activity” will be performed at the SDC in order to assess the quality of these data. The LAD NRT Level 2 data are used by the SOC to communicate with the PIs preliminary results of their ongoing observational programs. This provides a convenient way to stop/continue/optimize further observations of the PI target. The LAD Level 2 CONS data will be distributed (when ready) to the PIs through the SOC; these data will then become publicly accessible through the *LOFT* Science Data Archive when the proprietary period expires.

Box 13: Overview of the LOFT science data products

		LAD	WFM	NRT	CONS
Level 0	- FITS event files (preliminary on-board calibrations applied)	- Sky images (sliced in time and energy) - Rate meters - Photon-by-photon (for LBAS triggers)	- Sky images (sliced in time and energy) - Rate meters - Photon-by-photon (for LBAS triggers)	Y	Y
Level 1	- Cleaned, corrected and barycentered event files (all ground calibrations and corrections applied)	- Same as above but with all corrections and ground calibrations applied	- Same as above but with all corrections and ground calibrations applied	Y	Y
Level 2	For the target source: - Lightcurve - Energy spectrum - Power spectrum	- Sky mosaic For all sources in the FOV: - Lightcurve - Energy spectrum - Power spectrum (if applicable)	- Sky mosaic For all sources in the FOV: - Lightcurve - Energy spectrum - Power spectrum (if applicable)	Y	Y
Level 3	- Multi-wavelength spectral energy distribution	- All sky mosaic (continuously updated) - Historical database of fluxes and spectral/timing states for all sources - Cross-catalogue identification	- All sky mosaic (continuously updated) - Historical database of fluxes and spectral/timing states for all sources - Cross-catalogue identification	N	Y
VHF Alerts	-	- Short text messages containing start time and position (1 arcmin accuracy) of LBAS triggers (fulfilling pre-defined criteria)	- Short text messages containing start time and position (1 arcmin accuracy) of LBAS triggers (fulfilling pre-defined criteria)	-	-

Note: Light-blue boxes indicate data that are made public as soon as available. For data in the yellow boxes a proprietary period of 1 year applies.

### 6.4.2 Processing software

All software to process the spacecraft telemetry into different data products will be developed and tested by the SDC, in consultation with the SOC and IOCs (where all knowledge about the instrument resides). A common software environment will be employed to facilitate integration with ESA archives and needs for users and operations. The LOFT data processing and analysis software will include:

- Pre-processing software: to organise the telemetry into usable science stream per instrument, producing Level 0 data. This will be installed and run at the SOC,
- Pipelines software: to process raw telemetry into NRT and CONS Level 1, 2, and 3 data. The pipelines apply calibrations to the NRT data to make them usable for the QLA/sky monitoring and to allow for prompt reaction to interesting events. The pipelines apply all refined corrections and instrument-specific calibrations to the CONS data. The latter are periodically reprocessed when updated calibration and instrument knowledge requires this. For both the NRT and CONS data, the pipeline produces standard sets of spectra, timing products and images. Pipelines for the processing of Level 1 data are installed and run at the SOC. Pipelines for the production of Level 2 and 3 data are run by the SDC.
- Interactive tools: to access NRT and CONS Level 1 data and extract “customized” Level 2 science products (using customizable versions of the scripts from the data processing pipelines and allowing for a larger parameter space to be exploited),
- Quick Look software (QLA): to provide the required interfaces to conveniently visualize and elaborate NRT LAD and WFM data.

### 6.4.3 Quick Look Analysis

The nature of the mission requires a dedicated effort to identify state changes in relevant sources. The aim of the Quick-Look Analysis (QLA) is to optimize the identification and eventually broadcast and follow-up any relevant (transient) astrophysical event that is discovered in the LOFT data and/or provided by external facilities. The QLA should also permit to decide if the on-going observation meets criteria established in the corresponding proposal, and may provide a means to terminate the current observing plan and trigger a new

one. To achieve these goals, it is essential to process and quick-look data from both the WFM and the LAD instrument.

QLA activities will be implemented at both the SOC and the SDC using NRT data and the QLA software. An automated QLA monitoring tool at the SOC provides alerts regarding the status of all core science targets of *LOFT* (i.e., about 100 sources). The QLA will further be used to monitor on-going observational campaigns to check whether the observation meets criteria established in the observing proposals (e.g. is still bright enough). The QLA for LAD data provides a way to assess the detailed spectral/brightness/timing status of the core science targets. Relevant information will be provided by the SOC to the proposal PIs to optimize the instrument settings for further observations of the same target or terminate the observing program if the source is in a state no longer interesting. At the SDC, the QLA software permits to access and display WFM data in order to perform a "sky monitoring" activity. Relevant events, not related to the *LOFT* core science goals, discovered through this activity can be used by the science community to trigger additional ToO programs, upon communication to the SOC. For new sources a number of additional checks might be applied by the SDC before they are publicly announced. The following output is expected from the QLA: timing info (power-density spectra), light curves, hardness curves, energy spectra, images, source lists, etc. Accumulation of this output allows building a historical reference (i.e., long-term) archive of the source behaviour in the X-ray domain. These QLA products will also be made available to the science community through proper interfaces accessible on-line.

The WFM QLA products will also be used by the LAC to verify and validate automatic alerts disseminated by the LBAS.

The typical data available to the user are listed in Box 14.

#### **6.4.4 Data archiving**

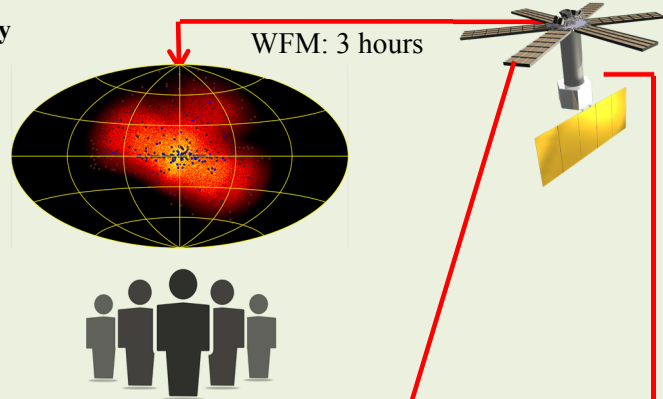
The European Space Astronomy Centre (ESAC) provides the legacy Science Archive for all ESA's current scientific missions, where the scientific community accesses data products. The SOC, based at ESAC, will be responsible for the *LOFT* Science Data Archive (LSDA). The LSDA will contain all the *LOFT* mission data products, together with all the information necessary to enable the scientific community to access, exploit and reprocess them as needed. This includes raw telemetry, processed science products and relevant auxiliary data, with user-friendly and powerful archive access, as well as results from the QLA, LBAS alerts, calibration data, data-analysis software, etc. The LSDA is thus the primary repository for all the science data products of all levels, and will be used as the central "hub" during all phases of the mission.

After the operational phase of the mission, the data (re-)processing system will come to its final status, and the final refinements of the system calibration are achieved in collaboration among the SOC, the SDC and the IOCs. The final ('legacy') reprocessing of all the mission data is performed using the ultimate version of the data processing tools and calibration, and the explanatory documentation is put into legacy form, all through the LSDA. The SOC ensures that all data (science data, calibration data, auxiliary data, etc.), processing tools and documentation are properly collected and archived into the LSDA. Assuming an average of about 6.7 Gbit of telemetry data to be downloaded per orbit and a nominal mission lifetime of 3 years plus 2 years extension, the size of the final, 'legacy', LSDA is expected to be ~500 TB. Note that this 'legacy' LSDA will continue to be supported as part of the overall ESAC infrastructure, beyond the end of the *LOFT* Post-Operations Phase.

**Box 14: Near-Real Time monitoring of the X-ray sky**

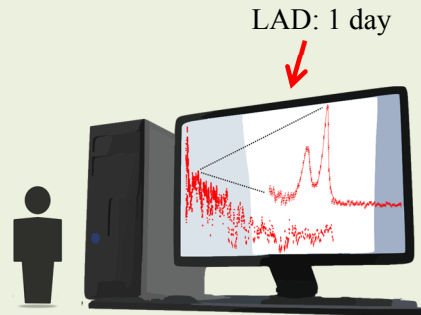
**WFM NRT data (2-50 keV):**

- Publicly available < 3 hours
- Provide for any source in the field of view:
  - Sky mosaic & sources identification
  - Lightcurves (max time res. 10  $\mu$ s)
  - Spectra (energy res. 300 eV)



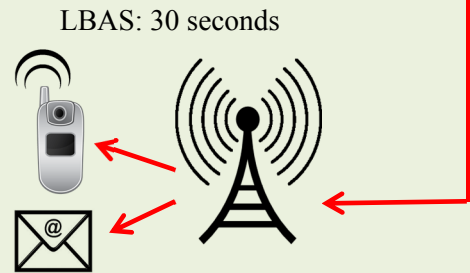
**LAD NRT data (2-30 keV):**

- Distributed daily to the observations PI
- Used to monitor on-going observations
- Include for the observed source:
  - Event files & lightcurves (max time res. 10  $\mu$ s)
  - Power and energy spectra (max energy res. 180 eV)



**LOFT Burst Alert System:**

- On-board localization of impulsive events ( $\sim 1$  arcmin)
- Broadcast of time and position to the ground (< 30 s)
- Provide “heads-up” for multi-wavelength facilities



# 7 Management

## 7.1 Project management

LOFT is envisaged as an ESA mission with contributions from ESA Member States and therefore the ‘usual’ project management approach for ESA missions will be followed.

*ESA management:* The overarching responsibility for all aspects of the *LOFT* mission rests with ESA’s Directorate of Science and Robotic Exploration and its director (D-SRE). During the development phase, ESA will appoint a Project Manager, who is responsible for implementing and managing ESA’s activities during this phase. This work will cover all industrial activities (procurement of the spacecraft, integration of the spacecraft and instruments, testing, the launch campaign and also the early in-orbit phase). After commissioning, the ESA Mission Manager assumes responsibility for operations of the spacecraft, its payload, and the ground segment.

The *LOFT* Project Scientist is ESA’s interface with the scientific community for all scientific matters. A *LOFT* Science Team (LST) will be set up by the Agency (with some representatives of the instrument consortium but also with external scientists) following the normal practice of the Agency. The LST advises the Project Scientist (who chairs the team). The Project Scientist advises the Project Manager during the development phase on all issues that affect the scientific performance of *LOFT*, and advises the Mission Manager during operations on all issues that affect the scientific output of the mission.

*Payload management:* The Payload consortium will provide the payload. All members of this consortium have a long track record and have in the past provided instruments for successful high-energy missions (*XMM-Newton*, *Chandra*, *BeppoSAX*, *INTEGRAL*, *AGILE*, *ROSAT*, *Astro-H* etc.) and as such have the right level of expertise. During the early phase of the Definition Phase activities, the ESA management team will work to secure multilateral agreements. These will be established between ESA and the Payload Consortium funding agencies to formalise the commitments and deliverables of all parties. A *LOFT* Steering Committee with representatives from the national funding agencies and ESA will then be set up to oversee the activities of the Payload Consortium and the timely fulfilment of the obligations of all parties to the MLA.

A *Science Data Centre* has been conceived as part of the consortium and is responsible for ensuring suitable pipeline processing tools for the science data to produce standard products for ingestion into the archive at ESA. The consortium will also provide the infrastructure and operational capability for a VHF-based *LOFT* Burst Alert System.

Whereas the full responsibility of the timely delivery of the instruments and the SDC rests with the PI who is supported by the PIs of the two instruments and the PI of the SDC, a consortium council will meet twice a year. In this council all contributing institutes are represented taking into account the relative size of the contributions and this body will advise the PI in case of conflicts or resource adjustments.

## 7.2 Procurement and member state contributions

*LOFT* is planned as an ESA-only mission, with no international contributions in its baseline design. The Payload and the Science Ground Segment will be provided by the *LOFT* Consortium, supported by the ESA Member States, with the noticeable exception of the LAD collimator for which ESA-supported manufacturing is planned, while the testing and integration into the LAD Collimator Assembly is still under full responsibility of the *LOFT* Consortium.

Table 7-1 Overview of member state contributions

Italy	Consortium PI and Project Office LAD co-PI LAD detectors procurement WFM detectors procurement LAD & WFM detection plane calibrations LAD pipeline software LAD science enhancement LAD response matrix & background simulations	Germany	LAD co-PI LAD MBEE & PBEE procurement LAD ICU procurement LAD Harness LAD detector plane calibrations (contribution) LAD end-to-end simulations WFM Digital Electronics
-------	---	---------	---

	WFM Detector simulations Malindi Ground Station		WFM science software LAD & WFM pre-processing software
UK	LAD PI and Project Office LAD Collimator AIV & calibration LAD & WFM PSU LAD onboard software LAD Modules AIV and calibrations Support to industry for Panel AIV LAD Instrument Operation Center	Denmark	WFM PI & Project Office WFM ICU hardware WFM camera calibrations WFM Instrument Operation Center
France	LAD co-PI LAD & WFM ASICs procurement LBOT onboard SW and operation WFM science enhancement	Spain	WFM co-PI WFM Mask, Collimator and Mechanics WFM camera AIV WFM Background Simulations
Switzerland	LAD co-PI LAD FEE procurement and AIV LOFT Science Data Center PI and Project Office LAD & WFM Data processing LBAS Procurement and Operation	Netherlands	WFM FEE procurement WFM detection plane AIV WFM Imaging simulations
ESA	Capillary Plate (LAD collimator) procurement	Poland	WFM ICU procurement & AIV
		Finland	WFM ICU onboard software

### 7.3 Mitigation actions for top risks

A detailed analysis of the risks associated to the payload development is reported in the IPRR data package, including a risk register in which highest level is yellow (acceptable risk). Here we summarize the top 6 risks and the implemented mitigation actions.

Table 7-2 Top level risks and mitigation strategy (already on-going)

Risk	Description	Mitigation Options
Radiation damage	Operating temperature depends on correct assessment of radiation environment	<ul style="list-style-type: none"> <li>✓ Radiation environment independently assessed by Consortium and ESA EEC-TEC</li> <li>✓ 2x design margin + 2x additional margin</li> <li>✓ Radiation damage verified by irradiation tests</li> <li>✓ Weak dependence of energy resolution: additional 3x worse radiation environment still acceptable for science case (10% loss in energy resolution)</li> </ul>
Response stability (micro-vibrations)	Simplified transfer function of micro-vibration (around 120 Hz) due to availability of only preliminary spacecraft design	<ul style="list-style-type: none"> <li>✓ Current industrial analysis shows compliance to LOFT requirements with good margins</li> <li>✓ Disturbance localized in frequency allowing removal from science data</li> </ul>
Non-operating temperature	Design optimization for hot case requires 2°C extension of non-op T requirement (from -50°C to -52°C)	<ul style="list-style-type: none"> <li>✓ Analysis has shown that lowering the non-operational temperature to -55°C is realistic (no need to modify processes only qualification and acceptance ranged)</li> <li>✓ Non-operating range extended down to limit allowed by MIL-STD, -55°C</li> <li>✓ Thermal design include 10°C margin</li> <li>✓ Thermo-mechanical prototype under development at DPNC (available end-2013)</li> <li>✓ Option to include SC-controlled Module heaters to ensure temperature limits</li> </ul>
Effective Area Loss	Final design not meeting effective area requirement	<ul style="list-style-type: none"> <li>✓ Module allocation margins in industrial design (125 and 124 vs requirement of 121)</li> </ul>

		<ul style="list-style-type: none"> <li>✓ Science case robust against ~10% effective area loss: almost entirely recoverable by longer observations</li> </ul>
MAIT Schedule	Delayed delivery of LAD Modules	<ul style="list-style-type: none"> <li>✓ Critical technology at TRL 6 end-2015</li> <li>✓ Early Qualification Model for Module</li> <li>✓ Early start of manufacturing of critical items</li> <li>✓ Direct involvement and endorsement of industries in the AIV planning already in Phase A</li> <li>✓ Very detailed planning (day-to-hour resolution) with Monte Carlo simulation of delivery date</li> <li>✓ &lt; 60% use of equipment and team capabilities and possibility to implement corrective actions very early in the program (long and repetitive sequence)</li> <li>✓ Independent 6-month margin on both Payload and Spacecraft activities</li> </ul>
ASIC Development	Late development	<ul style="list-style-type: none"> <li>✓ Most challenging performance (low-noise with low-power) already very good in first prototype</li> <li>✓ Full mixed-signal ASIC prototype manufacture Oct. 2013</li> <li>✓ Next ASIC versions already in the plan</li> <li>✓ Plan to TRL 6 by end-2015</li> <li>✓ Performance demonstrated by the VEGA ASIC (Italy), also available as technology back-up</li> </ul>

## 7.4 Schedule

The LOFT schedule is consistent with a launch date at 2022 with the appropriate margins. The LAD modules defines the critical path of the payload implementation. The other elements (LAD ICU and PBEEs, WFM ICU and Cameras) are less critical. The ESA Reference Schedule and project key dates and reviews are shown in Figure 7-1. This schedule is based on several key considerations:

- Overall a 6 months schedule contingency for the prime contractor is considered before FAR.
- A comfortable duration of 7 month has been allocated for integration of the LAD Modules on the S/C. Begin and end of this activity define the need dates for the first and last LAD Module. As the actual MAIT of the LAD Modules will have a duration of ~2 years, there will be already a large number of Modules on stock when the integration of the LAD Modules to the Panel starts.
- To ensure that late P/L deliveries do not delay the S/C schedule, an additional 6 month margin has been taken for each P/L item. The first LAD Module delivery is therefore scheduled for January 2020, the last LAD Module delivery for July 2020.
- To guarantee the LAD Module deliveries in 2020, the manufacturing of long lead items (MPCs, ASICs, SDDs) has to start already in Phase C of the System Level Schedule. This is possible thanks to an already very detailed and consolidated LAD Module design available at PRR and the expected TRL 6 at SRR. This will allow developing and testing a LAD Module Qualification Model (QM) already before Instrument PDR (I-PDR, Oct 2017) which will then be combined with a LAD Module QR. The LAD Module QM MAIT will start in 2016 leaving more than two years after Mission Selection for remaining developments and design optimisations (mainly needed for the ASIC).
- Together with the LAD Module QMs, several LAD Module EMs are manufactured in the course of 2017. These act as a first test run for the mass production that allows the early detection of potential manufacturing issues and fine tuning of the mass production MAIT flow.
- The AIT process for the LAD will run in parallel to the manufacturing (following the delivery of the first batch of components AIT will start and at the same time the next batch can be produced). The location of various activities has been optimized and also the facilities for production and AIT take into account down time and working hours. Month-long pauses in the assembly chain included in the plan as a contingency. This gives flexibility in the production or AIT rate if needed. Past missions (e.g., Fermi, 84 m<sup>2</sup>) demonstrated that even tighter AIT schedules are realistic.

- The S/C system level schedule follows a standard approach with engineering and qualification models in Phase D followed by a System QR at the end of 2020. The envisaged models include a structural model, a reduced thermal model and an electrical functional model

This System Level development schedule is in line with similar ESA developments and is considered to be of acceptable risk.

## 7.5 Science management

A detailed Science Management Plan has not yet been defined. In this section we describe the basic principles of the Science Management Plan with a focus on the allocation of observing time. The prime goal of the science management plan is to ensure the best possible scientific results for the mission which implies that the best scientists should have a key role. At the same time there should be a reasonable return to the member states that have funded the instruments. This leads to the following approach:

1. *LOFT* will operate as an observatory. Observing time will be open to the world-wide scientific community and allocated via annual Announcement of Opportunities (AOs) and scientific peer review organized by the SOC.
2. Time will be allocated to the core science goals of the mission as some of the core scientific goals of the *LOFT* cannot be achieved by aggregating a number of individual GO proposals. So it is proposed to devote a fraction of total observing programme to *Key Projects* to ensure a co-ordinated approach to a sub-set of the science goals. A separate AO will be executed for the formation of *Key Project Teams* during the implementation phase. Before this call it will be decided for which topics a key project will be established (and how much time will be reserved). The topics for the key projects will be set by ESA based on advice from the science advisory team closer to the launch. For these core science goals proposals can be submitted by individual scientists or groups of scientists. This is open to the scientific community and does not require an involvement in the instrumentation. Again, based on peer review, the key project teams will be selected.
3. A fraction of the total observing time will be allocated to the instrument consortium to ensure a reasonable return for their investment. The fraction will be decided by ESA. This time will be evenly distributed over the total mission duration. This helps to guarantee that the instrument teams remain actively involved in the optimisation and calibration of the instruments following their delivery to ESA.

The instrument teams' observing proposals will participate in the OTAC selection process as for any external scientist, but it is envisaged that they will receive a guaranteed fraction of the time if they do not achieve it based on the quality of their proposal (the instrument team proposals will have priority over higher ranked observation proposals till the fraction reserved for the instrument teams is achieved). This ensures that the top level ranked proposals will be executed irrespective of the instrument involvement but the lower ranked proposals might be substituted for proposals of the instrument teams in case the instrument proposals do not already fill their fraction based on science ranking only.

4. Targets of Opportunity can be proposed by the scientific community and the ESA project Scientist will decide about this (eventually after consulting the relevant members of the OTAC). Depending on the nature of the ToO either the one year proprietary data rule can be applied or the data will be made available to the science community in general.
5. The standard 1 year proprietary data rights are assumed for the LAD (from the point level 1 data is available). After this period all data become public.
6. For the Wide Field Monitor no proprietary data rights will apply and this data should be made available to the community on a much shorter time scale. During routine operations level 1 data will be produced typically in 3 hours after the observation (NRT data).

- The data of the Burst Alert System will be distributed to the community in 30 seconds using the appropriate systems and no data rights will apply

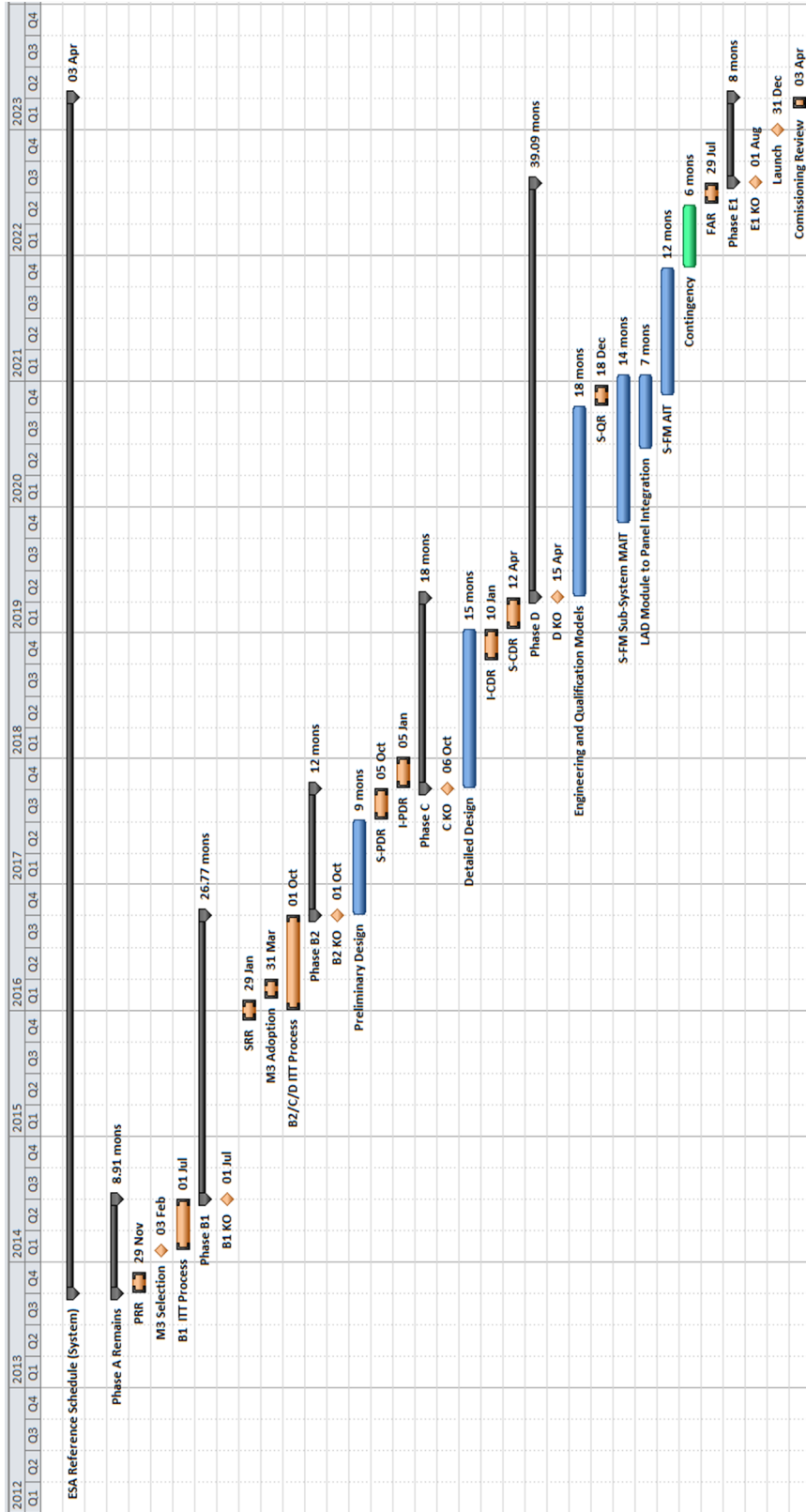


Figure 7-1 ESA Reference Schedule and Key Dates

## 8 Communications and Outreach

ESA will be responsible for planning and coordinating education and outreach activities related to LOFT, with the support of the Payload Consortium. An outreach and education plan will be developed and executed jointly by ESA and the Payload Consortium under supervision of the LOFT Science Team (LST). The following guidelines apply to ESA missions:

- ESA leads and coordinates the execution of all education and outreach activities within the data rights framework of the mission;
- For the purpose of public relation activities, LOFT Payload Consortium will provide to ESA unlimited access to all processed and analysed data, even during their proprietary period (if applicable); this material will anyway follow the data rights policy for matters concerning scientific publication purposes;
- Members of the LST and the Payload Consortium have a duty to support ESA with regards to education and outreach;
- ESA gives credit to members of the LST and the Payload Consortium regarding scientific and technical results when applicable.

The LST and IOCs have the duty to exploit the outreach and educational potential of LOFT. The contributions from national funding agencies to the science exploitation phase will include resources to develop plans and produce education and outreach material such as high quality website, children booklets, secondary school material, press releases, popular science-level material, animations and simulations, audio-visual kits, etc.. As appropriate, the consortium members will develop locally targeted educational material, and cultivate local contact points to broaden the Europe-wide network of outlets for the PR activities.

While the SDC concentrates on the access to the science community of WFM legacy data products, the consortium will also develop these for citizen science participation, such as simplified tools to explore the variable X-ray sky, explore source behaviours and flag interesting events, provide target advocacy and participation, connect with public robotic telescope networks etc. During the mission implementation phase the consortium will gather feedback from existing citizen science projects (e.g., Kepler light curves, Solar Stormwatch) to better understand the lessons learned on engagement, tools, interfaces and data production. This will be used to inform the LOFT outreach programme for maximising the participation and expediting the websites to be ready near launch.

## 9 Bibliography

- Abdo, A.A. et al., 2009. *Science*, 325, p.840.
- Abdo, A.A. et al., 2010. *Science*, 329, pp.817-21.
- Abramowicz, M.A. & Kluzniak, W., 2001. *A&A*, 374, p.L19.
- Aharonian, F. et al., 2009. *A&A*, 502, p.749.
- Alford, M.G. et al., 2012. *PhRvD*, 85(2), p.024007.
- Alford, M.G. et al., 2008. *Reviews of Modern Physics*, 80, pp.1455-515.
- Allafort, A. et al., 2013. *ApJ*, 777, p.2.
- Alpar, M.A. et al., 1982. *Nature*, 300, pp.728-30.
- Altamirano, D. et al., 2008. *ApJL*, 674, pp.L45-48.
- Altamirano, D. et al., 2012. *ApJL*, 759, p.L20.
- Amati, L. et al., 2013. *Nucl. Phys. B Proc. Suppl.*, 239, pp.109-12.
- Amati, L. et al., 2000. *Sci*, 290, pp.953-55.
- Andersson, N. et al., 2005. *MNRAS*, 361, p.1153.
- Andersson, N. et al., 2009. *MNRAS*, 396, pp.894-99.
- Antoniadis, J. et al., 2013. *Science*, 340, p.448.
- Anzolin, G. et al., 2009. *A&A*, 501, pp.1047-58.
- Archibald, A.M. et al., 2009. *Science*, 324, p.1141.
- Arons, J., 1992. *ApJ*, 388, pp.561-78.
- Artigue, R. et al., 2013. *MNRAS*, 433, pp.L64-68.
- Atwood, W.B. et al., 2006. *ApJL*, 652, pp.L49-52.
- Bakala, P. et al., 2013. *IAU Symposium*, 290, p.185.
- Band, D.L., 2003. *ApJ*, 588, pp.945-51.
- Bao, G. et al., 1994. *ApJ*, 435, pp.55-65.
- Bao, G. & Ostgaard, E., 1995. *ApJ*, 443, pp.54-63.
- Barnes, S.A., 2003. *ApJ*, 586, pp.L145-47.
- Barret, D., 2013. *ApJ*, 770, p.9.
- Bauböck, M. et al., 2013. *ApJ*, 777, p.68.
- Bauswein, A. et al., 2012. *PhysRevD*, 86(6).
- Beardmore, A.P. & Osborne, J.P., 1997. *MNRAS*, 290, pp.145-59.
- Becker, P.A. et al., 2012. *A&A*, 544, p.A123.
- Becker, P.A. & Wolff, M.T., 2007. *ApJ*, 654, pp.435-57.
- Bednarek, I. et al., 2012. *A&A*, 543, p.157.
- Belloni, T.M. et al., 2012. *MNRAS*, 426, pp.1701-09.
- Berger, E. et al., 2012. *ApJ*, 748, p.36.
- Bernardini, F. et al., 2012. *A&A*, 542, p.A22.
- Bhattacharya, D. & van den Heuvel, E.P.J., 1991. *PhR*, 203, pp.1-124.
- Bhattacharyya, S. et al., 2005. *AIPC*, 774, pp.291-93.
- Bhattacharyya, S. & Strohmayer, T.E., 2005. *ApJL*, 634, pp.L157-60.
- Bildsten, L., 1998. *ApJ*, 501, p.89.
- Blaes, O., 2013. *SSRv*.
- Bode, M.F. et al., 2006. *ApJ*, 652, pp.629-35.
- Bogdanov, S., 2013. *ApJ*, 762, p.96.
- Bogdanov, S. et al., 2008. *ApJ*, 689, pp.407-15.
- Boutloukos, S. et al., 2006. *ApJ*, 653, pp.1435-44.
- Brenneman, L.W. & Reynolds, C.S., 2006. *ApJ*, 652, p.1028.
- Brenneman, L.W. et al., 2012. In Petre, R. et al., eds. *American Institute of Physics Conference Series.*, 2012.
- Broderick, A.E. et al., 2012. *ApJ*, 752, p.22.
- Burrows, D.N. et al., 2011. *Nature*, 476, pp.421-24.
- Caballero, I. & Wilms, J., 2012. *MmSAI*, 83, p.230.
- Cackett, E.M. et al., 2010. *ApJ*, 720, pp.205-25.
- Cadeau, C. et al., 2007. *ApJ*, 654, p.458.
- Campana, R. et al., 2013. *ExA*, in press, pp.arXiv:1305.3789.
- Campana, R. et al., 2011. *NIMPA*, 633, pp.22-30.
- Casares, J. et al., 2006. *MNRAS*, 373, pp.1235-44.
- Casella, P. et al., 2008. *ApJL*, 674, pp.L41-44.
- Cavecchi, Y. et al., 2013. *MNRAS*, 434, pp.3526-41.
- Cenko, S.B. et al., 2012. *ApJ*, 753, p.77.
- Chang, P. & Bildsten, L., 2003. *ApJ*, 585, p.464.
- Chang, P. et al., 2005. *ApJ*, 998-1007, p.629.
- Chang, P. et al., 2010. *ApJ*, 723, p.719.
- Cheung, C.C. et al., 2012. *Atel*, 4284.

- Colaiuda, A. & Kokkotas, K.D., 2011. *MNRAS*, 414, pp.3014-22.
- Cook, G.B. et al., 1994. *ApJ*, 424, pp.823-45.
- Cordes, J. et al., 2009. In *astro2010: The Astronomy and Astrophysics Decadal Survey*, 2009.
- Cornelisse, R. et al., 2000. *A&A*, 357, pp.L21-24.
- Cumming, A. & Bildsten, L., 2001. *ApJ*, 559, pp.L127-30.
- Cunningham, C.T., 1975. *ApJ*, 202, pp.788-802.
- Dauser, T., 2010. [Online] Available at: [http://www.sternwarte.uni-erlangen.de/~dauser/research/publications/diploma\\_thesis\\_tdauser.pdf](http://www.sternwarte.uni-erlangen.de/~dauser/research/publications/diploma_thesis_tdauser.pdf).
- Dauser, T. et al., 2013. *MNRAS*, 430, p.1694.
- de Marco, B. et al., 2009. *A&A*, 507, pp.159-69.
- Demorest, P.B. et al., 2010. *Nature*, 467, pp.1081-83.
- Díaz Trigo, M. et al., 2013. *Nature*, p.in press.
- Díaz Trigo, M. et al., 2007. *A&A*, 462, pp.657-66.
- Doeleman, S.S. et al., 2009. *ApJ*, 695, pp.59-74.
- Dolence, J.C. et al., 2012. *ApJL*, 746, p.L10.
- Done, C. et al., 2007. *ARA&A*, 15, pp.1-66.
- Dovciak, M., 2004. PhD thesis. arXiv:astro-ph/0411605.
- Dovčiak, M. et al., 2004. *MNRAS*, 350, pp.745-55.
- Dubus, G., 2013. *AARv*. in press (arXiv:1307.7083).
- Duncan, R.C., 1998. *ApJL*, 498, p.L45.
- Eckert, D. et al., 2013. *Atel*, 4925.
- Egron, E. et al., 2011. *A&A*, 530, p.A99.
- Elvis, M. et al., 2004. *ApJL*, 615, pp.L25-28.
- Ezuka, H. & Ishida, M., 1999. *ApJS*, 120, pp.277-98.
- Fabian, A.C., 1989. *MNRAS*, 238, pp.41P-4P.
- Falcke, H. et al., 2000. *ApJ*, 528, pp.L13-16.
- Finke, J.D. & Böttcher, M., 2007. *ApJ*, 667, pp.395-403.
- Fragile, P.C., 2013. *SSRv* in press, pp.(arXiv:1304.5541).
- Fragile, P.C. et al., 2007. *ApJ*, 668, pp.417-29.
- Fragile, P.C. & Blaes, O.M., 2008. *ApJ*, 687, pp.757-66.
- Fragile, P.C. & Blaes, O.M., 2008. *ApJ*, 687, pp.757-66.
- Fukushima, K. & Hatsuda, T., 2011. *Report on progress in physics*, 74(1).
- Gabler, M. et al., 2013. *PhRvL*, 111(21).
- Galloway, D.K. et al., 2007. *ApJL*, 654, pp.L73-76.
- Galloway, D.K. et al., 2008. *ApJS*, 179, pp.360-422.
- Gandolfi, S. et al., 2012. *PhysRevC*, 85(3), p.032801.
- Gehrels, N. et al., 2009. *ARA&A*, 47, p.567.
- Gendreau, K.C. et al., 2012. In *Society of Photo-Optical Instrumentation Engineers (SPIE) Conference Series*, 2012.
- Gezari, S. et al., 2012. *Nature*, 485, pp.217-20.
- Gezari, S. et al., 2009. *ApJ*, 698, pp.1367-79.
- Ghirlanda, G. et al., 2007. *MNRAS*, 379, pp.73-85.
- Ghosh, P. & Lamb, F.K., 1978. *ApJ*, 223, p.83.
- Gierliński, M. et al., 2008. *Nature*, 455, pp.369-71.
- Gilfanov, M. et al., 2000. *MNRAS*, 316, pp.923-28.
- Glendenning, N.K., 2000. New York: Springer.
- Guillot, S. et al., 2013. *ApJ*, 722, p.7.
- Haensel, P. et al., 2009. *A&A*, 502, pp.605-10.
- Hayashi, T. & Ishida, M., 2013. *MNRAS*, arXiv:1307.7881.
- Hays, E. et al., 2013. unpublished. ATEL 5302.
- Hebeler, K. et al., 2013. *ApJ*, 773, p.11.
- Hebeler, K. & Schwenk, A., 2010. *PhysRevC*, 82(1), p.014314.
- Henisey, K.B. et al., 2009. *ApJ*, 706, pp.705-11.
- Hermesen, W. et al., 2013. *Science*, 339, p.436.
- Hernanz, M. & Tatischeff, V., 2012. *BaltA*, 21, p.62.
- Hessels, J.W.T., 2008. *AIP Conference Proceedings*, 1068, pp.130-34.
- Hessels, J.W.T. et al., 2006. *Science*, 311, pp.1901-04.
- Ho, W.C.G. et al., 2011. *Physical Review Letters*, 107(10), p.101101.

- Hotokezaka, K. et al., 2011. *PhysRevD*, 83(12), p.124008.
- in 't Zand, J.J.M. et al., 1998. *A&A*, 331, p.25.
- Ingram, A. & Done, C., 2012. *MNRAS*, 427, pp.934-47.
- Ingram, A. & van der Klis, M., 2013. *MNRAS*, 434, pp.1476-85.
- in't Zand, J.J.M. & Weinberg, N.N., 2010. *A&A*, 520, p.A81.
- Israel, G.L. et al., 2005. *ApJL*, 628, pp.L53-56.
- Israel, G.L. et al., 2008. *ApJ*, 685, pp.1114-28.
- Iwasawa, K. et al., 2004. *MNRAS*, 347, pp.411-20.
- Janka, H.-T. et al., 2007. *physrep*, 442, pp.38-74.
- Johnson-McDaniel, N.K. & Owen, B.J., 2013. *PhysRevD*, 88(4), p.044004.
- Kara, E. et al., 2013. *MNRAS*, 428, pp.2795-804.
- Kara, E. et al., 2013. *MNRAS*, 434, pp.1129-37.
- Keane, E.F., 2013. *Proceedings of the International Astronomical Union*, 291, pp.295-300.
- Keek, L. & Heger, A., 2011. *ApJ*, 743, p.189.
- Keek, L. et al., 2012. *ApJ*, 752, p.150.
- Keek, L. et al., 2008. *A&A*, 479, pp.177-88.
- King, A.R. & Kolb, U., 1999. *MNRAS*, 305, pp.654-60.
- Kiziltan, B. & Thorsett, S.E., 2009. *ApJ*, 693, pp.109-12.
- Klein, R.I. et al., 1996. *ApJ*, 457, p.L85.
- Klochkov, D. et al., 2011. *A&A*, 532, p.A126.
- Knigge, C. et al., 2011. *Nature*, 479, pp.372-75.
- Komossa, S., 2002. In Schielicke, R.E., ed. *Reviews in Modern Astronomy*, 2002.
- Kortelainen, M. et al., 2010. *PhysRevC*, 82(2), p.024313.
- Kramer, M. et al., 2006. *Science*, 314, p.97.
- Kramer, M. & Wex, N., 2009. *Classical and Quantum Gravity*, 26(7), p.073001.
- Krolik, J.H. & Hawley, J.F., 2002. *ApJ*, 573, pp.754-63.
- Lackey, B.D. et al., 2012. *PhysRevD*, 85(4), p.044061.
- Lai, D. & Tsang, D., 2009. *MNRAS*, 393, pp.979-91.
- Lamb, F.K. et al., 2009. *ApJ*, 706, p.417.
- Lattimer, J.M. & Prakash, M., 2001. *ApJ*, 550, pp.426-42.
- Lattimer, J.M. & Prakash, M., 2007. *physrep*, 442, pp.109-65.
- Lattimer, J.M. & Schutz, B.F., 2005. *ApJ*, 629, pp.979-84.
- Levan, A.J. et al., 2011. *Science*, 333, pp.199-.
- Levin, Y., 2007. *MNRAS*, 377, pp.159-67.
- Lewin, W.H.G. et al., 1993. *SSRv*, 62, pp.223-389.
- Lindblom, L., 1992. *ApJ*, 398, pp.569-73.
- Lo, K.H. et al., 2013. *ApJ*, 776, p.19.
- Lorimer, D.R., 2008. *LRR*, 11, p.8.
- Lyne, A. et al., 2010. *Science*, 329, p.408.
- Maggio, A. et al., 2000. *A&A*, 356, p.627.
- Maiolino, R. et al., 2010. *A&A*, 517, p.A47.
- Maitra, D. et al., 2009. *MNRAS*, 398, pp.1638-50.
- Margon, B. et al., 1979. *ApJ*, 233, p.63.
- Markoff, S. et al., 2005. *ApJ*, 635, pp.1203-16.
- Mauche, C.W., 2002. *ApJ*, 580, pp.423-28.
- McClintock, J.E. et al., 2011. *Classical and Quantum Gravity*, 28(11), p.114009.
- McClintock, J.E. & Remillard, R.A., 2006. *Compact stellar X-ray sources*, 39, pp.157-213.
- McClintock, J.E. et al., 2006. *ApJ*, 652, pp.518-39.
- McKinney, J.C. et al., 2012. *MNRAS*, 423, pp.3083-117.
- McLerran, L. & Pisarski, R.D., 2007. *Nucl. Phys.*, A796, pp.83-100.
- Méndez, M. et al., 2001. *ApJ*, 561, p.1016.
- Mereghetti, S., 2008. *A&ARv*, 15, p.225.
- Messenger, C., 2011. *PhRvD*, 84, p.3003.
- Mészáros, P., 2006. *Rep. Prog.Phys.*, 69, p.2259.
- Metzger, B.D. et al., 2010. *MNRAS*, 406, pp.2650-62.
- Middleditch, J., 1982. *ApJ*, 257, pp.L71-75.
- Miller, J.M., 2007. *ARA&A*, 45, pp.441-79.
- Miller, M.C. et al., 2013. *IAU Symposium*, 290, pp.101-08.
- Miller, M.C. & Lamb, F.K., 1998. *ApJ*, 37, p.499.
- Miniutti, G. et al., 2007. *PASJ*, 59, pp.315-25.

- Miyamoto, S. et al., 1991. *ApJ*, 383, pp.784-807.
- Morsink, S.M. et al., 2007. *ApJ*, 663, p.1244.
- Motch, C. et al., 2013. *ArXiv e-prints*.
- Motta, S.E. et al., 2013. *ArXiv e-prints (arXiv1309.3652M)*.
- Mucciarelli, P. et al., 2006. *MNRAS*, 365, pp.1123-30.
- Müller, S. et al., 2013. *A&A*, 551, p.A6.
- Muno, M.P. et al., 2002. *ApJ*, 581, pp.550-61.
- Muñoz-Darias, T. et al., 2008. *AIPC*, 984, p.15.
- Murray, N. et al., 2010. *ApJ*, 709, pp.191-209.
- Nakar, E., 2007. *physrep*, 442, pp.166-236.
- Nelson, T. et al., 2008. *ApJ*, 673, pp.1067-79.
- Nordlund, Å. et al., 2009. *Living Rev.Solar Phys.*, 6, p.2.
- Nowak, M.A. et al., 2011. *ApJ*, 728, p.13.
- O'Neill, S.M. et al., 2012. *MNRAS*, 422, pp.1436-52.
- Orlandini, M. & Morfill, G.E., 1992. *ApJ*, 386, pp.703-09.
- O'Shaughnessy, R. et al., 2008. *ApJ*, 672, pp.479-88.
- Osten, R.A. et al., 2010. *ApJ*, 721, pp.785-801.
- Özel, F., 2013. *RPPh*, 76, p.016901.
- Özel, F. & Psaltis, D., 2009. *PhysRev*, 80(10).
- Papitto, A. et al., 2013. *Nature*, 501, pp.517-20.
- Passamonti, A. & Lander, S.K., 2013. *MNRAS*, 429, pp.767-74.
- Pelangeon, A. et al., 2008. *A&A*, 491, p.157.
- Piekarewicz, J. et al., 2012. *PhysRevC*, 85(4), p.041302.
- Pieper, S.C. et al., 2001. *PhysRevC*, 64(1), p.014001.
- Piran, T., 2004. *RvMP*, 76, pp.1143-210.
- Podsiadlowski, P. et al., 2002. *ApJ*, 565, p.1107.
- Ponti, G. et al., 2012. *MNRAS*, 422, p.11.
- Poutanen, J. & Beloborodov, A.M., 2006. *MNRAS*, 373, pp.836-44.
- Psaltis, D., 2008. *Living Reviews in Relativity*, 11, p.9.
- Psaltis, D. & Özel, F., 2013. *ArXiv e-prints (arXiv1305.6615)*.
- Psaltis, D. et al., 2013. *ApJ (submitted)*, pp.arXiv:1311.1571.
- Puccetti, S. et al., 2007. *MNRAS*, 377, pp.607-16.
- Pye, J.P. & McHardy, I.M., 1983. *MNRAS*, 205, pp.875-88.
- Radhakrishnan, V. & Srinivasan, G., 1982. *Science*, 51, p.1096.
- Ramsay, G. & Cropper, M., 2004. *MNRAS*, 347, pp.497-507.
- Ramsay, G. & Cropper, M., 2007. *MNRAS*, 379, pp.1209-16.
- Ramsay, G. et al., 2001. *A&A*, 365, pp.L288-93.
- Rashevsky, A. et al., 2001. *Nucl. Instr. and Meth.*, 461, p.133.
- Read, J.S. et al., 2013. *PhysRevD*, 88(4), p.044042.
- Rea, N. & Esposito, P., 2011. *High-Energy Emission from Pulsars and their Systems, Astrophysics and Space Science Proceedings*, p.247.
- Rees, M.J., 1988. *Nature*, 333, pp.523-28.
- Reis, R.C. et al., 2012. *Science*, 337, p.949.
- Remillard, R.A. et al., 1999. *ApJL*, 517, pp.L127-30.
- Revnivtsev, M. et al., 1999. *A&A*, 347, pp.23-26.
- Reynolds, C.S., 2013. *ArXiv e-prints*.
- Rezzolla, L. et al., 2003. *MNRAS*, 344, pp.L37-41.
- Risaliti, G. et al., 2013. *Nature*, 494, pp.449-51.
- Risaliti, G. et al., 2011. *MNRAS*, 417, pp.178-83.
- Roca-Maza, X. et al., 2011. *Physical Review Letters*, 106(25), p.252501.
- Romanova, M.M. et al., 2008. *ApJL*, 673, pp.L171-74.
- Romanova, M.M. et al., 2013. *MNRAS*, 430, pp.699-724.
- Rosswog, S., 2010. *ArXiv e-prints (arXiv1012.0912)*.
- Ruderman, M., 1991. *ApJ*, 366, p.261.
- Russell, D.M. et al., 2012. *MNRAS*, 419, pp.1740-51.
- Salvaterra, R. et al., 2012. *ApJ*, 749, p.68.
- Samuelsson, L. & Andersson, N., 2007. *MNRAS*, 374, pp.256-68.

- Sathyaprakash, B.S. & Schutz, B.F., 2009. *Living Reviews in Relativity*, 12, p.2.
- Schmitt, J.H.M.M. & Favata, F., 1999. *Nature*, 401, p.44.
- Schwarz, G.J. et al., 2011. *ApJS*, 197, p.31.
- Shakura, N. et al., 2012. *MNRAS*, 420, pp.216-36.
- Shaposhnikov, N. et al., 2012. *ApJ*, 757, p.159.
- Smits, R. et al., 2009. *A&A*, 493, pp.1161-70.
- Sobolewska, M.A. et al., 2011. *MNRAS*, 417, pp.280-88.
- Sokoloski, J.L. et al., 2006. *Nature*, 442, pp.276-78.
- Steiner, A.W. & Gandolfi, S., 2012. *Physical Review Letters*, 108(8), p.081102.
- Steiner, A.W. et al., 2013. *ApJL*, 765, p.L5.
- Steiner, A.W. & Watts, A.L., 2009. *Physical Review Letters*, 103(18), p.181101.
- Stella, L. et al., 1999. *ApJL*, 524, pp.L63-66.
- Stone, J.R. & Reinhard, P.-G., 2007. *Progress in Particle and Nuclear Physics*, 58, pp.587-657.
- Strohmayer, T.E. & Brown, E.F., 2002. *ApJ*, 566, pp.1045-59.
- Strohmayer, T.E. & Markwardt, C.B., 2002. *ApJ*, 577, pp.337-45.
- Strohmayer, T.E. & Mushotzky, R.F., 2003. *ApJ*, 586, pp.L61-64.
- Strohmayer, T.E. & Watts, A.L., 2005. *ApJL*, 632, pp.L111-14.
- Strohmayer, T.E. & Watts, A.L., 2006. *ApJ*, 653, pp.593-601.
- Strohmayer, T.E. et al., 1996. *ApJL*, 469, p.9.
- Stuchlík, Z. et al., 2012. *AcA*, 62, pp.389-407.
- Suleimanov, V. et al., 2011. *ApJ*, 742, p.122.
- Suleimanov, V. et al., 2012. *A&A*, 545, p.120.
- Tagger, M. & Varnière, P., 2006. *ApJ*, 652, pp.1457-65.
- Tamii, A. et al., 2011. *Physical Review Letters*, 107(6), p.062502.
- Tanaka, Y. et al., 1995. *Nature*, 375, pp.659-61.
- Tatischeff, V. & Hernanz, M., 2007. *ApJ*, 663, pp.L101-04.
- Tauris, T.M. et al., 2012. *MNRAS*, 425, pp.1601-27.
- Tauris, T.M. & van den Heuvel, E.P.J., 2006. Cambridge, UK: Cambridge Astrophysics Series. pp.623 - 665.
- Taylor, J.H. et al., 1992. *Nature*, 355, pp.132-36.
- Thompson, C. & Duncan, R.C., 1995. *MNRAS*, 275, p.255.
- Tiengo, A. et al., 2013. *Nature*, 500, p.312.
- Török, G. et al., 2005. *A&A*, 436, pp.1-8.
- Török, G. et al., 2010. *ApJ*, 714, pp.748-57.
- Török, G. et al., 2012. *ApJ*, 760, p.138.
- Trippa, L. et al., 2008. *PhysRevC*, 77(6), p.061304.
- Tsang, M.B. et al., 2009. *Physical Review Letters*, 102(12), p.122701.
- Uttley, P. et al., 2011. *MNRAS*, 414, pp.L60-64.
- Vacchi, A. et al., 1991. *Nucl. Instr. and Meth.*, 306, p.187.
- van der Klis, M., 2006. In W.H.G. Lewin & M. van der Klis, eds. *Compact stellar X-ray sources*. pp.39-112.
- van der Klis, M. et al., 1985. *Nature*, 316, pp.225-30.
- van der Klis, M. et al., 1996. *ApJL*, 469, p.L1.
- van Straaten, S. et al., 2003. *ApJ*, 596, pp.1155-76.
- Vaughan, S. et al., 2011. *MNRAS*, 413, pp.2489-99.
- Venter, C. et al., 2012. *ApJ*, 744, p.34.
- Verbiest, J.P.W. et al., 2008. *ApJ*, 679, pp.675-80.
- Volonteri, M. & Bellovary, J., 2012. *Rep. Prog. Phys.*, 75, p.12.
- Wagoner, R.V. et al., 2001. *ApJL*, 559, pp.L25-28.
- Warner, B., 2004. *PASP*, 116, p.115.
- Watts, A.L. & Reddy, S., 2007. *MNRAS*, 379, pp.L63-66.
- Weinberg, N.N. & Bildsten, L., 2007. *ApJ*, 670, pp.1291-300.
- Wheatley, P.J. et al., 1996. *A&A*, 307, p.137.
- Wijnands, R. & van der Klis, M., 1998. *Nature*, 394, pp.344-46.
- Wilkins, D.R. & Fabian, A.C., 2013. *MNRAS*, 430, pp.247-58.
- Wilkinson, T. & Uttley, P., 2009. *MNRAS*, 397, pp.666-76.
- Wilms, J. et al., 2006. *A&A*, 447, pp.245-61.

Wiringa, R.B. et al., 1995. *PhysRevC*, 51, pp.38-51.

Witten, E., 1984. *PhysRevD*, 30, pp.272-85.

Wu, K., 2000. *SSRv*, 93, pp.611-49.

Yaqoob, T. et al., 2003. *ApJ*, 596, pp.85-104.

Zdunik, J.L. & Haensel, P., 2013. *A&A*, 551, p.61.

Zdziarski, A.A. et al., 2012. *MNRAS*, 423, pp.663-75.

Zhang, B. & Mészáros, P., 2002. *ApJ*, 581, p.1236.

Zoghbi, A. et al., 2012. *MNRAS*, 422, pp.129-34.

# 11 List of Acronyms

AGN	Active Galactic Nucleus	MHD	MagnetoHydroDynamic
AOCS	Attitude and Orbit Control System	MLI	Multi-Layer Insulation
ASIC	Application Specific Integrated Circuit	MOC	Mission Operations Centre
BH	Black Hole	MPPT	Maximum Power Point Tracking
BHCT	Black Hole Transient	MPS	Mission Planning System
CFDP	CCSDS File Delivery Protocol	MSP	MilliSecondPulsar
C&DH	Command and Data Handling	MTQ	MagnetoTorquer
CXB	Cosmic X-ray Background	NICER-	Neutron star Interior Composition
CONS	Consolidated (data)	SEXTANT	ExploreR
CSS	Coarse Sun Sensor	NIEL	Non-Ionising Energy Loss
EoS	Equation of State	NICA	Nuclotron-based Ion Collider Facility
eFoR	Extended Field of Regard	NRT	Near Real Time
ESA	European Space Agency	NS	Neutron Star
ESAC	European Space Astronomy Centre	NSCL	National Superconducting Cyclotron Laboratory
FAIR	Facility for Antiproton and Ion Research	NuSTAR	Nuclear Spectroscopic Telescope Array
FAR	Flight Acceptance Review	OBCP	On-board Control Procedures
FD	Flight Dynamics	OBT	On Board Time
FDIR	Failure Detection Isolation & Recovery	OGS	Operations Ground
FITS	Flexible Image Transport System	OTAC	Observing Time Allocation Committee
FRIB	Facility for Rare Ion Beams	PBEE	Panel Back End Electronics
FWHM	Full Width Half Maximum	PCA	Proportional Counter Array
FoR	Field of Regard	PDHU	Payload Data Handling Unit
GCR	Galactic Cosmic Rays	PDR	Preliminary Design Review
GEANT	“Geometry and tracking” simulation tool	PLM	Payload Module
GPS	Global Positioning System	POS	Preferred Operation Sequence
GNSS	Global Navigation Satellite System	PPS	Pulse Per Second
GSI	Helmholtzzentrum für Schwerionenforschung	PRR	Preliminary Requirements Review
GTO	Guaranteed Time	QCD	Quantum ChromoDynamics
ICU	Instrument Control Unit	QLA	Quick Look Analysis
IOC	Instrument Operations Centres	QM	Qualification Model
ISCO	Innermost Stable Circular Orbit	QPO	QuasiPeriodic Oscillation
LAD	Large Area Detector	RCS	Reaction Control System
LBAS	<i>LOFT</i> Burst Alert System	RMU	Rate Measurement Unit
LEO	Low Earth Orbit	RPE	Relative Position Error
LEOP	Launch and Early Operations	RW	Reaction Wheel
LGA	Low gain Antenna	RXTE	Rossi Timing Explorer
LHC	Large Hadron Collide	SAA	Solar Aspect Angle
LMXB	LowMass X-ray Binary	SAA	Southern Atlantic Anomaly
LOFAR	Low Frequency Array	S/C	Space Craft
LSDA	<i>LOFT</i> Science Data Archive	SDD	Silicon Drift Diode
LSST	Large Synoptic Survey Telescope	SDC	Science Data
LST	<i>LOFT</i> Science Team	SGR	Soft Gamma-ray Repeater
MAIT	Manufacture Assembly Integration and Test	SGS	Science Ground Segment
MBEE	Module Back End Electronics	SKA	Square Kilometer Array
MCP	MicroChannel Plate	SMOS	Soil Moisture Ocean Salinity
METOP	Meteorological Operational	SOC	Science Operations Centre
		STR	Star Tracker
		SVM	Service Module

SVOM	Space-based multi-band astronomical Variable Object Monitor
TAC	Time Allocation Committee
TDE	Tidal Disruption Event
TOO	Target of Opportunity
TRL	Technology Readiness Level
WFM	Wide Field Monitor
XSPEC	X-Ray Spectral Fitting Package

## 12 Acknowledgements

The LOFT Science Team is grateful to all members of the LOFT Instruments Teams, Science Working Groups<sup>8</sup>, Community<sup>9</sup> and supporters<sup>10</sup>, today reaching in total about 600 members. The success of the LOFT phase-A study could be achieved only thanks to the effort and support of everyone.

The LOFT Instruments Teams:

M. Feroci<sup>1,1b</sup>; J.W. den Herder<sup>2</sup>; E. Bozzo<sup>3</sup>; D. Barret<sup>8</sup>; S. Brandt<sup>19</sup>; M. Hernanz<sup>6</sup>; M. Pohl<sup>25</sup>; A. Santangelo<sup>17</sup>; S. Zane<sup>29</sup>; M. Ahangarianabhari<sup>14</sup>; L. Alvarez<sup>6</sup>; C. Amoros<sup>8</sup>; A. Argan<sup>1</sup>; B. Artigues<sup>6</sup>; P. Azzarello<sup>3</sup>; G. Baldazzi<sup>103</sup>; M. Barbera<sup>12,106</sup>; C. van Baren<sup>2</sup>; G. Bertuccio<sup>14</sup>; P. Binko<sup>3</sup>; P. Bodin<sup>114</sup>; L. Bradley<sup>29</sup>; C. Budtz-Jørgensen<sup>19</sup>; F.R. Cadoux<sup>25</sup>; P. Cais<sup>26</sup>; G.A. Caliendo<sup>6</sup>; R. Campana<sup>1,1b</sup>; F. Château<sup>16</sup>; E. Cavazzuti<sup>10</sup>; J. Coker<sup>29</sup>; A. Collura<sup>106</sup>; T. Courvoisier<sup>3</sup>; A. Cros<sup>8</sup>; E. Del Monte<sup>1,1b</sup>; J.P.C. Dercksen<sup>2</sup>; S. Di Cosimo<sup>1</sup>; S. Diebold<sup>17</sup>; Y. Evangelista<sup>1,1b</sup>; S. Fabiani<sup>77</sup>; Y. Favre<sup>25</sup>; C. Feldman<sup>35</sup>; G.W. Fraser<sup>35</sup>; M. Frericks<sup>2</sup>; F. Fuschino<sup>7</sup>; J.L. Galvez Sanchez<sup>6</sup>; E. Garcia-Berro<sup>6</sup>; A.B. Giles<sup>39</sup>; D. Götz<sup>16</sup>; M. Grassi<sup>56</sup>; M. Gschwender<sup>17</sup>; L. Guy<sup>3</sup>; D. Haas<sup>2</sup>; F. Hansen<sup>19</sup>; M. Hailey<sup>29</sup>; A. Hornstrup<sup>19</sup>; R. Hudec<sup>23,72</sup>; J. Huovelin<sup>45</sup>; J.J.M. in't Zand<sup>2</sup>; D. Karelin<sup>6</sup>; D. Kataria<sup>29</sup>; T. Kennedy<sup>29</sup>; S. Korpela<sup>45</sup>; I. Kuvvetli<sup>19</sup>; H.M. Jacobs<sup>2</sup>; F. Jetter<sup>17</sup>; P.P. Laubert<sup>2</sup>; C. Labanti<sup>7</sup>; I. Lecoeur-Taïbi<sup>3</sup>; D. Linder<sup>29</sup>; N. Lund<sup>19</sup>; D. Macera<sup>14</sup>; S. Maestre<sup>8</sup>; D. Maier<sup>17</sup>; P. Malcovati<sup>56</sup>; M. Marisaldi<sup>7</sup>; A. Martindale<sup>35</sup>; T. Mineo<sup>57</sup>; C. Motch<sup>65</sup>; G. Mouret<sup>8</sup>; J. Mulačová<sup>19</sup>; F. Muleri<sup>1,1b</sup>; P.E.H. Olsen<sup>19</sup>; P. Orleanski<sup>68</sup>; L. Pacciani<sup>1,1b</sup>; E. Perinati<sup>17</sup>; V. Petracek<sup>72</sup>; C. Pittori<sup>10</sup>; J. Portell<sup>6</sup>; P. Le Provost<sup>16</sup>; D. Rambaud<sup>8</sup>; M. Rapisarda<sup>1,1b</sup>; A. Rachevski<sup>77</sup>; I. Rachevskaya<sup>77</sup>; P. Ramon<sup>8</sup>; M. Reina Aranda<sup>63</sup>; R. de la Rie<sup>2</sup>; R. Rohlf<sup>3</sup>; A. Rousseau<sup>29</sup>; L. Sabau-Graziati<sup>63</sup>; J. Sandberg<sup>134</sup>; S. Schanne<sup>16</sup>; C. Schmid<sup>187</sup>; J.-Y. Seyler<sup>114</sup>; P.J. Smith<sup>29</sup>; P. Soffitta<sup>1</sup>; A. Spencer<sup>29</sup>; S. Suchy<sup>17</sup>; C. Tenzer<sup>17</sup>; A. Trois<sup>1</sup>; P. Uter<sup>17</sup>; A. Vacchi<sup>77</sup>; D. Walton<sup>29</sup>; H. Wende<sup>17</sup>; B. Winter<sup>29</sup>; G. Zampa<sup>77</sup>; N. Zampa<sup>77</sup>; F. Zwart<sup>2</sup>.

The LOFT Science Working groups:

M. van der Klis<sup>5</sup>; L. Stella<sup>27</sup>; A. Watts<sup>5</sup>; J. Wilms<sup>87</sup>; C. Albertus<sup>137</sup>; M. Alford<sup>139</sup>; A. Alpar<sup>4</sup>; D. Altamirano<sup>5</sup>; L. Amati<sup>7</sup>; N. Andersson<sup>9</sup>; A. Antonelli<sup>10</sup>; R. Artigue<sup>8</sup>; J.-L. Atteia<sup>8</sup>; P. Bakala<sup>86</sup>; S. Balman<sup>11</sup>; S. Bhattacharyya<sup>132</sup>; A. Baykal<sup>11</sup>; T. Belloni<sup>13</sup>; F. Bernardini<sup>111</sup>; S. Bianchi<sup>59</sup>; A. Bianchini<sup>15</sup>; P. Blay<sup>125</sup>; F. Bocchino<sup>99</sup>; I. Bombaci<sup>117</sup>; J.-M. Bonnet Bidaud<sup>16</sup>; S. Boutloukos<sup>17</sup>; J. Braga<sup>18</sup>; E. Brown<sup>49</sup>; N. Bucciantini<sup>21</sup>; L. Burderi<sup>22</sup>; M. Burgay<sup>115</sup>; M. Bursa<sup>23</sup>; E. Cackett<sup>111</sup>; S. Campana<sup>13</sup>; J. Casares<sup>82</sup>; P. Casella<sup>27</sup>; A.J. Castro-Tirado<sup>116</sup>; P. Cerda-Duran<sup>125</sup>; D. Chakrabarty<sup>28</sup>; J. Chenevez<sup>19</sup>; R. Cole<sup>29</sup>; R. Cornelisse<sup>82</sup>; A. Cumming<sup>31</sup>; G. Cusumano<sup>57</sup>; A. D'Ai<sup>12</sup>; V. D'Elia<sup>10</sup>; A. De Luca<sup>85</sup>; D. De Martino<sup>31</sup>; M. De Pasquale<sup>29</sup>; A. De Rosa<sup>1</sup>; T. Di Salvo<sup>12</sup>; I. Donnarumma<sup>1</sup>; A. Drago<sup>32</sup>; M. Durant<sup>33</sup>; D. Emmanoulopoulos<sup>107</sup>; M.H. Erkut<sup>135</sup>; P. Esposito<sup>85</sup>; A. Fabian<sup>24</sup>; M. Falanga<sup>34</sup>; V. Ferrari<sup>128</sup>; C. Ferrigno<sup>3</sup>; M. Finger<sup>133</sup>; M. H. Finger<sup>36</sup>; M. Gabler<sup>125</sup>; D.K. Galloway<sup>37</sup>; B. Gendre<sup>141</sup>; S. Gezari<sup>62</sup>; M. Gilfanov<sup>40</sup>; P. Giommi<sup>10</sup>; G. Giovannini<sup>102</sup>; M. Giroletti<sup>102</sup>; E. Gogus<sup>4</sup>; A. Goldwurm<sup>105</sup>; K. Goluchová<sup>86</sup>; C. Gouiffes<sup>16</sup>; P. Groot<sup>42</sup>; L. Gualtieri<sup>128</sup>; C. Guidorzi<sup>32</sup>; P. Haensel<sup>50</sup>; D.H. Hartmann<sup>42</sup>; C.A. Haswell<sup>43</sup>; K. Hebel<sup>140</sup>; A. Heger<sup>37</sup>; W. Hermsen<sup>2</sup>; J. Homan<sup>28</sup>; A. Ingram<sup>5</sup>; G. Israel<sup>27</sup>; K. Iwasawa<sup>20</sup>; L. Izzo<sup>47</sup>; T. Johannsen<sup>118,127</sup>; H.M. Jacobs<sup>2</sup>; P. Jonker<sup>2</sup>; J. Josè<sup>126</sup>; P. Kaaret<sup>49</sup>; G. Kanbach<sup>123</sup>; V. Karas<sup>23</sup>; L. Keek<sup>49</sup>; D. Klochkov<sup>17</sup>; W. Kluzniak<sup>50</sup>; K. Kokkotas<sup>17</sup>; C. Kouveliotou<sup>51</sup>; I. Kreykenbohm<sup>87</sup>; L.M. Kuiper<sup>2</sup>; D. Lai<sup>52</sup>; F.K. Lamb<sup>53</sup>; F. Lebrun<sup>105</sup>; D. Lin<sup>8</sup>; G. Lodato<sup>54</sup>; F. Longo<sup>55</sup>; T.J. Maccarone<sup>131</sup>; S. Mahmoodifar<sup>62</sup>; I. Mandel<sup>120</sup>; V. Mangano<sup>57</sup>; A. Manousakis<sup>50</sup>; A. Markowitz<sup>109</sup>; G. Matt<sup>59</sup>; I.M. McHardy<sup>107</sup>; A. Melatos<sup>60</sup>; M. Mendez<sup>61</sup>; S. Mereghetti<sup>85</sup>; S. Migliari<sup>20</sup>; R. Mignani<sup>29,108</sup>; M.C. Miller<sup>62</sup>; J.M. Miller<sup>49</sup>; G. Miniutti<sup>112</sup>; S. Morsink<sup>64</sup>; S. Motta<sup>13</sup>; M. Mouchet<sup>66</sup>; T. Muñoz-Darias<sup>9</sup>; I. Negueruela<sup>95</sup>; J. Neilsen<sup>28</sup>; A.J. Norton<sup>43</sup>; M. Nowak<sup>28</sup>; P. O'Brien<sup>35</sup>; M. Orienti<sup>102</sup>; M. Orío<sup>99,110</sup>; M. Orlandini<sup>7</sup>; J.P. Osborne<sup>35</sup>; R. Osten<sup>69</sup>; F. Ozel<sup>70</sup>; M. Paolillo<sup>119</sup>; A. Papitto<sup>6</sup>; J. M. Paredes<sup>20</sup>; A. Patruno<sup>5</sup>; B. Paul<sup>71</sup>; A. Pellizzoni<sup>115</sup>; A.V. Penacchioni<sup>47</sup>; M.A. Perez<sup>136</sup>; J. Pons<sup>95</sup>; A. Possenti<sup>115</sup>; J. Poutanen<sup>73</sup>; M. Prakash<sup>122</sup>; D. Psaltis<sup>70</sup>; G. Ramsay<sup>76</sup>; P.S. Ray<sup>78</sup>; N. Rea<sup>6</sup>; S. Reddy<sup>80</sup>; P. Reig<sup>113,81</sup>; R. Remillard<sup>28</sup>; C. Reynolds<sup>62</sup>; L. Rezzolla<sup>124</sup>; M. Ribo<sup>20</sup>; A. Riggio<sup>115</sup>; A. Rios<sup>138</sup>; P. Rodríguez-Gil<sup>82,104</sup>; J. Rodríguez<sup>16</sup>; P. Romano<sup>57</sup>; E.M.R. Rossi<sup>83</sup>; A. Rozanska<sup>50</sup>; F. Ryde<sup>84</sup>; G. Sala<sup>6</sup>; R. Salvaterra<sup>85</sup>; A. Sanna<sup>61</sup>; S. Scaringi<sup>130</sup>; J. Schee<sup>86</sup>; S. Shore<sup>117</sup>; R. Schneider<sup>27</sup>; A. Schwenk<sup>88</sup>; A.D. Schwobe<sup>89</sup>; A. Shearer<sup>90</sup>; A. Smith<sup>29</sup>; D.M. Smith<sup>58</sup>; V. Sochora<sup>23</sup>; P. Soleri<sup>61</sup>; B. Stappers<sup>91</sup>; A.W. Steiner<sup>80</sup>; N. Stergioulas<sup>92</sup>; G. Stratta<sup>27</sup>; T.E. Strohmayer<sup>93</sup>; Z. Stuchlik<sup>86</sup>; V. Sulemainov<sup>17</sup>; T. Takahashi<sup>94</sup>; F. Tamburini<sup>15</sup>; T. Tauris<sup>129</sup>; L. Tolos<sup>6</sup>; F. Tombesi<sup>62</sup>; J. Tomsick<sup>121</sup>; G. Torok<sup>86</sup>; J.M. Torrejon<sup>95</sup>; D.F. Torres<sup>96</sup>; A. Tramacere<sup>3</sup>; R. Turolla<sup>15</sup>; S. Turriziani<sup>101</sup>; P. Uttley<sup>5</sup>; P. Varniere<sup>105</sup>; S. Vaughan<sup>35</sup>; S. Vercellone<sup>57</sup>; V. Vrba<sup>97</sup>; S. Watanabe<sup>94</sup>; R. Wawrzaszek<sup>68</sup>; N. Webb<sup>8</sup>; N. Weinberg<sup>28</sup>; P. Wheatley<sup>98</sup>; R. Wijers<sup>5</sup>; R. Wijnands<sup>5</sup>; M. Wille<sup>87</sup>; C.A. Wilson-Hodge<sup>44</sup>; K. Wood<sup>78</sup>; L. Zampieri<sup>99</sup>; L. Zdzunik<sup>50</sup>; A. Zdziarski<sup>50</sup>; B. Zhang<sup>100</sup>.

<sup>8</sup> <http://www.isdc.unige.ch/loft/index.php/loft-team/science-working-groups>

<sup>9</sup> <http://www.isdc.unige.ch/loft/index.php/loft-team/community-members>

<sup>10</sup> <http://www.isdc.unige.ch/loft/index.php/structure-of-the-consortium/loft-supporter-page>

Affiliations: (1) IAPS-INAF, Rome, Italy, (1b) INFN, Sez. Roma Tor Vergata, Italy, (2) SRON, Utrecht, The Netherlands, (3) ISDC, Geneva University, Switzerland, (4) Sabanci University, Istanbul, Turkey, (5) University of Amsterdam, Amsterdam, The Netherlands, (6) IEEC-CSIC-UPC-UB, Barcelona, Spain, (7) INAF-IASF-Bologna, Bologna, Italy, (8) IRAP, Toulouse, France, (9) University of Southampton, United Kingdom, (10) ASDC, Frascati, Italy, (11) Middle East Technical University, Ankara, Turkey, (12) Palermo University, Italy, (13) INAF-OA Brera, Merate, Italy, (14) Politecnico Milano, Italy, (15) University of Padova, Italy, (16) CEA Saclay, DSM/IRFU/SAP, Gif sur Yvette, France, (17) IAAT University of Tuebingen, Germany, (18) INPE, Brazil, (19) Technical University of Denmark, Lyngby, Denmark, (20) DAM and ICC-UB, Universitat de Barcelona (IEEC-UB), Spain, (21) Arcetri Observatory, Firenze, Italy, (22) Cagliari University, Monserrato, Italy, (23) Astronomical Institute of the Academy of Sciences of the Czech Republic, Ondrejov, Czech Republic, (24) Cambridge University, United Kingdom, (25) DPNC, Geneva University, Switzerland, (26) Laboratoire d'Astrophysique de Bordeaux, France, (27) INAF-OA Roma, Monte Porzio Catone, Italy, (28) MIT, Cambridge, United States, (29) MSSL, Surrey, United Kingdom, (30) McGill University, Montréal, Canada, (31) INAF-OA Capodimonte, Napoli, Italy, (32) Ferrara University, Italy, (33) University of Toronto, Canada, (34) ISSI Bern, Switzerland, (35) Leicester University, United Kingdom, (36) Universities Space Research Association, Alabama, United States, (37) Monash University, Clayton, Australia, (38) Johns Hopkins University, Baltimore, United States, (39) University of Tasmania, Hobart, Australia, (40) MPA Garching, Germany, (41) Radboud University, Nijmegen, The Netherlands, (42) Clemson University, United States, (43) Open University, United Kingdom, (44) Astrophysics Office, NASA/Marshall Space Flight Center, Huntsville, United States, (45) University of Helsinki, Finland, (46) Durham University, United Kingdom, (47) Sapienza University and ICRA, Italy, (48) University of Iowa, United States, (49) Michigan state University, East Lansing, United States, (50) Copernicus Astronomical Center, Warsaw, Poland, (51) Science and Technology Office, NASA/Marshall Space Flight Center, Huntsville, United States, (52) Cornell University, Ithaca, United States, (53) University of Illinois, Urbana, United States, (54) Università degli Studi di Milano, Italy, (55) University of Trieste, Italy, (56) Pavia University, Italy, (57) INAF IASF, Palermo, Italy, (58) University of California, Santa Cruz, United States, (59) University of Rome III, Italy, (60) University of Melbourne, Parkville, Australia, (61) University of Groningen, The Netherlands, (62) University of Maryland, United States, (63) National Institute of Aerospace Technology (INTA), Torrejón de Ardoz, Spain, (64) University of Alberta, Edmonton, Canada, (65) Observatoire Astronomique de Strasbourg, France, (66) Université Paris Diderot 5, France, (67) INAF-OA Torino, Italy, (68) Space Research Centre, Warsaw, Poland, (69) Space Telescope Institute, Baltimore, United States, (70) University of Arizona, Tucson, United States, (71) Raman Research Institute, Sadashivanagar, India, (72) Czech Technical University in Prague, Czech Republic, (73) University of Oulu, Finland, (76) Armagh Observatory, United Kingdom, (77) INFN, Trieste, Italy, (78) NRL, Washington, United States, (80) University of Washington, Seattle, United States, (81) University of Crete, Greece, (82) Instituto de Astrofísica de Canarias, Tenerife, Spain, (83) Leiden Observatory, The Netherlands, (84) KTH Royal Institute of Technology, Stockholm, Sweden, (85) INAF-IASF-Milano, Milano, Italy, (86) Silesian University in Opava, Czech Republic, (87) University of Erlangen-Nuremberg, Germany, (88) Technische Universität, Darmstadt, Germany, (89) Leibniz-Institut fuer Astrophysik Potsdam, Germany, (90) National University of Ireland Galway, Ireland, (91) University of Manchester, United Kingdom, (92) Aristotle University of Thessaloniki, Greece, (93) Goddard Space Flight Center, Greenbelt, United States, (94) ISAS, Kanagawa, Japan, (95) University of Alicante, Sant Vicent del Raspeig, Spain, (96) ICREA, Barcelona, Spain, (97) Physical Institute of the Academy of Sciences of the Czech Republic, Prague, Czech Republic, (98) University of Warwick, Coventry, United Kingdom, (99) INAF-OA Padova, Italy, (100) University of Nevada, Las Vegas, United States, (101) University of Rome Tor Vergata, Italy, (102) INAF-IRA-Bologna, Italy, (103) University of Bologna and INFN section of Bologna, Italy, (104) Universidad de La Laguna, Santa Cruz de Tenerife, Spain, (105) APC, AstroParticule & Cosmologie, Université Paris Diderot, CEA/Irfu, Observatoire de Paris, Paris, France, (106) INAF- Osservatorio Astronomico di Palermo, Italy, (107) University of Southampton, Southampton, United Kingdom, (108) Kepler Institute of Astronomy, University of Zielona Góra, Poland, (109) University of California, San Diego, United States, (110) University of Wisconsin, United States, (111) Wayne State University, Detroit, United States, (112) Centro de Astrobiología (CSIC--INTA), Madrid, Spain, (113) Foundation for Research and Technology, Heraklion, Greece, (114) CNES, Toulouse, France, (115) INAF-OA Cagliari, Capoterra, Italy, (116) Instituto Astrofísica de Andalucía (IAAC-CSIC), Granada, Spain, (117) University of Pisa, Italy, (118) Perimeter Institute for Theoretical Physics, Waterloo, Canada, (119) Università di Napoli Federico II, Napoli, Italy, (120) University of Birmingham, United Kingdom, (121) University of California, Berkeley, United States, (122) Ohio University, United States, (123) Max-Planck-Institut fuer extraterrestrische Physik, Garching, Germany, (124) Max Planck Institute for Gravitational Physics, Germany, (125) University of Valencia, Spain, (126) Technical University of Catalonia, Spain, (127) Department of Physics and Astronomy, University of Waterloo, Canada, (128) Sapienza University, Rome, Italy, (129) Argelander-Institut für Astronomie, Bonn, Germany, (130) Institute for Astronomy K.U. Leuven, Celestijnenlaan 200D, 3001, Leuven Belgium, (131) Texas Tech University, United States, (132) Tata Institute of Fundamental Research, India, (133) Charles University in Prague, Czech Republic, (134) Jorgen Sandberg Consulting, Denmark, (135) Istanbul Kültür University, Turkey, (136) Fundamental Physics Department, Facultad de Ciencias-Trilingüe University of Salamanca, Plaza de la Merced s/n, E-37008 Salamanca, Spain; (137) Departamento de Física Atómica, Molecular y Nuclear, Facultad de Ciencias, Universidad de Granada, E-18071-Granada-Spain, (138) University of Surrey, United Kingdom, (139) Washington University in St. Louis, United States, (140) Technische Universität Darmstadt, Germany, (141) ARTEMIS, rue de l'église 31480 Lagrault St Nicolas, FRANCE.